Unfolding the regulation of stress response pathways upon liver injury

Niemeijer, M.C.

UNFOLDING THE REGULATION OF STRESS RESPONSE PATHWAYS UPON LIVER INJURY

Marije Niemeijer

Cover design: Jasper Kloosterboer

Thesis lay-out: Marije Niemeijer

Printing: Ipskamp Printing

ISBN: 978-94-6421-966-1

UNFOLDING THE REGULATION OF STRESS RESPONSE PATHWAYS UPON LIVER INJURY

Proefschrift

ter verkrijging van de graad van doctor aan de Universiteit Leiden,

op gezag van rector magnificus prof.dr.ir. H. Bijl,

volgens besluit van het college voor promoties

te verdedigen op 7 februari 2023

klokke 16:15 uur

door

Marie Cornelia (Marije) Niemeijer

geboren te Zuidhorn, Nederland

in 1991

Promotor: Prof. dr. B. van de Water

Promotiecommissie:

Prof. dr. H. Irth	
Prof. dr. J.A. Bouwstra	
Prof. dr. E.H.J. Danen	
Prof. dr. L.J.W. van der Laan	Erasmus Medical Center
Dr. H. Vrieling	Leiden University Medical Center

The research described in this thesis was performed at the division Drug Discovery and Safety of the Leiden Academic Centre for Drug Research (LACDR), Leiden University (Leiden, The Netherlands). The research was financially supported by IMI MIP-DILI project (grant agreement 115336) and the EU-ToxRisk project (grant agreement 681002) funded by the European Union under the Horizon 2020 programme.

Table of contents

Chapter 1

Introduction, aim and scope of thesis

Drug-induced liver injury (DILI) is one of the main reasons for drug attrition during pre-clinical and clinical phases of drug development as well as for drug withdrawal post-marketing[1]. The development of DILI can result in severe outcomes, giving high risk for liver failure and death with a fatality rate of 7.6%[2]. Therefore, it is of major concern during drug development and in the clinic. To improve the prediction and understanding of DILI at an early stage during drug development, there is a need for improved mechanism-based in vitro hepatotoxicity testing methods. The activation of specific adaptive stress response pathways is a way for cells to cope with drug-induced stress to restore homeostasis and is one of the early key events in the development of DILI[3,4]. Determining the activation of these stress responses could very well serve as early predictors for DILI. In this thesis, the regulation of the activation of adaptive stress responses has been studied using high content imaging, gene silencing and high throughput transcriptomics approaches to improve the understanding and prediction of DILI. Furthermore, the inter-individual variability in stress response activation was mapped to enable the usage of accurately defined uncertainty factors to account for human population variability for DILI liabilities during safety testing. In this chapter, a general introduction will be given of DILI, adaptive stress responses activation and liver in vitro models for studying hepatotoxicity, followed by an overview of this thesis.

Drug-induced liver injury

DILI has been classified into three different types; direct, idiosyncratic, and indirect DILI[5]. Direct DILI is recognized as being dose-dependent, predictable, and usually occurs within a short time frame. In contrast, idiosyncratic DILI is not dose-dependent, unpredictable, with a variable latency period, often not picked up in pre-clinical trials and has an incidence as low as 1 on 100.000 patients only affecting a small subpopulation of the patients[6]. Typically, the occurrence of idiosyncratic DILI is provoked by the combination of specific drug properties, patient characteristics and certain environmental factors. Indirect DILI, the third category proposed recently, involves liver injury associated with the indirect action of the drug such as provoking aggravation of pre-existing liver disease usually upon a long latency period.

Different cell types within the liver can be affected during liver injury, as such DILI is further categorized as being hepatocellular, cholestatic or mixed. During the acute phase of DILI this is defined by the ratio between alanine aminotransferase (ALT) and alkaline phosphatase (ALP) activity both expressed in relation to the upper limit of the normal range (ULN) defined as the R value. Depending on affected cell types, DILI can lead to various liver disease phenotypes, such as hepatic necrosis, hepatitis, cholestasis, hepatic steatosis, fatty liver or neoplasia. In severe cases having extensive hepatic necrosis, this may lead to acute liver failure whereafter liver transplantation is needed for survival. Of all liver failure cases, dependent on geographical area, 8 up to 26% was caused by DILI being one of the main causes for liver failure[7–9].

Monitoring the development of DILI traditionally relies on the assessment of the general function of the liver by measuring serum levels of ALT, aspartate aminotransferase (AST), ALP, glutamyl transpeptidase (GGT) and total bilirubin (TBL)[10]. The combination of biomarkers ALT and TBL are used as a prognostic marker for severe DILI during drug safety assessment, also referred to as the Hy's Law, with the criteria of ALT at least three times and TBL two times higher than ULN giving a risk of at least 10% for the need of a liver transplant or death[2,10,11]. However, especially TBL is only elevated upon significant hepatocellular injury and is not always specific for liver toxicity. Therefore, there is a need of novel mechanism-based biomarkers elevated at an early stage during development of DILI. Recent efforts enabled the identification of the biomarkers microRNA miR-122 and glutamate dehydrogenase (GLDH) as being highly liver-specific and more sensitive compared to traditional biomarkers[12–14]. Combining in silico modelling approaches, such as DILIsym developed by the DILI-sim Initiative[15], with the monitoring of both traditional and novel biomarkers aids in increasing accuracy of predicting DILI.

Adaptive stress response activation upon drug exposure

One of the key events leading to DILI is the activation of adaptive stress response pathways, a way for cells to cope with drug-induced stress and restore homeostasis[16]. These include the oxidative stress response pathway regulated by transcription factor nuclear factor erythroid 2-related factor 2 (NRF2/*NFE2L2*) and sensor Kelch Like ECH Associated Protein 1 (KEAP1)[17,18], the unfolded protein response (UPR) upon endoplasmic reticulum (ER) stress regulated by sensors activating transcription factor 6 (ATF6), eukaryotic translation initiation factor 2-alpha kinase 3 (PERK/*EIF2AK3*) and inositol-requiring enzyme 1α (IRE1α/*ERN1*)[19–21], the DNA damage response regulated by transcription factor tumor protein p53 (p53/*TP53*)[22–24] and the inflammatory response regulated by transcription factor nuclear factor kappa-light-chain-enhancer of activated B cells (NF-κB)[23–26]. Qualifying and quantifying the activation dynamics of these stress response pathways upon drug exposure could aid in the prediction of the development of DILI. Indeed, the usage of a panel of stress response BAC-GFP reporter HepG2 cell lines together with high-content single cell confocal imaging enabled to recognize drugs classified with a DILI-concern[27–29]. Transcriptomic approaches reveal activation of specific gene networks such as stress response activation upon drug exposure that can inform on DILI susceptibility. Advances in the field of transcriptomics, such as targeted RNA-sequencing TempO-seq technology[30], enables to screen candidate drugs at a higher-throughput level and establish dose-response relationships at both the single gene and network level[31,32].

Liver in vitro models for safety testing

Liver cancer cells, such as HepG2, have been extensively used in mechanistic studies to predict and unravel underlying molecular mechanisms of drug-induced hepatotoxicity and is a highly reproducible, cost-effective and easy to handle liver test system. However, these transformed cell lines express very low amounts of liver specific enzymes and transporters localized at the

membrane[33]. Due to low amounts of liver specific enzymes, the effect of the formation of reactive metabolites on the induction of hepatotoxicity and activation of specific stress responses is likely overlooked in this in vitro test system. In addition, other pathways may be activated due to their capability of unlimited cell division and self-renewal. Due to these shortcomings, transformed immortal liver cell lines may not be the ideal in vitro model to study underlying molecular mechanisms of DILI.

Primary human hepatocytes (PHHs), currently still the gold standard, possess relatively high expression of enzymes and transporters most comparable to the human liver[34]. In addition, PHHs allow to study inter-individual variability by evaluating toxicological responses in PHHs derived from multiple donors. However, since these are scarcely available, do not divide and dedifferentiate over time especially when applied as a monolayer culture, there is a need for other liver in vitro systems having an unlimited source, remain stable and highly reflective of the human liver. To allow long-term culture of PHHs, recently different techniques have been developed, such as dedifferentiation towards hepatic progenitor cells enabling expansion[35,36], blockage of the dedifferentiation process[37] or by culturing them in a 3D structure as spheroids, microtissues or organoids[38–41]. Although advances have been made, expansion is still limited or do not entirely reflect fully mature hepatocytes. Alternatively, using the upcyte technology PHHs can be transformed allowing unlimited expansion although reduces hepatocyte functionality[42].

Another source is the HepaRG cell line consisting of hepatic progenitor cells, derived from a patient with hepatocarcinoma and hepatitis C infection, which can be differentiated towards mature hepatocytes expressing similar levels for many cytochrome P450 (CYP) enzymes as PHHs[43]. On transcriptome level, HepaRG cells in 3D setup more closely resemble liver tissue than HepG2 although not as similar as PHHs[44]. Despite, both PHHs and HepG2 cells appeared to be more accurate in recognizing drugs classified with a DILI-concern than HepaRG[45]. Moreover, the need of differentiation results in higher costs and is more time-consuming compared to HepG2. Since both HepaRG and HepG2 cells derive from only a single donor, they do not allow for the evaluation of inter-individual variability. More specifically, HepaRG derived from a donor being a poor metabolizer for CYP2D6 affecting its sensitivity for drugs metabolized by CYP2D6[46].

Recently, great progress has been made in the generation of hepatocytes from human induced pluripotent stem cells (hiPSCs) derived from somatic cells. In 2006, Takahashi and colleagues were the first to generate such hiPSCs[47]. These hiPSCs are capable of being differentiated in all three germ lines, namely endoderm, mesoderm and ectoderm. Indeed, hiPSCs can be transformed into any cell type of interest. Recent reports showed that hiPSCs can be efficiently differentiated into hepatocyte-like cells (HLCs)[48–51]. HiPSCs are first differentiated into definitive endoderm via stimulation with Activin A, a member of the TGF-β superfamily and mimics Nodal signaling[52]. Thereafter, hepatoblast formation is initiated by certain growth factors. Eventually, these hepatoblasts are differentiated into immature and subsequent mature hepatocytes.

Various differentiation protocols have been described resulting in HLCs, which were capable of albumin secretion, urea production, glucose storage, and drug metabolism and transport[48–51,53]. Deriving hiPSCs from multiple donors allows for the evaluation of inter-individual variability in drug-induced toxicity in the cell type of interest such as HLCs[54]. To further mimic the human liver, hiPSC-derived HLCs are combined with other liver cell types such as Kupffer and stellate cells enabling to study multi-cellular responses[55,56]. Culturing these cells in a 3D format or within an organ-on-a-chip platform could advance maturation and resembles the environment in vivo[57,58]. Although, great progress has been made in mimicking the differentiation process and 3D environment, hiPSC-HLCs still do not reach the full maturation status of PHHs in vivo and needs further optimization.

To improve the recognition of DILI liabilities during drug safety testing it is of great importance to further improve or establish novel liver in vitro test systems as well as further characterization and thorough comparisons of existing test systems. This will allow for optimal selection of test systems fit-for-purpose in a tiered approach to improve drug safety testing strategies. Since the activation of stress response pathways are one of the early key events in the development of DILI, it is essential to accurately map the difference in activation of these responses and sensitivity between different liver in vitro test systems such as HepG2, hiPSC-HLCs and PHHs which is currently still lacking. Furthermore, mapping of the impact of the culture method, such as 2D vs 3D or type of culture medium, on stress response activation and sensitivity for drug-induced toxicity is vital. Also, currently the tight regulation of these stress responses and the switch towards cell death signalling is not yet fully understood. Here, improved insight will aid in a better prediction of DILI liabilities. During drug safety testing to account for inter-individual variability, currently the standard safety factor of 10 is used[59]. However, this standard factor is not data-driven, endpoint or drug specific and may not be enough to capture the full variability within the population. Therefore, there is a high need to accurately map the inter-individual variability in drug-induced toxicity and stress response activation to allow for the usage of data-driven safety factors to improve risk assessment.

Overview of the thesis

In this thesis, the regulation and inter-individual variability of the activation of stress response pathways upon drug exposure has been studied to improve the mechanistic understanding and prediction of DILI. Here, an overview will be given of the individual chapters.

In **chapter 2**, an overview is given of the utility of stress response BAC-GFP HepG2 reporters for the assessment of DILI liabilities of drugs and increase mechanistic understanding by combining with RNAi screening approaches. Here, key stress response pathways and the development and technical usage of the reporters are described.

The mapping of the crosstalk between the oxidative stress and DNA damage response is described in **chapter 3**. By using the HepG2 BAC-GFP reporters for both adaptive stress response

pathways in combination with live confocal imaging at single cell level, dose-response relationship and activation dynamics upon chemical exposure could be identified. By combining with RNAi-mediated silencing of specific genes within the oxidative stress or DNA damage response, the interplay between both pathways upon chemical exposure was mapped.

In **chapter 4**, the influence of the culture method of HepG2 BAC-GFP DNA damage reporters on the sensitivity to identify genotoxicants was studied. HepG2 reporter cells were cultured in 2D or 3D setup using standard or amino-acid rich (AAGLY) medium, exposed with genotoxic compounds and imaged using confocal microscopy. This enables to define a testing strategy of genotoxicants possibly in a tiered approach.

The regulation of CHOP during chemical-induced ER stress and UPR activation is determined in **chapter 5**, by combining computational modelling with confocal imaging of HepG2 BAC-GFP UPR reporters upon chemical exposure. The UPR was induced using tunicamycin in a broad concentration range and followed by ATF4, XBP1, CHOP and BIP-GFP reporter activation. Based on this data, a dynamic model was constructed exemplifying the crucial role of ATF6 in CHOP regulation.

To further dissect the regulation of CHOP and the UPR, we performed a large siRNA screen, targeting 3,457 genes, in HepG2 CHOP-GFP cells described in **chapter 6**. Here, the influence of silencing of individual genes on CHOP upregulation during chemical exposure is evaluated. The role of key regulators of CHOP, which were validated upon a secondary screen, is evaluated in both HepG2 and PHHs using a transcriptomics approach.

In **chapter 7**, the difference in regulation of stress response activation upon chemical exposure was evaluated using a targeted transcriptomics approach between different liver in vitro models, namely HepG2 cells, PHHs and hiPSCs-HLCs. Specific inducers for the oxidative stress response, UPR, DNA damage response and inflammation signalling was used in a broad concentration range.

To evaluate the inter-individual variability in stress response activation in **chapter 8**, the transcriptome of a panel of PHHs derived from 50 donors was evaluated upon exposure with specific stress inducers in a broad concentration range. Dose-response modelling allowed to evaluate the variability in the point-of-departures for gene induction. This was combined with computational modelling to evaluate the probability in estimating the correct variability and defining safety factors to correct for inter-individual variability during risk assessment.

In **chapter 9** I will discuss the overall outcome of the studies and identify requirements for future research

.

Chapter 2

Systems microscopy approaches in unravelling and predicting DILI

This chapter has been published as:

M. Niemeijer, S. Hiemstra, S. Wink, W. den Hollander, B. ter Braak, B. van de Water

Systems microscopy approaches in unraveling and predicting DILI

In: Chen M., Will Y. (eds) Drug-Induced Liver Toxicity. Methods in Pharmacology and Toxicology.

Humana, New York, NY. 2018. doi: 10.1007/978-1-4939-7677-5_29

Abstract

The occurrence of drug-induced liver injury (DILI) after drug approval has often led to withdrawal from the market. Especially idiosyncratic DILI forms a major problem for pharmaceutical companies, due to its independency of dose or duration of exposure, idiosyncratic DILI is considered as unpredictable. New in vitro test systems are now evoking to improve the prediction of DILI in the pre-clinical phase of drug development. Most conventional compound toxicity screening systems rely on single end-point assays most of which are based on relatively late-stage toxicity markers. When monitoring key events upstream in various adaptive stress signalling pathways combined in a single assay, the sensitivity to pick up hepatotoxic drugs will be increased while also mechanistic insight will be gained. Integrating with high-content imaging (HCI), time and high resolution single cell dynamics can be captured together with features for translocation between specific subcellular compartments. Efforts have been made to use specific dyes, antibodies or nanosensors in a multiplexed fashion using HCI, to assess multiple toxicity markers. However, these markers are still relatively downstream of toxicity signalling pathways which do not pinpoint to the molecular initiation event (MIE) of a drug. Here, we describe the application of a HepG2 BAC GFP reporter platform for the assessment of DILI liabilities by monitoring key components of adaptive stress pathways combining with HCI. Detailed insight in the regulation of these adaptive stress pathways during drug adversity can be reached by integrating these reporters with RNAi screening. Ultimately, this may lead to the recognition of novel biomarkers which can be used in the development of novel toxicity testing strategies.

Keywords: Systems microscopy, drug-induced liver injury, stress-response dynamics, BAC-GFP reporter platform, mechanism-based toxicity screening

Introduction

Drug-induced liver injury (DILI) can present in various different pathologies: e.g. cholestasis (accumulation of bile), steatosis (accumulation of fatty acids) or phospholipidosis (accumulation of phospholipids). Mostly, these are mild perturbations, which will be counteracted by the target tissue ultimately establishing a new physiological homeostasis. However, DILI can also lead to severe liver failure due to a necrotic liver or extensive inflammatory responses. Of all liver failures presented in the clinic, > 50% are caused by drugs[7]. A large amount of these liver failures is caused by an overdose of acetaminophen. However, still 13% of all liver failures are caused by drugs taken on other prescribed dose regimens[7]. In most cases, these adverse reactions are called idiosyncratic reactions; idiosyncratic DILI (iDILI) occurs in rare cases and has a variable latency time. These features are the main reason these drugs are missed during preclinical safety testing and that liver injury is the leading cause for drug market withdrawal[60].

Cellular and biochemical perturbations underlie DILI, primarily in hepatocytes, that contribute to adverse outcome[61]. The past decade, the field of predictive toxicology has initiated the integration of mechanistic insights in chemical adversity in toxicological screening approaches. Adaptive stress response pathways are central in toxicological responses[3,4]. The amplitude of adaptive stress response pathway activation is the determining factor in the switch between adaptation and cell death, which makes them essential in toxicity. Quantitative assessment of adaptive stress responses and key event activation likely will contribute to a more accurate prediction of DILI based on mechanistic insight[62].

For quantitatively monitoring the adaptive stress response activation in drug safety assessment, systems microscopy will be essential. We define systems microscopy as the systematic high-throughput and high-content quantitative understanding of cell biology. Systems microscopy can be used to grasp detailed single cell protein dynamics, providing its own niche to cover the mechanistic insight spectrum in toxicological screening. Various imaging-based approaches have been established that enable the quantification of biological changes during chemical exposure[63–76]. These approaches have largely been based on the use of specific cell permeable dyes in a multiplexed fashion as indicators for the development of cellular injury in real-time in combination with automated high-content screening (HCS). In these assays, cellular structures such as nuclei, mitochondria or the cellular membrane as well as specific functional characteristics like transporter activity, or mitochondrial function can be assessed and applied in the prediction of DILI [63–73]. While these approaches allow the quantification of various biochemical markers for toxicants, these are conventional late markers of cell injury and in close proximity to the tipping point towards cell death. These markers provide limited insight in adaptive stress response pathway activation, which typically occurs earlier and at lower concentrations and are likely more representative for the mode of action (MoA). More MoA-related markers that reflect the adaptive stress response pathways may increase the sensitivity to identify hepatotoxicity liabilities. Ideally, high resolution time dynamics of multiple key events in the early phase of stress signalling pathways would be monitored on single cell level to improve the prediction and understanding of DILI liabilities. In this chapter, we will discuss the application of fluorescent protein reporter cell lines to monitor these adaptive stress signalling pathways using a systems microscopy approach to improve DILI liability assessments.

Adaptive stress response pathway activation and DILI

Cellular stress can lead to adaptation via activation of adaptive stress responses; however when the cell cannot cope with the severity of the stress, adaptive stress responses will switch to adversity and will induce cytotoxicity. The mechanism of how these stress responses exert their function in adaptation is reviewed extensively in previous reviews[3,4,77–81]. Therefore, here, we will briefly discuss four prominent main stress response pathways and their involvement in adaptation and relationship to cellular adverse outcomes.

Anti-oxidant response: Xenobiotic exposure can induce large amounts of reactive oxygen species (ROS). ROS accumulation may affect KEAP1 cysteine residues determining Nrf2 stabilization and subsequent nuclear translocation. In the nucleus, Nrf2 transcribes a large battery of anti-oxidant proteins which can detoxify the cell[77]. Yet, when the induced ROS is overwhelming, adaptation cannot rescue the overall overt cellular damage, thus leading to onset of cell death due to perturbation of both cellular bioenergetics and redox homeostasis[82]. The Nrf2-dependent oxidative stress response exemplifies the relevance of adaptive stress responses in the protection against liver injury: Nrf2 knock out mice are highly susceptible to various hepatotoxicants[83–85].

ER stress and unfolded protein response (UPR): When cells suffer from impaired protein folding, the load of unfolded proteins will accumulate in the endoplasmic reticulum (ER). To reduce the amount of unfolded proteins, three UPR signalling branches, involving PERK, IRE1α and ATF6 activation, ensure production of chaperones including BiP, enlargement of the ER capacity and inhibition of the translational machinery. In addition, the UPR induces the expression of the transcription factor C/EBP homologous protein (Chop). Chop subsequently initiates transcription of target genes that trigger the onset of apoptotic signaling[86,87]. Thus, Chop is a critical factor in the switch from adaptation to adversity in the unfolded protein response. This is illustrated by studies of Chop knock out mice which have reduced liver injury after acetaminophen treatment[88,89].

DNA damage response: Upon accumulation of single or double stranded DNA breaks or covalent modification of nucleotides, various sensor and kinase signalling events result in the accumulation of p53. P53 is known as a tumor suppressor as it reduces the effects of massive DNA damage[80]. In the adaptive phase it activates cell cycle inhibitors, such as p21, and DNA repair mechanisms. However, upon severe DNA damage, p53 is able to transcribe apoptosis regulators as BAX, FAS, NOXA and PUMA[90]. This results in a key role for p53 in the switch between adaptation and cell death by apoptosis.

Inflammatory TNFα signalling: Inflammatory signalling is initiated by the production of cytokines by immune cells such as resident liver Kupffer cells. Pro-inflammatory cytokine TNFα is able to bind the TNFα-receptor which results in NF-κB translocation and subsequent target gene expression[81]. Together these target genes induce an inflammation response to clear potential cellular damage and inhibit the onset of death receptor-mediated apoptosis. However, certain cytokine/drug combinations can induce synergistic cell death, whereby the anti-apoptosis signalling by the TNFα-receptor is switched to a pro-apoptotic signalling route[25]. This exemplifies the subtle switch from adaptation to adversity by otherwise cytoprotective cytokine signalling.

These four adaptive stress responses demonstrate that cellular states can easily switch from re-establishment of cellular homeostasis after injury to necrosis and/or apoptosis. The amplitude and duration of stress response pathway activation are likely critical determinants for final cellular outcome. By quantitatively assessing the activation of these adaptive stress pathways by

candidate drugs using a reporter system combined with systems microscopy, insight may be given in their DILI liabilities at the early-phase of toxicity signalling.

A HepG2 BAC-GFP reporter platform as a tool for predicting and unravelling DILI

To allow the assessment of adaptive stress response activation over time, we tagged different key components of the ER stress response, oxidative stress response, TNFα inflammation and DNA damage response pathways with enhanced green fluorescent protein (eGFP) in hepatocellular carcinoma HepG2 cells. Confocal microscopy enables us to monitor live cell dynamics in a high-throughput fashion. GFP is integrated with bacterial artificial chromosome (BAC) recombineering technology: BACs are large plasmids (~150-200 kB) able to carry a whole eukaryotic locus including introns and promotor regions. In 2008, Poser et al. established a method to apply GFP-tagging of BACs in a high-throughput manner[91]. We used this BAC recombineering method to tag different components of adaptive stress responses with GFP[27,79]. Transfection of BAC-GFP constructs allows the incorporation of very large pieces of DNA in the host genome, ultimately ensuring control of the engineered genes by the endogenous promotor region and other regulatory sequences. In relation to the earlier introduced adaptive stress response pathways, we have generated a broad range of BAC-GFP reporter lines aimed to capture the complexity of DILI[27,79].

Development of the reporter platform

Below we describe the detailed approach to establish BAC-GFP reporters. We introduce these reporters in HepG2 cells, but any other cell line can be used.

Identification of a stress pathway specific biomarker. Both literature and transcriptomics mining allows the discovery of hepatotoxic drug responses (e.g. TG-GATES and Drug Matrix) and the identification of candidate biomarker genes that can be translated into reporter assays[92,93]. In this way, key regulators of specific adaptive stress pathways have been identified. For our HepG2 BAC-GFP platform, both early sensors, downstream transcription factors and their subsequent target genes were selected to resemble the activation of critical stress response pathways at different signalling levels.

Cloning of the BAC-GFP plasmid. Using an online tool (http://www.mitocheck.org/cgi-bin/BACfinder), BAC constructs can be ordered that contains the selected human gene of interest, containing all the regulatory elements; also the necessary GFP overhang primers can be found here. Using a multi-step cloning strategy, the BAC-GFP fusion plasmid can be generated[91].

Transfection and cell reporter cloning. HepG2 wildtype cells are seeded in a 6-well plate format and simultaneously transfected (lipofectamin-based) to introduce the BAC-GFP construct to the cells. Geneticin (G418) selection is used to select BAC-GFP HepG2 positive clones. Monoclonal BAC-GFP HepG2 clones are picked (generally 10 to 24 clones) and expanded. PCR is used to confirm correct genomic integration of the BAC-GFP. Next, the expression of the target gene (quantitative PCR) and protein (Western blot) is determined to quantify the levels of GFP-tagged

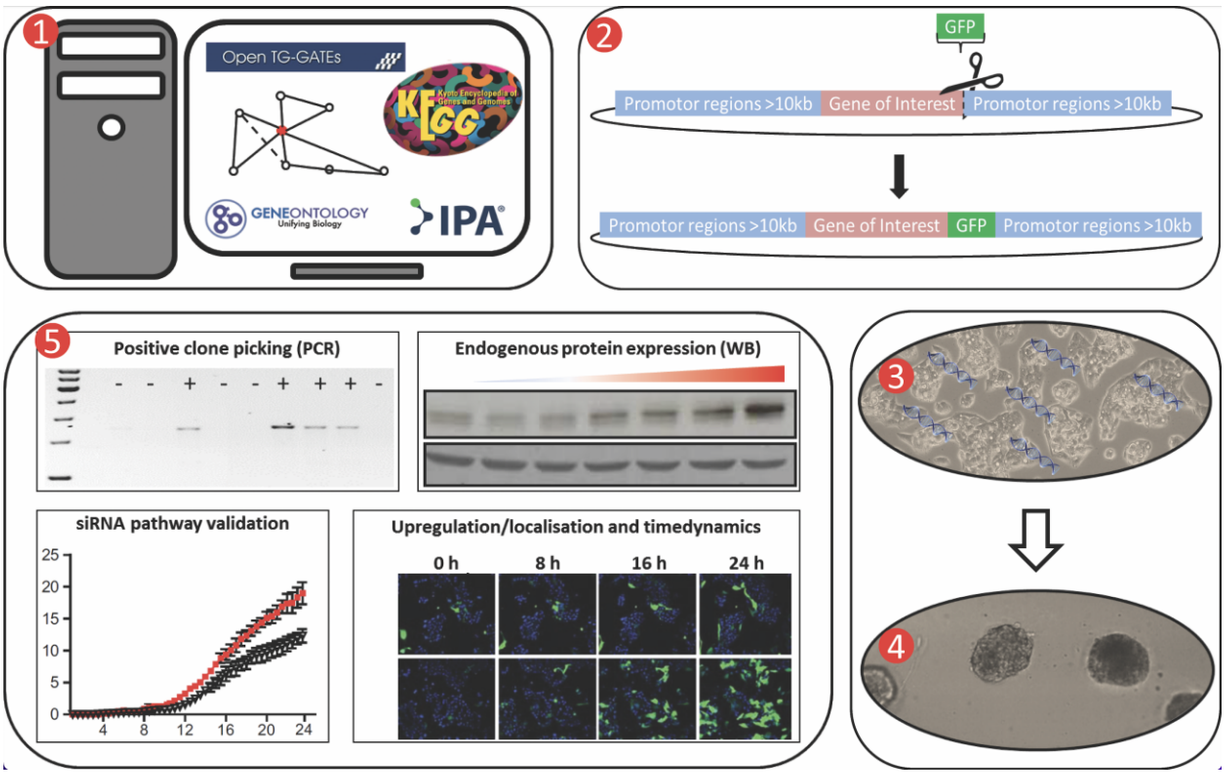

Fig. 1. Generation of the HepG2 BAC reporter platform. 1. Identifying the target proteins that can serve as biomarkers for certain stress responses. 2. Generating the BAC-GFP fusion plasmid. 3.Transfect HepG2 wt cells. 4. Selection and clonal expansion. 5. Validation of the HepG2 BAC reporters.

target gene or protein. The GFP-fusion protein size should correspond to the corresponding gene fusion product. Live cell imaging will then validate a correct localization of the GFP-protein fusion, the population variability, and the inducibility by xenobiotic treatment. At last, RNA interference experiments are performed to verify GFP-target gene specificity. See figure 1 for an overview of BAC-GFP reporter line generation.

Application of BAC-GFP HepG2 reporters

The BAC-GFP reporter panel covers multiple adaptive stress responses (e.g. oxidative stress response, ER stress response, DNA damage response and NF-κB signalling) at different signalling levels and is able to reveal subcellular localization of the different components during stress induction when combined with confocal microscopy. Furthermore, intracellular translocation events and specific cellular accumulation can be captured with this system. The analysis of the GFP signal in each subcellular compartment needs a different image analysis strategy which is based on the usage of CellProfiler and ImageJ (Fig. 2). Retrieved data sets can contain cell population as well as single cell features making it possible to capture valuable single cell dynamics. Thus, the use of high-content high-throughput imaging of BAC-GFP reporter cell lines enables identification of spatial-temporal single cell dynamics of adaptive stress response cellular signalling underlying DILI.

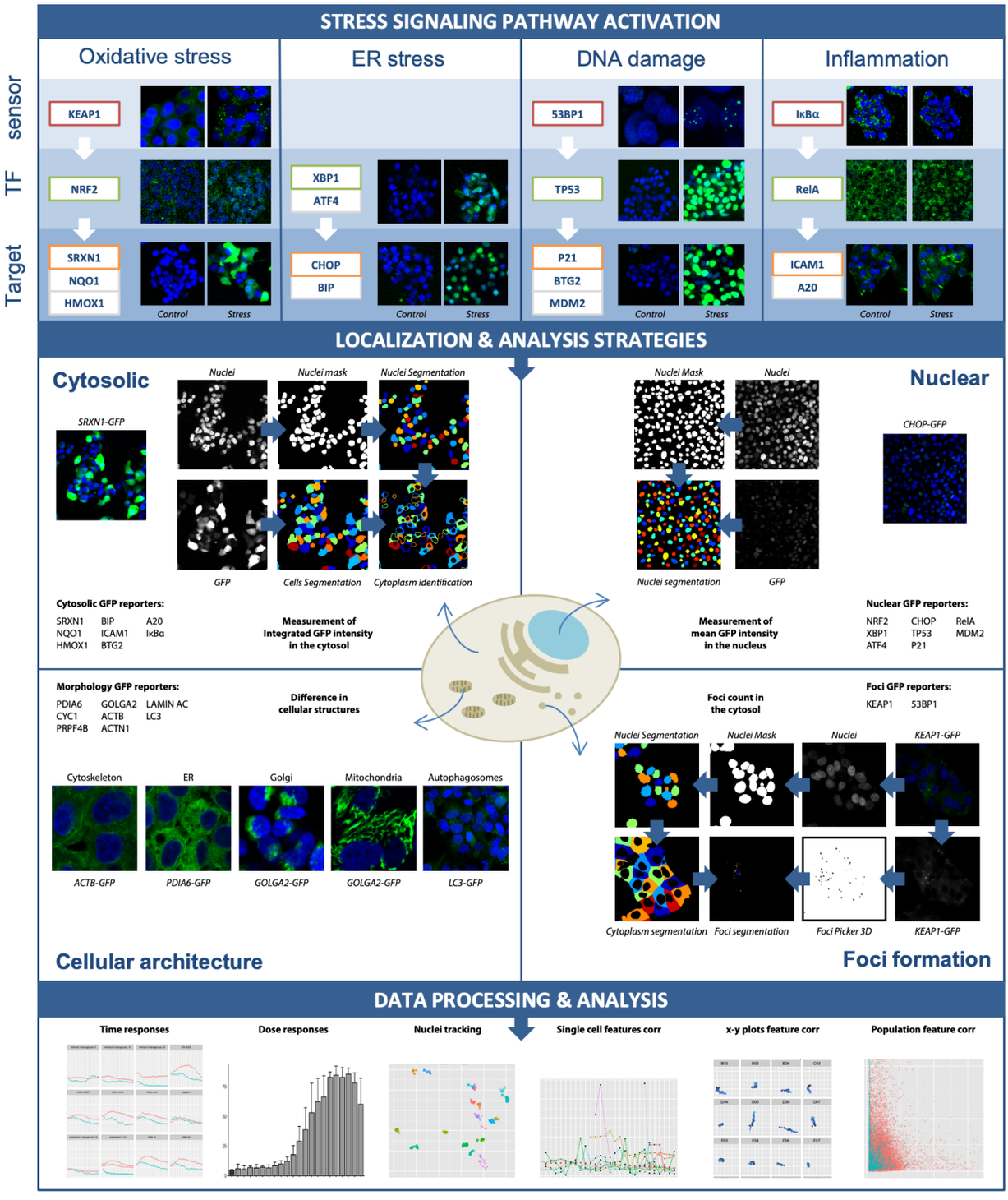

Fig. 2. Overview of HepG2 BAC-GFP reporter platform. Overview of different reporters for the oxidative stress, ER stress, DNA damage or inflammation response sensing at different levels with the signalling pathway. Depending on the specific reporter, GFP signal can be quantified either in the cytosol, nucleus, in foci or alterations in cellular structure can be examined. Each strategy has its own specific segmentation and analysis pipeline. In the end, high-content data can be further processed to obtain time or dose responses, single cell tracking, subpopulations identifications or specific translocation in between different subcellular compartments.

We see two major application domains for BAC-GFP reporters in the context of DILI: prediction and mechanistic understanding. The application of the BAC-GFP reporter system in the DILI

prediction domain allows to identify the activation levels of multiple adaptive stress responses giving a certain MoA toxicity fingerprint for each drug.

These fingerprints can be linked to DILI liability classification and used for future hazard identification of potential new drugs. In this way, DILI liabilities can be predicted and simultaneously reveal the underlying MoA. The other domain, namely the application in mechanistic studies, focuses on the underlying cause of toxicity in contrast to DILI predictions and obtains a better understanding of why some patients are more prone to develop DILI. In addition, this may give more insight in the precise regulation of these adaptive stress responses and their balance between adaptation and adversity. Here, we will present examples of the application domains of these BAC-GFP reporters.

Drug testing for cellular stress pathway activation supporting the prediction of DILI

DILI prediction can make use of features specific to drugs attributed as a DILI liability. We performed an imaging-based screen with a set of 131 drugs classified as either most-, less- or non-DILI concern by Chen et al.[94] in a broad concentration range using a panel of 8 different BAC-GFP reporter cell lines. The BAC reporters used involved Srxn1 and Hmox1 (oxidative stress); Chop and BiP (ER stress pathway); Hspa1b (heat shock response); p21 and Btg2 (DNA damage); Icam1 (cytokine signalling) (Fig. 3). The responses of the different reporters together show clusters of drugs enriched for most-DILI classification which activates one or more adaptive stress responses. In this way, utilizing a classifier a prediction of the DILI liability can be made based on its adaptive stress responses activation pattern for newly developed drugs.

A major advantage of the BAC-GFP reporter cell lines is the imaging-based assessment of the dynamics of the cellular stress response activation. The definition of transcription factor activation and oscillatory behaviour dynamics as well as the rate and induction of key-node signalling proteins will be an important future application to better understand DILI related stress responses. Recently, we used high-content imaging single cell temporal dynamics of several BAC-GFP reporters for statistical inference and demonstrated the possibility to capture imaging-based single cell temporal responses in so called base functions[95]. Functional data analysis opens up possibilities of detailed temporal dynamic information including transcription factor translocation rates, calculations of local maxima and oscillatory periods or dampening parameters; the latter finds applications for oscillatory signalling processes such as observed for NF-κB. Thus, we have applied the NF-κB reporter to quantify the oscillatory perturbations following exposure to DILI drugs linked to inflammatory signaling[96]. Perturbations of NF-kB oscillatory behaviour will affect the downstream target gene activation and hence affect the biological outcome of cytokine-mediated signalling. Here, NF-κB oscillatory behaviour in single cells was tracked during time-lapse imaging. Our high-content imaging and image analysis approach allowed us to define that diclofenac and carbamazepine inhibits the oscillatory

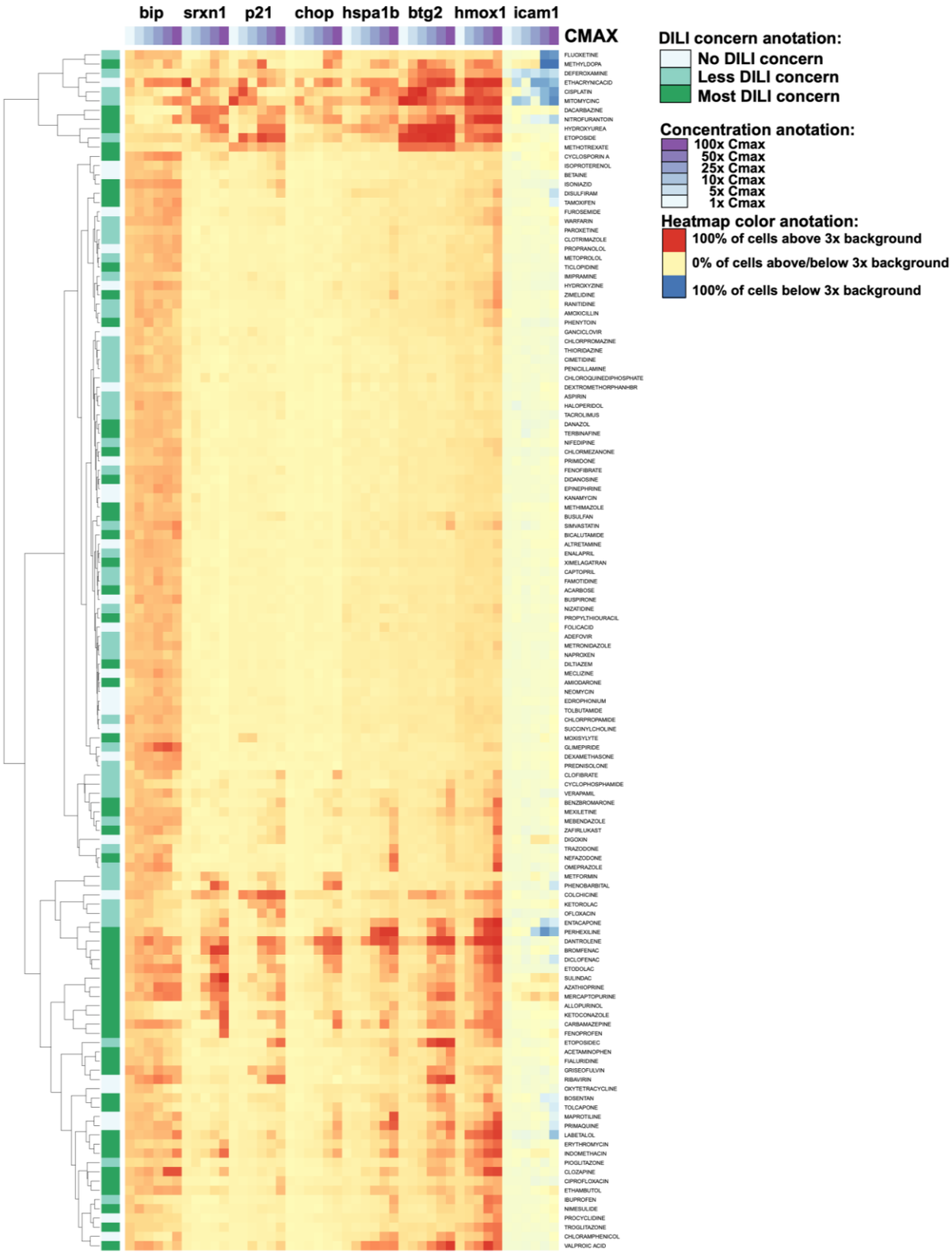

Fig. 3. Heatmap of the effect of a set of 131 classified drugs on the activation of multiple adaptive stress BAC-GFP reporters. The drug set consists of drugs classified as either most-, less- or non-DILI. HepG2 BAC-GFP reporters (BiP-, Srxn1-, p21-, Chop-, HSPA1B-, Btg2-, Hmox1- and ICAM1-GFP) were exposed for 72 hours to drugs in a broad concentration range (1 to 100x Cmax) and imaged using confocal microscopy. GFP activation levels are depicted as fraction of cells three times above the background levels.

behaviour of NF-κB. This effect was associated with a sensitization to TNFα-induced pro-apoptotic signalling.

Identification of novel key regulators of stress signalling pathways

There is a need to gain insight in the underlying mechanisms of DILI. One aspect involves the unravelling how drugs perturb the cellular physiology and as a consequence switch on cellular stress responses that define cellular adaptation or adverse outcomes. Such improved mechanistic understanding will identify candidate biomarkers that can be integrated in safety testing strategies in either early drug development or as part of the investigative toxicology toolbox[97].

Revealing underlying mechanisms of DILI using BAC-GFP stress response reporters

Toxicogenomics has been an efficient means to hypothesize mechanisms[92,93,98]. Yet, functional relevance of gene expression changes to mode-of-action of toxicity is hard to define. High-throughput functional siRNA-based screening provides direct functional insight in the role of individual genes in adverse outcome. We have successfully applied targeted RNAi approaches to discern the role of oxidative stress and ER stress in onset of DILI[97]. Furthermore, we applied a large siRNA survival screen targeting individual kinases, phosphatases and transcription factors, to gain deeper understanding of the regulation of the DNA damage response in embryonic stem cells[99]. This success allowed us to apply large scale RNAi screening to identify the signalling components that modulate stress response signalling. For this, we integrate our BAC-GFP reporters with imaging-based siRNA screening to identify modulators of Nrf2, UPR and NF-κB signalling. As an example, to unravel novel components that are crucial in the regulation of this oscillatory behaviour of NF-κB, we have performed an siRNA screen, consisting of kinases, ubiquitinases and Toll like Receptors/TNF receptors, using the HepG2 RelA-GFP reporter cell line. Diclofenac pre-treatment of HepG2 cells inhibits the oscillatory behaviour of NF-kB[25]; RNAi is an excellent means to identify modulators that cause this effect. Therefore, HepG2 RelA-GFP reporters were pre-exposed with diclofenac for 8 hours and subsequently with TNFα (Fredriksson et al., unpublished data). Multiparametric analysis revealed the identification of novel genes, including A20, CDK12 and UFD1L, that could regulate this oscillatory behaviour which may ultimately lead to insights why some patients are prone to the development of DILI. Using the same approach, key regulators could also be identified for other adaptive stress pathways, such as the oxidative stress pathway, using the Srxn1-GFP reporter, and the ER stress response, using the Chop-GFP reporter (unpublished data).

Recognition of novel key events for Adverse Outcome Pathway development

Based on improved mechanistic insight, better predictions can be made for the development of DILI, especially when this knowledge is placed in a structured adverse outcome pathway (AOP) framework. This opens up the opportunity to implement this knowledge into a test system for the assessment of DILI liabilities and, thereby, improving its accuracy for predictivity. Likewise,

systems microscopy approaches can be used for the development of new AOPs. Work by Fredriksson et al. identified underlying molecular mechanisms of the synergistic apoptotic response of hepatotoxic drugs and TNFα and could be the basis for a novel AOP. First, transcriptomic analysis of HepG2 cells treated with synergistic hepatotoxic drugs (such as diclofenac and carbamazepine) with or without TNFα at different time points was performed and revealed after Ingenuity Pathway Analysis (IPA) the importance of EIF2/ER stress signalling, Nrf2-mediated oxidative stress response and death receptor signalling in this synergistic apoptotic response. Combining siRNA-mediated knockdowns of important genes in these pathways with high-content imaging of AnnexinV-Alexa633, a dye for apoptosis, and HepG2 oxidative stress GFP reporters, a model was proposed whereby compound-mediated activation of PERK and Chop together with oxidative stress sensitizes towards TNFα-induced apoptotic signaling[97]. This work highlights the strength of combining omics techniques and siRNA-based functional microscopy approaches to reveal new insight in the molecular mechanisms that define drug adversities.

3D culture HepG2 BAC-GFP reporter system with improved hepatic phenotype suitable for long-term toxicity assessment

HepG2 cells have reduced metabolic capacity and a lack in the resemblance with the liver phenotype[100]. Also the proliferative nature of HepG2 hinders chronic repeat testing. To overcome these issues, a method to culture HepG2 as spheroids in a 3D hydrogel was developed[101]. 3D HepG2 spheroids show enhanced metabolic capacity of phase I and phase II metabolizing enzymes, functional expression of liver phenotypical properties and enable culturing over several weeks due to lack of proliferation. We have established the application of our panel of BAC-GFP HepG2 reporters in 3D spheroids and defined their functionality using automated confocal live cell imaging applications. These models can be used for repeated dose toxicity evaluation for up to two weeks. This allowed us to quantify the activation of stress response pathways by DILI compounds in 3D spheroids[29]. Our findings indicate that 3D BAC-GFP HepG2 spheroids and integration with automated imaging, allows for high-throughput assessment of DILI liability.

Future directions of DILI testing using fluorescent toxicity pathway reporter technology

We have established the functionality of HepG2 BAC-GFP reporter cells to quantitatively assess stress response pathway activation using an automated confocal microscopy approach. Moreover, we demonstrated that these reporter cells are a valuable tool for DILI safety assessment[27,102]. In addition, these reporters have further application in investigative toxicology as well as mechanistic molecular understanding of DILI. While the HepG2 cell line is a robust and cheap cell system which allows easy scaling for high-throughput screening[103], several issues may require further optimization.

Firstly, we need to address the limitation of the lack of drug metabolizing capacity in HepG2 cells and consequences for predicting DILI[104]. Various DILI drugs require metabolism for bioactivation

and leading to toxicity[105–107]. By integrating drug metabolism in the reporter platform, thus increasing clearance as well as bioactivation capacity, we can address the question what the overall consequences will be for sensitivity and specificity of the reporter platform.

Secondly, the iPSC model in combination with CRISPR/Cas9 genome editing technology will allow the generation of iPSC-based fluorescent reporter systems. The CRISPR/cas9 tool makes it possible to make very specific genomic changes, including integration of fluorophores[108,109]. These fluorescent hiPSC reporters can then be differentiated in hepatocyte-like cells (HLC), proposed as an improved model for toxicity screening[110,111], using established differentiation protocols[112–114]. Further optimization of these differentiation protocols is still ongoing. These novel hiPSC derived HLC reporter lines can then be used for high-throughput screening. This work will require strong investments in generation of reporter systems and re-assessing the sensitivity and specificity of these new reporters for DILI liability evaluation. Regardless of the outcome, these reporters can also be used for the generation of other cell lineages representing other target organs.

Thirdly, an advancement in generation of BAC-GFP HepG2 3D spheroids that contain additional non-parenchymal cell types that are critical for DILI, including Kupffer cells, stellate cells and endothelial cells, thus creating a micro-environment similar to the normal liver[115].

Finally, using either BAC-GFP approaches or CRISPR/Cas9-mediated GFP tagging technology will lead to expression of GFP-fusion products at the endogenous expression levels. We observed differences in the levels of GFP reporter expression, with in particular transcription factor GFP-fusion products being expressed at low levels. This requires in particular high-end image acquisition systems to allow sensitive and fast detection of reporters. Moreover, high resolution imaging at both the 2D and 3D level will facilitate the image segmentation and quantification of GFP-reporter levels as well as subcellular localization.

In conclusion, we have established an advanced cell stress reporter platform which finds its application in DILI liability evaluation in pre-clinical drug development. The above innovations will likely improve the quality and the applicability of these reporters in safety assessment.

Acknowledgements

This work was supported by the FP7 DETECTIVE project (grant agreement 266838), IMI MIP-DILI project (grant agreement 115336) and the H2020 EU-ToxRisk project (grant agreement 681002).

Chapter 3

Comprehensive landscape of Nrf2 and p53 pathway activation dynamics by oxidative stress and DNA damage

---

This chapter has been published as:

M. Niemeijer*, S. Hiemstra*, E. Koedoot, S. Wink, J.E. Klip, M. Vlasveld, E. de Zeeuw, B. van Os, A. White and B. van de Water

* Both authors contributed equally

A comprehensive landscape of Nrf2 and p53 pathway activation dynamics by oxidative stress and DNA damage

Chem Res Toxicol. 2017 Apr 17;30(4):923-933. doi: 10.1021/acs.chemrestox.6b00322.

Abstract

A quantitative dynamics pathway map of the Nrf2-mediated oxidative stress response and p53-related DNA damage response pathways as well as the crosstalk between these pathways has not systematically been defined. To allow the dynamic single cell evaluation of these pathways, we have used BAC-GFP recombineering to tag for each pathway three key components: for the oxidative stress response, Keap1-GFP, Nrf2-GFP and Srxn1-GFP; for the DNA damage response, 53bp1-GFP, p53-GFP and p21-GFP. The dynamic activation of these individual components was assessed using quantitative high throughput confocal microscopy after treatment with a broad concentration range of diethyl maleate (DEM; to induce oxidative stress) and etoposide (to induce DNA damage). DEM caused a rapid activation of Nrf2, which returned to base line levels at low concentrations, but remained sustained at high concentrations. Srxn1-GFP induction and Keap1-GFP translocation to autophagosomes followed later, with upper boundaries reached at high concentrations, close to onset of cell death. Etoposide caused rapid accumulation of 53bp1-GFP in DNA damage foci, which was later followed by the concentration dependent nuclear accumulation of p53-GFP and subsequent induction of p21-GFP. While etoposide caused activation of Srxn1-GFP, a modest activation of DNA damage reporters was observed for DEM at high concentrations. Interestingly, Nrf2 knockdown caused an inhibition of the DNA damage response at high concentrations of etoposide, while Keap1 knock down caused an enhancement of the DNA damage response already at low concentrations of etoposide. Knock down of p53 did not affect the oxidative stress response. Altogether, the current stress response landscapes provide insight in the time course responses of and crosstalk between oxidative stress and DNA-damage and defines the tipping points where cell injury may switch from adaptation to injury.

Key words: High throughput imaging, BAC-GFP reporter platform, point of departure, stress-response dynamics, drug-induced toxicity

Introduction

In the last decades, there is an urging need in the field of toxicology to develop new methods which assess toxicity pathways unravelling underlying mechanisms of toxicity[116]. The pivotal aspect in toxicity pathways is the balance between adaptation and cell death. Adaptive stress response pathways allow the recovery from cell injury, thus re-establishing cellular homeostasis. However, when the stress is too severe, adaptive stress response pathways may reach their boundaries of activation prohibiting full recovery and provoking cell death as a consequence. Previously, we established a bacterial artificial chromosome (BAC)-GFP reporter platform in hepatocellular carcinoma HepG2 cells, highly suited for BAC GFP transgenomics and often used for high throughput toxicity assessment, to study the live cell dynamics of adaptive stress response pathway after cellular injury[27,79]. We tagged different signalling components of stress response pathways with green fluorescent protein (GFP), including the oxidative stress response

and the DNA damage response, two critical pathways in chemical-induced injury. Both upstream regulators, critical pathway transcription factors and downstream target genes were tagged. By quantitatively assessing different components of the stress response pathways, we are now able to determine a detailed compound specific mode of action[27]. Furthermore, the integration of these reporters with high-throughput live cell imaging technologies allows the determination of the point-of-departure and/or tipping point in concentration and time course experiments. This allows a full reflection of the cell physiological programs and is central in the assessment of the balance between adaptation and adversity[117]. In this study, we systematically mapped in detail the landscape of the oxidative stress response and the DNA damage signalling pathways as well as their crosstalk.

Oxidative stress occurs when cells suffer from an increase in intracellular reactive oxygen species (ROS). ROS can damage proteins, nucleic acids and lipids[77]. Upon increase of intracellular concentrations of ROS, the anti-oxidant response pathway is activated by nuclear translocation of key transcription factor nuclear factor, erythroid 2-like 2 (*NFE2L2*/Nrf2) (Fig. 1A). Under normal conditions, Nrf2 is bound by kelch-like ECH-associated protein 1 (Keap1) and targeted for proteasomal degradation through ubiquitination by Cul3[118]. Upon oxidative stress, ROS can modify cysteine residues of Keap1, thereby causing intracellular changes preventing the ubiquitination of Nrf2. This ensures that all newly synthesized Nrf2 accumulates in the nucleus, where Nrf2 binds the anti-oxidant response element (ARE)[119]. This results in transcription of hundreds of target genes, including detoxifying enzymes like NAD(P)H Quinone Dehydrogenase 1 (Nqo1), Heme Oxygenase 1 (Hmox1), Thioredoxin (Trx) and Sulfiredoxin 1 (Srxn1)[120]. All together these targets ensure, amongst others, neutralization of ROS and cellular protection against oxidative stress.

The DNA damage response (DDR) is activated after the induction of double stranded breaks (DSBs). DSBs can be caused by a wide range of agents including irradiation and chemicals. DSBs are sensed by proteins including DNA-dependent protein kinase (DNA-PK), Ataxia Telangiectasia Mutated (ATM), Ataxia Telangiectasia And Rad3-Related Protein (ATR) and the MRN complex. In order to transduce the signal, mediators p53 binding protein 1 (53bp1), Mediator of DNA Damage Checkpoint 1 (Mdc1) and Breast Cancer 1 (Brca1) locate to the DSBs at so-called DNA damage foci, and kinases Checkpoint Kinase 1 and 2 (Chk1 and Chk2) are activated. This leads to phosphorylation, stabilization and nuclear accumulation of tumor protein 53 (*TP53*/p53) and subsequent transcription of p53 targets. These targets include groups of genes which are responsible for cell cycle arrest (e.g. *CDKN1A*/p21), DNA repair and apoptosis (e.g. Bax and Puma) (Fig. 2A)[121].

Previous research showed contradictory links between the Nrf2 and p53 pathway signalling. Murine double minute 2 (Mdm2), a transcriptional target of p53, targets p53 for ubiquitination and proteasomal degradation serving as a negative feedback to restore homeostasis when DSBs

are repaired[122]. Mdm2 is shown to be a target of Nrf2 in murine embryonic fibroblasts (MEFs) ovarian carcinoma A2780 and murine primary tubular epithelial cells[123,124]. This suggests that Nrf2 stimulation would lead to p53 down-regulation via Mdm2 up-regulation. In contrast, NAD(P)H:quinone oxidoreductase 1 (Nqo1), a transcriptional target of Nrf2, is proven to stabilize p53 during onset of oncogene-induced senescence in human diploid fibroblasts (HDF)[125]. A detailed assessment of crosstalk between these pathways has been limited due to the lack of dense concentration and time course experiments.

Here, using automated live cell high-throughput confocal microscopy, we followed single cell time dynamics of the oxidative stress response components (Keap1-GFP, Nrf2-GFP, Srxn1-GFP) and the DNA damage signalling components (53bp1-GFP, p53-GFP and p21-GFP). We systematically assembled the concentration and time course landscapes for all six HepG2 BAC-GFP reporter cell lines after exposure to diethyl maleate (DEM) and etoposide. DEM is an electrophilic chemical, which alkylates the sulfhydryl group of glutathione and subsequently produces oxidative stress[126]. Etoposide inhibits DNA topoisomerase II activity. Topoisomerase II functions in DNA replication, transcription, DNA repair and chromatin remodelling. When topoisomerase II function is blocked by etoposide, DSBs will occur[127]. Mechanistic understanding of the crosstalk between these pathways was further investigated using RNA interference approaches.

Materials and Methods

Chemicals and antibodies

Etoposide and diethyl maleate (DEM) were purchased at Sigma (Zwijndrecht, the Netherlands). Compound stock solutions were made in dimethylsulfoxide (DMSO) from BioSolve (Valkenswaard, the Netherlands) and aliquots were stored at -20°C. The end concentration of solvent DMSO was equal or less than 0.2% (v/v). The antibody against GFP for Western Blot analysis was from Roche (Almere, the Netherlands). The antibody against tubulin was purchased at Sigma (Zwijndrecht, the Netherlands).

Cell culture

Human hepatocellular carcinoma HepG2 cell lines obtained from American Type Culture Collection (ATCC, Wesel, Germany) were cultured in Dulbecco's Modified Eagle Medium (DMEM) containing 10% (v/v) fetal bovine serum (FBS), 25 U/mL penicillin and 25 µg/mL streptomycin up until passage 20. Cells were cultured in a 5% CO2 humidified incubator at 37°C.

RNA interference

Transient knock down of specific genes in HepG2 cells was achieved through reverse transfection of 50 nM siGENOME SMARTpool siRNAs from Dharmacon GE Healthcare (Eindhoven, the Netherlands) in combination with 0.3% INTERFERin transfection reagents from Polyplus (Leusden, the Netherlands). For the following genes transient knock down was performed, namely *KEAP1*, *NFE2L2* and *TP53*. As control, mock was used where no siRNA was added. Medium

was refreshed 24 hours after transfection. Thereafter, the effect of knock down was evaluated 72 hours after transfection.

Confocal live cell imaging of HepG2 GFP reporters

To evaluate stress response activation, HepG2 BAC-GFP reporter cell lines for Keap1, Nrf2, Srxn1, 53bp1, p53 and p21 were established using BAC recombineering as described previously[27,79,91,97,128]. To assess the effect of compound exposure on stress response activation, HepG2 GFP reporter cells were plated in µclear 384 wells plates from Greiner Bio-One (Alphen aan den Rijn, the Netherlands). After attachment for 1 to 3 days, cells were stained for one hour with 100 ng/mL $Hoechst_{33342}$ and exposed to a broad concentration range of etoposide (0.001 - 100 µM) or diethyl maleate (0.01 - 1000 µM). As solvent control, cells were exposed to 0.2% DMSO. To evaluate the induction of cell death, medium also contained 0.05% AnnexinV-Alexa633 and 100 nM propidium iodide (PI). The induction of GFP in the different reporters and cell death was examined through live cell automated confocal imaging for 24 hours after exposure using Nikon TiE2000 including an automated xy-stage, an integrated Perfect Focus System (Nikon, Amsterdam, the Netherlands) and 408, 488, 561 and 647 nm lasers.

Imaging data analysis

Quantification of the signal intensity was done using CellProfiler version 2.1.1 (Broad Institute, Cambridge, USA) with an analysis pipeline build up from different modules, including an in-house developed module utilizing the watershed masked algorithm[129] for nuclear segmentation, followed by the IdentifyPrimaryObjects, IdentifySecondaryObjects, IdentifyTertiaryObjects, RelateObjects, MeasureObjectIntensity, and MeasureObjectSizeShape modules as previously described[27] either to quantify the GFP intensity in the nuclei or in the cytoplasm for each individual cell. Keap1 and 53bp1-GFP foci were first quantified using the FociPicker3D plug-in[130] in ImageJ and further analysed in CellProfiler assigning foci to individual cells. Image analysis data was stored as HDF5 files. For further analysis, the graphical user interface of the R package 'H5CellProfiler' (Wink et al., manuscript in preparation) and Rstudio (Boston, USA) was used to extract data of interest. For each imaging plate, the mean value of DMSO was calculated which resembled the background level. Thereafter, to determine the percentage of GFP positive cells, the fraction of cells which were three times above the background level was determined. Each replicate and each cell line was fitted with the b-spline method with 10 degrees of freedom, except for 53bp1 which was fitted with 3 degrees of freedom, and 3rd degree polynomials using the base-r lm and bs function from the splines R package to achieve resampling of the data with similar time points.

Western blot analysis

Samples were collected by washing cells twice with cold 1x PBS and lysis with Radioimmunoprecipitation assay (RIPA) buffer containing freshly added 1% (v/v) protease inhibitors cocktail from Sigma (Zwijndrecht, the Netherlands). Cell lysate was centrifuged at

13.000 rpm for 10 minutes at 4°C and supernatant was collected. To determine protein concentrations, BCA protein assay was performed. Thereafter, protein was dissolved with 1× sample buffer supplemented with 10% v/v β-mercaptoethanol and heat-denatured at 95 °C for 5 min. After SDS-page protein separation, proteins were blotted onto polyvinylidene difluoride (PVDF) membranes. Antibody incubations were performed in 1% bovine serum albumin (BSA) in tris-buffered saline (TBS)-0.05%Tween20. For detection, Enhanced Chemiluminescent (ECL) Western Blotting substrate from Thermo Scientific (Bleiswijk, The Netherlands) was used and visualized using the ImageQuant LAS4000 from GE Healthcare (Eindhoven, the Netherlands).

Statistics

Results are shown as the mean ± the standard deviation from three biological replicates. Data analysis was done using GraphPad Prism 6.00 (GraphPad software, La Jolla, California, USA) and Rstudio (Boston, USA) using R 3.2.3 and the following R packages, namely ggplot2[131],

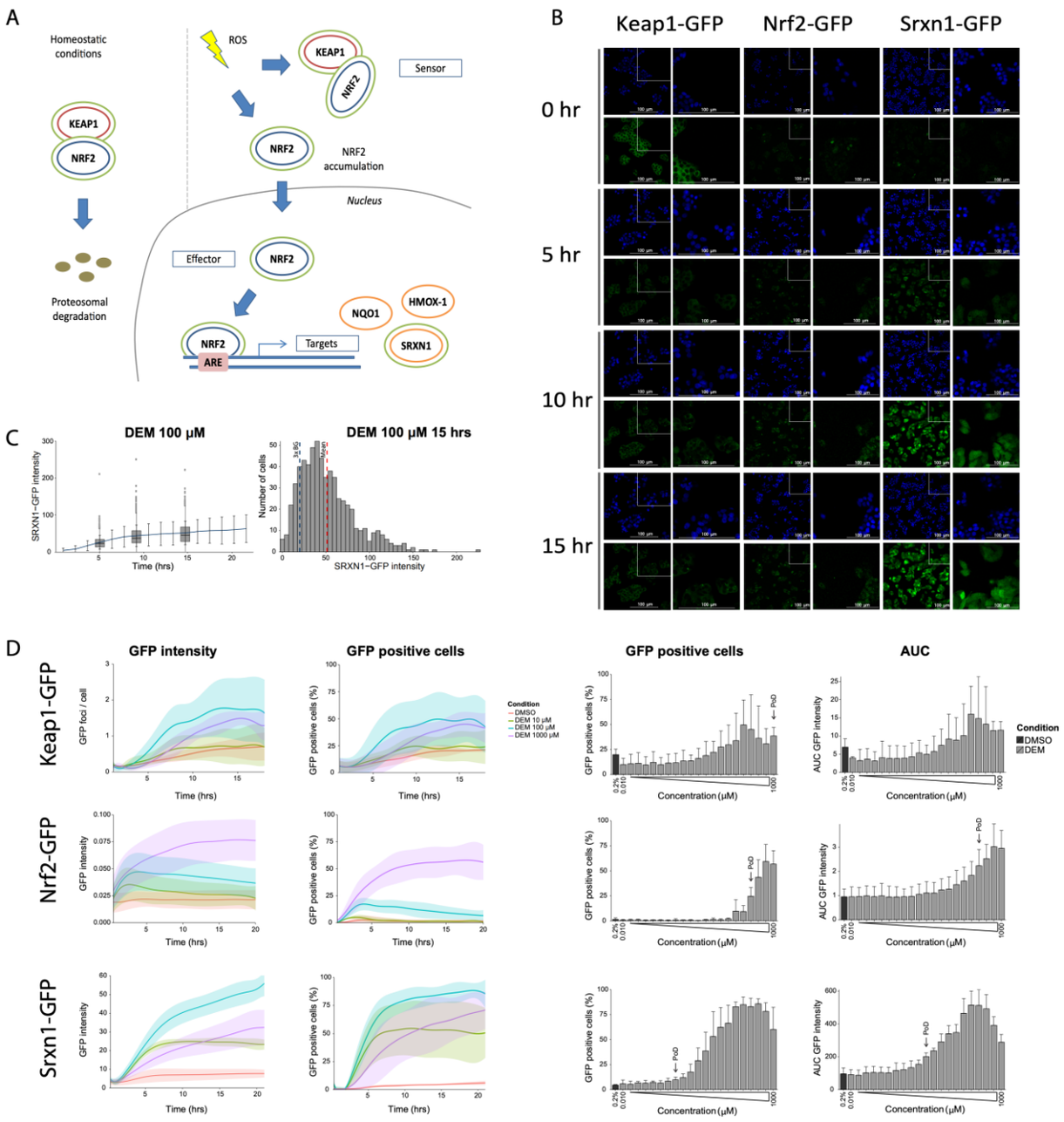

← Fig. 1. Imaging based Nrf2 anti-oxidant pathway response to diethyl maleate (DEM). A) Nrf2 pathway regulation. In normal conditions the Keap1-Nrf2 complex is degraded. Under ROS conditions, Nrf2 accumulates and translocates to the nucleus. Nrf2 binds the anti-oxidant response element (ARE) and transcribes its targets. Pathway components indicated with a green circle are tagged with Green Fluorescent Protein (GFP). B) Example images of 100 µM DEM for 0, 5, 10 and 15 hours after exposure. One time point consists of four images per reporter, an overview image of nuclear staining (upper left image), an overview image of GFP (lower left image), a zoom image of nuclear staining (upper right image) and a zoom image of GFP (lower right image). C) Variation in Srxn1-GFP of one replicate experiment, plotted as GFP intensity over time including standard deviation and boxplots to display the single cell variation (left panel) and plotted as a histogram displaying number of cells over GFP intensity including blue bar to indicate three times background levels and red bar indicating the mean GFP intensity (right panel). D) DEM responses of Keap1-GFP, Nrf2-GFP and Srxn1-GFP, shown in four graphs per reporter. GFP foci count (Keap1) and GFP intensity (Srxn1 and Nrf2) over time for DMSO, 10 µM, 100 µM and 1000 µM DEM (first column), fraction GFP positive cells over time for DMSO, 10 µM, 100 µM and 1000 µM DEM (second column), GFP foci count (Keap1) and GFP intensity (Srxn1 and Nrf2) displayed in dose response (third column) and area under the curve (AUC) of GFP foci count (Keap1) and GFP intensity (Srxn1 and Nrf2) time responses displayed in dose response (last column). Standard deviations are shown for three independent replicates.

data.table[132], pheatmap[133], reshape2[134], dplyr[135], scales[136], tidyr[137], stats, splines and graphics. Significance levels were calculated using Student's t-test, *p < 0.05, **p < 0.01, ***p < 0.001.

Results

High content live cell imaging of oxidative stress and DNA damage HepG2 GFP reporters

To evaluate the Nrf2 anti-oxidant response pathway and the p53 DNA damage repair pathway in detail, different components of the pathways tagged with GFP were imaged after administration of an inducer of oxidative stress (DEM) and of DNA damage (etoposide) in HepG2 cells. For both stress pathways an upstream 'sensor', a 'transcription factor' and a specific transcriptional 'target' were chosen (supplemental figure 1). For the Nrf2 anti-oxidant pathway, Keap1 was chosen as a sensor, Nrf2 as the transcription factor and sulfiredoxin1 (Srxn1) as the specific downstream target of Nrf2. For the p53 DNA damage repair pathway, p53 binding protein 1 (53bp1) was chosen as a sensor, p53 as the transcription factor and $p21^{CIP1/WAF1}$ as the specific downstream target of p53. These six HepG2 GFP reporters were exposed to a broad dose range of DEM (from 10 nM to 1 mM) and etoposide (1 nM to 100 µM). Live cell confocal imaging allowed single cell image analysis to identify GFP intensity in the cytoplasm (Srxn1-GFP) and nucleus (Nrf2-GFP, p53-GFP and p21-GFP) and cytoplasmic and nuclear foci count (Keap1-GFP, 53bp1-GFP) (supplemental figure 1).

Nrf2 pathway activation after administration to DEM showed a time and concentration dependent increase for each component of the pathway (figure 1B, 1D and supplemental movies). With increasing concentrations of DEM, increased pathway activation was observed. However, concentrations above 316 µM led to a reduction in Srxn1-GFP and Keap1-GFP activation; this was associated with the onset of cell death (supplemental figure 2). At 1 mM

DEM, a sustained nuclear accumulation of Nrf2-GFP was observed, while simultaneously Srxn1-GFP accumulation did not reach its maximal activation, indicating that Nrf2 was highly activated, but was not able to turn on a strong adaptive program. To assess the single cell time dynamics of transcriptional activity of Nrf2, Srxn1-GFP cytoplasmic intensity was evaluated. Exposure to 100 µM DEM led to a small increase in Srxn1-GFP intensity after 2 hours, which further increased until 24 hours. A small population of Srxn1-GFP cells were high responders, which had about two to three times higher GFP intensity (figure 1C). The broad concentration range allowed us to define the point of departure (PoD) concentration defined by the lowest concentration being significant different from solvent control. Therefore, we defined this concentration for GFP intensity, fraction positive cells and area under the curve (AUC) values for each reporter (table 1). The PoD of Srxn1-GFP was ~50- to 100-fold lower than PoD of Keap1-GFP and Nrf2-GFP. This seems

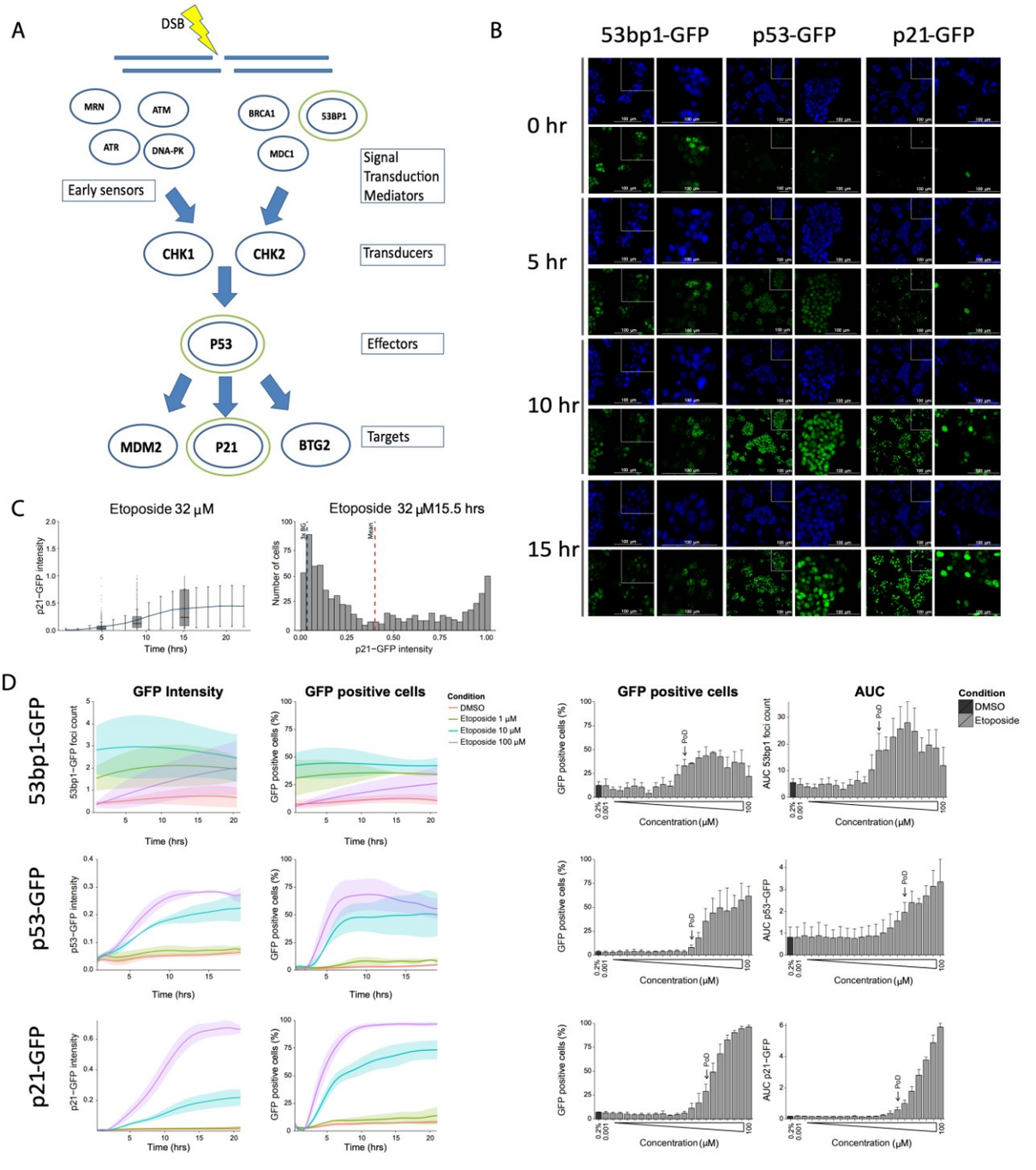

← Fig. 2. p53 DNA damage pathway response to etoposide. A) p53 pathway regulation. Double stranded breaks (DSBs) in the DNA are sensed by proteins including MRN complex, ATM, ATR and DNA-PKs. Adaptor/mediator proteins including BRCA1, MDC1 and 53bp1 transduce the signal to CHK1 and CHK2, which subsequently activate p53. p53 accumulates in the nucleus and transcribes targets as p21, Btg2 and Mdm2. Pathway components indicated with a green circle are tagged with Green Fluorescent Protein (GFP). B) Example images of 32 µM etoposide for 0, 5, 10 and 15 hours after exposure. One time point consists of four images for each reporter, an overview image of nuclear staining (upper left image), an overview image of GFP (lower left image), a zoom image of nuclear staining (upper right image) and a zoom image of GFP (lower right image). C) Variation in p21-GFP of one replicate experiment, plotted as GFP intensity over time including standard deviation and boxplots to display the single cell variation (left panel) and plotted as a histogram displaying number of cells over GFP intensity including blue bar to indicate three times background levels and red bar indicating the mean GFP intensity (right panel). D) Etoposide responses of 53bp1-GFP, p53-GFP and p21-GFP, shown in four graphs per reporter. GFP foci count (53bp1) and GFP intensity (p21 and p53) over time for DMSO, 1 µM, 10 µM and 100 µM etoposide (first column), fraction GFP positive cells over time for DMSO, 1 µM, 10 µM and 100 µM etoposide (second column), GFP foci count (53bp1) and GFP intensity (p21 and p53) displayed in dose response (third column) and area under the curve (AUC) of GFP foci count (53bp1) and GFP intensity (p21 and p53) time responses displayed in dose response (last column). Standard deviations are shown for three independent replicates.

counterintuitive as Nrf2 and Keap1 first need to be activated before Srxn1 can be produced. A likely explanation is the sensitivity of the reporters, as Srxn1-GFP exhibits higher levels of GFP signal.

Etoposide administration led to a robust concentration and time dependent increase of p53-GFP and p21-GFP (figure 2B, 2D and supplemental movies). 53bp1-GFP foci count showed a dose dependent effect in percentage GFP positive cells and AUC of the time curves. However, at 1 and 10 µM etoposide a time dependent activation was not observed. Single cell p21-GFP intensities resulted in larger variation compared to Srxn1-GFP (figure 1C and 2C left panels). This was due to a larger population of high responding p21-GFP cells (figure 2C, right panel). The PoD for

Table 1. Point of departure (PoD) concentrations of p53 and Nrf2 signalling GFP reporters exposed to DEM and etoposide*

		DEM		etoposide	
pathway		% positive cells	AUC	% positive cells	AUC
oxidative stress	Keap1-GFP	1000 μM	NS	NS	NS
	Nrf2-GFP	178 μM	178 μM	NS	NS
	Srxn1-GFP	0.563 μM	3.16 μM	17.8 μM	10 μM
DNA damage response	53bp1-GFP	NS	NS	0.56 μM	0.56 μM
	p53-GFP	178 μM	NS	1.0 μM	5.6 μM
	p21-GFP	316 μM	178 μM	3.2 μM	3.2 μM

*Point of departure concentration for Keap1-GFP, Nrf2-GFP, Srxn1-GFP, 53bp1-GFP, p53-GFP and p21-GFP as percentage cells exceeding two times background and area under the curve (AUC) of 24 hour time courses in response to diethyl maleate (DEM) and etoposide. All concentrations are in µM, NS is not significant.

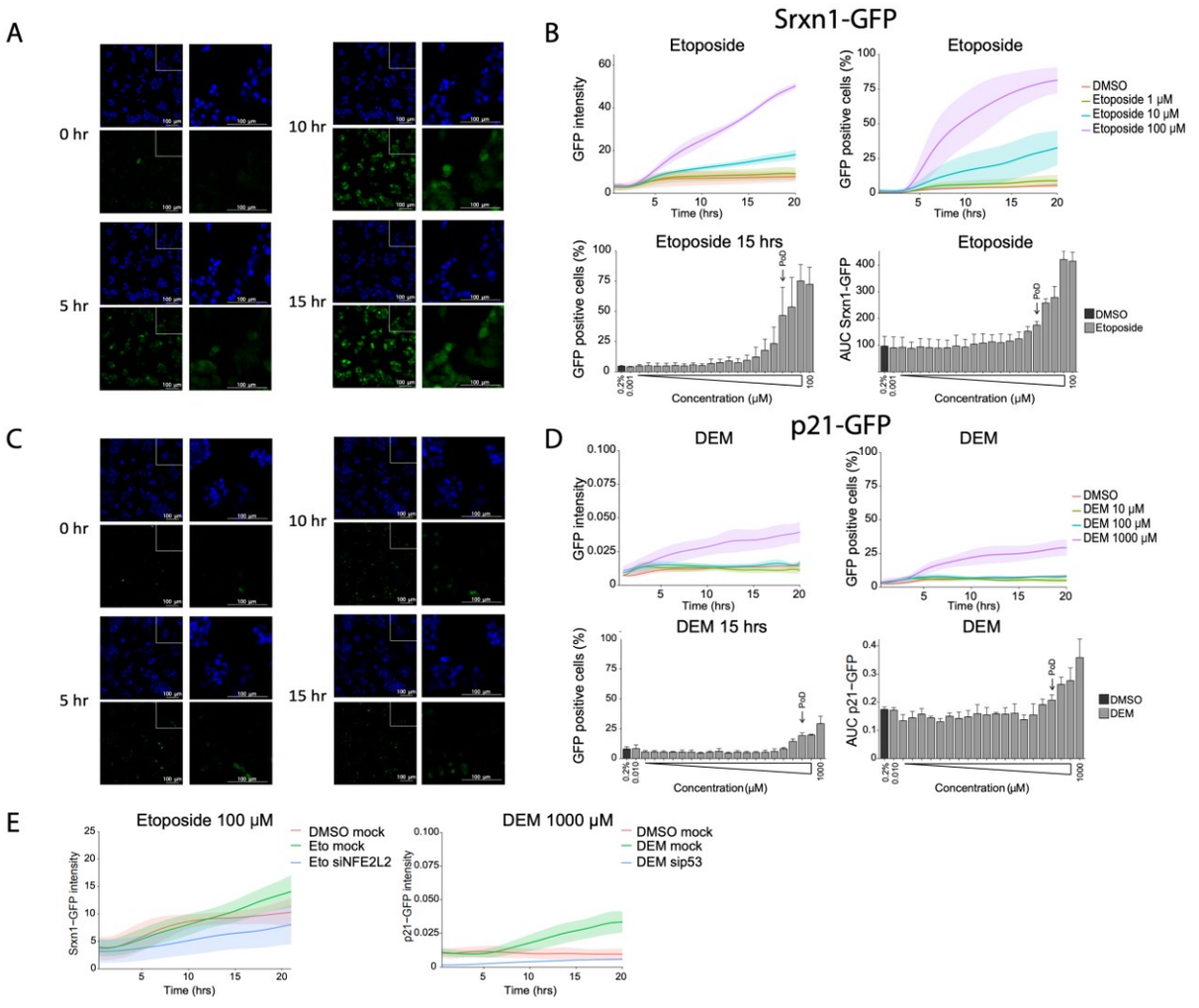

Fig. 3. Crosstalk between oxidative stress and DNA damage only occurs at high concentrations of etoposide and DEM respectively. A) Example images of Srxn1-GFP exposed to 32 µM etoposide for 0, 5, 10 and 15 hours. One time point consists of four images for each reporter, an overview image of nuclear staining (upper left image), an overview image of GFP (lower left image), a zoom image of nuclear staining (upper right image) and a zoom image of GFP (lower right image). B) Etoposide responses of Srxn1-GFP, shown in four graphs: GFP intensity over time for DMSO, 1 µM, 10 µM and 100 µM etoposide (upper left), fraction GFP positive cells over time for DMSO, 1 µM, 10 µM and 100 µM etoposide (upper right), GFP intensity displayed in dose response (lower left) and area under the curve (AUC) of GFP intensity time responses displayed in dose response (lower right). Standard deviations are shown for three independent replicates. C) Example images of p21-GFP exposed to 100 µM DEM for 0, 5, 10 and 15 hours. One time point consists of four images for each reporter, an overview image of nuclear staining (upper left image), an overview image of GFP (lower left image), a zoom image of nuclear staining (upper right image) and a zoom image of GFP (lower right image). D) DEM responses of p21-GFP, shown in four graphs: GFP intensity over time for DMSO, 10 µM, 100 µM and 1000 µM DEM (upper left), fraction GFP positive cells over time for DMSO, 10 µM, 100 µM and 1000 µM DEM (upper right), GFP intensity displayed in dose response (lower left) and area under the curve (AUC) of GFP intensity time responses displayed in dose response (lower right). E) Srxn1-GFP intensity over time after etoposide treatment with mock or siNFE2L2 transfection (left panel). p21-GFP intensity over time after DEM exposure with mock or sip53 transfection (right panel). Standard deviations are shown for three independent replicates.

53bp1-GFP was lower than for p53-GFP and p21-GFP (table 1). This indicates that 53bp1 foci formation already occurred at lower concentrations, without full p53 pathway activation.

High concentrations of etoposide and DEM activate Srxn1-GFP and p21-GFP respectively

Next, we examined possible crosstalk between the protective Nrf2 pathway and the p53 pathway. We focused on the Srxn1-GFP and p21-GFP, respectively, since these represent the entire pathway activation and are both sensitive, allowing most accurately determination of the amplitude of pathway activity. The PoD concentration of the AUC of Srxn1-GFP exposed with etoposide was 17.8 µM; at 100 µM etoposide, more than 75% of the cells were positive for Srxn1-GFP (three times higher GFP intensity than background levels; figure 3A and B). Thus, etoposide could activate the Nrf2 response, but was much less potent than DEM. Similarly, we determined the effect of DEM on p21-GFP activation. The PoD of p21-GFP exposed to DEM was 178 µM; in addition, 1000 µM DEM was a less potent inducer of p21-GFP than 100 µM etoposide of Srxn1-GFP, as only 25% of p21-GFP cells were counted as GFP positive, with an overall intensity which was four times lower than for p21-GFP cells exposed to etoposide.

Knock down of KEAP1 caused an increase of p21-GFP

Since activation of p21-GFP by DEM and Srxn1-GFP by etoposide was observed at higher concentrations, secondary responses could play a role. To systematically assess the requirements for Nrf2 and p53 in the activation of Srxn1-GFP by etoposide and p21-GFP by DEM, we performed RNA interference experiments. Indeed, knock down of *NFE2L2* inhibited the Srxn1-GFP activation by etoposide, while knock down of *TP53* prevented the p21-GFP activation by DEM (fig. 3E). Next, we also evaluated the interdependency of Srxn1-GFP and p21-GFP levels for Nrf2 and p53, which was determined after knock down of *KEAP1*, *NFE2L2* and *TP53*. As expected knock down of *KEAP1* resulted in significantly higher levels of Srxn1-GFP even in the absence of any stimulus (figure 4A and B). Moreover, knock down of *NFE2L2* led to significantly lower Srxn1-GFP levels after induction with DEM. Knock down of *TP53* caused a significant yet slight decrease in DEM-induced Srxn1-GFP expression. Knock down of *TP53* caused a drastic inhibition of the etoposide-induced p21-GFP induction. Interestingly, siKEAP1 itself caused the induction of p21-GFP level and also enhanced the induction of p21-GFP at low concentrations of etoposides. Knock down of *NFE2L2* caused a slight inhibition of the activation of p53 at high concentrations of etoposide. Together these data suggest a mild crosstalk between the p53 and the Nrf2 pathway.

KEAP1 knock down caused upregulation of different components of both the Nrf2 and p53 pathway

The above results suggest a direct interaction between the Nrf2 and the p53 pathway, whereby knock down of *KEAP1* stimulates the p53 pathway. To assess this central role of Keap1 in further detail, we first performed knock down in additional GFP reporter cell lines. Previous work suggest Nqo1 and Mdm2 as important modulators in bridging the Nrf2 and p53 pathway[122,124,125]. For that reason, Nqo1-GFP and Mdm2-GFP reporters were used for further study. These reporters were

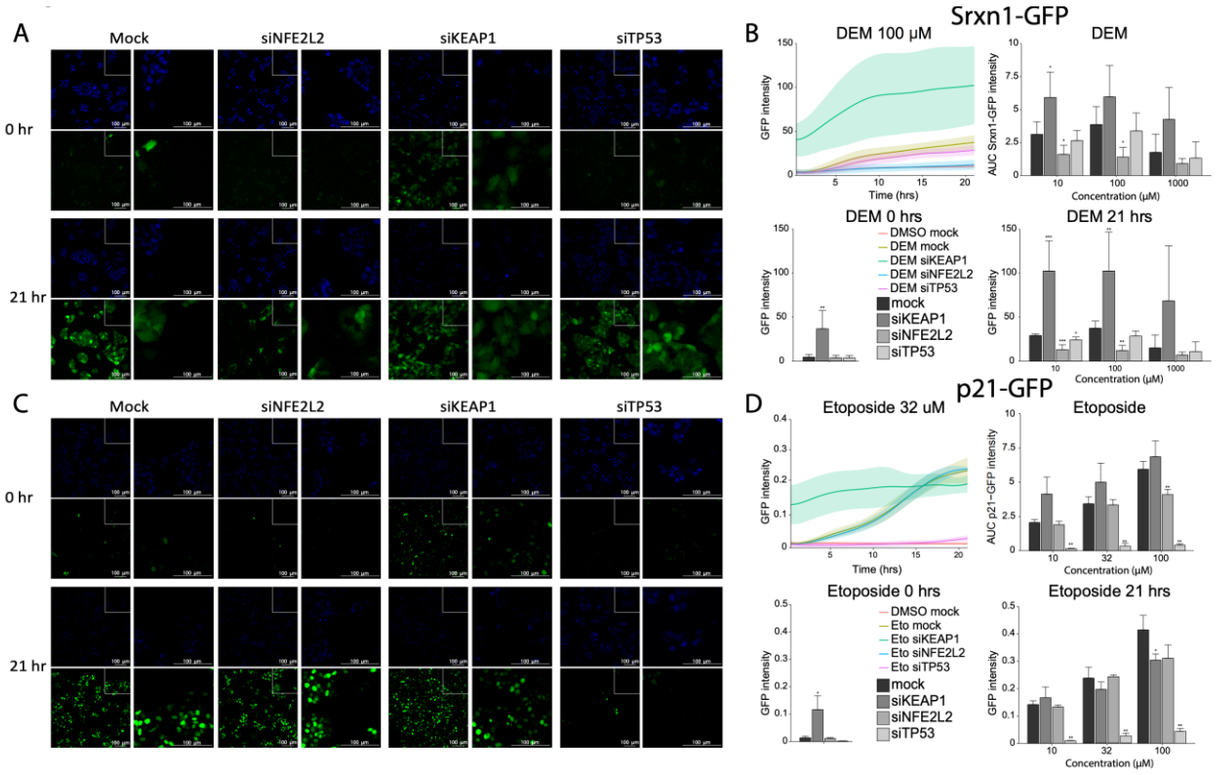

Fig. 4. Effect of knock down of KEAP1, NFE2L2 and TP53 on Srxn1-GFP and p21-GFP activation. A) Example images of Srxn1-GFP without knock down (mock) and with knock down (siNFE2L2, siKEAP1 and siTP53) with exposure to 100 µM DEM for 0 and 21 hours. One time point consists of four images for each reporter, an overview image of nuclear staining (upper left image), an overview image of GFP (lower left image), a zoom image of nuclear staining (upper right image) and a zoom image of GFP (lower right image). B) DEM responses of Srxn1-GFP, shown in four graphs: GFP intensity over time for mock, siKEAP1, siNFE2L2 and siTP53 after exposure to 100 µM DEM (upper left), area under the curves of GFP time response after exposure to 10 µM, 100 µM and 1000 µM DEM (upper right), GFP intensity displayed for 0 hours of DEM exposure after mock and siKEAP1, siNFE2L2 and siTP53 (lower left) GFP intensity displayed for 21 hours of DEM exposure after mock and siKEAP1, siNFE2L2 and siTP53 (lower right). Standard deviations are shown for three independent replicates. Significance (* = $p < 0,05$, ** = $p < 0,01$) calculated with a one-tailed Student's t-test for 0 hours DEM and a two-tailed Student's t-test for AUC and 21 hours DEM. C) Example images of p21-GFP without knock down (mock) and with knock down (siNFE2L2, siKEAP1 and siTP53) with exposure to 32 µM etoposide for 0 and 21 hours. One time point consists of four images for each reporter, an overview image of nuclear staining (upper left image), an overview image of GFP (lower left image), a zoom image of nuclear staining (upper right image) and a zoom image of GFP (lower right image). D) Etoposide responses of p21-GFP, shown in four graphs: GFP intensity over time for mock, siKEAP1, siNFE2L2 and siTP53 after exposure to 32 µM etoposide (upper left), area under the curves of GFP time response after exposure to 10 µM, 32 µM and 100 µM etoposide (upper right), GFP intensity displayed for 0 hours of etoposide exposure after mock and siKEAP1, siNFE2L2 and siTP53 (lower left) GFP intensity displayed for 21 hours of etoposide exposure after mock and siKEAP1, siNFE2L2 and siTP53 (lower right). Standard deviations are shown for three independent replicates. Significance (* = $p < 0,05$, ** = $p < 0,01$) calculated with a one-tailed Student's t-test for 0 hours etoposide and a two-tailed Student's t-test for AUC and 21 hours etoposide.

validated with reference compound activation and siRNA knock downs (supplemental figure 4). In addition, we tested p53-GFP reporter as an additional component of the p53 pathway. First, we validated knock down of *KEAP1* in two targets of Nrf2: Srxn1-GFP and Nqo1-GFP. Both showed significant upregulation ensuring these reporters are Keap1 regulated (figure 5B). Next, we tested knock down of *KEAP1* in DNA damage components p53-GFP, p21-GFP and Mdm2-GFP. Again, Keap1 knock down demonstrated significant upregulation of p21-GFP, as well as p53-GFP. Mdm2-GFP was not affected by *KEAP1* knock down (figure 5B). This suggests a role for Keap1 in the p53-p21 axis. To identify whether this role was Nrf2 dependent, a double knock down of *KEAP1* and *NFE2L2* was performed for p21-GFP and p53-GFP. The double knock down did not result in a significant increase in p21-GFP, however it did in p53-GFP (figure 5B). In both p21-GFP and p53-GFP, double knock down showed less induction compared to knock down of *KEAP1* alone, indicative for a role of Nrf2 in this response either mediated directly by Nrf2 itself or one of its target genes. To further elucidate whether the p21 activation by *KEAP1* knock down is dependent on the Nrf2 target gene Nqo1, we performed a *KEAP1* and *NQO1* double knock down. This showed a decrease in p21 activation compared to *KEAP1* knock down alone indicating a partial role of Nqo1 on p21 activation. However, there was still a significant increase compared to mock suggesting the presence of additional Nrf2-independent mechanisms in regulation of p53 signalling by Keap1.

Discussion

Chemical exposure can lead to cellular injury and activation of adaptive stress response pathways. Little is known on the dynamics of these pathways and on how these pathways are integrated and controlled by similar key events and signalling components. Therefore, it is essential to map the dynamics of the activation of adaptive stress responses and their intracellular relationship, such as the oxidative and DNA damage stress response. Using a HepG2 GFP reporter panel specific for oxidative and DNA damage stress signalling in combination with live cell high-content confocal imaging, concentration and time-dependent activation of Nrf2 and p53 pathway components by relevant reference compounds could be observed. Reference compounds, DEM and etoposide, activate Nrf2 and p53 signalling, respectively. The application of a broad concentration range allowed the accurate determination of the PoD. Etoposide did also activate the Nrf2 pathway, while DEM activates p53 pathway, albeit both at a much higher PoD. This suggests cross talk between these stress response pathways, in particular when the chemical insult is more severe. The interdependencies between the pathways was supported by RNA interference studies. Overall, our current data provide comprehensive maps of dynamics of two adaptive stress response pathways that are critical in chemical-induced injury. We anticipate that high content imaging of pathway activation will be instrumental for a systems biology understanding of pathway of toxicity regulation.

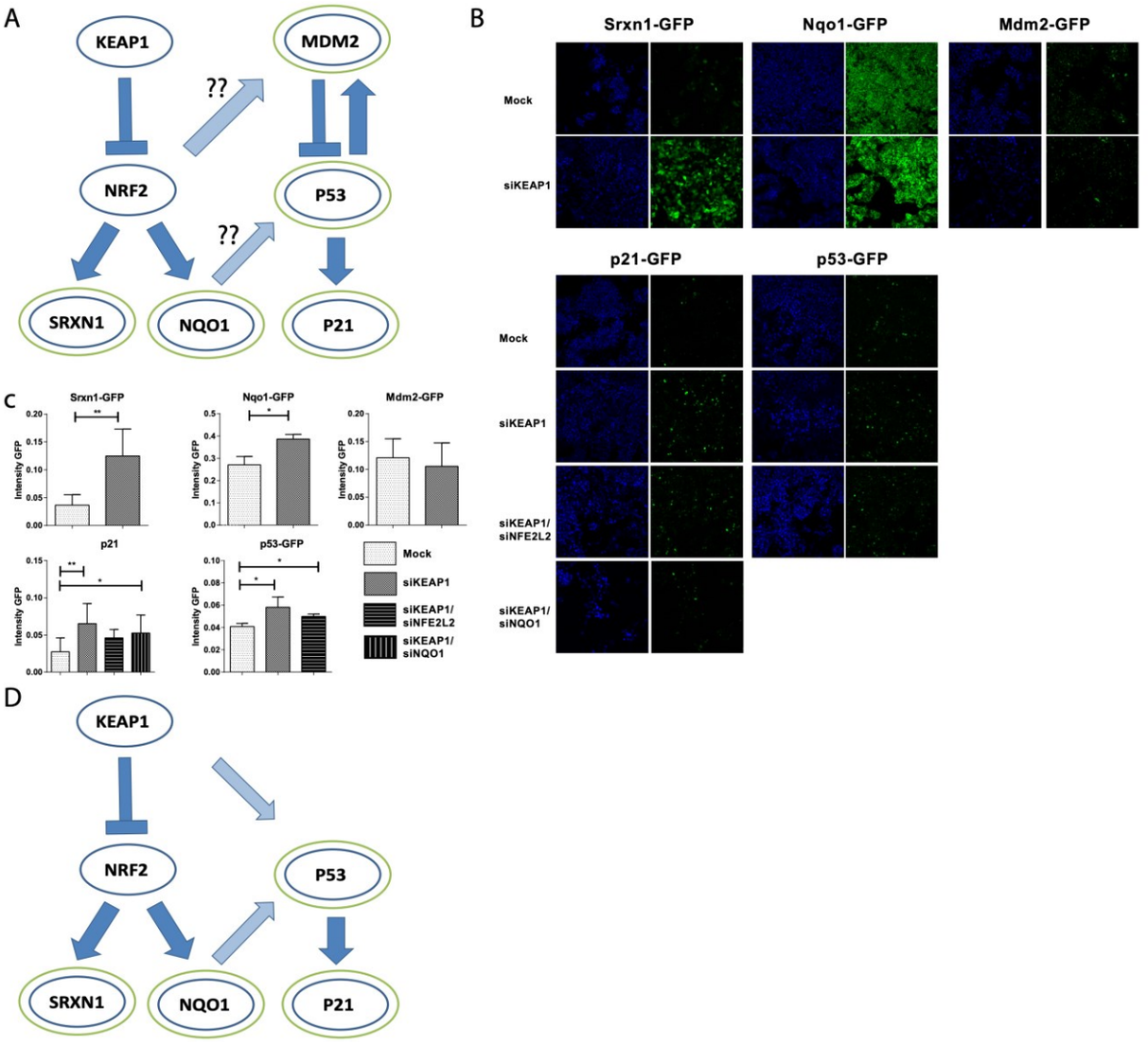

Fig. 5. Knock down of KEAP1 in Srxn1-GFP, p21-GFP, Nqo1-GFP, Mdm2-GFP and p53-GFP. A) Possible crosstalk mechanism between Nrf2 and p53 pathway. Pathway components indicated with a green circle are tagged with Green Fluorescent Protein (GFP). B) Example images of Srxn1-GFP, Nqo1-GFP, Mdm2-GFP, p21-GFP and p53-GFP without knock down (mock) and with knock down (siKEAP1, siKEAP1/siNFE2L2 and siKEAP1/siNQO1). One condition consists of two images for each reporter, an image of nuclear staining (left image) and an image of GFP (right image). C) Knock down of KEAP1 for Srxn1-GFP, Nqo1-GFP, Mdm2-GFP, p21-GFP and p53-GFP compared to the mock condition. Double knock down with KEAP1 and NFE2L2 for p21-GFP and p53-GFP. Standard deviations are shown for three independent replicates. Significance (* = $p < 0,05$, ** = $p < 0,01$) calculated with a one-tailed Student's t-test. D) Schematic overview of the crosstalk mechanism between Nrf2 and p53 pathway. Proposed links according to observed data are depicted in light blue.

The diethyl maleate-induced oxidative stress caused increased levels of Keap1 foci, Nrf2 and Srxn1 in HepG2 reporter cells over time. Upon oxidative stress, Keap1 is no longer able to target Nrf2 for proteasomal degradation[118]. First, Keap1 is bound by Sequestosome 1 (SQSTM1/p62) and targeted for degradation [138]; second, Nrf2 accumulates in the nucleus and third, Srxn1 and other Nrf2 targets are upregulated. Our observed time-dynamics of the Nrf2 response activation by DEM revealed initial rapid Nrf2 induction, within 1 hour with a maximum at ~4 hours, followed

by a late, >4 hours, and sustained onset of Keap1 foci formation. It has been suggested that Keap1 turnover is mainly governed by autophagy in a p62-dependent manner[139]. Indeed, Keap1-GFP foci co-localize with p62 (data not shown). Importantly, Nrf2 directly activates the expression of Keap1 as well as p62[120]. Thus, upon Nrf2 stimulation, all newly assembled Keap1 cannot bind to Nrf2 and will bind to p62 instead. Thus, our late Keap1 foci formation is likely rather a consequence than a cause of Nrf2 activation. These findings exemplify the explicit enhanced information of a quantitative imaging-based analysis of the dynamic behaviour of individual Nrf2 signalling components.

Regarding the time dynamics of the DNA damage response, exposure to model compound etoposide led to the almost immediate formation of 53bp1 DNA damage foci, within ~3 hours followed by p53 upregulation and almost direct subsequent increased levels of p21. Despite the clear increase in 53bp1-GFP foci, a considerable variation in number of 53bp1 foci between the replicates was observed during exposure to etoposide. This is possibly due to higher zoom used for image acquisition to allow sufficient resolution of foci detection, but consequently each image contained less cells. In addition, due to the longer image acquisition time, the time resolution was ~2.5 hours, which limited the more detailed analysis of the entire dynamics of foci formation. A fast 53bp1 foci formation response with a peak at 1 hour post etoposide exposure was reported in HeLa cells[140], and for irradiation 20 minutes was the maximal 53bp1 response[141]. Possibly due to our current imaging limitations, we have missed the steep initial dynamics of 53bp1 foci formation at the lower concentrations of etoposide. Intriguingly, the highest concentration of etoposide showed a gradual and sustained increase of 53bp1 foci for the entire 24 hours period exposure; possibly this high concentration affects the effectiveness of the DNA damage recognition programs and prohibits the rapid association of 53bp1 at DNA damage sites. Yet, this reduced 53bp1 accumulation was not reflected by an inhibition of p53-GFP stabilization and reduced p21-GFP induction. This suggests that there does not seem to be a direct quantitatively relationship between foci number and p53 activity. Future studies should elucidate the mechanism of reduced foci formation at high concentrations of etoposide.

The broad concentration range of DEM and etoposide allowed precise identification of the PoD for each pathway component. PoD identification revealed a specific pathway response: DEM showed a much lower PoD for Nrf2 activation (1.8 µM) than for p53 activation (178 µM); yet, etoposide demonstrated a PoD for Nrf2 activation (5.6 µM) that was close to the PoD of p53 activation (1.0 µM). These results suggest crosstalk as DEM and etoposide can activate p53 and Nrf2 signalling, respectively. Although we have not measured the actual effect of DEM on cellular glutathione homeostasis, we suspect that at the lower levels no major glutathione decrease has occurred, and that the Nrf2 activation is directly mediated by modulation of cysteine residues of Keap1. At a higher concentration, glutathione might become decreased, allowing the onset of oxidative stress and thereby initiation of ROS mediated DNA damage, which is detected by the

p53 pathway. The fact that the PoD for etoposide for both p53 and Nrf2 activation are in a comparable range, suggests a similar molecular initiation events, i.e. the DNA damage, causes activation of both program, albeit that the etoposide-induced Nrf2 activation does not parallel the efficiency and amplitude as observed for DEM.

Depletion of Keap1 due to RNA interference resulted in an increase of basal p53 and p21 activation levels, suggesting either a direct inhibitory role of Keap1 on the DNA damage response. Alternatively, Keap1 has an indirect role through inhibition of Nrf2, and thus, increased Nrf2 activity would promote the p53-mediated induction of p21 expression. Indeed, double knock down of Keap1 and Nrf2 resulted in a partial restoration of p21 and p53 basal levels indicating that Nrf2 accumulation partially facilitates crosstalk leading to upregulation of p53 signalling. This activating role of Nrf2 on p53 signalling could either be a direct effect or mediated through one of its target genes. Recently, Nrf2-induced Nqo1 was shown to promote p53 accumulation during oncogene-induced senescence which was Mdm2 independent[125]. As expected, downregulation of Keap1 resulted in significant higher levels of Nqo1, a bona fide Nrf2 target gene. As such, upregulation of Nqo1 after Keap1 knock down could then modulate p53 levels, followed by p21 upregulation. A double knock down of Keap1 and Nqo1 also resulted in a partial restoration of p21 levels. Although this is not a significant effect, this implies a role of Nqo1 in the crosstalk between oxidative stress and DNA damage. However, since double knock down of Keap1 with either Nrf2 or Nqo1 only partially restores basal p21 levels, Keap1 might in addition partly regulate p53 signalling through other Nrf2-independent mechanisms. Therefore, we propose a mechanism shown in figure 5D where Nqo1 is one of the switches between oxidative stress and p53 signalling in HepG2 cells.

Regarding the crosstalk between p53 signalling and the Nrf2 pathway, it is noteworthy that p21 can bind the DLG and ETGE motifs of Nrf2 and thereby competing with Keap1 for Nrf2 binding; the p21 binding leads to enhanced accumulation of Nrf2[142]. Possibly the etoposide-induced Nrf2 activation is partly related to this p21-mediated Nrf2 stabilization effect.

Here, we utilized our established HepG2 GFP reporters to provide a detailed mapping of the dynamics landscape of the oxidative stress response and DNA damage signalling pathways. We recognize that the components used are only a reflection of the complexity of the entire pathways. Regardless, the current reporters provide an overall high level of detail on the dynamics of several key components. We feel that these detailed quantitative landscapes are fit-for-purpose to define PoD for pathway activation as well as possible crosstalk. In addition, this data can be used for mathematical modelling to assess detailed information on pathway regulation in response to adaptive stress response activation. Future directions will involve integration of multiple adaptive stress response reporters in one cell line to closely follow the dynamics of individual stress response pathway components at the single cell level and unravel their synchronized timing of activation at their variations at the population level.

Acknowledgements

This work was supported by a Unilever SEAC research grant, the IMI MIP DILI project (grant agreement number 115336) and the EU FP7 Seurat-1 Detective project (grant agreement number 266838).

Supplemental figures

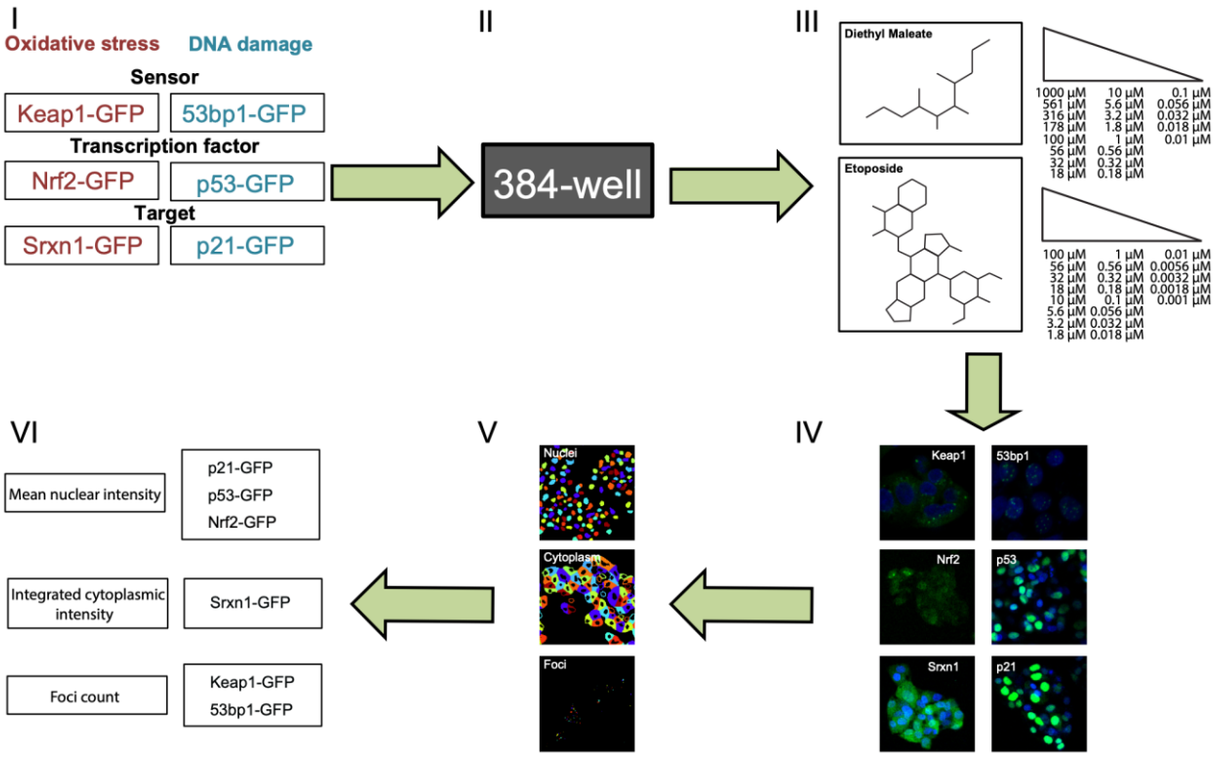

Fig. S1. Workflow of GFP reporter exposure, image acquisition and image analysis. I) Three GFP reporters of both Nrf2 and p53 pathway are II) seeded in a 384-well format, III) exposed to a broad dose range of model compounds diethyl maleate and etoposide followed by IV) image acquisition, V) image analysis and VI) GFP read-out.

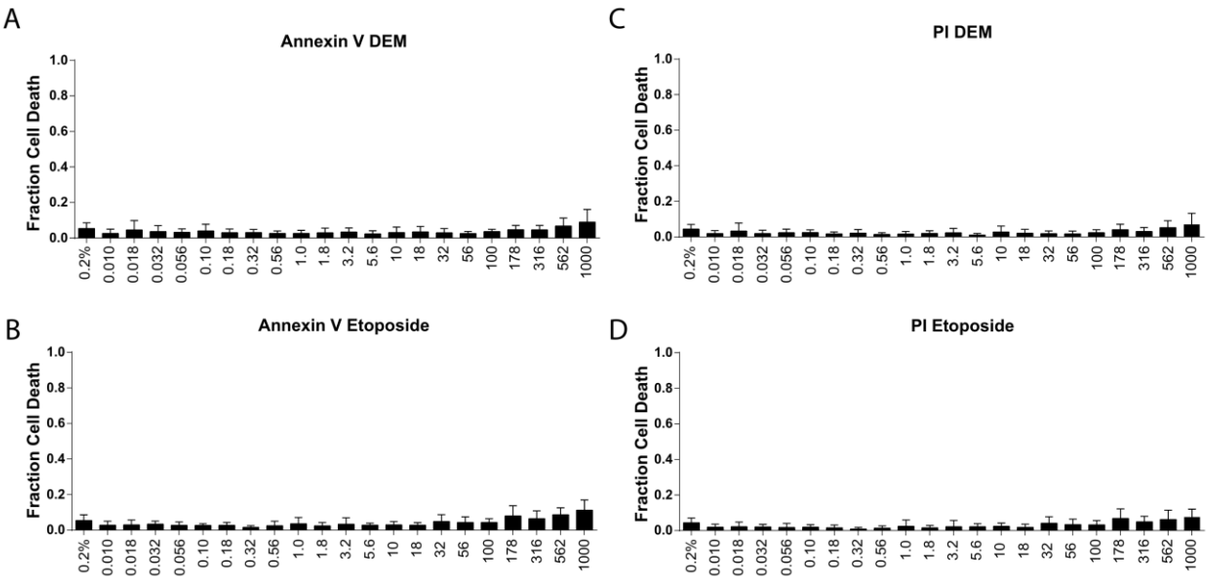

Fig. S2. Cell death markers for DEM and etoposide. A) AnnexinV in fraction positive cells for 0.2% DMSO and 21 concentrations of DEM. B) Propidium iodide (PI) in fraction positive cells for 0.2% DMSO and 21 concentrations of DEM C) AnnexinV in fraction positive cells for 0.2% DMSO and 21 concentrations of etoposide. D) Propidium iodide (PI) in fraction positive cells for 0.2% DMSO and 21 concentrations of etoposide. Mean and standard deviation shown for three replicates of reporters Nrf2-GFP, Srxn1-GFP, p21-GFP and p53-GFP.

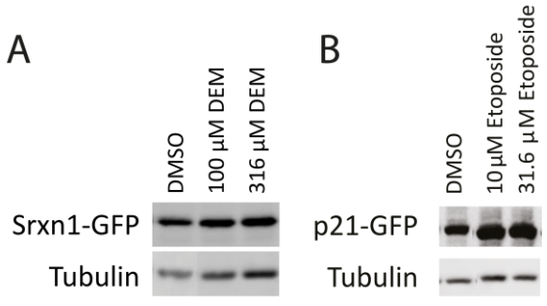

Fig. S3. Western blot analysis of Srxn1-GFP and p21-GFP after DEM and etoposide exposure respectively. A) Western blotting with the GFP antibody in Srxn1-GFP cells exposed to DMSO (0.2%), 100 µM and 316 µM DEM. B) Western blotting with the GFP antibody in p21-GFP cells exposed to DMSO (0.2%), 10 µM and 32 µM etoposide.

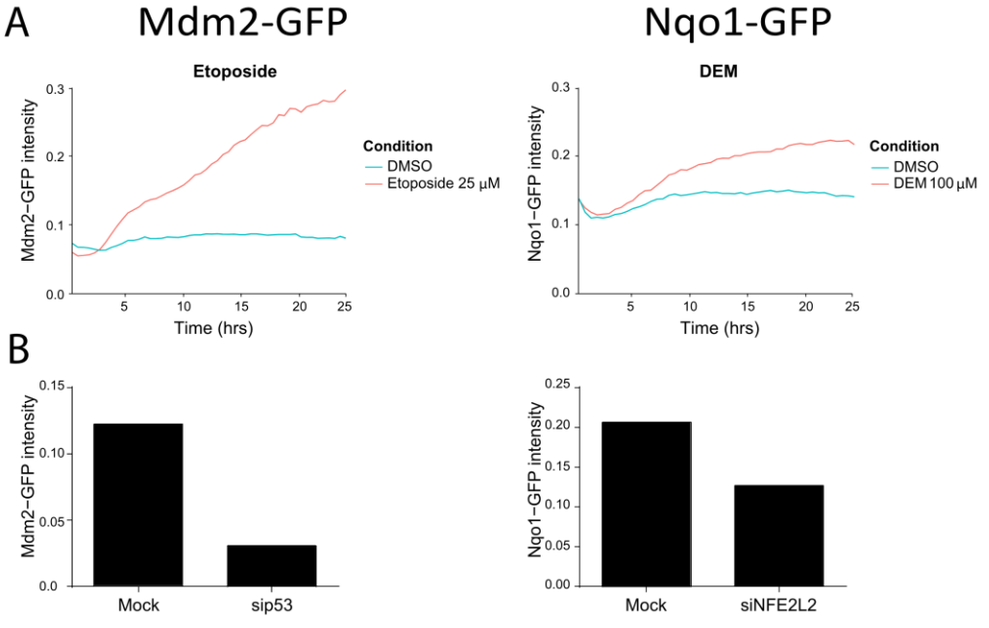

Fig. S4. Characteristics of Mdm2-GFP and Nqo1-GFP. A) Time dynamics of nuclear Mdm2-GFP intensity for DMSO and 25 µM of etoposide (left graph) and of cytoplasmic intensity of Nqo1-GFP for DMSO and 100 µM DEM (right graph). B) Nuclear Mdm2-GFP intensity for the untransfected control "mock" and siTP53 after 7 hours of treatment with 25 µM etoposide (left graph) and cytoplasmic Nqo1-GFP intensity for the untransfected control "mock" and siNFE2L2 after 7 hours of treatment with 30 nM CDDO-me.

Chapter 4

Towards an advanced testing strategy for genotoxicity using image-based 2D and 3D HepG2 DNA damage response fluorescent protein reporters

This chapter has been published as:

M. Niemeijer*, B. ter Braak*, L. Wolters, S. Le Dévédec, P. Bouwman, B. van de Water

* Both authors contributed equally

Towards an advanced testing strategy for genotoxicity using image-based 2D and 3D HepG2 DNA damage response fluorescent protein reporters

Mutagenesis. 2021 Aug 27:geab031. doi: 10.1093/mutage/geab031.

Abstract

In vitro assessment of mutagenicity is an essential component in the chemical risk assessment. Given the diverse modes of action by which chemicals can induce DNA damage, it is essential that these in vitro assays are carefully evaluated for their possibilities and limitations. In this study, we used a fluorescent protein HepG2 reporter test system in combination with high content imaging. To measure induction of the DNA damage response (DDR), we used three different green fluorescent protein reporters for p53 pathway activation. These allowed for accurate quantification of p53, p21 and BTG2 (BTG anti-proliferation factor 2) protein expression and cell viability parameters at a single cell or spheroid resolution. The reporter lines were cultured as 2D monolayers and as 3D spheroids. Furthermore, liver maturity and cytochrome P450 enzyme expression were increased by culturing in an amino acid-rich (AAGLY) medium. We found that culture conditions that support a sustained proliferative state (2D culturing with normal DMEM medium) give superior sensitivity when genotoxic compounds are tested that do not require metabolisation and of which the mutagenic mode of action is dependent on replication. For compounds, which are metabolically converted to mutagenic metabolites, more differentiated HepG2 DDR reporters (e.g. 3D cultures) showed a higher sensitivity. This study stratifies how different culture methods of HepG2 DDR reporter cells can influence the sensitivity towards diverse genotoxicants and how this provides opportunities for a tiered genotoxicity testing strategy.

Key words: DNA damage, mutagenicity, test method, HepG2 BAC GFP, 3D model, drug metabolism, high content imaging, next generation risk assessment (NGRA), new approach methods (NAMs)

Introduction

In the current chemical risk assessment, the evaluation of genotoxicity is quite different from other chemical-induced adverse reactions as the typical 'safe threshold analysis' is thought to be not applicable to genotoxicants. This is because even low doses of genotoxicants can lead to DNA damage and thereby increase the chance to develop malignancies. However, besides directly damaging DNA, genotoxic compounds may also interfere with specific cellular processes (e.g. DNA synthesis or repair), thereby having indirect genotoxic effects. For compounds with such indirect genotoxic mode of action, it is relevant to determine the concentration level where no DNA damage effects occur[22].

Several well-established test systems are currently being used to identify potential genotoxic effects of chemicals. With the prokaryotic Ames test, specific mutagenic events, such as frameshifts or point mutations, can be observed using specific Salmonella tester strains. Although this test system is fast, inexpensive and easy to use, it suffers from poor sensitivity, likely due to differences in the response to drugs and DNA damage in prokaryotes versus higher eukaryotes[143]. Another well- known genotoxicity test system is the Comet assay developed in 1988 by Singh and

colleagues[144], which can detect DNA strand breaks in individual eukaryotic cells by quantifying the DNA track on an agarose gel. Since then many advances have been made to the standard Comet assay, so that it can identify different types of DNA damage[145,146]. However, this highly sensitive assay is still difficult to standardise because of a lack of consensus and potentially suffers from a relative high rate of false positives due to cytotoxicity effects[147,148]. Besides, the comet assay can only be used to determine if exposure to a compound results in DNA breaks, other types of DNA damage (e.g. point mutations) are not revealed[143]. A third genotoxicity test, which is also recommended by the OECD guidelines for chemical testing, is the Micronucleus test. Micronuclei are cytoplasmic bodies containing either a portion of an acentric chromosome or lagging whole chromosomes, a result of incorrect chromosome segregation during anaphase. The micronuclei can be quantified and are a measure for genotoxicity[149]. Limitations of this assay are that a cell division is required in the test cells, the relatively low specificity and the fact that gene mutations cannot be detected with this assay[143]. In the last few decades, several variants of the Ames test, Comet assay and Micronucleus test have been developed to improve throughput, human relevance and robustness, but concerns on limited predictivity remain.

A new type of genotoxicity testing does not focus on quantification of chemically induced genomic injury itself, but on the quantification of the cellular mechanisms that repair this DNA damage. It is expected that this strategy results in test methods with a higher sensitivity, as these repair mechanisms are already induced at low levels of DNA damage. Furthermore, for the different types of genotoxicity, different repair mechanisms can be identified, so that the chemical mode of action by which the damage is induced can be eluded[22]. The simplest variants of these assays comprise of antibody fluorophore staining, targeting focal accumulation of biomarker proteins involved in DNA damage repair of which γH2AX, 53BP1 and RAD51 are examples[150]. Lack of robustness and the limitation of a single end point measurement in fixed cells are major draw- backs of antibody-based methods. A more sophisticated method would be to use fluorescent reporter models[151]. The GADD45a-based fluorophore and luciferase reporter assays, GreenScreen and BlueScreen, are applied for high-throughput genotoxic hazard identification[152]. With a FACS-based measurement the ToxTracker can quantify chemically induced DNA damage repair using reporter stem cell lines. By using a combination of different reporter lines, this technology is able to detect both direct and indirect genotoxic effects and it can discriminate between clastogenic and aneugenic modes of action[128,153].

We have previously developed a large panel of fluorescent reporters for adaptive cellular stress responses, including the DNA damage response (DDR) in the human liver cancer cell line, HepG2[151,152]. We have applied these reporters for the prediction of drug- induced liver injury[27,28,79]. In these reporter cell lines, chemical induction activates expression of fluorescent-tagged stress biomarker proteins. By combining live cell confocal imaging with an automated image segmentation pipeline, the biomarker expression level as well as its subcellular localisation

can be accurately quantified over time and at a single cell level. Besides 2D culturing, these cell lines can also be cultured as spheroids in a 3D Matrigel environment[29,101]. These spheroids are stable for at least 2 weeks, which allows for repeated dosing. Furthermore, the HepG2 spheroids are metabolically more active as compared to HepG2 cells grown on a 2D surface, showing physiologically relevant levels of cytochrome P450 enzymes[101]. Most chemicals are metabolised in the human liver, which either leads to toxic clearing or the production of toxic metabolites; therefore, the presence of drug-metabolising enzymes in a test system is an important feature[154]. Of interest, when HepG2 cells are cultured in an amino acid-rich (AAGLY; Amino Acid-rich normal DMEM medium supplemented with 2% GLYcine) medium they change their glucose-dependent metabolism to an amino acid-fuelled profile, thus promoting further differentiation and expression of P450 enzymes at levels similar to primary human hepatocytes (PHHs), even in a 2D environment[53].

Here, we systematically investigated the application of p53 pathway DDR reporters in human liver models with different levels of maturation and metabolic competence. We used three HepG2 DNA damage green fluorescent protein (GFP) reporter cell lines; p53-GFP, p21-GFP and BTG2-GFP. These reporter cell lines were cultured in four different conditions: 2D using conventional Dulbecco's Modified Eagles's Medium (DMEM) or AAGLY medium, and 3D using DMEM/F12 or AAGLY medium. To assess sensitivity of the different culture conditions towards DNA damage, we exposed these models to five different chemicals that are known to cause a direct or indirect genotoxic effect with a distinct mode of action (Table 1). We envision that this study contributes to a better understanding of the different culture conditions that impact on metabolic competence and assay sensitivity in the context of the DDR. This will allow refinement of chemical safety testing strategies for a better-informed risk evaluation.

Materials and Methods

Chemicals or reagents

Mitomycin C and aflatoxin B1 were obtained from Sigma-Aldrich (Zwijndrecht, The Netherlands). Gemcitabine was acquired from Eli Lilly (Indianapolis, IN, USA) and brequinar was obtained from Fluorochem (Hadfield, UK). Cisplatin was acquired from Ebewe Pharma (Unterach am Attersee, Austria). Compounds were dissolved in dimethylsulfoxide (DMSO), except for mitomycin C [phosphate-buffered saline (PBS)], cisplatin (PBS) and gemcitabine (sterile H2O). The maximum final DMSO concentration used was 0.2% (v/v).

Cell culturing

Human hepatocellular carcinoma HepG2 cells were obtained from the American Type Tissue Culture Collection (ATCC, Wessel, Germany). The HepG2 BAC-GFP reporters for human BTG2, p21 and p53 were generated previously and used to monitor the DDR[29,79]. Cells were maintained in DMEM high glucose (Gibco) supplemented with 10% (v/v) fetal bovine serum (FBS), 25 U/ml penicillin and 25 µg/ml streptomycin (referred to as normal DMEM medium) at 37°C and 5% CO2.

Table 1. List of compounds with the concentration range used in this study.

Compound	Abbreviation	Tested concentration range
Aflatoxin B1	AFB	0.10 – 21.54 µM
1. Aflatoxin B1 is converted into reactive intermediate AFB1-8,9-epoxide mainly by CYP3A4. *2. AFB1-8,9-epoxide forms DNA adducts.* *3. DNA damage is induced with direct compound-DNA interaction.*[155]		
Brequinar	BRE	0.22 – 100 µM
1. Brequinar inhibits dihydroorotate dehydrogenase (DHOD). *2. Pyrimidine biosynthesis is blocked.* *3. DNA/RNA synthesis and repair is inhibited.* *4. DNA damage is induced indirectly without compound-DNA interaction.*[156]		
Cisplatin	CIS	0.10 – 21.54 µM
1. Cisplatin is taken up by the cell by copper transporters. *2. Cisplatin crosslinks (mainly intrastrand) with the purine bases on the DNA.* *3. Interference with DNA repair mechanisms.* *4. DNA damage is induced with direct compound-DNA interaction.*[157,158]		
Gemcitabine	GEM	0.0037 – 0.80 µM
1. Gemcitabine is phosphorylated by deoxycytidine kinase to its active form. *2. Gemcitabine diphosphate or triphosphate (dFdCTP) incorporates at the end of the elongating DNA strand.* *3. RAD51-dependent Homologous recombination and DNA synthesis is inhibited.* *4. DNA damage is induced with direct compound-DNA interaction.*[159]		
Mitomycin C	MMC	0.10 – 21.54 µM
1. Mitomycin C makes DNA cross-links (both inter and intrastrand) *2. DNA damage is induced with direct compound-DNA interaction* *1. Cytochrome P450 reductase induces redox cycling of Mitomycin C.* *2. Reactive oxygen species (ROS) are formed.* *3. ROS leads to an indirect DNA damage effect.*[158,160]		

The genotoxic mode of action based on literature.

The reporter cells were tested between passages 19–21 throughout the data presented (Supplementary Figure 1).

2D cell culturing in normal DMEM medium

Cells were plated in Greiner Bio-One black SCREENSTAR 384-well plates (Alphen aan den Rijn, The Netherlands), at 10.000 cells per well in normal DMEM medium. Cells were allowed to adhere for 24 h before treatment or RNA isolation.

2D cell culturing in AAGLY medium

Cells were plated in Greiner Bio-One black µClear 384-well plates (Alphen aan den Rijn, The Netherlands), at 18.000 cells per well in normal DMEM medium. Forty-eight hours after plating, cells switched from normal DMEM medium to AAGLY medium consisting of DMEM low glucose supplemented with 7.7% (v/v) FBS, 20 U/ml penicillin, 20 µg/ml streptomycin, 160 µl/ml MEM non-essential amino acids solution (100×), 80 µl/ml MEM essential amino acids (50×) solution and 2% glycine with a pH of 7[53]. To drive hepatic differentiation, cells were cultured for 30 days before treatment or RNA isolation. Medium was refreshed twice a week.

3D cell culturing in DMEM/F12 medium

3D culturing was performed as described previously[29,101]. Briefly, cells were cultured in a layer of 5 mg/ml Matrigel matrix basement membrane, growth factor reduced (Corning, Cat#354230,

Lot#6130005) in Greiner Bio-One black µclear 384-well plates (Alphen aan den Rijn, The Netherlands) at a density of 1000 cells per well to form liver spheroids in 21 days before treatment or RNA isolation. Spheroids were maintained in DMEM/F12 high glucose and phenol red free supplemented with 10% FBS and 25 U/ml penicillin and 25 µg/ml streptomycin (referred to as DMEM/F12 medium). Medium was refreshed twice a week.

3D cell culturing in AAGLY medium

3D culturing was performed as described above. However, 7 days post seeding, DMEM/F12 medium was replaced by AAGLY medium with no phenol red. AAGLY medium was then refreshed twice a week until 21 days before treatment or RNA isolation.

Cell treatment and viability

Two different compound exposure scenarios were performed: a single exposure in 2D and a 4-day repeated exposure in 3D. A schematic overview of the tested exposure scenarios for each HepG2 model has been depicted in Figure 1. For the single exposure scenario in 2D, medium was replaced by freshly diluted compound in medium 24 h post seeding. DDRs were monitored after 24, 48 and 72 h by live cell confocal imaging (Figure 1A and B). For the 4-day repeated exposure scenario in 3D, each day medium was replaced by freshly diluted compound in medium for four consecutive days (Figure 1C and D). The imaging was started 24 h after the last exposure. For both scenarios, five compounds in eight concentrations were tested. DMSO, PBS or ultrapure H2O were used as solvent controls. The ATP-lite luminescence kit (Perkin Elmer) was used according to supplier's protocol to measure cell viability. Measurements were performed 72 h or 24 h post single or repeated exposure, respectively. Absolute IC_{50} values have been calculated over the ATP-lite data by determining the intersect of the fitted concentration–response curve with the 50% viability baseline via GraphPad prism 8.1.1.

Cell imaging

Prior to imaging, cells were stained with Hoechst 33342 at a concentration of 0.1 µg/ml to visualise the nuclei. To examine compound-induced cell death using confocal microscopy, propidium iodide (PI) was added during all compound exposures at a concentration of 100 µM to stain for necrotic or late apoptotic cells. The induction of GFP intensities and PI were monitored with a Nikon Eclipse Ti confocal laser microscope (Nikon, Amsterdam, The Netherlands), equipped with lasers at wavelengths 408, 488 and 561, an automated stage and perfect focus system at 37°C and 5% CO2. Images for 2D cultures were acquired with a Nikon 20x Dry Plan Apo VC NA 0.75 objective. Images for 3D cultures were acquired with a Nikon 10x Dry Plan Fluor NA 0.3 objective. For each condition, a z-stack of 9–11 images was generated with a step size of 30 µm.

Quantitative image analysis

For 2D cultures, image quantification was performed with Cell Profiler version 2.2.0 (Broad Institute, Cambridge, USA) using modules described previously[79]. Nuclei segmentation based on

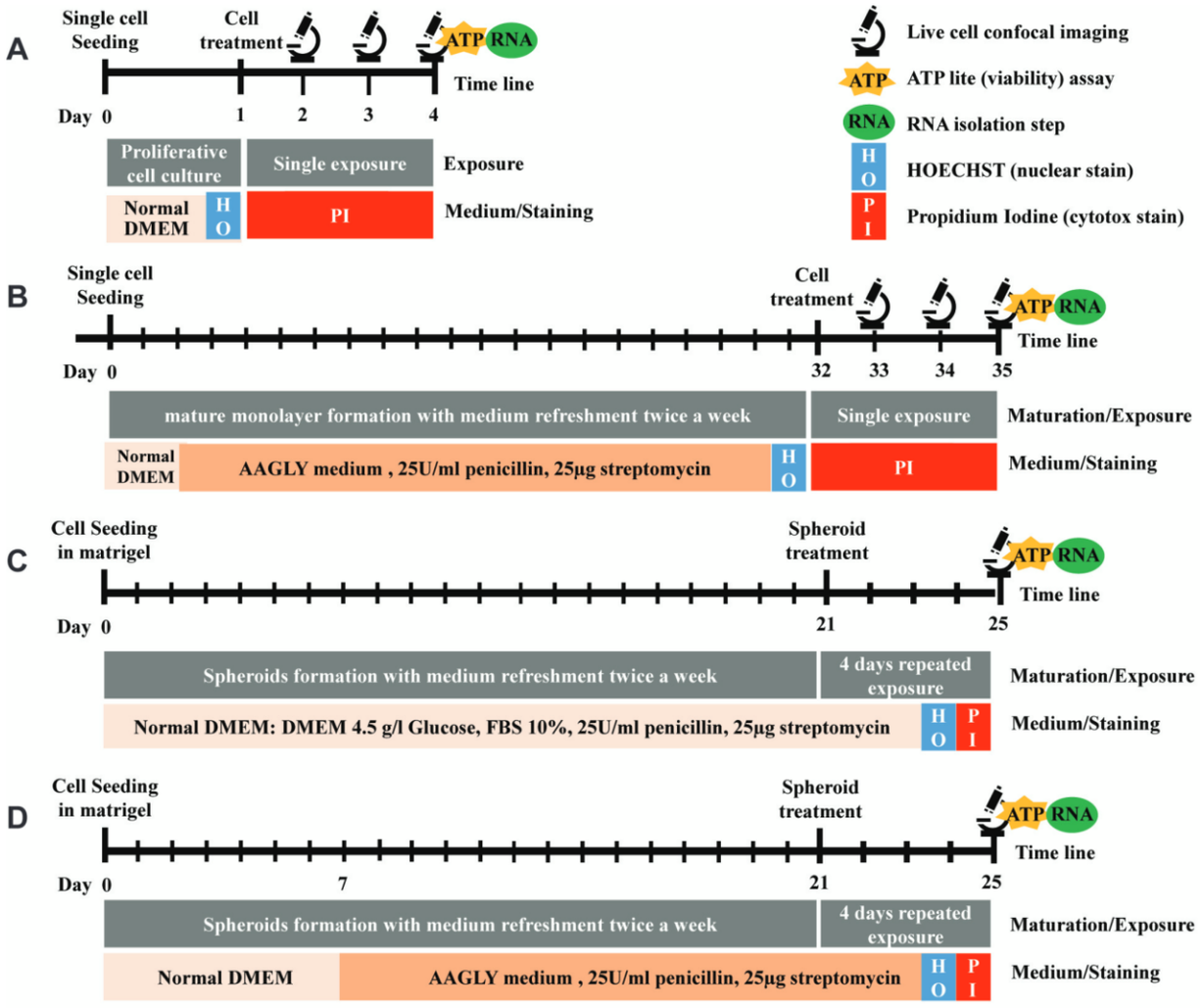

Fig. 1. Overview of the four different HepG2 models used in this study. Schematic overview of the experimental procedures of the different models with in the upper right corner the legend: HepG2 cultured in 2D and DMEM medium (A), HepG2 cultured in 2D and AAGLY medium (B), HepG2 cultured in 3D and DMEM medium (C), HepG2 cultured in 3D and AAGLY medium (D).

Hoechst was done in ImageJ using an in-house developed macro based on the watershed masked clustering algorithm[129]. Segmentation of the cytoplasmic area was done using the Distance N method expanding the edges of nuclear objects with six pixels followed by subtraction of the nuclear area. p21 and p53-GFP intensities were measured in the nuclei and BTG2-GFP in the cytoplasm. The PI-positive cells were identified by an overlay of the PI signal and the segmented nuclei. A cell was considered positive when there was at least 10% overlap. Results were stored in HDF5 format[161]. To extract summarised data for further analysis and visualisation, in-house developed R-scripts were used in RStudio (version 1.0.153) (Boston, MA, USA)[131,135,137]. The mean nuclear and cytoplasmic intensities of all measured single cells and the fraction of PI-positive cells for each image were extracted as output from the HDF5 files.

For 3D cultures, the NIS Elements analysis software (Nikon, Amsterdam, The Netherlands) was used to quantify the GFP intensity and PI-positive area within spheroids. First, a 2D projection per replicate treatment was created based on the maximum Hoechst intensity across z-stacks.

Then, spheroids were segmented by setting a threshold for the Hoechst signal. The GFP intensity was measured in the spheroids and the PI-positive area within spheroids was determined by the overlap of PI signal within spheroids. Further analysis was performed using in-house developed R-scripts in RStudio (version 1.0.153) (Boston, MA, USA).

To compare the GFP induction of the tested models, first GFP in- tensities were min-max normalised for each model. Then, a hierarchical clustering analysis was performed using R package pheatmap[133]. First, Euclidean distances were calculated between different models, reporters and exposure durations. Thereafter, the mean of the Euclidean distances for the three different reporters for each model and exposure duration was used for hierarchical clustering using the complete linkage method. For the end points for cell death, a hierarchical clustering was performed based on Euclidean distance between each model, exposure duration and end point.

Real-time qPCR

Total RNA from the 2D and 3D cultures was isolated each from eight wells of a 384-well plates using the NucleoSpin® mRNA isolation kit or Trizol reagent (Invitrogen) according to manufacturer's instructions, respectively. Isolated RNA was considered of sufficient quality when A260/280 and A260/230 ratios were higher than 1.9 and 1.5, respectively. The RevertAid first-strand cDNA synthesis kit (Thermo Fisher) with Oligo(dT) 18 primers was used to generate the template from 500 ng RNA for the real time quantitative PCR (RT-qPCR) experiments. SYBR green master mix (Thermo Fisher) was used as a dye to monitor the accumulation of the PCR product using 25 ng cDNA template. In Supplementary Table 1, the primers sequences can be found that were used in the PCR reaction; denaturation (95°C for 30 s), annealing (60°C for 1 min), extension (72°C for 30 s) with 40 cycles. The $2^{-\Delta\Delta CT}$ method was used to quantify relative gene expression profiles using GAPDH identified as a stable housekeeping gene for HepG2[162] and the HepG2 2D model as a reference sample[163].

TempO-seq transcriptomics

Similarity between HepG2 wild-type and DDR reporter cells in p53 signalling was evaluated by measuring the mRNA expression of a targeted gene set consisting of the S1500+ gene list[164] using the TempO-seq technology by BioSpyder Technologies Inc. (Carlsbad, CA, USA)[30]. In brief, HepG2 cells were seeded in 96 wells plates (Corning, Amsterdam, The Netherlands) at a density of 156.000 cells/cm^2. Next day, cells were exposed to cisplatin in a wide concentration range for 8 or 24 h followed by sample collection using 1× BNN lysis buffer (BioSpyder). Samples were lysed for 15 min at room temperature, stored at −80°C and shipped for transcriptome analysis by BioSpyder. The TempO-seqR package was used for the alignment of raw reads, followed by normalisation using DESeq2 R package[165] of the read counts and log2 transformed.

Data analysis

Point of departures (PODs) have been determined using an in-house established R package 'modelpod'. Concentration–response curves are fitted with Loess regression using the loess function from the base stats R package (with a span of 2/4 and 1 polynomial degree). The intersect of this fitted curve with the sum of the DMSO control value and two times the standard deviation (SD) from the regression of the DMSO gives an X value, the lowest concentration at which we observe a significant (positive or negative) effect defined as the PoD.

Statistics

For all experiments three independent biological replicates were performed. Additionally, for the imaging of the 2D models two positions per well have been imaged which were treated as technical replicates. Error bars in the concentration–response plots represent the SD of the three biological replicates. Significance for quantitative PCR (qPCR) data was determined using two-way ANOVA with Tukey's multiple testing correction represented as *$P_{adj} < 0.05$, **$P_{adj} < 0.01$ and ***$P_{adj} < 0.001$.

Results

Characterisation of hepatic phenotype of HepG2 models

Previously, we generated the HepG2 BAC-GFP reporter platform as a tool for the assessment of chemical-induced toxicity. Using live cell confocal microscopy, we accurately quantified stress response activation of a total of eight different stress response pathways using 20 different biomarkers[27,28,79]. In this study, we focussed on BTG2, p21 and p53 reporters of the DDR. Since differences in drug metabolism capacity can have profound genotoxic consequences, we tested different 2D and 3D culture set-ups to study their suitability for the recognition of chemical-induced DNA damage.

These HepG2 reporter cells were cultured in 2D either using normal medium having limited metabolic activity or medium with high levels of amino acids (AAGLY medium) to induce hepatocyte maturation for 30 days (Figure 2A), as previously described by Boon and colleagues[53]. Culturing HepG2 cells with AAGLY medium stops the proliferating capacity and allows the formation of a monolayer which was highly similar to the morphology of a PHH 2D culture (Figure 2A).

Previously, we have shown that 3D culturing of the HepG2 reporter model also resulted in a liver model with an increased metabolic potential[29]. By culturing HepG2 cells in a layer of Matrigel, cells clustered, stopped proliferating and formed well-rounded spheroids in 3 weeks resulting in an improved hepatic phenotype (Figure 2). We also combined the 3D culturing of the HepG2 reporter cells with the AAGLY medium. Since the AAGLY medium stopped the cell proliferation, which was necessary for spheroid formation, we used normal DMEM medium for the first 7 days. We anticipated that 2 weeks of AAGLY medium would further enhance the HepG2 hepatocyte

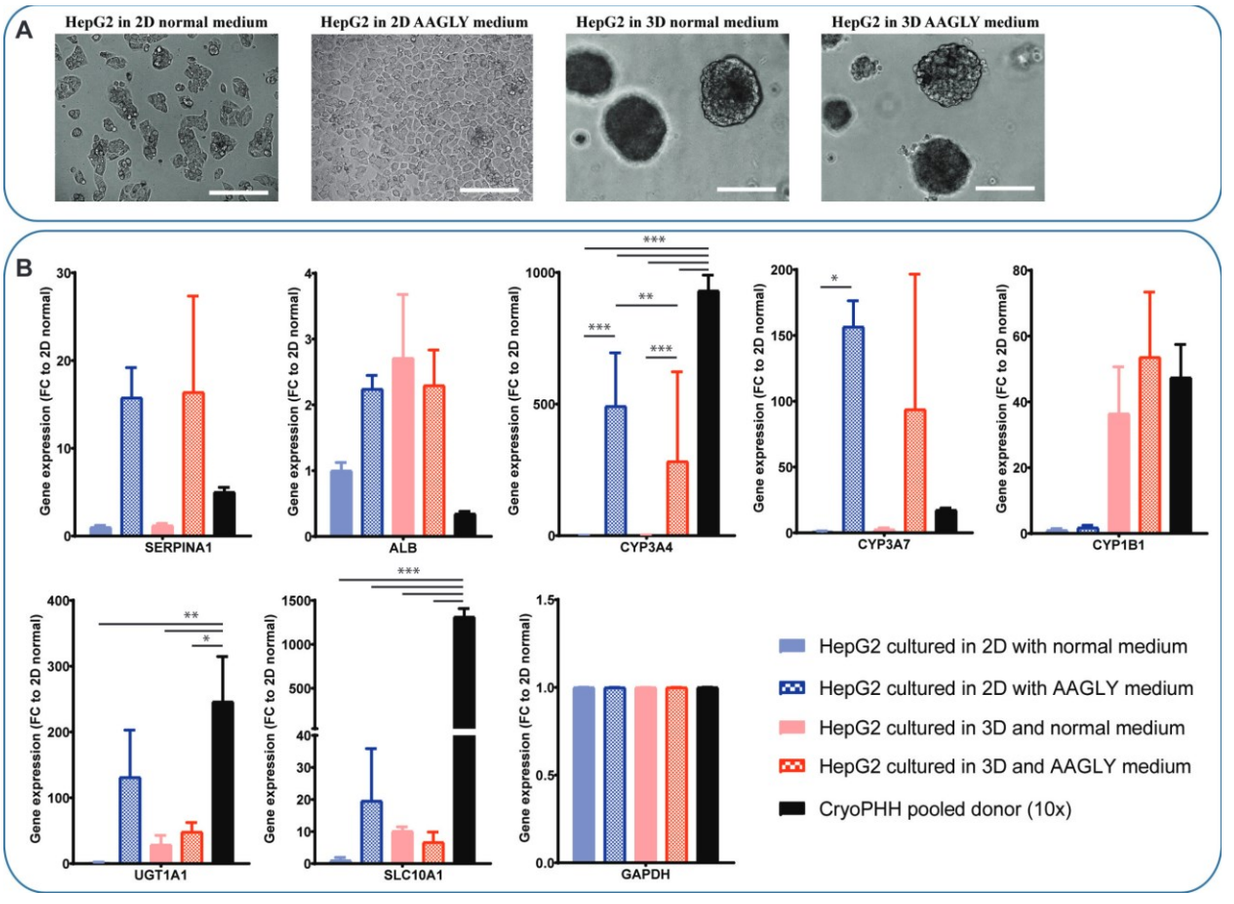

Fig. 2. Hepatocyte maturation status of four different HepG2 models. A) Bright field pictures showing morphological differences between the different models; HepG2 cultured in 2D and DMEM medium, HepG2 cultured in 2D and AAGLY medium, HepG2 cultured in 3D and DMEM medium, HepG2 cultured in 3D and AAGLY medium from left to right. B) Gene expression profiles of some hepatocyte markers (SERPINA1 and ALB), CYP enzymes (3A4, 3A7 and 1B1) and transporters (UGT1A1 and SLC10A1) and the housekeeping genes (GAPDH). Gene expression values are relative to model 1 (HepG2 cultured in 2D and DMEM medium) and benchmarked to a pool of 10 different donors of cryopreserved PHHs (10x). N=6; error bars represent SD; significance levels represented as *padj<0.05, **padj<0.01 and ***padj<0.001.

maturation in the 3D set-up. The morphology of both 3D models was similar in the 3D AAGLY medium condition (Figure 2).

To evaluate the relative differentiation level of the different cultures, we determined several key hepatocyte differentiation markers. Culturing HepG2 cells in AAGLY medium had the greatest effect on hepatocyte maturation, with strong upregulation of hepatocyte markers *SERPINA1*, *CYP3A4*, *CYP3A7*, *UGT1A1* and *SLC10A1* as compared to normal DMEM medium (Figure 2B). However, the addition of AAGLY medium did not lead to induction of *CYP1B1* in 2D, while it was upregulated by ~50-fold in the 3D culturing conditions. In general, culturing in a 3D set-up in DMEM led to increased expression of *ALB*, *CYP1B1*, *UGT1A1* and *SLC10A1* compared to 2D in DMEM, although this upregulation was not significant due to higher variance. Combining AAGLY medium with the 3D set-up led to a clear induction of *CYP3A4*, *SERPINA1* and *CYP3A7* compared to DMEM, reaching similar levels as 2D in AAGLY medium. While the more mature models

showed hepatocyte gene expression profiles similar to plated cryopreserved PHH, some genes like *SLC10A1* were still markedly lower as compared to this gold standard.

DDR activation and quantification

Next, we tested a set of compounds (see Table 1) on the three different DDR reporters under the various culture conditions. To verify the similarity in p53 signalling between these three different DDR reporters, the expression of key related genes has been evaluated upon exposure to cisplatin for 8 or 24 h. Here, no significant difference in stress response was measured indicative of preservation of wild-type p53 signalling during reporter development and passaging (Supplementary Figure 1).

Since proliferation of HepG2 cells cultured in the conventional normal DMEM medium hampered long-term culturing without passaging, only a single compound treatment was tested for 24, 48 or 72 h. Therefore, for comparison, also the AAGLY medium in 2D was evaluated using the same treatment regime. In 3D both conventional normal DMEM medium and AAGLY medium spheroids are stable and allowed for repeated 4-day exposure. DDR reporter activation was observed in all the different culture conditions and upon treatment of three different example compounds, aflatoxin B1, cisplatin and mitomycin C (Figure 3A). When exposed to the different genotoxic compounds, the BTG2-GFP was strongly induced while in control conditions no induction of BTG2-GFP was seen (Figure 3B). Importantly, the various culture conditions had a very different effect on the sensitivity towards the genotoxicants. For example, when HepG2 cells were cultured in 2D with conventional normal DMEM medium, aflatoxin B1 led to a steady concentration-dependent induction of BTG2-GFP with a peak at 10 µM. In contrast, when cultured in AAGLY medium, the HepG2 became more sensitive and the maximum BTG2 upregulation was seen at ~40 times lower concentrations. Unexpectedly, this increased sensitivity of HepG2 cells cultured in 2D with AAGLY medium with respect to BTG2-GFP activation for aflatoxin B1 did not translate to an increased sensitivity towards cell death, possibly more mature HepG2s are better equipped to counteract the aflatoxin B1-induced adversity. For direct mutagens like cisplatin, the 2D and 3D model in normal DMEM medium showed the highest BTG2-GFP sensitivity. These models were also most sensitive with the cell viability readout with this compound. For mitomycin C, we could clearly observe that at low concentrations all models showed a strong BTG2-GFP response and at high concentrations cell death was induced, visualised by the PI-positive cells/spheroids and a concentration-dependent reduction of ATP content. In contrast, the (in)direct anti-metabolites gemcitabine and brequinar only induced BTG2-GFP responses in the proliferating HepG2 cultured in 2D in normal DMEM medium (Supplementary Figure 2).

Cell death induction upon chemical-induced DNA damage in HepG2 models

Severe DNA damage may decrease cellular viability, and although this is a non-specific adverse outcome, it may be a sensitive general readout of toxicity. To evaluate cell death induction upon

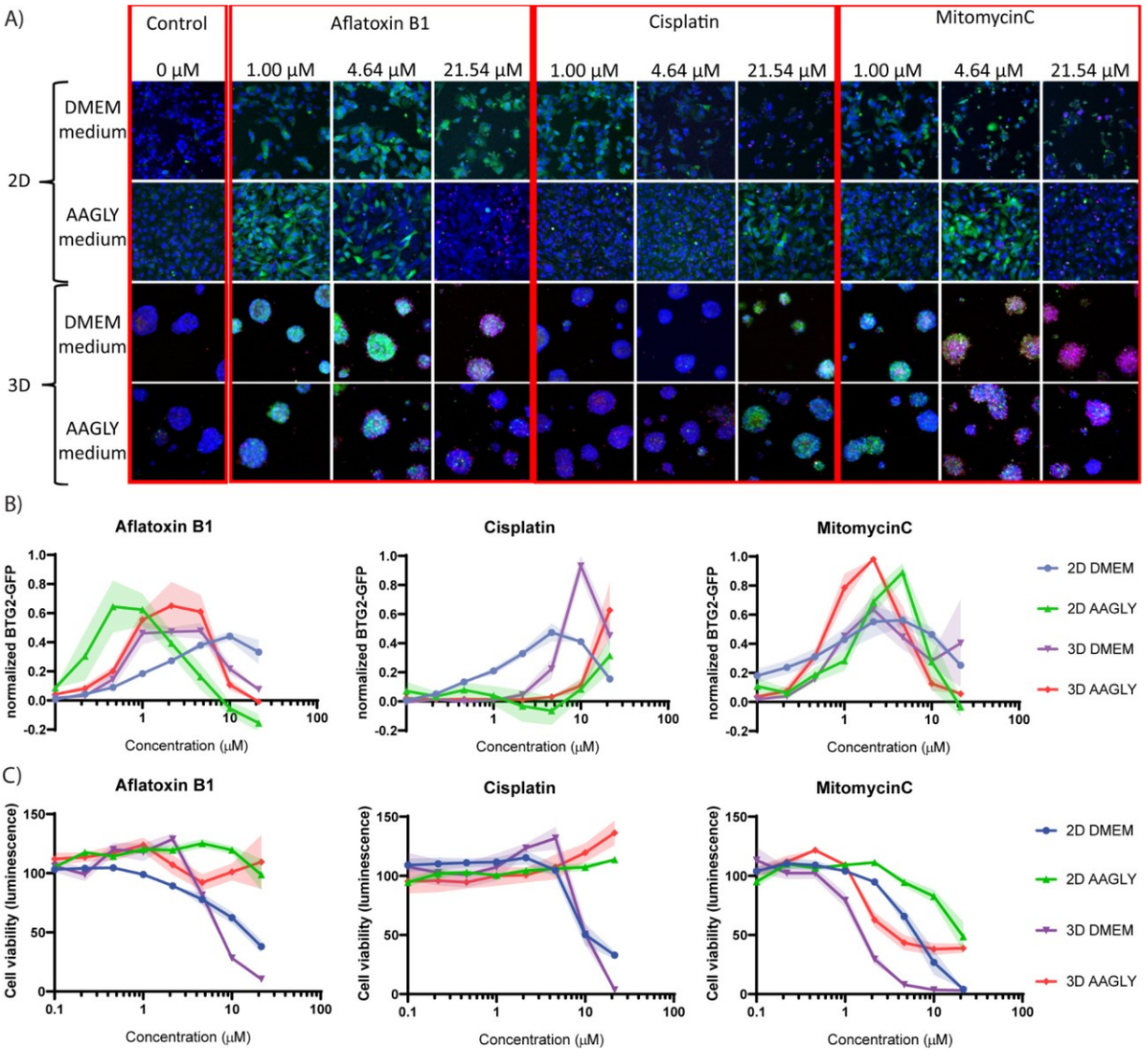

Fig. 3. Example images of fluorophore reporter activation and corresponding concentration response plots. A) Representative examples of confocal images of the BTG2-GFP reporter upon activation by aflatoxin B1, cisplatin or mitomycin C in the 4 different culture conditions. For the 2D, only images are shown of the 72 hr timepoint. The blue pseudo colour represents Hoechst (nuclei) staining, green represents the GFP reporter activation and red shows the PI (cell death) staining. B) Concentration response plots of the min-max normalized BTG2-GFP reporter activation upon treatment with aflatoxin B1, cisplatin or mitomycin C in the four different culture conditions. Fluorophore data is shown as fold changes as compared to basal (solvent) conditions. N=3; the light-coloured shaded area represents error bars (SD). C) Concentration response plots of cell viability (ATP-lite) upon activation by aflatoxin B1, cisplatin or mitomycin C in the four different culture conditions. Fluorophore data is shown as fold changes as compared to basal (solvent) conditions. N=3; the light-coloured shaded area represents error bars (SD).

exposure to DNA damage inducing agents in the different HepG2 culture conditions, cell viability was determined by evaluating the PI-positive fraction and ATP content (Supplementary Figures 3 and 4) followed by hierarchical clustering of all the data (Figure 4). Clustering of both cell death end points showed in general that HepG2 cells exposed for a longer duration (4-day repeated in 3D or 72 h in 2D), clustered together based on the medium type that was used. Most cell death

was seen with mitomycin C exposure, where HepG2 cells grown in 3D with normal DMEM medium were most sensitive with an IC_{50} of 1.58 µM. When cells were grown in 2D with normal DMEM medium, their tolerance of mitomycin C was about 4-fold higher, with an IC_{50} of 6.31 µM. HepG2 cells grown in 2D with AAGLY medium were less sensitive, showing only reduction in ATP content at the highest concentration with 72 h exposure (IC_{50} of 20.43 µM). Cell death was also observed upon cisplatin treatment at concentrations higher than 10 µM, but this was only the case for HepG2 cells grown in normal DMEM medium either in 2D or 3D. No cell death was seen with cisplatin when cells were grown in AAGLY medium. Brequinar only induced cell death at the highest concentration of 100 µM in HepG2 cells grown in 3D in both medium types or in 2D in combination with AAGLY medium. When cells were cultured in 2D using normal DMEM medium, no cell death was seen for brequinar, suggesting that an improved hepatic phenotype is needed to identify brequinar-mediated adversity. Aflatoxin B1 showed highest cell death induction in HepG2 cells grown in 3D with DMEM/F12 medium at concentration levels of 2.15 µM or higher. Cells grown in 2D with normal DMEM medium were less sensitive showing adversity at 10 µM or higher. When AAGLY medium was used no cell death could be observed during aflatoxin B1 exposure, although DDR activation was seen. Gemcitabine did not show cell death induction in all the models.

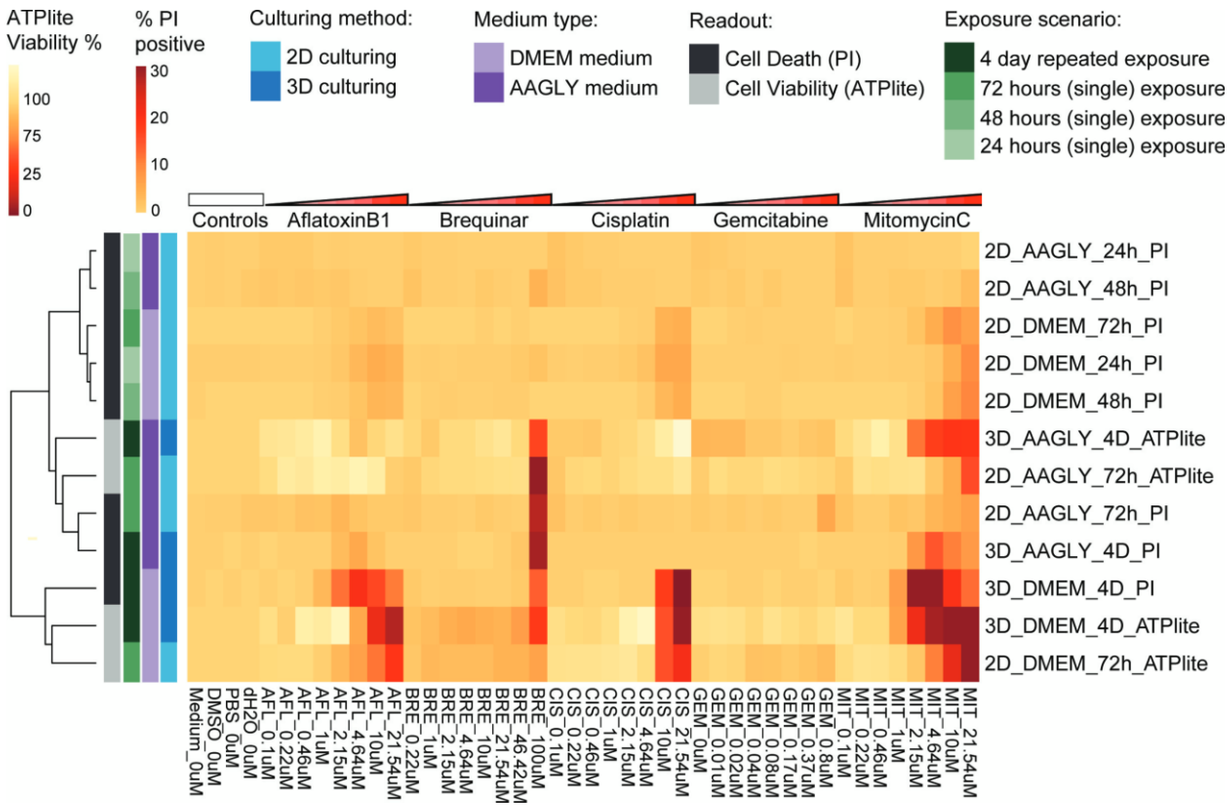

Fig. 4. Hierarchical clustering of cell death data. Hierarchical clustering (Euclidean distance with Ward's distance) of propidium iodide (PI) positive fraction and ATP content (viability) upon exposure to 5 compounds at 8 concentrations in HepG2 cells cultured using 4 different culture conditions. Data is represented as the mean of 3 biological replicates of three reporter models.

Shift in sensitivity for chemical-induced DDR activation

To assess genotoxic mechanisms that may underlie the observed compound-induced cytotoxicity, we systematically compared the difference in DNA damage signalling activation among the HepG2 models upon chemical exposure. We created a hierarchical clustering of the activation of the three DNA damage GFP reporters at all test conditions from which the shifts in sensitivity between the different conditions can be clearly observed (Figure 5). The dendrogram on the left indicated that reporter data of the HepG2 cultured in the normal DMEM medium in 2D separated from the other, more metabolically active, culture conditions. The reporter data of HepG2 cultures in 3D with the two different media types showed the highest resemblance with each other.

When examining individual compounds, aflatoxin B1 induced DNA damage reporters (BTG2, p21 and p53) in all culture conditions. However, the more metabolically active models, e.g. 2D HepG2 cells cultured in AAGLY medium, were more sensitive as the induction was already observed at the lowest concentration of 0.1 µM aflatoxin B1 (Supplementary Figure 2). Interestingly, for the HepG2 reporters cultured in 2D, the reporter induction by aflatoxin B1 was more prominent, up to ~4.5-fold, when measured at later time points (48 and 72 h). In general, the BTG2-GFP and p53-GFP reporters were most sensitive towards aflatoxin B1-induced DNA damage.

Brequinar, an inhibitor of pyrimidine synthesis, only led to mild induction of the DNA damage reporters, of which p53 was most sensitive (Supplementary Figure 2) in particular with the 2D set-up using normal DMEM medium resulting in maximal ~3-fold higher induction compared to other reporters. Interestingly, no DDR was observed at 24 h after brequinar exposure. In the 4-day repeated dosing scenario in 3D in combination with AAGLY medium, brequinar induced a DDR (p21 and p53 activation) at the highest concentration, but this was not seen when using normal DMEM medium.

All DNA damage reporters showed a very clear concentration-dependent activation upon exposure to the direct mutagen cisplatin in 2D with normal DMEM medium at 0.46 µM or higher. However, when AAGLY medium was used or when the cells were cultured in 3D, this effect was much less pronounced (see also Supplementary Figure 2) where clear activation was only seen at 10 µM or higher. It is likely that cell cycle progression is required for cisplatin-induced DNA damage effects. Similar results were obtained for gemcitabine (see also Supplementary Figure 2). Only in proliferative culture conditions (2D with normal DMEM medium), the genotoxic effects of gemcitabine were revealed, which seem to be almost absent in the other culture conditions.

The last compound tested, mitomycin C, had both a direct as well as an indirect DNA-damaging effect. HepG2 3D spheroids in combination with repeated dosing were most sensitive to identify DDRs by mitomycin C showing the highest reporter induction at lower concentrations compared to the other models.

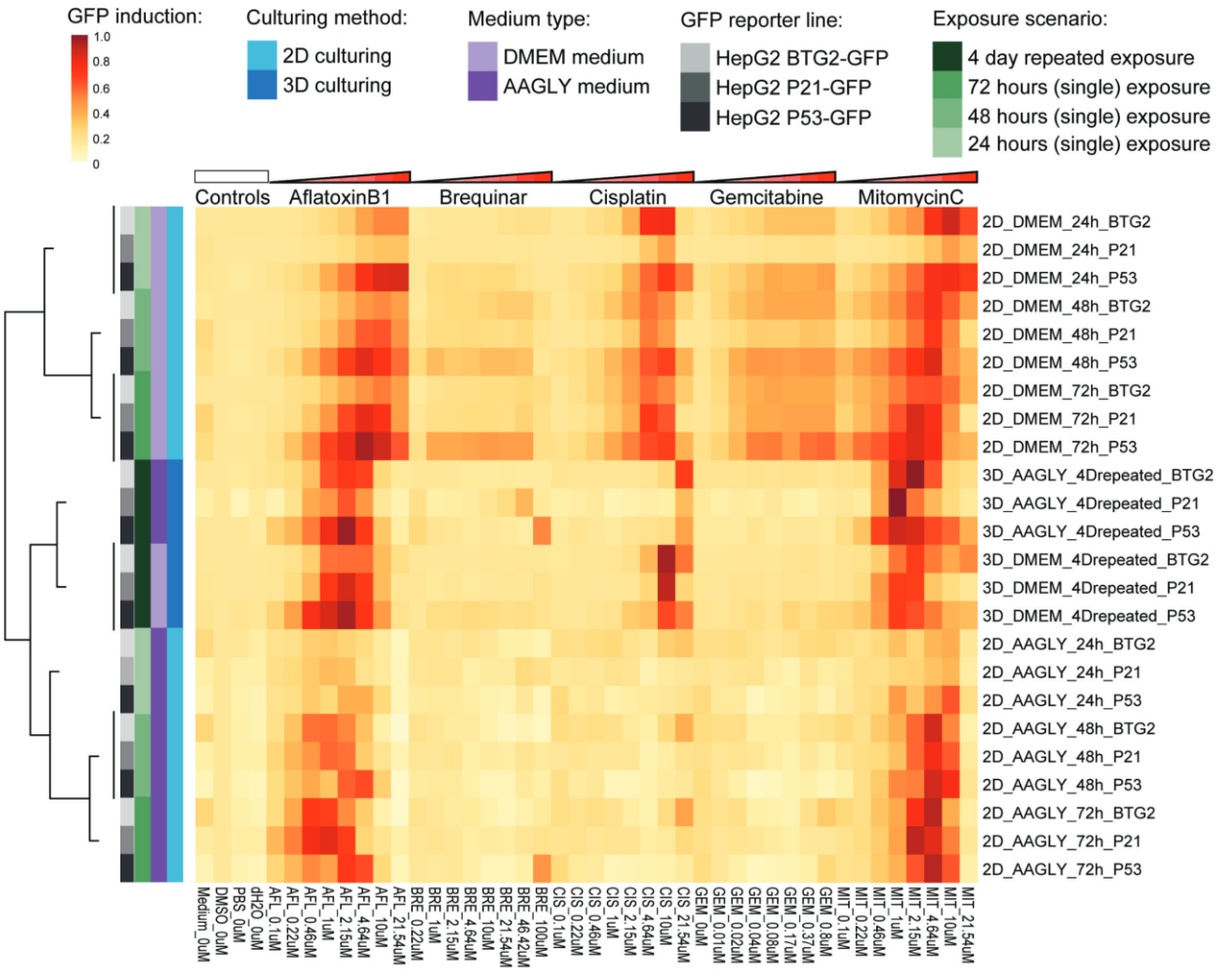

Fig. 5. Hierarchical clustering of the reporter activation. Hierarchical clustering (Euclidean distance with Ward's distance) based on fold change GFP reporter data, including 7 compounds, at 8 concentrations, in 3 different reporter models (P53, P21 and BTG2-GFP) at 4 different culture conditions. N=3.

To get more insight in the sensitivities of our DDR reporters in the different culture conditions, we calculated for each compound and condition the PoD values of reporter activation. PoD values were defined as the lowest compound concentrations resulting in significant induction of reporter activity. Hierarchical clustering of the PoD values for the three DDR stress pathway reporters (p21-, p53- or BTG2-GFP) confirmed their similarities in response, and showed that drug sensitivity was largely dependent on culture conditions (Figure 6). By culturing the HepG2 cells in 2D with normal DMEM medium, PoDs could be determined for all compounds. This model seemed to be especially sensitive for gemcitabine, for which very low PoD values were calculated of 0.028 µM or lower. This compound did not induce a quantifiable genotoxic effect in the other models. 3D culturing conditions with repeated dosing increased the sensitivity of the reporters for the genotoxic effects of mitomycin C, as in these conditions the lowest PoD was 0.32 µM mitomycin C while for 2D conditions the lowest defined PoD was 0.74 µM. Genotoxic effects of aflatoxin B1, a compound that required bioconversion to a genotoxic metabolite, could be best picked up using the 3D culturing or by using AAGLY medium. The delayed DDR after brequinar

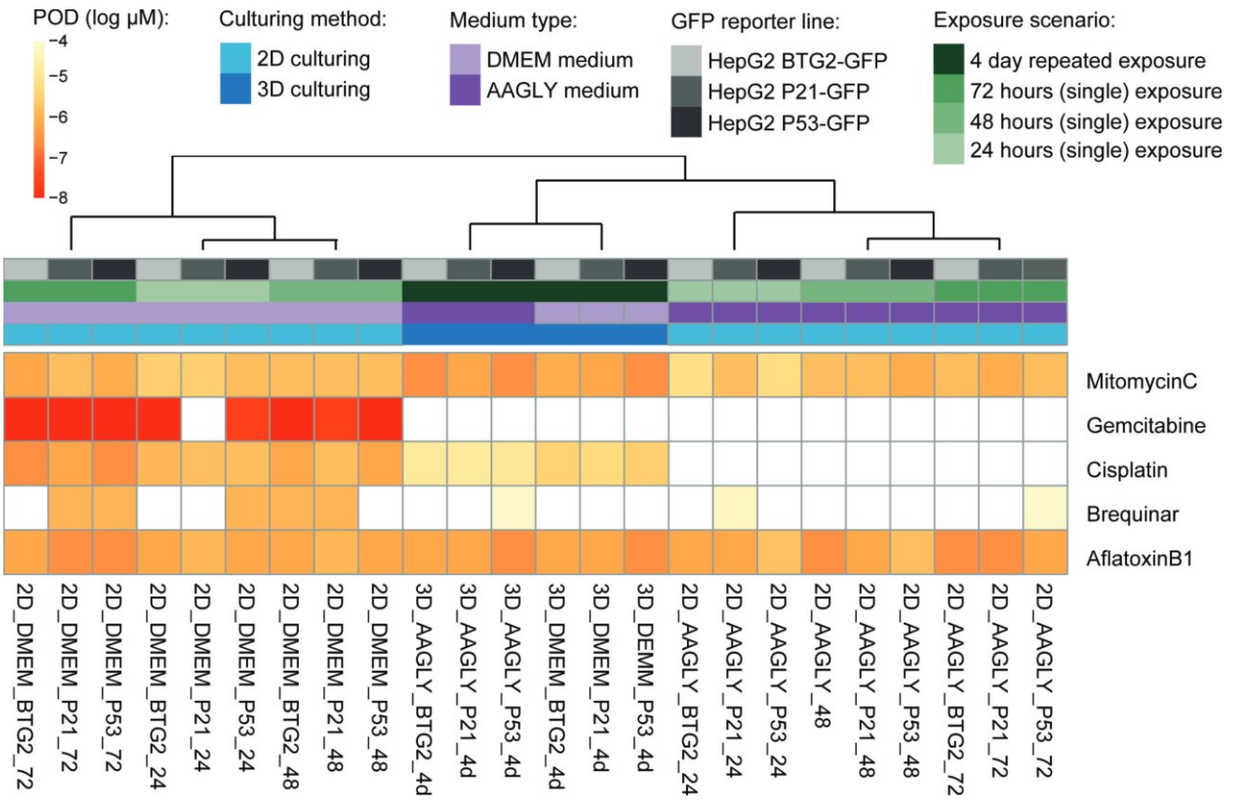

Fig. 6. Hierarchical clustering of the reporter activation point of departures (PoDs). Hierarchical clustering (Euclidean distance with Ward's distance) based on the PODs of GFP reporter intensity concentration response curves.

treatment was best measured at the later time points in the 2D cultures, which could not be picked up with the 4-day repeated dosing scenario in the 3D set-up. DNA-damaging effects at low concentrations of cisplatin were detected in the 2D culture with normal DMEM medium giving PoDs of 0.32–1.83 µM. In 3D, this effect was also observed but at higher concentrations ranging from 3.35 to 17.2 µM, especially in combination with AAGLY medium. By using the combination of 2D culturing and AAGLY medium, cisplatin-induced DDR could not be detected.

When comparing PoDs of the DNA damage reporter activation (Figure 6; Supplementary Figure 2) with the compound concentrations at which the cell viability was affected (Figure 4; Supplementary Figures 3 and 4), we found that the readout for DDR reporters is much more sensitive. Typically, the DNA damage BAC-GFP reporter cell lines were activated at 10–50 times lower concentrations as compared to the concentrations at which cell death (PI) and cell viability (ATP-lite) were observed.

Discussion

In this study, we systematically compared the impact of differentiation-inducing 3D culturing and AAGLY medium on the detection of (in)direct genotoxicity in HepG2 liver cancer cells. For this purpose we used three fluorescent HepG2 reporters for p53 pathway activation in the DDR: p53-GFP, BTG2-GFP and p21-GFP. The key findings of our study are: (i) HepG2 DDR reporters are more sensitive to DNA-damaging agents than HepG2 cell death or viability assay; (ii) proliferating

HepG2 DDR reporters cultured under standard 2D conditions are generally sensitive to diverse DNA-damaging agents with diverse modes of action; (iii) differentiated HepG2 DDR reporters cultured in 3D or AAGLY medium are not sensitive to the genotoxic drugs cisplatin, brequinar and gemcitabine; (iv) 2D and 3D HepG2 DDR reporters with non-proliferative differentiated phenotypes are more sensitive towards genotoxicants that require bioactivation by P450 enzyme systems. These findings suggest that a genotoxicity testing strategy with our panel of HepG2 DDR reporters should consist of (i) proliferating HepG2 DDR reporters in normal culture medium followed by (ii) differentiated HepG2 DDR reporters using AAGLY medium with enhanced expression of P450 mimicking primary hepatocyte levels.

The DDR reporter activities induced by cisplatin, gemcitabine and brequinar were mainly observed in normal proliferating 2D cells. Since the genotoxic effects of these drugs depend on replication, this is likely explained by the fact that HepG2 cells cease to proliferate in 3D or AAGLY medium[29,101]. Many other known genotoxic compounds have similar replication-dependent modes of action, which advocates for the use of 2D HepG2 reporter systems in the early phase of genotoxic hazard characterisation.

HepG2 DDR reporters cultured under conditions with enhanced differentiation characteristic were most sensitive towards aflatoxin B1. This suggests that differentiation of HepG2 DDR reporters would in general increase the sensitivity to compounds that require metabolism to become genotoxic. The genotoxic effect of aflatoxin B1 depends completely on liver-specific metabolisation to its reactive forms aflatoxin B1-8,9-exo-epoxide, 8,9-dihydroxy-8-(N7) guanyl-9-hydroxy aflatoxin B1 and aflatoxin B1 formaminopyrimidine (38). Interestingly, for the HepG2 lines cultured in 2D the reporter induction by aflatoxin B1 was more prominent when measured at later time points (48 and 72 h), which might suggest that the reactive metabolite of aflatoxin B1 (AFB1-8,9-epoxide) is accumulating over time. *CYP3A4* and *CYP3A7* were highly expressed in differentiated HepG2 cell culture conditions in the presence of AAGLY medium. Indeed, our p53 pathway reporters were most sensitive to aflatoxin B1 in AAGLY medium. The advantage of these differentiated HepG2 test systems is that it allows repeated dosing regimens mimicking better real-life exposures. This is generally hampered in proliferating 2D-cultured HepG2 cells. Besides aflatoxin B1, also mitomycin C was able to induce strong DDR reporter activity in differentiated HepG2 test systems. Which makes sense as mitomycin C can directly damage DNA through DNA cross-linking and inhibit both DNA replication as well as transcription. It can also indirectly induce DNA damage via cytochrome P450-mediated redox cycling and reactive oxygen species (ROS) formation[160]. What is the overall added value of physiologically more relevant liver model systems for the assessment of genotoxicity? To answer this question, there are a couple issues to consider. To begin with, our p53 pathway reporters do not directly measure DNA damage itself, but rather the cellular response to it. This allows sensitive and early detection of low levels of DNA damage, which justifies benchmarking this reporter system against other genotoxicity

test systems using PoD analyses. A recent evaluation of cisplatin genotoxicity using the high-throughput CometChip assay shows a PoD of 6.3 µM in PHH[166], which is considerably higher than the PoD values of 0.32–1.83 µM obtained with our DDR reporters. Thus, HepG2 BAC-GFP DDR reporter cell lines may be more sensitive than established genotoxicity assays, which should be further evaluated using a broader spectrum of genotoxicants. Moreover, the GFP-protein fusions also make it possible to follow dynamics of p53 pathway activation, which is an important determinant of cell fate[24]. For the HepG2 DDR reporters grown in 2D we have evaluated reporter activation at three time points, within a 3-day period, but could be extended using increased time resolution to more accurately map the DDR activation dynamics upon exposure. Together, our reporters give a robust representation of p53 pathway activation, because protein expression levels of p53 and its target genes BTG2 and CDKN1A are similarly induced by DNA damage and highly co-regulated[23]. However, the p53 pathway may also be upregulated by non-genotoxic compounds[167]. Dihydroorotate dehydrogenase inhibitors such as brequinar, for which we only detected reporter activity in standard 2D culture, have recently been shown to increase p53 protein expression without preceding or concomitant induction of more direct markers of DNA damage such as ataxia-telangiectasia mutated (ATM) or ATM and Rad3-related (ATR) phosphorylation[168]. Mechanistically, the increased p53 protein expression was suggested to be a consequence of accumulation of cancer cells in S-phase. Thus, it is possible that some of the activity of the standard-2D culture does not reflect actual DNA damage. Since HepG2 reporter lines cultured in a more differentiated state will undergo G0/G1 arrest, short-term effects on their cell cycle distribution seem less likely. Whether there may be other non-genotoxic triggers for p53 reporter activity in differentiated HepG2 cells remains to be determined.

Some compounds cause the cellular formation of ROS, which can have an effect on the stability of the DNA and therefore have a delayed genotoxic effect[169]. Furthermore, there seems to be cross talk from the inflammation to the DNA damage pathway and vice versa[170]. By extending the reporter panel with the previously generated Nrf2 (oxidative stress) and NF-κB (inflammation) pathway reporter cell lines[79] it may be possible to discriminate between direct and indirect genotoxic modes of action[153].

In addition, we tested only a few compounds, and we do anticipate that various compounds at risk for genotoxicity may require bioactivation through cytochrome P450 enzyme system, which are insufficiently expressed in HepG2 cells in standard 2D culture. For an accurate estimation of the performance (sensitivity, predictivity and accuracy scoring) of the 2D and 3D systems a larger screen, including different classes of genotoxic and non-genotoxic compounds should be performed[171]. More importantly, the added value of cell culture-based assays for genotoxicity over classical assays such as the Ames test in bacteria lies not only in the detection of indirect genotoxicity alone. The ultimate goal is to use cell culture-based toxicity assays as quantitative,

predictive tools for adverse outcome[22]. For that purpose, it is essential to use model systems that accurately reflect the human bioactivation in vivo response to toxic chemicals.

Taken together, our data indicate that standard 2D HepG2 models are capable of identifying diverse mechanisms of DNA responses but are not optimally equipped to effectively detect indirect genotoxicants that require bioactivation through drug-metabolising enzymes. The reverse is the case for differentiated HepG2 cell culture systems that are highly insensitive for genotoxicants that impact on DNA replication, but seem particularly more sensitive for genotoxicants that require bioactivation. Therefore, we propose a tiered testing strategy with the combination of both standard 2D HepG2 cells and differentiated HepG2 cells cultured in 2D or 3D in AAGLY medium. A broader follow-up screen based on a larger and unbiased set of compounds is necessary to assess the true potential of such a combined screening strategy.

Acknowledgements

This work was supported by the EU-ToxRisk project funded by the European Commission under the Horizon 2020 program (grant agreement number 681002). The authors gratefully acknowledge the Leiden University Cell Observatory, the imaging core facility, for their support and assistance in this work.

Conflict of interest

The used HepG2 BAC GFP reporters are now licensed to Toxys. BtB and LW are currently employed at this company.

Supplemental figures

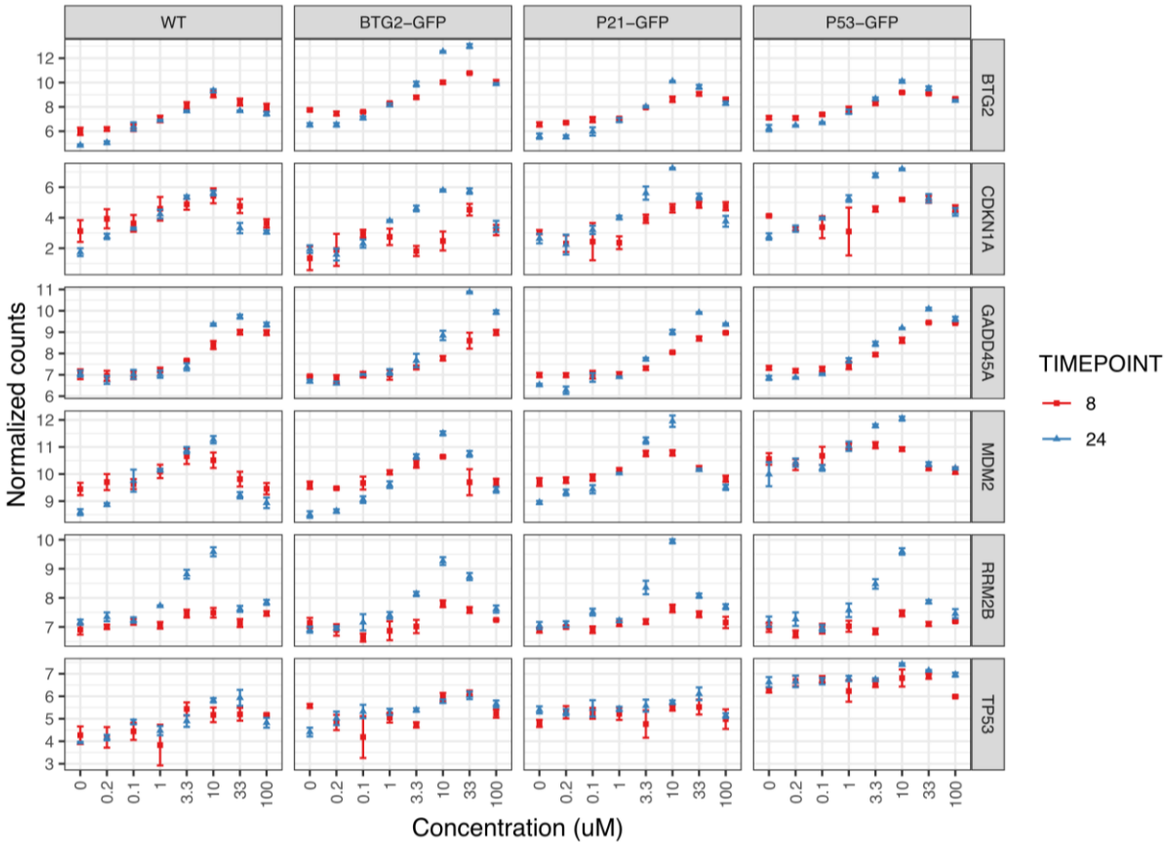

Fig. S1. Upregulation of mRNA expression of DNA damage response genes in HepG2 wild-type or reporter cells upon cisplatin treatment for 8 or 24 h.

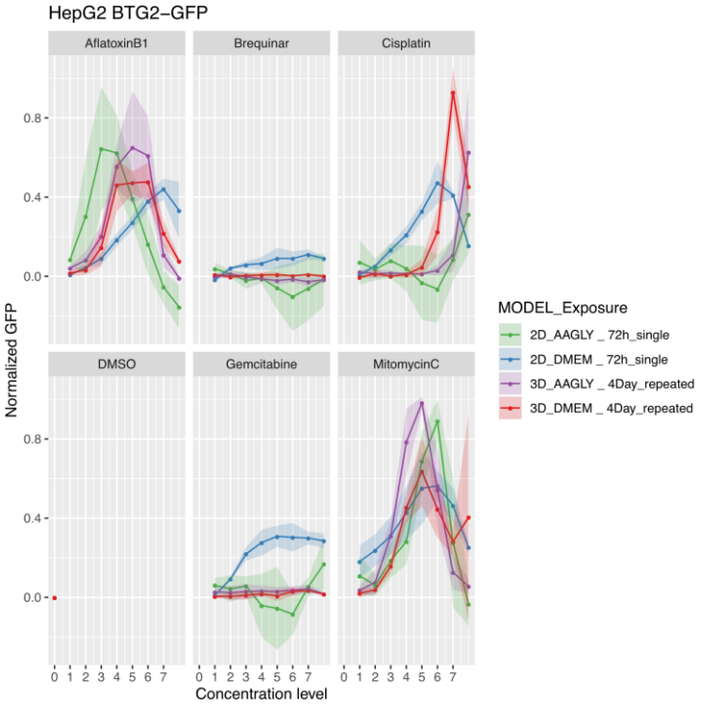

Fig. S2. Concentration-dependent induction of BTG2-GFP upon chemical exposure in various HepG2 culture models.

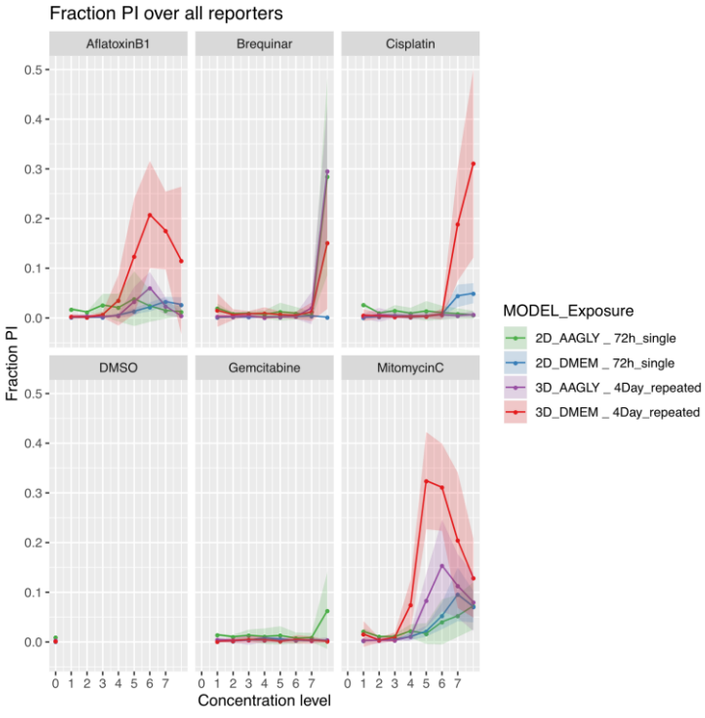

Fig. S3. Cell death induction upon chemical exposure in various HepG2 culture models measured by fraction propidium iodide (PI) positive cells.

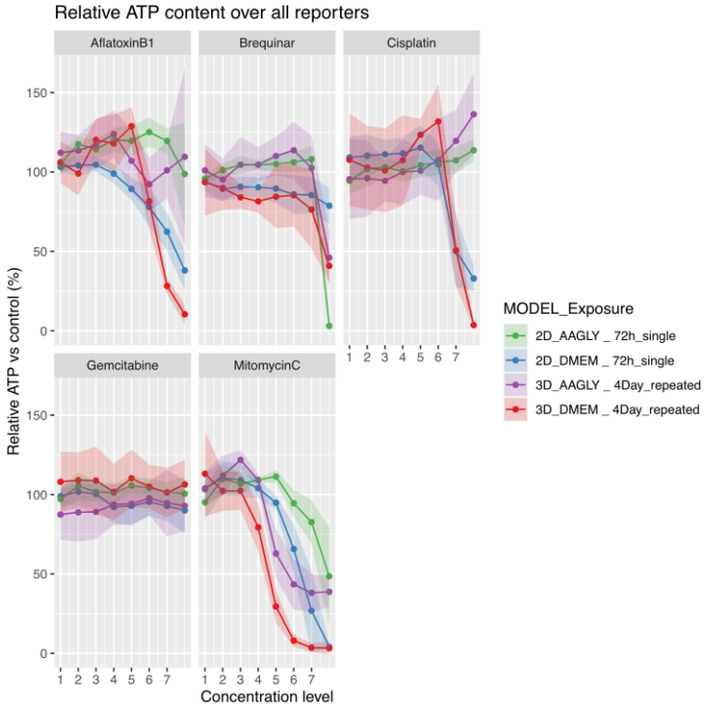

Fig. S4. Cell death induction upon chemical exposure in various HepG2 culture models based on ATP content.

Table S1.

#	Oligo Name	Gene	Marker	Sequence 5' to 3' (include modification codes if applicable)
1	H_AAT1_fw	AAT1	Hepatocytes	ACTGGGGTGACCTTGGTTAAT
2	H_AAT1_rv			GACGGCATTGTCGATTCACTG
3	H_AFP_fw	AFP	Fetal hepatocytes	TGAGCACTGTTGCAGAGGAG
4	H_AFP_rv			GTGGTCAGTTTGCAGCATTC
5	H_ALB_fw	Albumin	Hepatocytes	ATGCTGAGGCAAAGGATGTC
6	H_ALB_rv			AGCAGCAGCACGACAGAGTA
11	H_CYP1A2_fw	CYP1A2	Hepatocytes	CTTTGACAAGAACAGTGTCCG
12	H_CYP1A2_rv			AGTGTCCAGCTCCTTCTGGAT
13	H_CYP1B1_fw	CYP1B1	Hepatocytes	ACCAGGTATCCTGATGTGCAGAC
14	H_CYP1B1_rv			AGGTGTTGGCAGTGGTGGCATGAG
17	H_CYP3A4_fw	CYP3A4	Hepatocytes	tTCCTCCCTGAAAGATTCAGC
18	H_CYP3A4_rv			GTTGAAGAAGTCCTCCTAAGCT
21	H_CYP3A7_fw	CYP3A7	Hepatocytes	AGATTTAATCCATTAGATCCATTCG
22	H_CYP3A7_rv			AGGCGACCTTCTTTTATCTG
27	H_GAPDH_fw	GAPDH	Housekeeping	TCAAGAAGGTGGTGAAGCAGG
28	H_GAPDH_rv			ACCAGGAAATGAGCTTGACAAA
31	H_HNF4a_fw	HNF4α	Hepatocytes	ACTACGGTGCCTCGAGCTGT
32	H_HNF4a_rv			GGCACTGGTTCCTCTTGTCT
35	H_NTCP_fw	NTCP	Hepatocytes	ATCGTCCTCAAATCCAAACG
36	H_NTCP_rv			CCACATTGATGGCAGAGAGA
41	H_RLP19_fw	RLP19	Housekeeping	ATTGGTCTCATTGGGGTCTAAC
42	H_RLP19_rv			AGTATGCTCAGGCTTCAGAAGA
49	H_CYP2A6_Fw	CYP2A6	Hepatocytes	TTTTGGTGGCCTTGCTGGT
50	H_CYP2A6_Rv			GGAGTTGTACATCTGCTCTGTGTTCA
51	H_CYP2D6_Fw	CYP2D6	Hepatocytes	CCTACGCTTCCAAAAGGCTTT
52	H_CYP2D6_Rv			AGAGAACAGGTCAGCCACCACT
55	H_CYP2E1_Fw	CYP2E1	Hepatocytes	AATGGACCTACCTGGAAGGAC
56	H_CYP2E1_Rv			CCTCTGGATCCGGCTCTCATT
47	H_UGT1A1_fw	UGT1A1	Hepatocytes	CAGCAGAGGGGACATGAAAT
48	H_UGT1A1_rv			ACGCTGCAGGAAAGAATCAT
59	H_CYP2C19_Fw	CYP2C19	Hepatocytes	CAACAACCCTCGGGACTTTA
60	H_CYP2C19_Rv			GTCTCTGTCCCAGCTCCAAG

Chapter 5

ATF6 is a critical determinant of CHOP dynamics during the unfolded protein response

This chapter has been published as:

H. Yang*, M. Niemeijer*, B. van de Water, J.B. Beltman

*Both authors contributed equally

ATF6 Is a Critical Determinant of CHOP Dynamics during the Unfolded Protein Response

iScience. 2020 Feb 21;23(2):100860. doi: 10.1016/j.isci.2020.100860.

Abstract

The unfolded protein response (UPR) pathway senses unfolded proteins and regulates proteostasis and cell fate through activity of the transcription factors ATF4, ATF6 and XBP1 within a complex network of three main branches. Here, we investigated contributions of the three branches to UPR activity in single cells using microscopy-based quantification and dynamic modelling. BAC-GFP HepG2 reporter cell lines were exposed to tunicamycin and activation of various UPR components was monitored for 24 hours. We constructed a dynamic model to describe the adaptive UPR signalling network, for which incorporation of all three branches was required to match the data. Our calibrated model suggested that ATF6 shapes the early dynamics of pro-apoptotic CHOP. We confirmed this hypothesis by measurements beyond 24 hours, by perturbing single siRNA knockdowns and by ATF6 measurements. Overall, our work indicates that ATF6 is an important regulator of CHOP, which in turn regulates cell fate decisions.

Keywords: Biocomputational Method; Bioinformatics; Optical Imaging; Systems Biology.

Introduction

Cells activate adaptive stress responses to be able to cope with different types of stress. For instance, various chemicals cause the accumulation of unfolded proteins within the endoplasmic reticulum (ER). Drugs, such as nefazodone and diclofenac, lead to such ER stress and as a consequence ER stress-related genes are upregulated, giving rise to the unfolded protein response (UPR) which counters chemical-induced protein stress[97,172]. Besides chemicals, also modifications in the rate of protein synthesis or in the cellular environment, such as nutrient level fluctuations or inflammation can trigger the UPR[173]. Moreover, the UPR can be exploited by malignant cells, assisting their development of drug resistance[174].

Under homeostatic conditions, the ER is responsible for protein synthesis and tightly controls the correct folding and maturation of proteins by various chaperones (such as heat shock protein (Hsp) 70 and 90 family members, ER-localized DnaJ like proteins and calnexin) and foldases (such as protein disulfide isomerases (PDIs) and prolyl peptidylcis–transisomerases (PPIases)). Afterwards, proteins are transported to the Golgi through a secretory pathway[175]. Upon disruption of ER homeostasis, cells react by activating the adaptive UPR. This will lead to an increase of the ER folding capacity, to temporary interruption of the translational machinery, and to degradation of unfolded proteins, altogether with the aim to recover from ER stress[173,176].

The UPR is under control of three sensors, each activating distinct signalling cascades and transcription factors (TFs), namely PKR-like ER kinase (PERK), inositol requiring 1α (IRE1α) and activating transcription factor 6 (ATF6) (Fig. 1). These sensors are bound to the chaperone binding immunoglobulin protein (BiP/*HSPA5*) and are kept in an inactive state in unstressed conditions[177,178]. Upon ER stress, the sensors are released by BiP[179] or bound by misfolded

protei[180] enabling their activation. After activation of IRE1α in the first UPR branch, its endoribonuclease domain splices the b-ZIP TF XBP1 mRNA resulting in the transcriptionally active protein pXBP1(S)[181] which induces the expression of ER stress related genes involved in protein folding[182], ER-associated degradation (ERAD)[183,184] and ER expansion[185]. In the second branch, active PERK phosphorylates eukaryotic translation-initiation factor 2 (eIF2α) leading to attenuation of the translation of mRNAs which reduces the protein load in the ER[186]. Moreover, the expression of some genes, such as a b-ZIP TF ATF4, depends on the phosphorylation status of eIF2α[187]. ATF4 induces the expression of ER stress related genes to restore homeostasis[188,189], but also induces the b-ZIP TF C/EBP homologous protein (CHOP) which promotes cell death[190–192]. In the third branch, ATF6 translocates to the Golgi where it is cleaved[193,194]. The ensuing ATF6 fragment (pATF6(N)) translocates to the nucleus and initiates the expression of its target genes such as chaperones, genes involved in ERAD, pXBP1(S), but also of the pro-apoptotic gene CHOP[195–197].

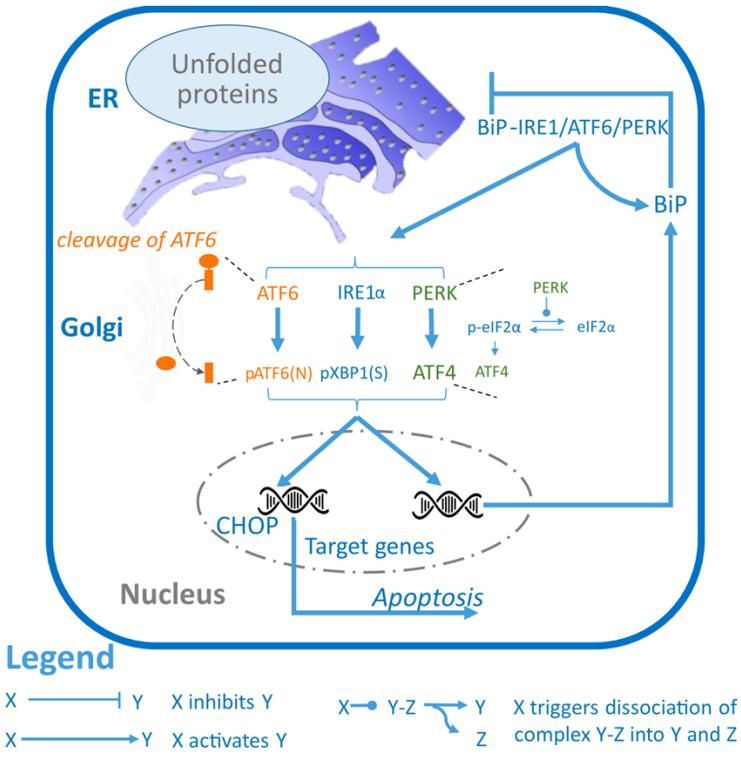

Fig. 1. Cartoon illustrating the UPR pathway involving multiple organelles and three branches, several TFs and downstream molecules involved in feedback loops.

As many molecules have some role in the UPR network and ample feedbacks have been identified, these interactions are expected to lead to complex dynamics. In order to mechanistically understand these dynamics and its role in cellular adversity, mathematical modelling is an indispensable tool to quantitatively understand this complexity[198,199]. Ordinary differential equation (ODE) models are well fit for this purpose because they take into account laws of biochemical reactions. Several dynamical models of the UPR have already been built by various groups. Cho et al. utilized discrete dynamical modelling to study a complex UPR network model, considering different biological processes to occur at similar time scales[200]. With respect to ODE models applied to the UPR, several studies focused on details of UPR sub-modules, e.g. on the IRE1α branch[201]. Taking into account all three branches, Erguler et al. (2013) proposed a comprehensive UPR model and highlighted potential emerging dynamics due to feedback loops[202]. A simpler three-branch model was derived using steady-state assumptions by Trusina et al.[203], which was subsequently used to study repeated

exposure and the effect of different types of stress during in silico simulations[204]. Interestingly, this work emphasized the potential importance of BiP accumulation during primary exposure leading to protection against renewed ER stress. Recently, Diedrichs et al. integrated gene expression data from mouse embryonic fibroblasts into a UPR model and validated their model predictions with knockout experiments, which focused on the feedback loop via CHOP-induced DNA damage-inducible protein 34 (GADD34) that leads to dephosphorylation of eIF2α and a consequent increase in protein load[205].

To further increase our mechanistic understanding of regulation of UPR TF activity during adaptation, we here present a new ODE model that we calibrate with a rich set of dynamic high-content imaging data. These data are generated utilizing our established liver carcinoma HepG2 BAC-GFP reporter platform[27,28,91]. The usefulness of combining high-content imaging of HepG2 reporter cell lines with mathematical modelling has recently been demonstrated for the NFκB-mediated inflammatory stress pathway[206]. Here, by applying high-content confocal imaging to HepG2 BAC-GFP UPR reporters for CHOP, ATF4, pXBP1(S) and BiP, we were able to precisely follow the activation dynamics of these UPR genes in response to a broad concentration range of tunicamycin, a highly specific ER stress inducer. By fitting our dynamic model to the data we dissected the contribution from single branches to UPR regulation. Furthermore, model selection suggested that ATF6 has an important role in shaping the CHOP dynamics during ER stress. Consistent with this, siRNA-mediated silencing of ATF6 led to diminished CHOP induction during the acute phase, yet still resulted in a prolonged induction of CHOP. This suggests that ATF6 is an important regulator for cell fate decisions under chronic ER stress.

Materials and Methods

Cell culture

HepG2 human hepatocellular carcinoma cells were purchased at American Type Culture Collection (ATCC, Wesel, Germany). To capture the induction of key proteins of the UPR, CHOP, ATF4, BiP and pXBP1(S) were GFP-tagged using a bacterial artificial chromosome (BAC) recombineering approach[27,79,91,128,207]. Hereby, stable HepG2 GFP-BAC reporter cell lines were established expressing protein-GFP fusions under control of the endogenous promoter for each gene. HepG2 cells were cultured in Dulbecco's Modified Eagle Medium (DMEM) containing 10% (v/v) fetal bovine serum (FBS), 25 U/mL penicillin and 25 µg/mL streptomycin at 37°C and 5% CO_2, and were used until passage 20. Cells were plated using a density of 70.000 to 140.000 cells/cm^2 when grown for 3 to 5 days.

Chemicals and antibodies

Tunicamycin was purchased at Sigma (Zwijndrecht, The Netherlands) which was dissolved in dimethylsulfoxide (DMSO) from BioSolve (Valkenswaard, The Netherlands) and stored at -20°C until usage. The maximum solvent end concentration of DMSO was at most 0.2% (v/v) to minimize the effect of the solvent itself. For western blotting, antibodies were used against

CHOP, ATF4, pXBP1(S) and ATF6 from Cell Signaling (Bioké, Leiden, The Netherlands), BiP from BD Biosciences (Vianen, The Netherlands) at a dilution of 1:1000, and Tubulin from Sigma (Zwijndrecht, The Netherlands) at a dilution of 1:5000.

RNA interference

siRNA-mediated transient silencing of genes of interest in HepG2 cells was done using a reverse transfection approach. Prior to transfection, siGENOME SMARTpool siRNAs from Dharmacon (Eindhoven, the Netherlands) were mixed with INTERFERin from PolyPlus (Leusden, the Netherlands) for 10 minutes to allow for complex formation. Hereafter, siRNA mix, resulting in a 50 nM siRNA and 0.3% INTERFERin end concentration, together with cells at a density of 78.000 cells/cm^2 were added to each well. As control, mock (only INTERFERin) and siRNA scrambled non-targeting control was employed. At 24 hours post-transfection, medium was refreshed. siRNA-silenced cells were evaluated at 72 hours post transfection or exposed to compounds to assess the effect of the knockdown on drug-induced ER stress response activation.

Confocal Microscopy

Cells were plated in SCREENSTAR 96 wells or µClear 384 wells plates from Greiner Bio-One (Alphen aan den Rijn, The Netherlands) at the earlier mentioned cell densities. Prior to confocal microscopy imaging, cells were stained with 100 ng/mL Hoechst33342 for a minimum of 30 minutes to allow for nuclei visualization and cell tracking. To measure the induction of BAC-GFP intensity, cells were imaged live using an automated Nikon TiE2000 confocal microscope (Nikon, Amsterdam, The Netherlands) including an automated xy-stage, Perfect Focus System and lasers at wavelength 408, 488, 561 and 647nm. Cells were kept at 37°C and 5% CO2 humidified atmosphere during imaging.

Image Analysis

Segmentation and quantification of the GFP intensity was done using CellProfiler version 2.1.1 (Broad Institute Cambridge, USA) using analysis modules described previously[79,208]. In brief, nuclear segmentation based on Hoechst signal was done using an in-house constructed watershed masking algorithm[129]. The propagation segmentation method based on GFP signal was used for cytoplasm segmentation. GFP intensity was measured in the nucleus as well as in the cytoplasm. For subsequent analysis, Rstudio version 1.0.153 (Boston, USA) was used. For alignment of the data acquired around discrete time points (1,2,..., 24 hours), we employed cubic interpolation of the GFP intensity such that standard deviations can be estimated from the individual replicates, which are integrated into the cost function for parameter estimation (see Supplementary text about single-cell data analysis for details).

TempO-seq transcriptomics

To assess mRNA levels, cells were seeded in 96 wells plates from Corning (Amsterdam, The Netherlands) using a density of 156.000 cells/cm^2. After compound exposure the following day, cells were washed with 1x PBS and lysed using 50 µL per well in 1x BNN lysis buffer from

BioSpyder (Carlsbad, USA). After a 15 minute incubation period at room temperature, lysates were frozen at -80°C. As internal control, 0.05 µg/µL Universal Human RNA Reference (MAQC) in 1x BNN lysis buffer was used. Lysates were sent to and analyzed by BioSpyder Technologies Inc. (Carlsbad, USA) using the TempO-seq technology[30]. In brief, a pair of detector oligos hybridized to its specific target mRNA leading to oligo pair ligation. This was followed by PCR amplification of ligated pairs of oligos incorporating also a sample-barcode and adaptors, which was subsequently sequenced. Alignment of raw reads was done using the TempO-seqR package (BioSpyder Technologies Inc., Carlsbad, USA). Read counts were normalized using the DESeq2 R package[165] and log2 transformed. UPR-related genes were defined by selecting target genes of transcription factors ATF4, ATF6, pXBP1(S) and DDIT3 that were based on DoRothEA (Discriminant Regulon Expression Analysis) v2[209] using confidence level A to D and that were present in the S1500+ geneset[164].

Western blot analysis

For western blot analysis, samples were collected after two wash steps with ice-cold 1x PBS by adding 1x sample buffer supplemented with 10% v/v β-mercaptoethanol and stored at -20°C. Prior to loading, samples were heat-denatured at 95°C for 10 minutes. Proteins were separated on SDS-page gels using 120 volt and transferred to polyvinylidene difluoride (PVDF) membranes at 100 volt for 2 hours. After blocking using 5% ELK, membranes were stained with primary and secondary HRP- or Cy5-conjugated antibodies diluted in 1% bovine serum albumin (BSA) in tris-buffered saline (TBS)-0.05%Tween20. Thereafter, Enhanced Chemiluminescent (ECL) western blotting substrate from Thermo Scientific (Bleiswijk, The Netherlands) enabled to visualize the HRP-conjugated antibody staining using the Amersham Imager 600 from GE Healthcare (Eindhoven, The Netherlands). Protein expression was quantified using ImageJ version 1.51h (National Institutes of Health, USA) and normalized to tubulin protein expression.

Statistics

Confocal microscopy data from three biological replicates is represented as the mean SE. TempO-seq gene expression data was represented either as log2 normalized counts SE or as log2 fold changes with standard error calculated using the DESeq2 R package[165]. Significance was determined with the Wald test and Benjamini Hochberg correction using the DESeq2 R package. Significance for TempO-seq gene expression data was determined at three threshold levels (*p_{adj} < 0.05, **p_{adj} < 0.01, ***p_{adj} < 0.001). Western blot data for ATF6 quantification originated from three biological replicates and were represented as the mean ± SE. Here, significance levels were calculated using unpaired Student's t test with Benjamini Hochberg multiple testing correction, represented as *p_{adj} < 0.1, **p_{adj} < 0.05, ***p_{adj} < 0.01. Processing and visualization of all data was done using Rstudio version 1.0.153 (Boston, USA) in combination with R 3.4.1 and the following R packages: ggplot2, RColorBrewer, data.table, dplyr, tidyr, reshape2, scales, stats and splines[131,135,137,210–212].

UPR model construction and simulation

We built a dynamic model of the UPR signalling network with six state variables: unfolded protein (U), pXBP1(S) (X), ATF4 (A4), ATF6 fragment(A6), BiP (B), and CHOP (C). These states represent concentrations of molecules per cell and their dynamics are mathematically described by a set of ordinary differential equations. The equations obey kinetics of biochemical reactions including mass-action, Michaelis-Menten or Hill kinetics. We simplified the model in a similar way as[203,205] with quasi-steady state assumptions for association or dissociation of complexes and modulation effects. Furthermore, we took multiple conservation terms into account in order to reduce the number of state variables. We extended the available model of[203] by incorporating ATF4 and CHOP. Furthermore, because ATF6 is proteolytically processed but this is not the case in the XBP1 branch[194], we considered the possibility that ATF6 and XBP1 need to be assigned different parameters (e.g., their degradation rates) to allow these branches to respond differently. To take the pharmacokinetics of the exposure into account, we modelled the intra-cellular concentration of tunicamycin as a function with two exponents, which represents the analytical solution to a linear system for two compartments (i.e., the medium in which cells reside and intra-cellular spaces).

The set of ODEs is mathematically represented as:

$$\dot{\mathbf{x}}(t) \;=\; \mathbf{f}(\mathbf{x}(\mathbf{t}), \mathbf{u}(\mathbf{t}), \theta), \qquad (1)$$

where $x(t)$ stands for the six state variables of the dynamic system, $u(t)$ is the input function, and θ contains the system parameters. The dynamics of the UPR state variables are described by:

$$\begin{cases} \dot{U} = f_1(x), \\ \dot{X} = f_2(x), \\ \dot{A}_4 = f_3(x), \\ \dot{A}_6 = f_4(x), \\ \dot{B} = f_5(x), \\ \dot{C} = f_6(x), \end{cases} \qquad (2)$$

with initial condition

$$\mathrm{x}_0 \;=\; (U_0, X_0, A_{4,0}, A_{6,0}, B_0, C_0) \qquad (3)$$

In the following the right hand sides of equations (2) are provided for each state. Our modeling work follows[203] assuming a quasi steady-state for sensors which can bind to BiP or to unfolded proteins. In addition, we incorporated the ATF6 branch and the downstream molecules ATF4 and CHOP[203]. This allows to integrate all experimental data obtained from our GFP reporter cell lines, i.e., pXBP1(S), ATF4, BiP and CHOP. We subsequently describe all equations for the system states, starting with the unfolded protein U:

$$f_1(\mathrm{x}) = \frac{E_t}{1+P_{act}} + s_s + S_i - \delta B_f - r_U U, \qquad (4)$$

where E_t denotes the base rate of translation, i.e., the formation of peptides or unfolded proteins from mRNA which can be modulated by translation attenuation. S_i represents the rate of production of unfolded proteins due to the exposure-related stressor, which is described explicitly as a function of time (see below). The parameter s_s represents a net folding/unfolding rate that is independent of BiP and of translation. Instead, it includes both the folding activity of chaperones other than BiP and unfolding activity of existing proteins. Because it represents a net effect, s_s can have a positive or negative value, depending on which process prevails. Unfolded proteins are removed by degradation, which occurs at rate r_U, or by their folding following binding to the chaperone BiP, which occurs at rate δ. The latter process depends on the amount of free form of BiP, which is given by

$$B_f = \frac{U}{U+K_{BU}} B, \quad (5)$$

where K_{BU} is the amount of unfolded proteins for which half of the BiP molecules is present in free form. Inhibition of translation is modelled by modification of the E_t term, where P_{act} denotes the active form of PERK and is given by

$$P_{act} = P_t(\frac{U}{K_{PU}})/(1 + \frac{B_f}{K_{BP}} + \frac{U}{K_{PU}}), \quad (6)$$

Where P_t is the effective/net amount of PERK, and K_{PU} and K_{BP} are Michaelis-Menten parameters describing the affinity of the complexes PERK:UP and BiP:UP, respectively.

The amount of spliced XBP1 is described by:

$$f_2(\mathrm{x}) = \beta_1 I_{act} - r_X X. \quad (7)$$

Here, β_1 represents the XBP1 splicing rate, which depends on the amount of active IRE1α. The latter is represented by I_{act} and is given by:

$$I_{act} = (\frac{U}{K_{IU}})/(1 + \frac{B_f}{K_{BI}} + \frac{U}{K_{IU}}), \quad (8)$$

where K_{IU} and K_{BI} are Michaelis-Menten parameters describing the affinity of the complexes IRE1α:UP and BiP:IRE1α, respectively. Spliced XBP1 is degraded at rate r_X.

The amount of ATF4 is described by:

$$f_3(\mathrm{x}) = b_0 + \beta_2 eIF2\alpha_p - r_{A_4} A_4, \quad (9)$$

Where r_{A_4} denotes the degradation rate of ATF4, b_0 indicates its basal production rate, and β_2 is the additional production rate of ATF4 due to $eIF2\alpha_p$, where $eIF2\alpha_p$ is the fraction of phosphorylated eIF2α that obeys:

$$eIF2\alpha_p = 1 - eIF2\alpha_{up} = 1 - (1 + \frac{P_t U}{K_{PU} + \frac{B_f K_{PU}}{K_{BP}} + U})^{-1}, \quad (10)$$

Where $eIF2\alpha_{up}$ denotes the fraction of unphosphorylated eIF2α. Note that the total amount of $eIF2\alpha$ (phosphorylated and unphosphorylated) is considered to be conserved.

The amount of pATF6(N) is described by:

$$f_4(\mathrm{x}) = \beta_3 A_{6,act} - r_{A_6} A_6, \quad (11)$$

where $A_{6,act}$ is the activated sensor (i.e., the free form of ATF6, which is not the same as pATF6(N)), which obeys

$$A_{6,act} = (\frac{U}{K_{AU}})/(1 + \frac{B_f}{K_{BA}} + \frac{U}{K_{AU}}). \quad (12)$$

As before, K_{AU} and K_{BA} are Michaelis–Menten parameters representing the affinity of the complexes ATF6:UP and BiP:ATF6, respectively.

The amount of BiP is described by:

$$f_5(\mathrm{x}) = \gamma_1 + \alpha_1 X + \alpha_2 A_4 + \alpha_5 A_6 - r_B B, \quad (13)$$

where γ_1 is the basal production rate of BiP, r_B is the degradation rate of BiP, and α_1, α_2, α_5 represent the additional BiP production rate due to activity of pXBP1(S), ATF4 and pATF6(N), respectively.

The amount of CHOP is described by:

$$f_6(\mathrm{x}) = \gamma_2 + \alpha_3 X + \alpha_4 A_4 + \alpha_6 A_{6,hill} - r_C C, \quad (14)$$

where γ_2 is the basal production rate of CHOP, r_C is the degradation rate of CHOP, and α_3, α_4, α_6 represent the additional CHOP production rate due to activity of pXBP1(S), ATF4 andpATF6(N), respectively. $A_{6,hill}$ describes the contribution of pATF6(N) to the CHOP transcription rate with a Hill function:

$$A_{6,hill} = \frac{A_6^n}{A_6^n + K_{A2C}^n}, \quad (15)$$

where n and K_{A2C} are the exponent and threshold in the Hill-function. Note that because there is not a clear peak in the dynamics of pXBP1(S) or ATF4 shown in Fig. 2D in the main text, a Hill function with an exponent larger than one is not needed to describe the effect of pXBP1(S) and ATF4 on CHOP (i.e., the fitting performance is not improved). Hence, for the sake of simplicity, we only used a Hill function for pATF6(N).

In addition to the six state variables, the exposure-related stressor S_i is a dynamic variable whose kinetics do not depend on the other system states. The intra-cellular concentration of the applied compound (S_c) is described explicitly with the following pharmacokinetics (see Supplementary material for details about its derivation):

$$S_c = E_i(e^{(-\tau_2 t)} - e^{(-\tau_1 t)})H(t). \quad (16)$$

Here E_i represents the effective intra-cellular concentration of the applied compound, with the subscript i denoting the applied concentration in µM. For 1 µM, we set $E_1 = 1$; for the other four concentrations we assign four free parameters that are estimated (see Supplementary Table 1). $H()$ stands for the Heaviside function. We consider the stressor to affect the signalling network

only when a threshold θ_{th} is crossed. We describe this by the above discussed S_i, i.e., the effective rate at which unfolded proteins are formed due to the stressor:

$$S_i = e_s(S_c - \theta_{th})H(S_c - \theta_{th}), \quad (17)$$

where e_s scales the effective intra-cellular concentration of tunicamycin to unfolded proteins. At equilibrium, the total production rate of unfolded proteins is $\frac{E_t}{1+P_{act}} + s_s$.

For each GFP-reporter cell line, we introduce scaling and offset parameters denoted as e_{GFP} and s_{GFP}, respectively. Those two parameters transform the state in the ODE to the observable. For example, for ATF4 we formulated the observable A_4^o as

$$A_4^o = e_{atf4}A_4 + s_{atf4}. \quad (18)$$

Hence, to map the concentrations of the proteins to the GFP intensities, we introduce eight parameters for the four UPR cell lines: e_{xbp1}, e_{atf4}, e_{bip}, e_{chop}, s_{xbp1}, s_{atf4}, s_{bip}, and s_{chop}.

All model simulations were conducted in python 2.7.14.

Model calibration and model selection

We fitted our models to the quantified dynamics of reporter cell lines, using the maximum likelihood approach to estimate parameters. Given the nonlinear nature of the model, multiple local optima of parameters could exist in the likelihood landscape. To find the global optimum, we employed a Monte Carlo method with multiple starting values. We generated a set of $N_s = 1000$ starting values $\{\theta_s\}$ in Θ using Latin hypercube sampling[213]. We listed the employed boundaries of the parameters in Supplementary Table 1. For each starting value, we use the Trust-Region-Reflective-Newton method to obtain the local minimum θ_f [214]. For a robust and efficient estimation, we incorporate the sensitivity equation[215] and a steady state constraint[216] into our local optimization. After applying this local optimization for all starting values, we take the estimate $\hat{\theta} = \theta_f$ with the minimal negative log-likelihood. Numerical optimization relied on the python package scipy. To quantify the uncertainty of parameter estimates, we applied a Hessian-based approach to explore the likelihood around the estimates. We quantified this as a 95% confidence interval of the estimates[217] (see details in the Supplement and confidence intervals of the estimates in Supplementary Table 1). Moreover, we performed a sensitivity analysis of the impact of single parameters on the CHOP level based on the maximum likelihood estimate, i.e., the most plausible set of parameters based on the measurements (see details in the Supplement).

Plausible models are expected to give a good fit to observations with a relatively small value of the negative-log likelihood at $\hat{\theta}$. We performed a likelihood-ratio-based test to evaluate the goodness of fit to the measurements, as for example applied in García-Pérez & Alcalá-Quintana et al.[218,219] aiming to get insight into processes underlying temporal-order and simultaneity judgments by observers. Specifically, García-Pérez & Alcalá-Quintana et al.[218] focused on a

likelihood- ratio based approach to check goodness of fit and García-Pérez & Alcalá-Quintana et al.[219] further incorporated the likelihood ratio into a Bayesian test when computing the ratio of two posterior distributions in order to derive a closed-form psychometric function about simultaneity judgments. In general, the test can be used to compare two models by the ratio of their likelihoods, denoted by ΔG, and a p value is computed from a χ^2 distribution. In our case, we used this approach to evaluate whether the data are more compatible with separate incorporation of the ATF6 branch (with estimates θ_2) rather than with lumping ATF6 and XBP1 into a single branch (with estimates θ_1).

Modelling of knockdown conditions

We simulated the calibrated model by incorporating single knockdown perturbations with siRNA treatments. We focused on the knockdowns with siDDIT3 and siATF4, and siATF6, setting the knockdown efficiencies at the values estimated by the analysis of the TempO-seq data. To account for variability of knockdown efficiencies over experiments and over time from different assays, we varied the knockdown efficiency by 20% more or less than the reference value and simulated the model accordingly.

Here we describe how we model knockdown experiments by siRNA treatments. The dynamics of the mRNA can be described by the following differential equation:

$$\tau_m \frac{d}{dt}[mRNA] = \lambda_m + tf(t) - d_m[mRNA], \quad (19)$$

where $[mRNA]$, represents the amount of mRNA of interest, τ_m is the time constant of the mRNA, $tf(t)$ is mRNA production rate due to TF activity, λ_m denotes the basal production rate, and d_m is the degradation rate of the mRNA. We consider knockdown of a gene of interest to increase the mRNA degradation rate compared to the control case. To study how this affects the protein dynamics over time, we first write the equation for the protein:

$$\tau_p \frac{d}{dt}[protein] = \lambda_p[mRNA] - d_p[protein], \quad (20)$$

where $[protein]$ represents the amount of protein of interest, τ_p is the time constant of the protein and d_p is the degradation rate of the protein.

Considering transcription to be much faster than (post-)translational processes, i.e. $\tau_m \ll \tau_p$, the mRNA will be at equilibrium, i.e., $[mRNA](t) = \frac{\lambda_m + tf(t)}{d_m}$.

Substitution of this relation into the translation step in (20) gives

$$\tau_p \frac{d}{dt}[protein] = \lambda_p \frac{\lambda_m}{d_m} + \lambda_p \frac{tf(t)}{d_m} - d_p[protein]. \quad (21)$$

Lumping $\frac{\lambda_m}{d_m}$ into λ_p^* and $\lambda_p \frac{\lambda_m}{d_m}$ into μ_p^* results in:

$$\tau_p \frac{d}{dt}[protein] = \mu_p^* + \lambda_p^* tf - d_p[protein]. \quad (22)$$

In this equation, μ_p^* and λ_p^* incorporate the effects of the increased mRNA degradation upon knockdown. Thus, these parameters are expected to decrease when cells are pre-treated with siRNA knockdowns. We define the knockdown efficiency e_{KD} as $1 - \frac{[mRNA]KD}{[mRNA]}$, which equals $1 - \frac{d_m}{d_{m,KD}}$, where $d_{m,KD}$ is the mRNA degradation rate upon knockdown. Then we obtain $d_{m,KD} = \frac{d_m}{1-e_{KD}}$, which propagates into the parameters for protein formation as $\mu_{p,KD}^* = (1 - e_{KD})\mu_p^*$ and $\lambda_{p,KD}^* = (1 - e_{KD})\lambda_p^*$. In conclusion, the knockdowns can be simulated by decreasing the protein production rates with a multiplier based on the measured knockdown efficiency. For ATF4, ATF6 and CHOP, for which we obtained knockdown efficiencies, we thus perturbed the production rates as follows: For siATF4, we set $\beta_2 = (1 - e_{KD})\hat{\beta}_2$ and $b_0 = (1 - e_{KD})\hat{b}_0$, where $\hat{\beta}_2$ and $\hat{b}_0$ are the estimated values in the absence of knockdown. For siATF6, we set $\beta_3 = (1 - e_{KD})\hat{\beta}_3$, where $\hat{\beta}_3$ is the estimated value in the absence of knockdown. For siDDIT3, we set $\gamma_2 = (1 - e_{KD})\hat{\gamma}_2$, $\alpha_3 = (1 - e_{KD})\hat{\alpha}_3$, $\alpha_4 = (1 - e_{KD})\hat{\alpha}_4$, and $\alpha_6 = (1 - e_{KD})\hat{\alpha}_6$, where $\hat{\gamma}_2$, $\hat{\alpha}_3$, $\hat{\alpha}_4$, and $\hat{\alpha}_6$ are the estimated values in the absence of knockdown.

Results

Image-based monitoring of UPR and cellular dynamics

To establish an ODE model that captures UPR network regulation and activation, experimental data are required that quantify the dynamics of induction of crucial UPR genes with a dense time resolution. We achieved such a resolution by combining our previously established liver carcinoma HepG2 BAC-GFP UPR reporters[27,28] with high-content confocal microscopy. We used the compound tunicamycin as an ER stress inducer, which inhibits N-glycosylation and therefore leads to the accumulation of unfolded glycoproteins[220]. Tunicamycin specifically induces ER stress, and is therefore an excellent compound to create a UPR specific ODE model.

We first examined whether our HepG2 UPR reporters for CHOP, ATF4, pXBP1(S) and BiP are representative for the behaviour of wild-type (WT) HepG2 cells. To this purpose, we established the protein expression of endogenous CHOP, ATF4, pXBP1(S) and BiP using western blotting in HepG2 WT cells after tunicamycin exposure for 4, 8, 16 and 24 hours. Both treatment with 1 and 6 µM tunicamycin resulted in a clear induction of UPR proteins (Fig. 2A). However, BiP was already highly expressed at basal levels and therefore it was unclear whether further induction occurred. A high tunicamycin concentration of 6 µM led to an earlier induction of UPR proteins than a low concentration of 1 µM (Fig. 2A).

Next, we assessed if all four HepG2 UPR reporters behaved similarly upon tunicamycin exposure as WT cells. Applying a TempO-seq targeted transcriptomics approach to all five HepG2 (WT and reporter) cell lines exposed to a broad concentration range of tunicamycin for 8 or 24 hours revealed that DDIT3 (i.e., the gene coding for the CHOP protein) expression across HepG2 wild

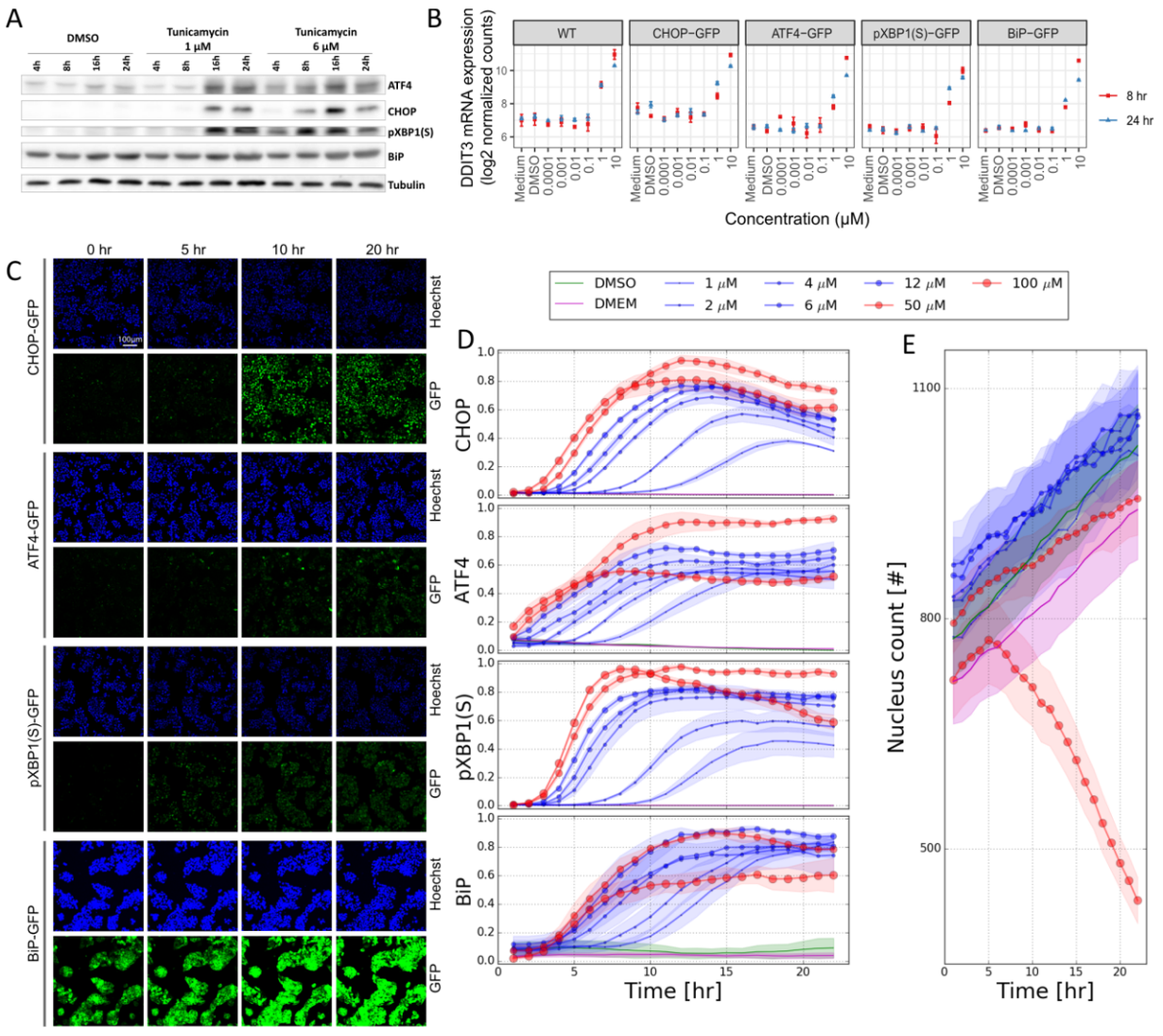

Fig. 2. Dynamic measurements of various UPR components to integrate with modelling. A) Western blot of CHOP, ATF4, pXBP1(S) and BiP protein at 4, 8, 16 and 24 hours upon exposure to DMSO or tunicamycin (1 and 6 µM) in WT HepG2 cells. Tubulin was used as protein loading control. B) Log2 normalized counts of DDIT3 mRNA expression analysed using TempO-seq transcriptomics at 8 or 24 hour after exposure with various concentrations of tunicamycin in HepG2 WT and UPR BAC-GFP reporter cell lines. C) Representative images of HepG2 UPR BAC-GFP reporter cell lines (CHOP, ATF4, pXBP1(S) and BiP) stained with Hoechst for nuclei visualization. Images were obtained using confocal microscopy with a 20x objective at the indicated time points after exposure to tunicamycin at 6 µM. Hoechst is represented in blue (upper rows) and GFP in green (lower rows). D-E) Quantification of single-cell-based GFP intensity of the HepG2 UPR BAC-GFP reporter cell lines after min-max normalization (D) and cell counts (E) after exposure to DMEM/DMSO or to a broad concentration range of tunicamycin and imaged live every hour for 24 hours after exposure using confocal microscopy. BiP-GFP intensity was quantified in the cytoplasm, all other reporters were quantified in the nuclei. Data in (B), (D) and (E) represents mean and standard error of the mean (SE) of three biological replicates.

type and BAC-GFP cell lines followed a similar dose response at both timepoints (Fig. 2B). For other UPR-related genes, the different cell lines also have a similar dose response behaviour and are highly correlated in gene expression (Supplementary Fig. 1). As expected based on having at least one additional copy of the gene, HepG2 CHOP-GFP exhibited a slightly higher DDIT3

expression at baseline compared to the other lines, but this did not influence the dose response of DDIT3 itself (Fig. 2B) or the expression of other UPR-related genes (Supplementary Fig. 1). Thus, all HepG2 UPR reporter behave similarly with respect to UPR gene expression.

To generate dynamic protein expression data to which results from an ODE model can be compared, we exposed HepG2 BAC-GFP UPR reporters for CHOP, ATF4, pXBP1(S) and BiP to a concentration range from 1 to 100 µM of tunicamycin and subsequently applied live imaging with confocal microscopy to capture the GFP induction in single cells and total cell count every hour until 24 hours of exposure (Fig. 2C-D). The dynamic pattern of CHOP-GFP expression exhibited a peak around 10-20 hours (Fig. 2C-D), which was consistent with the CHOP expression in WT HepG2 cells observed with western blotting (Fig. 2A). Increasing concentrations of tunicamycin led to earlier maxima of CHOP expression levels (Fig. 2C). For all four reporters, a concentration-dependent increase in maximal GFP intensity occurred. However, at the highest concentration (100 µM) of tunicamycin, the maximal GFP intensity was equal or lower compared to 50 µM, which is indicative of cellular toxicity. Consistent with this interpretation, the total number of cells dramatically decreased at 100 µM of tunicamycin (Fig. 2E). At 50 µM of tunicamycin, there was also a slower increase in cell count over time compared to lower concentrations. Therefore, only concentrations below 50 µM of tunicamycin were taken along for the ODE-model development since we here focus on the adaptive UPR signalling network. In summary, the gene expression as well as protein expression levels of BAC-GFP HepG2 UPR reporter cell lines and WT HepG2 cells exhibited similar baseline levels and dynamic patterns upon exposure to tunicamycin. Therefore, we concluded that the BAC-GFP UPR cell lines were sufficiently representative for WT HepG2 cells to be used for subsequent dynamical modelling.

UPR model with ATF6 provides excellent fit to the data

Because we had dynamic information on four BAC-GFP reporter cell lines, we initially constructed an ODE model with four variables representing the protein expression level for these reporters as well as a variable for the amount of unfolded proteins in the cell (Fig. 3A). This model was a modification of an earlier published model by Trusina et al.[203]. We did not incorporate ATF6 explicitly but it was considered to behave similarly to IRE1α, i.e. these sensors were considered to be in quasi steady state[203]. In addition, we modelled the downstream molecules ATF4 and CHOP. Finally, because the experimentally observed dynamics of intensity of all UPR reporters exhibited a concentration-dependent delay of activation for tunicamycin concentrations below 12 µM (Fig. 2D), we incorporated this phenomenon in a pharmacokinetic module preceding the signalling module. Specifically, we added a threshold in the effective intra-cellular concentration of tunicamycin, i.e., we consider the UPR signalling to be triggered only when a particular intra-cellular stress level is crossed, which leads to some delay of pathway activation (see simulated pharmacokinetic profiles in Supplementary Fig. 2).

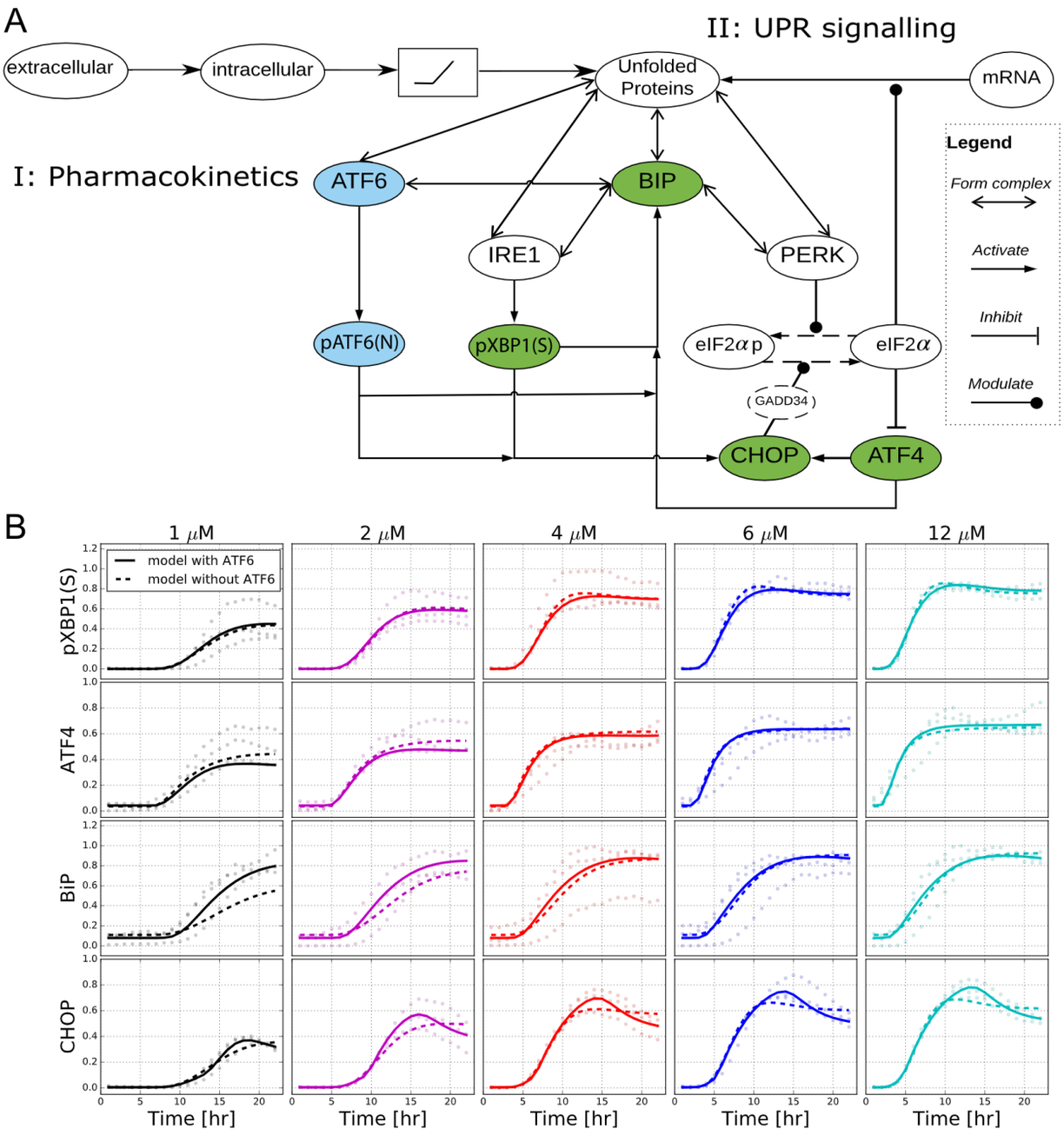

Fig. 3. Model structure and fit. A) Schematic diagram of the modelled UPR pathway with both pharmacokinetics and signalling network. B) Model fits to the experimentally observed levels of pXBP1(S), ATF4, BiP and CHOP upon tunicamycin exposure at five concentrations. Dots present values for three replicates. Optimized fits from models with ATF6 branch (solid curves) or without (dashed curves) are plotted.

This initial model could roughly describe the reporter dynamics, yet this could not capture the consistently observed dynamic peak in CHOP expression (Fig. 3B, dashed line). Therefore, we also created a model variant including the ATF6 branch explicitly (for which no BAC-GFP reporter cell line was available). The model with all three UPR branches contains 47 parameters, while the model without ATF6 has 39 parameters (for equations see Materials and Methods). After fitting of both models to the experimental data (for parameter estimates see Supplementary Table 1, for their estimated standard errors see Supplementary Fig. 3 and for their sensitivity see

Supplementary Fig. 4), visual comparison of the two model variants showed that only the model with ATF6 was able to describe the CHOP peak (Fig. 3B, solid line). This visual impression was confirmed by application of a likelihood-ratio based approach to compare the models to the data (ΔG = 119 and 271 for the full and ATF6-free models, respectively; $\rho < 0.001$), and by calculation of the information criteria AIC and BIC (Pawitan, 2001) for the two competitive models (AIC full model: 2 x 119 + 2 x 47 = 332; AIC ATF6-free model: 2 x 271 + 2 x 39 = 620 ; BIC full model: 2 x 119 + ln (440) 47 = 524.08; BIC ATF6-free model: 2 x 271 + ln (440) 39 = 779.38. The above results thus suggest that the ATF6 branch plays an important role in shaping the early CHOP dynamics, and we continued with the calibrated model including ATF6 for further exploration and validation.

Model correctly predicts CHOP dynamics beyond 24 hours

The transcription of CHOP can be induced by binding of UPR TFs, i.e., ATF4, pXBP1(S) and pATF6(N), at the AARE and ERSE promoter motifs (Fig. 4A [221,222]). However, previous work has suggested that induction of CHOP is predominantly regulated by ATF4 and pATF6(N), and to a minimal extent by pXBP1(S)[205,223,224]. Having the parameterized full UPR model in place allowed us to explore both the speed of activation of the three sensors and the contribution of each of the three downstream TFs to CHOP induction at different time points. With respect to the speed of activation of the sensors, ATF6 is the sensor responding most quickly, followed by IRE1α and finally PERK (Supplementary Fig. 5). With respect to the contribution of the downstream TFs to CHOP transcription, we investigated this by separating the mathematical term representing the CHOP production rate into the individual TF contributions forming this term. This analysis showed that the ATF6 branch shapes the early dynamics of CHOP production, whereas ATF4 dominates the CHOP production at late time points (Fig. 4B-D). This explains why ATF4 is typically considered

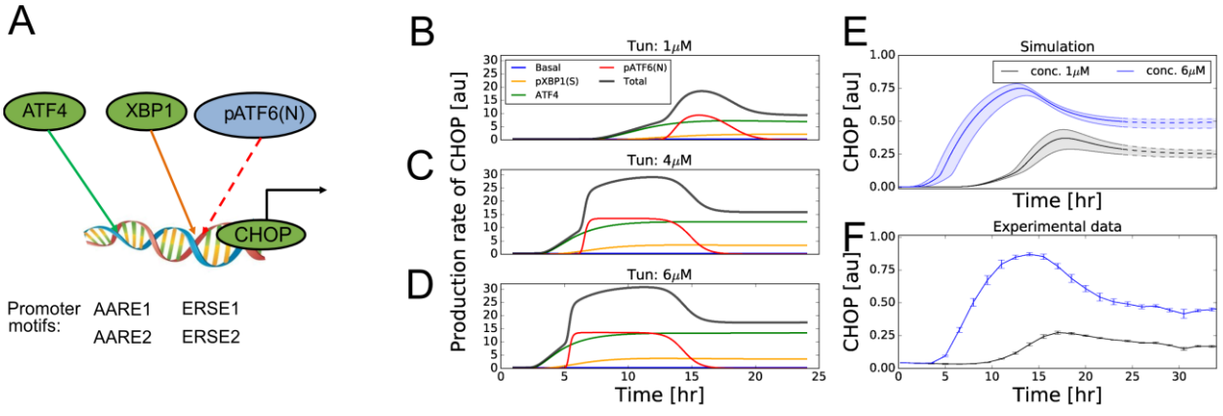

Fig. 4. Model-based prediction of CHOP transcription. A) Illustration of the TFs contributing to CHOP transcription. B-D) Simulations of the contributions of pXBP1(S), ATF4 and pATF6(N) to the CHOP production rate at the indicated tunicamycin concentrations. E) Model prediction of CHOP levels within the first 24 hours (solid line) and between 24 and 34 hours (dashed line). Simulations were conducted with various strengths of exposure (between 30% and 130% of the reference value) shown as shaded areas. F) Image-based experimental observation of CHOP for 34 hours represented as the mean ± SE of three biological replicates.

the primary TF responsible for CHOP production[190,225], yet our analysis suggests that pATF6(N) also has an important contribution to CHOP production at early time points. This happens because pATF6(N)-mediated CHOP transcription starts and ends relatively abruptly due to the high cooperativity (n = 46.32 in the best fit) in the Hill function describing pATF6(N) activity. Once pATF6(N) drops below the Hill threshold K_{A2C} (which equals 0.717 in the best fit), the effect of the still relatively high pATF6(N) levels on CHOP transcription quickly becomes negligible. Note that such a high cooperativity is required to explain the exact height of the CHOP peak (Supplementary Figs. 6, 7 and 8). Furthermore, our analysis confirmed the minimal role of pXBP1(S) in CHOP transcription, which is due to low pXBP1(s) levels rather than to low TF activity of the present pXBP1(s) (Supplementary Fig. 9).

Given the model prediction that the ATF4-driven CHOP production rate remains relatively high around 24 hours, we simulated the model for a duration longer than the 24 hours on which the parameterization was based. Beyond 24 hours the CHOP level was predicted to stay around the same level for tunicamycin concentrations of 1 and 6 µM (Fig. 4E) rather than quickly returning to baseline level. Our simulations predicted that this was due to a gradual increase of the intra-cellular stress levels, which saturated after 20 hours and did not yet decrease (Supplementary Fig. 2). The sustained high ATF4 level is attributed to its upstream molecules PERK and eIF2α that tightly follow the dynamics of the intra-cellular stressor and of unfolded protein (Supplementary Fig. 9). To validate this model prediction, we performed imaging experiments of a duration beyond 24 hours, which showed that indeed CHOP-GFP levels in HepG2 cells remained at a relatively high level up to 34 hours (Fig. 4F). Thus, although the model was based on 24-hour measurements, it correctly predicted sustained CHOP levels beyond 24 hours.

Knockdown experiments confirm role of ATF6 in CHOP dynamics

We next challenged our model further by evaluating the effect of perturbing single UPR-related genes, including ATF6, on activation of other UPR components using siRNA-mediated silencing. To confirm success of knockdown by siRNA and to quantify its efficiency, we first measured the expression of DDIT3, ATF4 and ATF6 after knockdown of these separate genes for 3 days and subsequent exposure to 6 µM tunicamycin for 16 hours. TempO-seq transcriptomics experiments showed that expression of these genes was indeed significantly decreased by siRNA-mediated silencing upon exposure to tunicamycin (Fig. 5A). To study the effect of perturbation of UPR-related genes on CHOP and ATF4 induction dynamics during ER stress, we then measured CHOP-GFP and ATF4-GFP in HepG2 BAC reporters using confocal imaging for 24 hours after 6 µM tunicamycin exposure when either no gene (Mock), DDIT3, ATF4 or ATF6 was silenced using siRNA (Fig. 5B and blue lines in Fig. 5C). Knockdown of DDIT3 and ATF4 led to reduced levels of respectively CHOP-GFP and ATF4-GFP, confirming the success of the knockdowns also at protein level. We then compared the experimental measurements upon knockdown to model

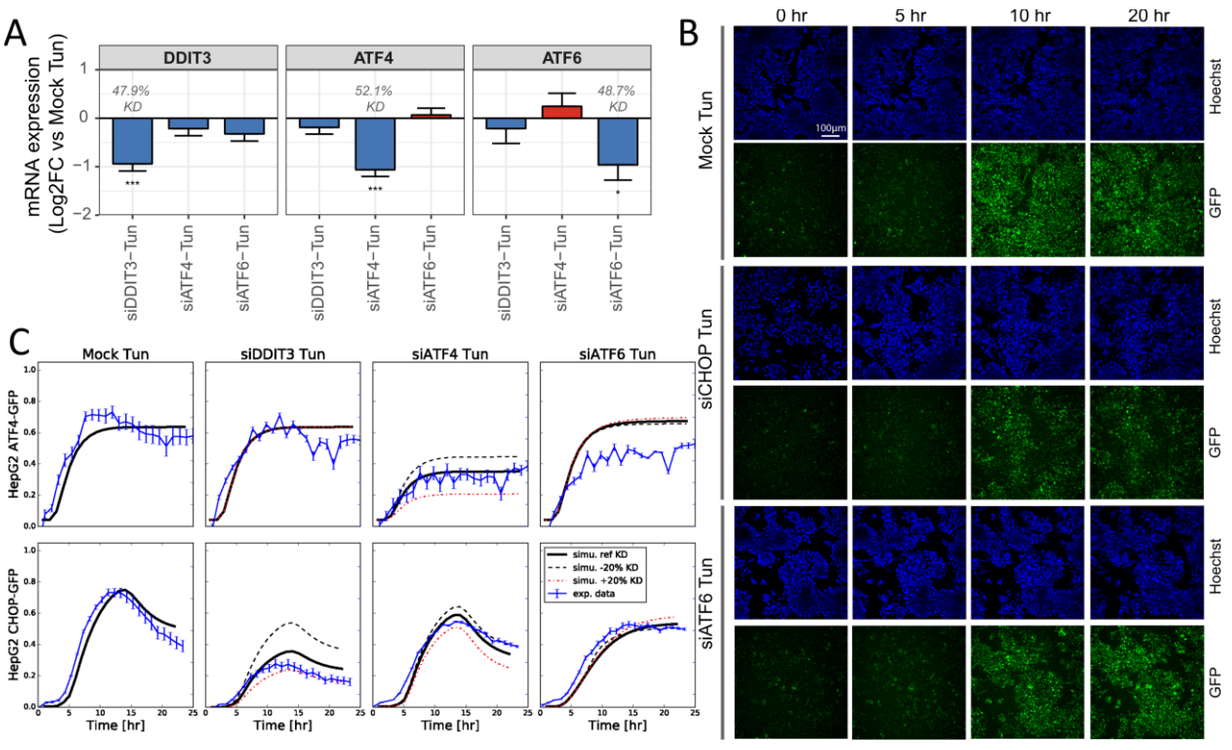

Fig. 5. Perturbation of UPR with siRNA knockdowns are consistent with model predictions. A) Log2 fold changes of mRNA expression of different siRNA-mediated gene knock-downs relative to siRNA mock negative control in HepG2 WT cells exposed to 6 µM of tunicamycin for 16 hours, determined using TempO-seq transcriptomics. Knockdown efficiencies of siRNAs are depicted in grey numbers. Data represents the mean ± SE of three biological replicates. B) Representative confocal microscopy images obtained with 20x objective of HepG2 CHOP-GFP reporter cells exposed to 6 µM of tunicamycin for 16 hours after CHOP, ATF6 or Mock siRNA. To visualize the nuclei, cells were stained with Hoechst (upper rows), and CHOP-GFP is represented in green (lower rows). C) Model simulation of ATF4 and CHOP (black curves) compared to quantified GFP data after exposure to 6 µM of tunicamycin for different siRNA-mediated knockdown conditions (blue line and error bars representing mean ± SE). Simulations with varied knockdown efficiency (black dashed: 20% less, red dashed: 20% more) are also plotted.

predictions incorporating the knockdown efficiencies that we measured for the different genes (Fig. 5C).

ATF4 and ATF6 knockdown both affected the CHOP-GFP dynamics, yet its effect was qualitatively different. ATF4 knockdown led to a decrease in CHOP induction, yet a clear peak remained present in the CHOP dynamics around 16 hours post tunicamycin exposure, indicating that ATF4 is not responsible for that peak (Fig. 5C). Similarly, ATF6 knockdown led to a reduced CHOP induction specifically in the initial phase. However, after 16 hours of exposure, CHOP levels did not decline again and CHOP levels at 24 hours were slightly higher when ATF6 was silenced than for the Mock control. Our model offers an explanation for these observations: First, the lowered activity of pATF6(N) due to ATF6 knockdown implies that the CHOP transcription rate contributed by pATF6(N) does not exceed the required threshold and that CHOP transcription fully depends on XBP1(S) and ATF4 activity. Second, the reduced pATF6(N) upon knockdown also lowers BiP expression, thus leading to an increased amount of unfolded proteins, XBP1(S) and ATF4, which

in turn slightly increases CHOP expression around 24 hours compared to a setting without knockdown (Supplementary Fig. 10). Thus, ATF6 affects the CHOP dynamics especially in the initial phase but also slightly in the later phase as was predicted by our model. Altogether, the experimentally observed alterations in ATF4 and CHOP induction could be accurately predicted with our model and this analysis confirmed the model prediction that ATF6 shapes CHOP dynamics. As ATF6 shapes the dynamic pattern of pro-apoptotic CHOP, i.e., initially increases CHOP but later decreases it due to initial BiP-mediated folding of unfolded proteins, we speculate that early ATF6 activity may in fact protect cells under chronic ER stress. This is consistent with experimental findings in ATF6 KO mice in which cell death increased upon exposure to tunicamycin after 18 h[223].

ATF6 activation peaks early as predicted by modelling

Since our model predicts that the peak in CHOP dynamics that follows tunicamycin exposure is due to early ATF6 activity, we evaluated the mRNA expression and activation dynamics of endogenous ATF6 in HepG2 WT cells by TempO-seq transcriptomics and Western blot. ATF6 mRNA expression increased by 2-fold at 10 µM of tunicamycin at 8 and 24 hours, but not at 1 µM (Fig. 6A), suggesting minor upregulation of ATF6 only at high concentrations. At protein level, exposure to 6 µM of tunicamycin clearly led to the expected inhibition of N-glycosylation, which became visible by the appearance of a low Western blot band representing unglycosylated, uncleaved ATF6 ($ATF6_{UG}$) and a decrease of the high band representing glycosylated ATF6 ($ATF6_{G}$) starting from 4 hours of exposure (Fig. 6B; quantification in Fig. 6C, first two panels). Exposure to a lower concentration of 1 µM tunicamycin also increased the formation of $ATF6_{UG}$, yet was only apparent at late time points (Supplementary Fig. 11).

The relation between $ATF6_{G}$ and $ATF6_{UG}$, which changes during tunicamycin exposure, is illustrated in Fig. 6D, i.e., both forms can degrade, but only ATF6G can lead to pATF6(N). The amount of total uncleaved ATF6 (i.e., $ATF6_{UG}$ + $ATF6_{G}$) decreased at early time points (6 hours, ρ = 0.016; 8 hours, ρ = 0.070) compared to DMSO control, but restored later on (Fig. 6C third panel). Since levels of endogenous cleaved ATF6 in HepG2 cells were difficult to capture using Western blot, we assessed ATF6 cleavage from the difference in total uncleaved ATF6 levels. Considering the ATF6 production and degradation rates to remain roughly unchanged at early time points in tunicamycin and DMSO conditions, the decreased amount of total uncleaved ATF6 at those time points can be attributed to ATF6 cleavage. Therefore, we used the difference in total uncleaved ATF6 between the first measured timepoint and subsequent timepoints as a measure for ATF6 cleavage (Fig. 6C, panel 4). The level of pATF6(N), as estimated through this approach, peaked at 6 hours post tunicamycin exposure (ρ = 0.044), which is consistent with the dynamics of predicted free ATF6 and pATF6(N) in our computational model (Fig. 6E).

In conclusion, the activation dynamics of ATF6 were early and concentration-dependent as predicted by our model. Together, our combination of experimental and computational

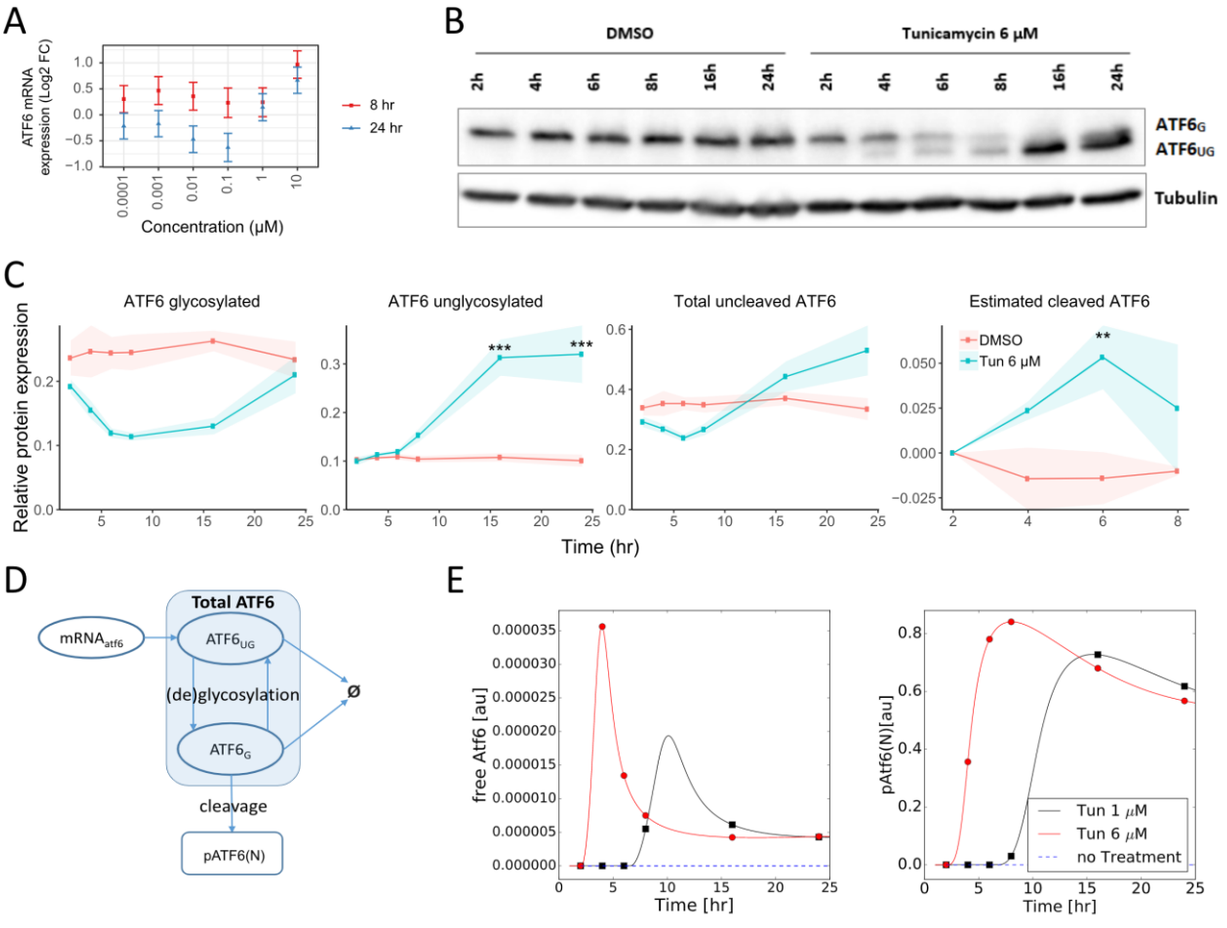

Fig. 6. Matching ATF6 dynamics in experiment and model. A) ATF6 mRNA expression after 8 or 24 hours of exposure to a broad concentration range of tunicamycin in HepG2 WT cells using TempO-seq, represented as the mean of log2FC ± SE of three biological replicates. B) Western blot of uncleaved ATF6 (G = glycosylated, UG = unglycosylated) measured in HepG2 WT cells at 2, 4, 6, 8, 16 or 24 hours after exposure to tunicamycin (6 µM) or DMSO. As protein loading control, tubulin protein expression was assessed. C) Quantified protein expression of the indicated ATF6 forms from three biological replicates after protein loading correction using tubulin (symbols and shaded area represents mean ± SE with the significance levels represented as $*p_{adj} < 0.1$, $**p_{adj} < 0.05$, $***p_{adj} < 0.01$). Cleaved ATF6 was estimated based on the difference between total uncleaved ATF6 at 4, 6 and 8 h versus the 2 h timepoint. D) Diagram of relation between different ATF6 forms during tunicamycin treatment, where $ATF6_G$ and $ATF6_{UG}$ represent glycosylated and unglycosylated forms, respectively. E) Model-predicted dynamics of free ATF6 and the downstream pATF6(N) upon exposure of tunicamycin at 1 and 6 µM.

modelling work shows that ATF6 is activated early after tunicamycin exposure and that this causes an early rise in CHOP expression. The CHOP expression subsequently drops to a lower level, yet remains relatively high due to ongoing presence of stress, keeping ATF4 expression at elevated levels.

Discussion

The basis of our work consisted of dynamic measurements detailing the induction of UPR regulators in HepG2 reporter cell lines during tunicamycin-induced ER stress. We exploited these data to establish a computational model representing the essential mechanisms shaping the UPR and fitted the model using 24-hour reporter dynamics. The strength of our approach was that we

exploited a large amount of high-content imaging data in order to obtain a quantitative understanding of UPR regulation. This combination of modelling and experiments helped to unravel the role of different molecules in the UPR dynamics. Specifically, the model predicted that the ATF6 branch was required to explain the observed UPR dynamics and this prediction was verified by knockdown experiments, prolonged experimental time courses and additional western blot measurements.

Some of the previously published UPR modelling work focused on theoretical understanding of network dynamics in different scenarios[202,203]. Specifically, in the extensive model of Erguler et al.[202] it was shown that the network could exhibit different kinds of structural behaviour depending on the parameter settings. For example, for some parameter conditions oscillations occur, showing that the network is in principle capable of generating such behaviour. However, our combined modelling and experimental analysis demonstrates that at least for HepG2 cells exposed to tunicamycin such oscillations do not occur. Due to the complexity of the model by Erguler et al.[202] precluding calibration to a data set that was limited in terms of number of monitored variables, we instead chose to extend the model by Trusina et al.[203] with CHOP and ATF6, rendering a new model with similar UPR TF activity that could be calibrated to our imaging data. A combination of experimental and computational work similar to ours has been recently reported by Diedrichs et al.[205], where model predictions were based on qPCR and Western blot experiments. Key differences with our approach include the choice of test compound and the balance of model complexity and measurements. With respect to the employed compounds, Diedrichs et al.[205] exposed MEFs to thapsigargin, a SERCA inhibitor disturbing calcium homeostasis, whereas we used tunicamycin, which inhibits N-glycosylation within the ER. The downside of using exposure to thapsigargin is that it not only leads to a strong UPR induction but also induces oxidative stress, at least in HepG2 cells[27]. With respect to model complexity and the amount of experimental data, time-lapse imaging data has as a major advantage that it easily delivers many data points at single cell level within specific sub-cellular compartments, i.e., we have more than 400 datapoints measured from four BAC-GFP reporters at five concentrations and at more than 20 time points.

Besides capturing the dynamics of UPR-related molecules, our quantitative modelling approach suggests that ATF6 is responsible for the early peak of CHOP. Both our knockdown experiments and ATF6 measurements using Western blotting at different time points are consistent with this hypothesis. Specifically, the decrease in total uncleaved ATF6 strongly suggested that cleavage of ATF6 peaked at early time points (around 6 hours). These findings are also consistent with those of Yoshida et al.[195], who reported a similar pattern with an overshoot in the nuclear active ATF6 fragment after tunicamycin treatment in HeLa cells. To verify the observed activation dynamics of ATF6 and to capture high-resolution activation dynamics at sub-cellular localization, future imaging-based dynamic readout of ATF6 and its fragments would be highly valuable. Based

on such data, the part of our model describing ATF6 could also be extended and better parameterized.

The parameters in our mechanistic model have a biological interpretation and their estimates thus provide quantitative insight into UPR regulation. First, the degradation rate of the protein CHOP (r_C) was estimated to be 5-fold larger than that of BiP (r_B), i.e., a similar difference as found by Rutkowski et al.[226]. Given the protective role of BiP through protein folding and the pro-apoptotic role of CHOP, this suggests that the distinct degradation rates represents one mechanism that explains initial adaptation to ER stress, followed by a switch towards adversity during prolonged ER stress. Second, the parameters K_{BP}, K_{BI}, and K_{BA} shape the response sensitivity amongst the three UPR branches PERK, IRE1α and ATF6, with the latter being the quickest (Supplementary Fig. 5). Interestingly, we showed that ATF6(N) transcriptional activity with respect to CHOP is also switched off early and abruptly due to the high predicted cooperativity of this response (Fig. 4).

In response to ER stress, cells have several coping strategies to eliminate the accumulation of misfolded proteins by activating the three UPR branches. However, in case ER stress becomes too severe or chronic, apoptotic signalling pathways will be activated and cells will switch from adaptive to pro-apoptotic signalling. In this switch, CHOP plays an important role through various mechanisms[89,191,227] and therefore regulators of CHOP can affect the sensitivity of cells to ER stress. Here, we found that ATF6 has such a crucial role in the dynamics of CHOP induction, where perturbation of ATF6 led to absence of the initial CHOP peak yet led to slightly increased CHOP levels at a later stage. Our findings are consistent with earlier work in which ATF6-knockout MEFs had lower CHOP levels until 12 hours of exposure to thapsigargin, while at later time points CHOP levels were higher compared to WT[205]. Given the importance of ATF6 in the regulation of CHOP activation dynamics as well as cytoprotective proteins such as BiP[228], ATF6 is also expected to play a role in the switch between adaptive to cellular adversity, especially in realistic scenarios with repeated exposure to chemicals. Indeed, it has been reported that ATF6 plays a role in the protection against chronic ER stress using ATF6 knockout mice and repeated exposures[223].

In conclusion, by combining high-throughput confocal imaging and ODE modelling, we captured the dynamics and role of individual components within the UPR, particularly pinpointing the importance of ATF6 in CHOP activation dynamics. Since the UPR plays an important role in both drug-induced toxicity as well as the development of drug resistance in cancer, improved insight in UPR signalling dynamics in relation to cell fate is important.

Limitations of the Study

Using a combined experimental and computational modelling study of UPR signalling, we showed that ATF6 has an important role in shaping the dynamic pattern of CHOP activity, thus likely affecting cell fate decisions under ER stress. However, we neither mathematically described the relation between UPR activity and cell fate, nor did we investigate experimentally whether cell

fate decisions are indeed affected by ATF6. Moreover, our findings are based on a single cell line and only on in vitro observations, hence the response may be different in in vivo scenarios. Finally, we do not know whether our observations hold for other UPR-invoking compounds and whether our model is able to describe UPR dynamics for such compounds, including their potential adversity.

Acknowledgments

This work has received funding from the ZonMW InnoSysTox programme (grant 40-42600-98-14016; to JBB and BvdW) and from the European Union's Horizon 2020 research and innovation programme (grant 681002; to JBB and BvdW).

Supplemental figures

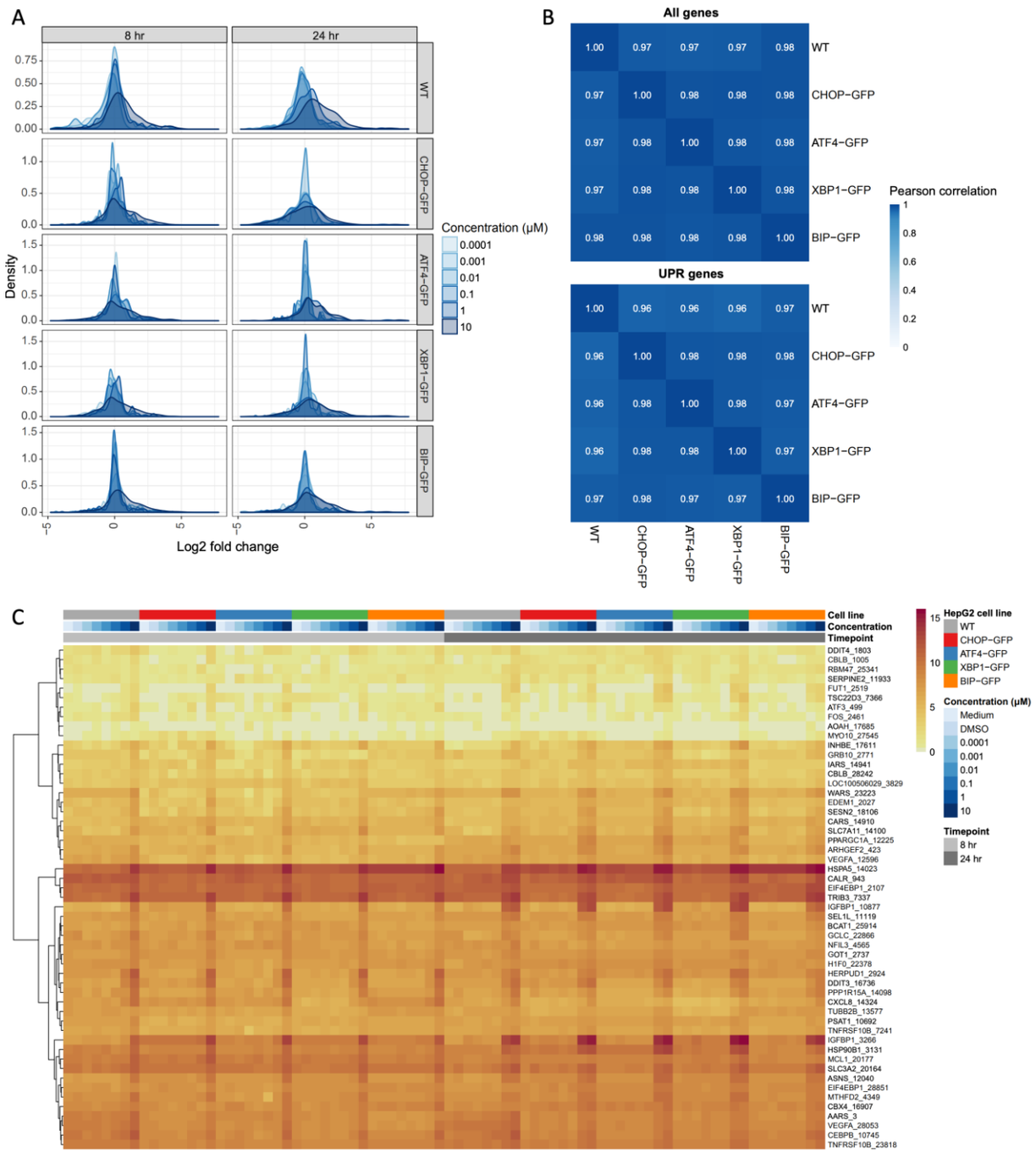

← Fig. S1. Transcriptomic profiling of HepG2 UPR BAC-GFP reporters. A) Distribution of log2 fold changes (compared to DMSO solvent control) of UPR-related genes across the indicated concentration range of tunicamycin for each HepG2 cell line (WT, CHOP-GFP, ATF4-GFP, pXBP1(S)-GFP and BiP-GFP) at 8 and 24 h exposure time. B) Pearson correlation matrix of different HepG2 cell lines based on either all genes (top panel) or UPR-related genes (lower panel). Correlations are the mean of correlations between cell lines at each concentration of tunicamycin. C) Heatmap of log2 normalized counts of UPR-related genes (selection based on upper quantile of log2 fold changes of all UPR-related genes at 10 µM) for each HepG2 cell line exposed to the indicated concentration range of tunicamycin either for 8 or 24 h. Hierarchical clustering of genes based on Euclidean distance.

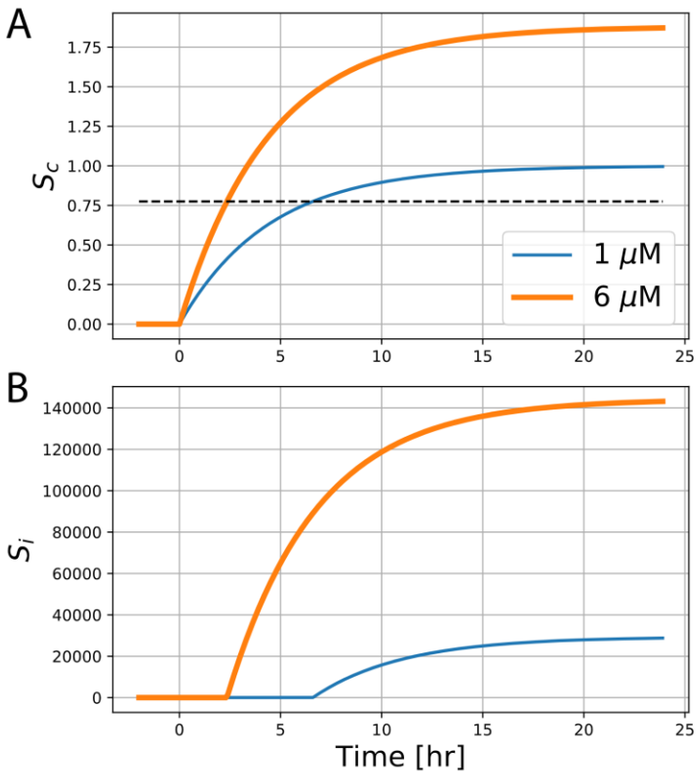

Fig. S2. Modelled pharmacokinetics of tunicamycin exposure. A) Effective intra-cellular concentration of tunicamycin $\boldsymbol{S_c}$ over time, B) exposure-related stressor $\boldsymbol{S_i}$ (unfolded proteins due to tunicamycin) which acts as input to the UPR signalling network.

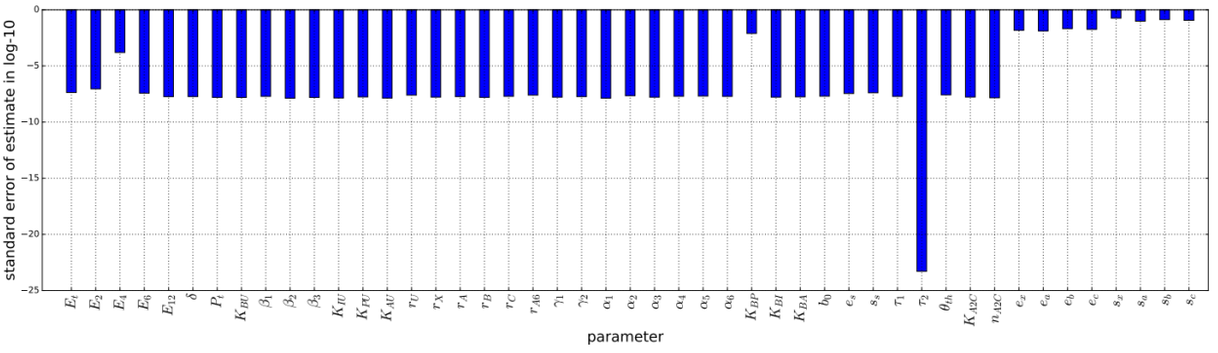

Fig. S3: Standard errors of model parameter estimates. The standard errors were approximated via a Hessian-based approach and are presented in log10 scale.

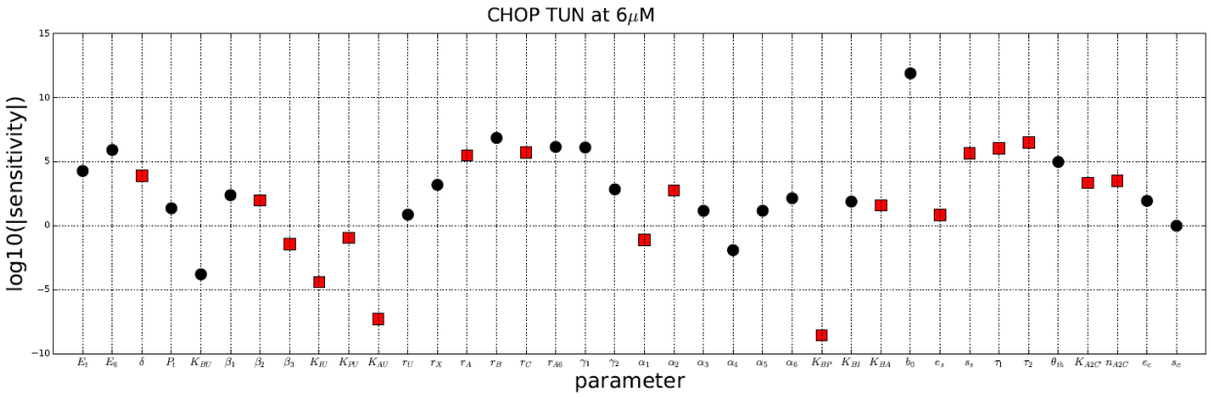

Fig. S4. Parameter sensitivity analysis of CHOP expression. In the sensitivity analysis, we considered the sensitivity of CHOP expression at 16 hours after exposure to 6µM of tunicamycin. Parameters positively affecting CHOP are shown in black, while parameters negatively affecting CHOP are shown in red.

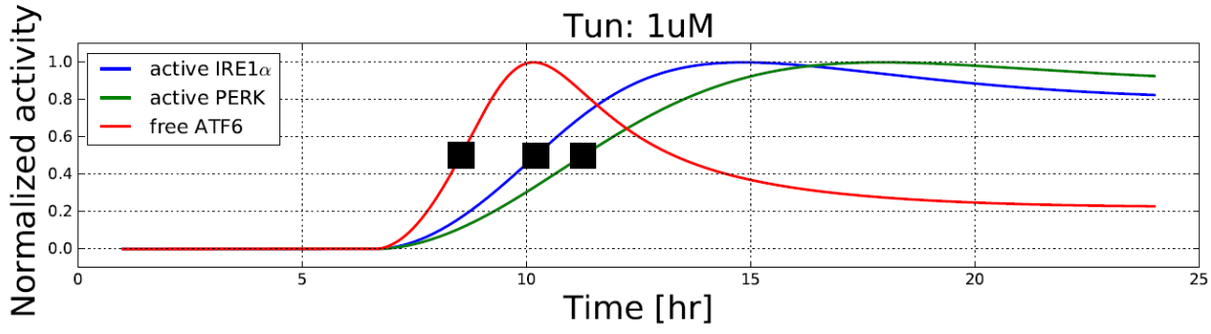

Fig. S5. Predicted dynamics of the three UPR sensors upon tunicamycin exposure. Plot of the dynamics of the sensors IRE1α (blue), PERK (green), and ATF6 (red), after normalization to their maximally obtained value during the studies time period. Black squares indicate the moment at which sensor activity is half-maximal.

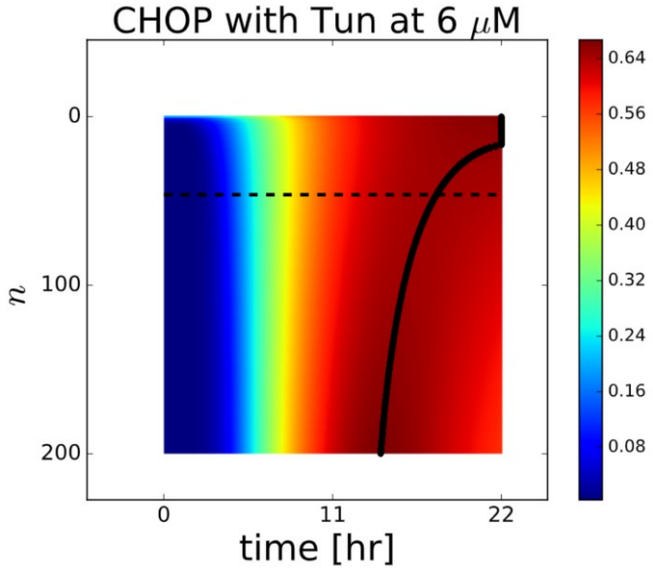

Fig. S6. Effect of non CHOP upon exposure to 6 µM of tunicamycin. Heatmap showing the temporal response of CHOP for a range of $\boldsymbol{n}$ values. The black solid line indicates the time point of maximal CHOP activity within the simulated time period. The black dashed line indicates the best fit value ($\boldsymbol{n}$ = 46.32).

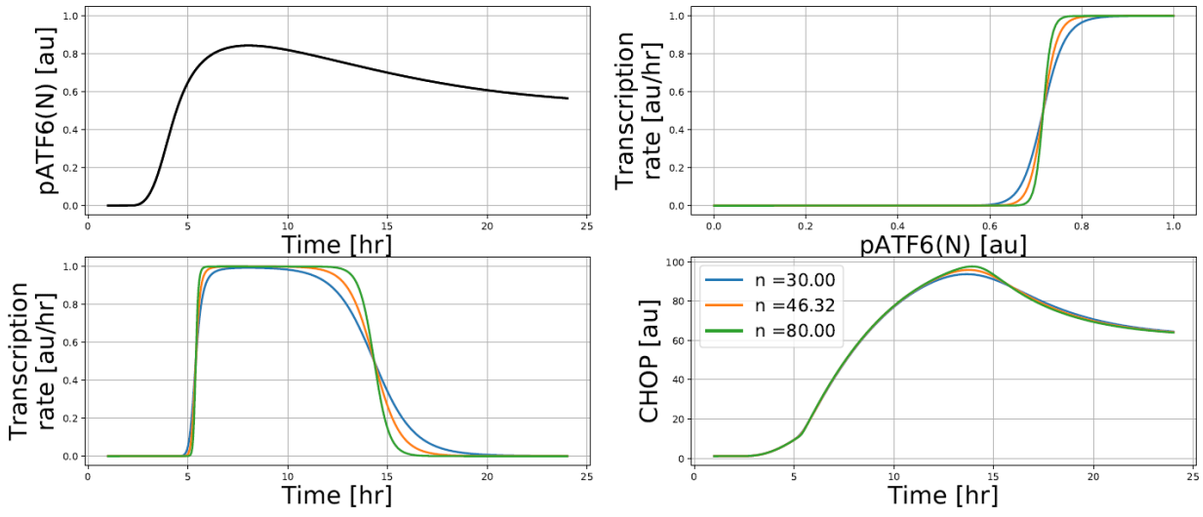

Fig. S7. Sensitivity of the CHOP response to the Hill coefficient describing the relation with pATF6(N). For three values of $\boldsymbol{n}$ (including the estimated value of $\boldsymbol{n}$ = 46.32), we plot the pATF6(N) response over time (upper left panel), the relation between CHOP transcription and pATF6(N) level (upper right panel), the CHOP transcription rate due to pATF6(N) over time (lower left panel) and CHOP dynamics (lower right panel).

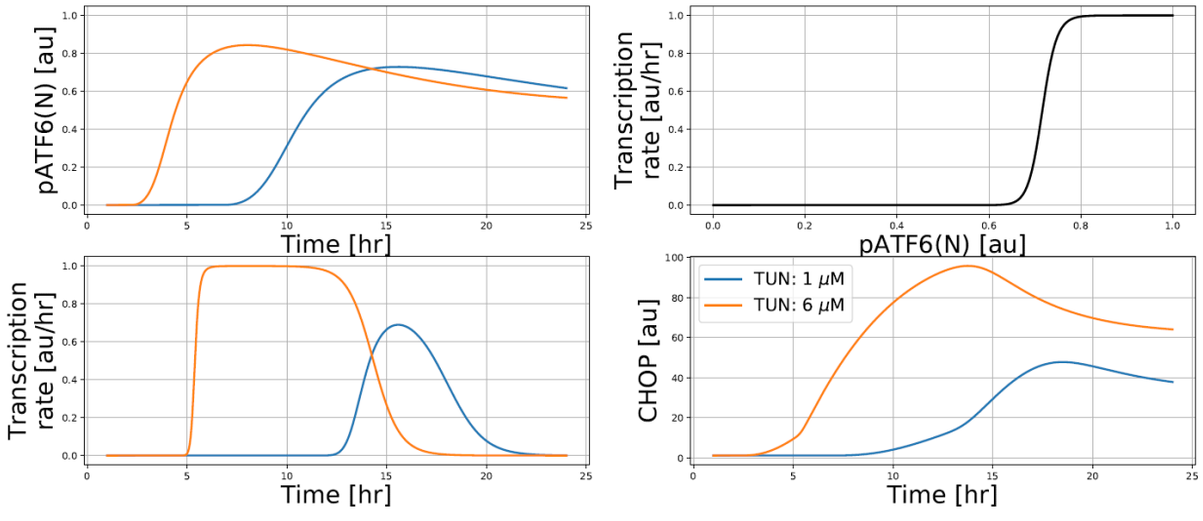

Fig. S8. Details of inner model states with respect to the CHOP response at different tunicamycin concentrations. For two tunicamycin concentrations, we plot the pATF6(N) response over time (upper left panel), the relation between CHOP transcription and pATF6(N) level (upper right panel), the CHOP transcription rate due to pATF6(N) over time (lower left panel) and CHOP dynamics (lower right panel).

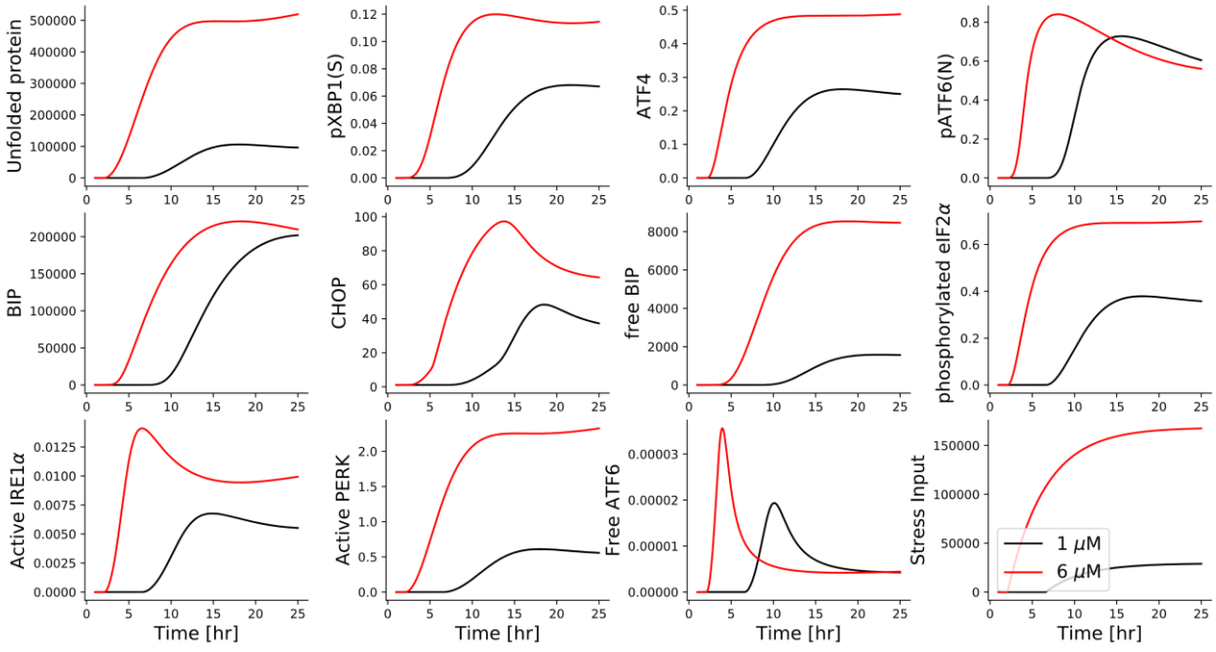

Fig. S9. Simulation of inner model states. Dynamics of modelled UPR network components are shown upon exposure to tunicamycin at 1 µM (black) and 6 µM (red). Note that free ATF6 stands for activated ATF6 sensor, i.e., free uncleaved ATF6. Among the three branches, ATF4 tightly follows the dynamics of eIF2α$\boldsymbol{p}$ and unfolded proteins.

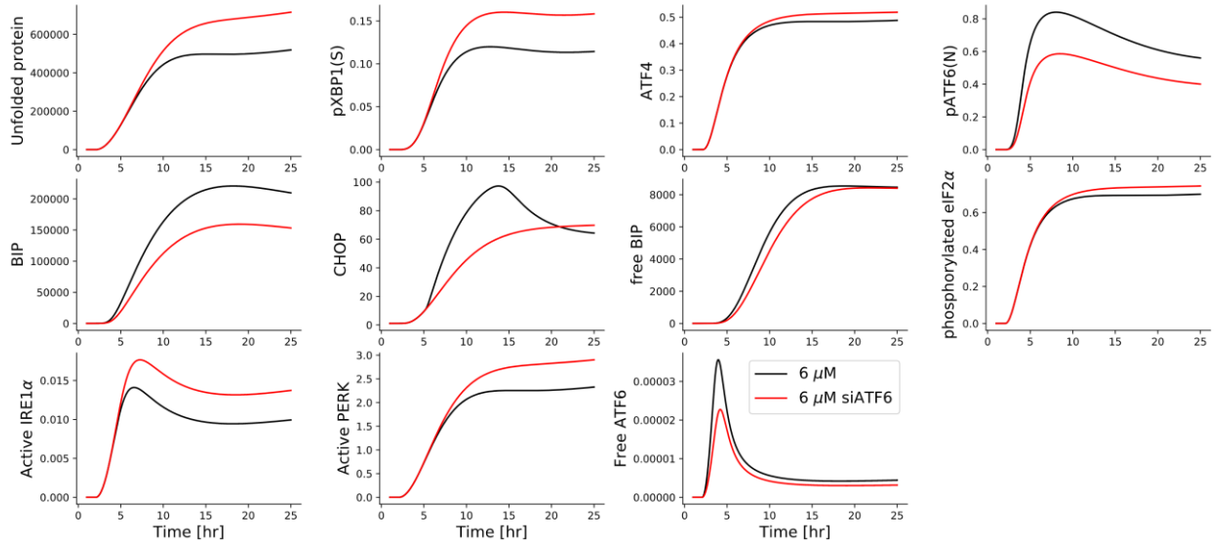

Fig. S10. Simulation of inner model states upon ATF6 knockdown. Dynamics of modelled UPR network components upon exposure to 6 µM tunicamycin, either with (red) or without (black) siATF6 treatment. Note that siATF6 results in lower BiP levels, which reduces the folding capacity. Hence, there are more unfolded proteins, which induces more ATF4 and pXBP1(S), in the long run leading to slightly higher CHOP levels compared to a setting without siATF6.

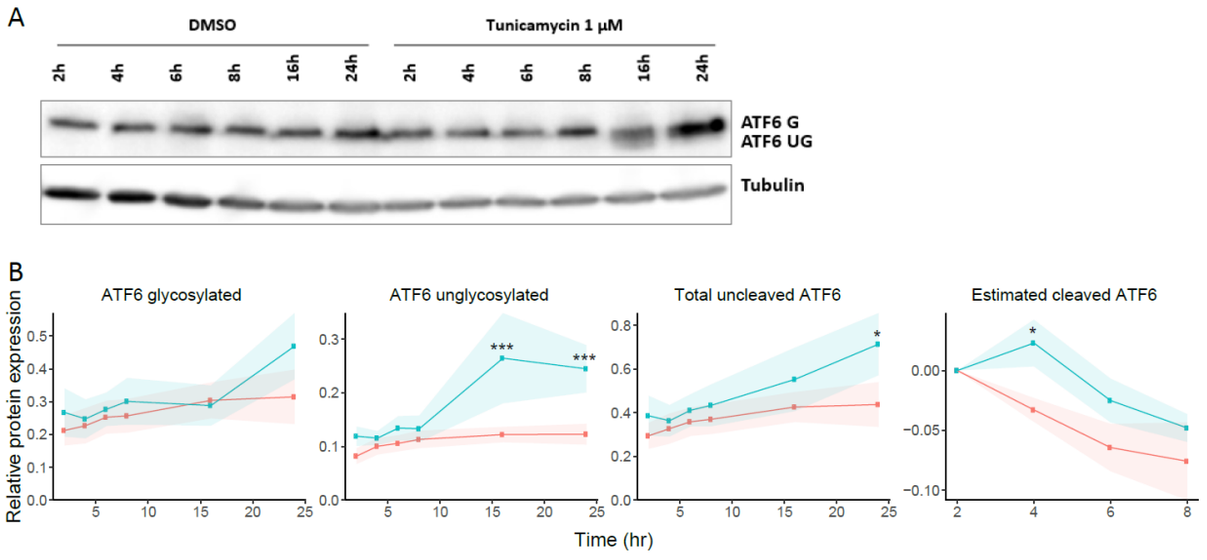

Fig. S11. Quantification of ATF6 forms after treatment of 1 µM tunicamycin. A) Western blot of uncleaved ATF6 (G = glycosylated, UG = unglycosylated) measured in HepG2 WT cells at 2, 4, 6, 8, 16 or 24 hours after exposure to tunicamycin (1 µM).Tubulin protein expression was used as protein loading control. B) Quantified protein expression of ATF6 forms from three biological replicates after protein loading correction using tubulin (symbols and shaded area represent mean ± SD). Cleaved ATF6 was estimated based on the difference between total uncleaved ATF6 at 4, 6, or 8 h and the total ATF6 at 2 h.

Supplemental materials

Analysis of single-cell data

For the analysis of single-cell imaging data, we applied the following steps: First, for each of three biological replicates (each consisting of two pooled technical replicates), we calculated the geometric mean (denoted by I) based on GFP measurements for thousands of cells per image well at all time points and for all treatment conditions. Second, from this analysis we obtained the minimum (denoted by I_{min}) and maximum (denoted by I_{max}) of these geometric means with respect to all conditions and time points (separately for every cell line in every plate). We then applied min-max normalization to obtain the normalized intensity (denoted by I_N) each time point according to:

$$I_N = \frac{I - I_{min}}{I_{max} - I_{min}}. \qquad (23)$$

Third, we interpolated the normalized means to the time points from 1h to 22h as described in the main text (note that some treatment conditions only had data before 23h). Finally, we took the arithmetic mean and standard deviation of the interpolated data for the biological replicates, which we used for further model fitting purposes.

Describing cellular exposure with a two-compartment model

To describe the exposure of cells to the chemical tunicamycin, we introduce a two-compartment

model describing the concentrations of the chemical in the medium ($[C_1]$) and in the cells ($[C_2]$):

$$\begin{cases} \frac{d[C_1]}{dt} = [D]\delta(t) - \tau[C_1], \\ \frac{d[C_2]}{dt} = \tau_1[C_1] - \tau_2[C_2]. \end{cases} \quad (24)$$

Here, τ_1 is the cellular absorption rate from the medium, τ_2 is the degradation rate of the chemical within cells and $[D]$ and $\delta(t)$ are the applied exposure and unit pulse input functions, respectively. To obtain the solution of the above set of ODEs, one can take a convolution: In general, for $g(t) = \int f(\tau)h(t-\tau)d\tau$, $g(t)$ is the output function, $f(t)$ is the input function and $h(t)$ is the transfer function of the linear system, which can be derived by Laplace transformation. In our case, the transfer functions for $[C_1]$ and $[C_2]$ are $exp(-\tau_1 t)H(t)$ and $exp(-\tau_2 t)H(t)$, respectively. For $[C_1](t)$ we then obtain the solution $[C_1](t) = [D]\, exp(-\tau_1 t)H(t)$. Furthermore, for $[C_2](t)$ we obtain:

$$[C_2](t) = [D]\exp(-\tau_2 t)(\exp(-(\tau_2 - \tau_1)t)\,(\tau_2 - \tau_1)^{-1} - (\tau_2 - \tau_1)^{-1}). \quad (25)$$

This simplifies to:

$$[C_2](t) = (\tau_2 - \tau_1)^{-1}\tau_1[D](\exp(-\tau_1 t) - \exp(-\tau_2 t)). \quad (26)$$

To avoid structural non-identifiability issues, we absorb the term $\tau_1(\tau_2 - \tau_1)^{-1}$ into the parameter e_s that scales the stressor (see Eq. (17) in main text), leaving us with:

$$[C_2](t) = [D](\exp(-\tau_1 t) - \exp(-\tau_2 t))H(t). \quad (27)$$

Activation of the three UPR sensors

Our calibrated model can be used to provide insight into the activation speed of the three UPR branches. We therefore quantified the moment at which the active forms of the sensors (active IRE1α, active PERK, and free ATF6) reach their half-maximal value, taking 1 µM of tunicamycin as a representative case (Supplementary Fig. 5).

Effect of Hill coefficient on CHOP transcription

Because the estimated value of the Hill coefficient in the relation between $A_{6,hill}$ and A_6 (Eq. (15) in main text) is very high (n = 46.32), this implies a switch-like response of CHOP transcription with increasing pATF6(N), questioning the suitability of a lower n value. In the model, the sigmoid dependency of CHOP expression on pATF6(N) levels is complemented by linear dependencies on XBP1 (with parameter α_3) and on ATF4 (with parameter α_4) (Eq. (14) in main text). In order to understand the effect of the Hill exponent n on CHOP regulation, we varied n over a wide range (from 0 to 200) while keeping the other model parameters the same and plotted the predicted CHOP response in a two-dimensional heat-map with time on the horizontal axis and n on the vertical axis (Supplementary Fig. 6). This analysis shows that an increase of the exponent beyond the calibrated value (n = 46.32) still has a clearly noticeable effect on the dynamics of CHOP. Consistent with sensitivity of the CHOP response to n, high values of n lead to a more pronounced peak in CHOP levels and an even more step-like response of CHOP transcription with pATF6(N)

concentration and with time compared to low values of n (Supplementary Figs. 7 and 8). As a side note, because CHOP in our model does not provide feedback to any of the other state variables, the Hill coefficient n will not affect the pATF6(N) concentration itself. Thus, this analysis shows that the value of the Hill exponent is important in determining the CHOP dynamics, especially around the time of its peak.

Contribution of pXBP1(S) and ATF4 to CHOP production

According to the model calibration, the coefficients describing pXBP1(S)-mediated and ATF4-mediated CHOP transcription respectively are α_3) = 31.77 (pXBP1(S)), and α_4 = 27.64 (ATF4), suggesting approximately equal contribution of these two TFs. However, besides these coefficients, the concentrations of ATF4 and pXBP1(S) themselves also have an important role in the contribution of the TFs to CHOP transcription. Because the amount of pXBP1(S) is much lower than ATF4 (Supplementary Fig. 9), this concentration effect dominates when one considers the product terms $\alpha_3 X$, $\alpha_4 A$ and $\alpha_6 A_{6,h}$ and the pXBP1(s) contribution to CHOP transcription is small (Fig. 4B-D).

Choice of parameter ranges

During model calibration, we did not restrict the allowed parameter ranges taking full biophysical details into consideration because the units of the normalized intensities in our imaging data were arbitrary, precluding determination of the unit of concentrations. Rather, we required all parameters (besides s_s) to be positive and based our choices of parameter ranges on trial simulations with Trusina et al.'s previously published model parameterization[203]. The parameter ranges considered and the units of parameters are provided in Table 1. Note that the high values for some of the Michaelis-Menten constants are due to the high levels of unfolded proteins in our simulations (for which we have no measurements) and should be interpreted in a relative rather than absolute manner.

Covariance matrix of estimates

In order to study the uncertainty of the estimated parameter values, we utilize the Jacobian matrix ($\mathbf{J}$) to approximate the Hessian matrix $\mathbf{H}$:

$$\mathbf{H} = \mathbf{J}^T \mathbf{J} S(\theta). \quad (28)$$

Here, the mean squared error $S(\theta)$ (i.e., the residual sum of squares divided by the number of degrees of freedom) is given by

$$S(\theta) = \frac{\mathbf{R}^T \mathbf{R}}{n_D - n_\theta}, \quad (29)$$

where R is the vector containing the residuals between model prediction and data, n_D = 440 denotes the number of data points and n_θ = 47 denotes the number of free parameters in our model with ATF6 branch. The squares of the standard errors of the estimates are the diagonal items in the co-variance matrix, expressed as the inverse matrix $\mathbf{H}^{-1}$. The standard errors of all

parameters are presented in Supplementary Fig. 3. We multiplied these values by 1.98 to obtain confidence intervals (CIs)[217] (shown together with the estimates in Table 1). Note that although the amount of experimental measurements is large compared to the number of parameters in our case, the CI for some parameters may be underestimated by the Hessian-based estimate.

Sensitivity analysis

We performed a sensitivity analysis to quantify the importance of the model parameters around our maximum likelihood estimate. Because CHOP is an important determinant in downstream cell fate and most of the signalling parameters are expected to indirectly affect the activity of CHOP especially around the peak, we focus on CHOP activity at 16 hours after treatment with 6 µM of tunicamycin. Thus, we performed a local sensitivity analysis around the maximal likelihood estimate $\hat{\theta}$ for the model with ATF6.

In the sensitivity analysis, we omitted parameters that should have no impact on CHOP in conditions of 6 µM tunicamycin treatment. Specifically, these are the effective tunicamycin concentrations of 2, 4, 12 µM, i.e. E_2, E_4 and E_{12}. Moreover, we omitted the three pairs of the scaling coefficients (e_{XBP1}, e_{ATF4}, and e_{BIP}) and offsets (s_{XBP1}, s_{ATF4}, and s_{BIP}) for the non-CHOP reporter cell lines. We varied each of the remaining parameters by both increasing and decreasing them by a small value (δ_θ) from its optimum. Subsequently, we quantified the sensitivity using the following equation:

$$\frac{\Delta C}{\Delta \theta_i} = \frac{C(\theta+\delta_\theta)-C(\theta-\delta_\theta)}{2\delta_\theta}, \qquad (30)$$

where for different parameters, we used different δ_θ. For τ_2 and r_U, we chose a value just above the machine precision (3e-16); for other parameters, we set δ_θ to 1e-6×$\hat{\theta}$, i.e., based on the maximum likelihood estimate. As the sensitivity can be negative or positive and the absolute value of sensitivities has a broad range, we plotted the log10 of the absolute values of the calculated sensitivities, with the colour indicating positive or negative sensitivity (Supplementary Fig. 4). The most straight forward parameters having a positive impact on CHOP are the scaling parameters e_C and s_C, and parameters representing direct inputs like E_6 and e_s. As expected, parameters with a negative impact typically arise from those promoting degradation of CHOP, like r_C.

Table S1. Model parameters, their units, their estimated values (±95% confidence interval) and the boundary values used during the estimation procedure. For the rationale behind the choice of boundary values see the section on parameter ranges in the Supplementary text.

Parameter	unit	description	estimated θ_1	estimated θ_2 ± 95% CI	lower boundary	upper boundary
E_t	-	general translation rate (from mRNA to unfolded protein)	2.21e+00	2.00e+00 ± 8.45e-08	1.0	200.0
E_2	au	effective exposure at 2 μM	1.16e+00	1.22e+00 ± 1.80-e07	1.0	20.0
E_4	au	effective exposure at 4 μM	1.55e+00	1.67e+00± 3.10e-04	1.0	20.0
E_6	au	effective exposure at 6 μM	1.88e+00	2.07e+00 ± 7.45e-08	1.0	20.0
E_{12}	au	effective exposure at 12 μM	2.11e+00	2.48e+00± 3.62e-08	1.0	20.0
δ	au/hr	BiP-mediated folding rate	1.84e+01	1.96e+01 ± 3.70e-08	0.10	200.0
P_t	-	total amount of PERK	1.87e+01	8.36e+00 ± 3.12e-08	1.0	2.0e5
K_{BU}	au	Michaelis-Menten constant for dissociation of BiP and unfolded proteins	1.24e+07	1.24e+07 ± 3.07e-08	1e3	1e10
β_1	au/hr	IRE1α-dependent formation rate of XBP1	4.90e+00	2.75e+00 ± 3.90e-08	1.0e-8	2.0e8
β_2	au/hr	PERK-dependent ATF4 formation rate	1.52e+01	4.35e+00 ± 2.67e-08	1.0e-8	2.0e8
β_3	au/hr	ATF6-dependent ATF6f formation rate	-	1.18e+04 ± 3.08e-08	1.0e-8	2.0e8
K_{IU}	au	Michaelis-Menten constant for dissociation of IRE1α and unfolded proteins	9.57e+06	9.56e+06 ± 2.75e-08	1e1	1e10
K_{PU}	au	Michaelis-Menten constant for dissociation of PERK and unfolded proteins	1.35e+06	1.35e+06 ± 3.42e-08	1e1	1e10
K_{AU}	au	Michaelis-Menten constant for dissociation of ATF6 and unfolded proteins	-	1.08e+09 ± 2.71e-08	1e1	1e10
r_U	1/hr	degradation rate of unfolded proteins	4.07e-02	2.02e-08 ± 4.95e-08	1.0e-8	2.0e3
r_X	1/hr	degradation rate of XBP1	5.16e-01	2.34e-01± 3.29e-08	1.0e-8	2.0e3
r_{A_4}	1/hr	degradation rate of ATF4	4.95e+00	6.26e+00± 3.68e-08	1.0e-8	2.0e3
r_B	1/hr	degradation rate of BiP	2.58e-01	1.52e-01± 3.14e-08	1.0e-8	2.0e3
r_C	1/hr	degradation rate of CHOP	9.95e-01	2.83e-0± 3.92e-08	1.0e-8	2.0e3
r_{A_6}	1/hr	degradation rate of ATF6f	-	1.05e-0± 4.96e-08	1.0e-8	2.0e3
γ_1	au/hr	basal BiP transcription rate	1.13e+00	6.25e-01± 3.26e-08	0	2e2
γ_2	au/hr	basal CHOP transcription rate	3.29e-01	2.96e-01± 3.68e-08	0	2e2
α_1	1/hr	XBP1-mediated BiP transcription rate	8.14e+04	8.14e+0± 2.68e-08	0	1e6
α_2	1/hr	ATF4-mediated BiP transcription rate	2.97e+03	2.60e+02± 4.43e-08	0	1e6
α_3	1/hr	XBP1-mediated CHOP transcription rate	3.15e+02	3.17e+01± 3.26e-08	0	1e6
α_4	1/hr	ATF4-mediated CHOP transcription rate	2.86e+02	2.88e+01± 3.94e-08	0	1e6
α_5	1/hr	ATF6f-mediated BiP transcription rate	-	5.09e+04± 4.08e-08	0	1e6
α_6	au/hr	ATF6f-mediated CHOP transcription rate	-	1.39e+01± 3.87e-08	0	1e6
K_{BP}	au	Michaelis-Menten constant for dissociation of BiP and PERK	5.03e+07	5.03e+07± 1.56e-02	0	1e9
K_{BI}	au	Michaelis-Menten constant for dissociation of BiP and IRE1α	8.81e+02	1.92e+03± 3.27e-08	0	1e9
K_{BA}	au	Michaelis-Menten constant for dissociation of BiP and ATF6	-	7.81e+01± 3.45e-08	0	1e9
b_0	au/hr	basal production rate of ATF4	2.91e-06	2.41e-06± 4.00e-08	0	2e2
e_s	au/hr	factor scaling the effective intra-cellular concentration to unfolded proteins	1.31e+05	1.31e+05± 6.88e-08	1e-3	2e7
s_s	au/hr	net production rate of unfolded proteins independent of translation attenuation and exposure	-1.870	-2.00 ± 8.01e-08	-20.0	2e3
τ_1	1/hr	time constant describing initial increase in stressor	2.47e-01	2.26e-01± 3.87e-08	1e-15	5.0
τ_2	1/hr	time constant describing stressor decay	8.90e-03	8.45e-15± 1.01e-23	1e-15	5.0
θ_{th}	au	threshold for stressor levels that activate signaling	7.37e-01	7.75e-01 ± 5.29e-08	0.0	1.0
K_{A2C}	au	ATF6f level at which ATF6f-dependent CHOP transcription is half-maximal	-	7.17e-01± 3.32e-08	1e-8	1e4
n	-	cooperativity in ATF6f-dependent CHOP transcription Hill kinetics	-	4.63e+01± 2.86e-08	1e-2	1.0e2
e_{XBP1}	au	GFP scaling factor for XBP1 reporters	5.64	6.60± 2.94e-02	1.0e-7	1.0e2
e_{ATF4}	au	GFP scaling factor for ATF4 reporters	2.28e-01	1.23e+00± 2.58e-02	1.0e-7	1.0e2
e_{BIP}	au	GFP scaling factor for BiP reporters	1.13e-05	3.68e-06± 4.12e-02	1.0e-7	1.0e2
e_{CHOP}	au	GFP scaling factor for CHOP reporters	1.45e-02	7.75e-03± 3.60e-02	1.0e-7	1.0e2
s_{XBP1}	au	GFP offset for XBP1 reporters	5.20e-04	5.65e-04 ± 3.55e-01	-1.0e2	1.0e2
s_{ATF4}	au	GFP offset for ATF4 reporters	3.54e-02	4.19e-02± 1.90e-01	-1.0e2	1.0e2
s_{BIP}	au	GFP offset for BiP reporters	1.09e-01	7.81e-02± 2.61e-01	-1.0e2	1.0e2
s_{CHOP}	au	GFP offset for CHOP reporters	-7.10e-04	-3.89e-03 ± 2.26e-01	-1.0e2	1.0e2

Chapter 6

Discovery of EMX1 as master regulator of the unfolded protein response and drug sensitivity of liver cells.

M. Niemeijer, N. Tahir, P. Kartal, M. Vlasveld, G. Callegaro, P. Bouwman and B. van de Water
Discovery of EMX1 as master regulator of the unfolded protein response and drug sensitivity of liver cells.
Ready for submission. 2022

Abstract

The unfolded protein response (UPR) aims to restore homeostasis after endoplasmic reticulum (ER) stress. Chronic ER stress may lead to apoptosis mediated by enhanced CHOP induction. To improve mechanistic understanding of the signalling programs that control UPR, we identified novel key regulators of CHOP by applying an imaging-based arrayed RNAi screen of the druggable genome targeting 3,457 genes in HepG2 CHOP-GFP reporter cells. A network of 74 genes impacted on UPR-mediated CHOP-GFP induction. Depletion of the transcription factor EMX1 consistently reduced UPR response by various ER stress inducers. Transcriptome analysis in HepG2 and primary human hepatocytes revealed EMX1 as an essential regulator of multiple ER stress signalling pathways. During treatment of hepatocellular carcinoma (HCC) with clinical relevant targeted therapeutics, regorafenib and sorafenib, silencing of EMX1 significantly decreased CHOP levels and increased survival. Our RNAi screen uncovered the signalling landscape that controls the ER stress response aiding to the understanding of development of hepatotoxicity and HCC treatments.

Keywords: Endoplasmic reticulum stress, drug-induced liver injury, RNAi screening

Introduction

Under homeostatic conditions, the endoplasmic reticulum (ER) is responsible for protein synthesis, correct protein folding, modifications and maturation by various chaperones and foldases. Upon correct folding, proteins are able to exit the ER via a secretory pathway, while incorrect folded proteins are kept inside the ER and flagged for proteasomal degradation[175]. This tightly balanced regulatory system can however be disrupted by for instance exposure to certain drugs or certain pathologies provoking the accumulation of misfolded proteins in the ER, which leads to ER stress. In response to ER stress, the unfolded protein response (UPR) is induced, aiming to restore balance by increasing folding capacity through upregulation of chaperones and ER biogenesis, temporary blockage of the translational machinery and increased removal of misfolded proteins[173,176].

The UPR consists is controlled by three sensors, namely Eukaryotic Translation Initiation Factor 2 Alpha Kinase 3 (PERK/*EIF2AK3*), Endoplasmic Reticulum To Nucleus Signaling 1 (IRE1α/*ERN1*) and Activating Transcription Factor 6 (ATF6)[229]. In unstressed conditions, these sensors are kept in an inactive state through binding with the chaperone protein Heat Shock Protein Family A (Hsp70) Member 5 (BiP/*HSPA5*)[230,231]. Upon ER stress, BiP releases its targets, leading to UPR sensor activation followed by temporary blockage of the translational machinery, removal of misfolded proteins, improving folding capacity and induction of genes important for restoration of homeostasis within the ER[231].

During chronic severe ER stress conditions, activation of the UPR signalling network might not be able to sufficiently restore homeostasis within the ER. Consequently, apoptotic pathways may be

activated leading to cellular injury, and subsequently at multicellular level to tissue injury[231]. One of these pathways is mediated by the transcription factor DNA Damage Inducible Transcript 3 (CHOP/*DDIT3*) which is induced by ATF4 and ATF6 during ER stress[232]. CHOP downregulates anti-apoptotic genes, upregulates pro-apoptotic genes, increases translation and increases ROS levels through upregulation of Endoplasmic Reticulum Oxidoreductase 1 Alpha (ERO1α)[191]. CHOP deficiency resulted in less hepatocellular apoptosis after ethanol feeding in mice[227]. Given these pro-apoptotic features, CHOP potentially plays a key role in the switch towards adverse signalling during severe or prolonged ER stress leading to injury.

Prolonged ER stress signalling in the liver can be provoked by both chemical or pathological insults, such as by drug exposure[21], by the development of certain pathologies (e.g. non-alcoholic fatty liver disease, alpha1-antitrypsin deficiency)[233,234] or during carcinogenesis[235]. Drugs known to induce liver injury in patients, such as nefazodone and diclofenac, have been shown to induce ER stress which contributes to onset of cell death[20]. However, it is not exactly clear how this ER stress induction may lead to liver injury. The UPR is also involved in the development of hepatocarcinogenesis[236,237]. Cancer cells may misuse the adaptive UPR to cope with increased protein load due to rapid cell growth or oxygen and nutrient deprivation[235,238]. By activating the UPR excessively, the initiation of pro-apoptotic signalling can be escaped and proliferation enhanced promoting a more aggressive phenotype[237,239,240].

Our objective was to obtain increased insight in signalling components that control the UPR in liver pathogenesis. We performed an imaging-based high throughput arrayed RNAi screen of the druggable genome, targeting 3,457 genes, in HCC HepG2 CHOP-GFP reporter cells. We identified the transcription factor EMX1 as a novel key regulator of the CHOP response under various ER stress conditions. Transcriptome analysis revealed its influence on multiple related ER signalling pathways in both HepG2 cells as well as in primary human hepatocytes. EMX1 was required for the activation of CHOP-mediated apoptosis caused by kinase inhibitors that target HCC in the clinic.

Materials and Methods

Cell culture

Human hepatocellular carcinoma HepG2 cells were purchased at American Type Culture Collection (ATCC, Germany) and cultured in a 5% CO_2 humidified incubator at 37°C using Dulbecco's Modified Eagle Medium (DMEM) supplemented with 10% (v/v) fetal bovine serum (FBS), 25 U/mL penicillin and 25 µg/mL streptomycin. Cells were used until passage 20. LIVERPOOL cryopreserved plateable primary human hepatocytes (PHHs, lot YFA) from 10 individuals with mixed gender were purchased at BioIVT (NY, USA). After thawing PHHs at 37°C in warm water bath, cells were resuspended in OptiThaw Hepatocyte Media (SEKISUI XenoTech, KS, USA) and spinned down for 10 min at 100xg at RT. Cells were seeded at a density of 260.000 cells per well in 24 well Collagen I Cellware BioCoat plates (Corning, Wiesbaden, Germany) in

RPMI 1640 plating medium supplemented with 2 % (v/v) FBS, 1 µM insulin, 2 mM L-glutamine, 0.1 mM hydrocortisone-21-hemisuccinaat, 50 U/mL penicillin and 50 µg/mL streptomycin. For sandwich culture after 18 hours, medium was replaced by 0.25 mg/mL Matrigel (growth factor reduced, Corning) in RPMI 1640 maintenance medium without FBS. Medium was refreshed daily using maintenance medium.

siRNA transfections

To transiently silence specific genes, HepG2 cells were transfected with siGENOME siRNAs from Dharmacon GE Healthcare (Eindhoven, The Netherlands) in combination with INTERFERin from PolyPlus (Leusden, The Netherlands). For the primary siRNA screen, the following siGENOME siRNA libraries from Dharmacon were used: transcription factors, protein kinases, ubiquitinases, deubiquitinases and phosphatases (see list of genes Suppl. Excel Table S4). Selection of siRNAs targeting the spliceosome were literature-based manually defined. After complex formation of siRNA with INTEFERin for 20 min in serum-free DMEM, HepG2 cells were added to each well containing siRNA mix leading to a final concentration of 50 nM siRNA and 0.3% INTERFERin. For siRNA transfections in PHHs, Lipofectamine2000 (Invitrogen) was mixed with siGENOME siRNAs in serum-free RPMI supplemented medium for 10 min to allow complex formation. Hereafter, PHHs resuspended in plating medium were plated in a 24 well BioCoat plate containing siRNA-Lipofectamine2000 mix leading to a final concentration of 40 µM siRNA and 2.4% (v/v) Lipofectamine2000. The effect of siRNA-mediated knockdown was evaluated after 72 hours.

Compound exposures & viability

To evaluate ER stress induction, cells were exposed to various ER stress inducers, namely tunicamycin, thapsigargin, nefazodone, omeprazole, diclofenac, troglitazone, regorafenib and sorafenib (Sigma, Zwijndrecht, The Netherlands). Compounds were dissolved in dimethylsulfoxide (DMSO) from BioSolve (Valkenswaard, The Netherlands) and stored at -20°C. The end concentration of DMSO was not higher than 0.2 % (v/v). To assess viability upon compound exposure, ATP-lite luminescence kit from PerkinElmer was used according to supplier's instructions to measure ATP content.

Confocal microscopy

The induction dynamics of ER stress specific genes was monitored by combining HepG2 BAC-GFP ER stress reporters (CHOP, BIP, ATF4 and XBP1-GFP) with confocal imaging. These BAC-GFP reporters were established as described previously using a BAC recombineering approach[27,28]. HepG2 GFP reporter cells were plated in 96 well µclear plates from Greiner Bio-One (Alphen aan den Rijn, The Netherlands). Prior to imaging, cells were stained with 100 ng/mL $Hoechst_{33342}$ to visualize nuclei, and with 0.05% AnnexinV-Alexa633 / 100 nM propidium iodide (PI) for cell death evaluation. GFP induction was evaluated using live cell automated confocal imaging with a Nikon TiE2000 equipped with an automated xy-stage, Perfect Focus System and 408, 488, 561 and 647

nm lasers (Nikon, Amsterdam, The Netherlands). During imaging, cells were kept at 37°C and 5% CO_2 humidified conditions.

Imaging data analysis

GFP signal intensity, either in the nuclei or cytoplasm, was quantified using CellProfiler 2.1.1 (Broad Institute, Cambridge, USA) using an in-house developed module using a watershed masked algorithm for nuclear segmentation. To extract data from the derived HDF5 files, an in-house developed Rscript 'H5CellProfiler' was used. Further confocal imaging data analysis was done using Rstudio (Boston, USA) and R 3.2.3 and the following R packages, ggplot2 [131], data.table [132], pheatmap [133], reshape [137], dplyr [135], tidyr. For the primary and validation siRNA screen, data was represented as the mean Z-score based on two biological replicates. Hits were selected if both replicates showed same direction of Z-score, if mean Z-score was lower than -2 or higher than 1.5, if the mean fold change was lower than 0.67 or higher than 1.25 and more than 90 cells per image to exclude knockdowns of essential genes. For the validation siRNA screen, more than 2 of 4 single siRNAs should meet the same criteria. For gene set enrichment analysis based on the Z-scores of all screened siRNAs in the primary screen in which validated hits from the validation screen were flagged, the R package HTSanalyzeR [241] was used. All other confocal microscopy data was shown as the mean ± the standard deviation based on three biological replicates. A Student's t-test with Benjamini-Hochberg correction was used to determine significant differences in GFP levels at certain timepoints after exposure. For 24 hour live cell imaging data, each replicate was resampled to obtain identical time points and were fitted using the b-spline method with 10 degrees of freedom and 3rd degree polynomials from splines R package. Significant differences between CHOP-GFP induction time dynamics from 0 to 24 hours after exposure was determined using a one-way ANOVA model and bootstrapping n = 200[242]. The following p-value annotation was used, *p < 0.05, **p < 0.01, ***p < 0.001.

Quantitative PCR analysis

Total RNA was isolated using the NucleoSpin RNA kit from Macherey-Nagel (Düren, Germany), followed by cDNA synthesis using RevertAid H Minus First Strand cDNA Synthesis Kit from ThermoFisher Scientific and oligoDT primers. For quantitative PCR analysis, 1 µL cDNA was mixed with 5 µL PowerUp SYBR Green master mix (Thermo Fisher) and 4 µL 1 µM forward and reverse primers (Sigma) in a MicroAmp Optical 384-well reaction plate from Applied BioSystems (MA, USA) and sealed with a MicroAmp Optocal Adhesive film. qPCR was done using a QuantStudio 6 Flex Real-Time PCR System from Applied Biosystems. Details of used primers can be found in Suppl. Table S5. mRNA expression levels were normalized to housekeeping gene TATA-box binding protein (TBP).

TempO-seq transcriptomics

Analysis of the transcriptome was done using targeted TempO-seq technology (BioSpyder Technologies, Inc., Carlsbad, CA, USA) in combination with the S1500+ gene set[164] covering all

known canonical pathways while also sufficiently reflecting stress response pathways. Prior to analysis, cells were washed with 1x PBS, lysed for 15 min at RT with 1x BNN lysis buffer from BioSpyder (Carlsbad, USA) and stored at -80°C until shipment to BioSpyder for TempO-seq analysis[30]. Reads were aligned by BioSpyder using the TempO-seqR package and normalized using the DESeq2 R package[165]. A threshold of lower than 0.05 was used for the adjusted p-value to define differentially expressed genes (DEGs). Pathway analysis was done using these DEGs with g:Profiler[243] in combination with GO biological processes[244] and Reactome biological pathways[245] as data source. Pathways were significantly enriched when adjusted p-value using Benjamini-Hochberg correction was lower than 0.05. Cytoscape[246] was used for pathway enrichment visualization in combination with EnrichmentMap[247], AutoAnnotate and WordCloud[248].

Western Blot

To study protein expression levels using western blot, cells were washed with 1x PBS and lysed by adding 1x sample buffer supplemented with 10% (v/v) β-mercaptoethanol. Samples were heat-denatured by boiling at 95°C for 10 min. Protein separation was done by running on SDS-page gels at 120 volt and transfer to polyvinylidene difluoride (PVDF) membranes at 100 volt for 2 h. Membranes were blocked using 5% (w/v) ELK and stained with primary and secondary HRP or Cy5 conjugated antibodies diluted in 1% (w/v) bovine serum albumin (BSA) in $Tween20_{0.05\%}$-tris-buffered saline (TBS). Used primary antibodies were EMX1 from Santa Cruz and tubulin from Sigma. For visualization of HRP conjugated antibodies, ECL western blotting substrate from Thermo Fisher (Bleiswijk, The Netherlands) was used and captured with the Amersham Imager 600 from GE Healthcare (Eindhoven, The Netherlands). Quantification was done using ImageJ version 1.51h (National Institutes of Health, USA). Tubulin protein expression was used for normalization.

Analysis of genetic alterations

To evaluate genetic alterations of EMX1 in cancer tissues, the software cBioPortal for Cancer Genomics[249,250] was used in combination with TCGA PanCancer datasets[251]. The OncoPrint, Mutations and Survival tabs were used for visualization of genetic alterations and its influence on overall survival.

Results

Arrayed siRNA screen identifies novel regulators of CHOP induction during ER stress

To screen for modifiers of ER stress signalling, we made use of previously established HepG2 BAC-GFP reporter cell lines for CHOP, ATF4, XBP1 and BiP[252,253]. Previous transcriptomics analysis demonstrated the suitability of these different UPR HepG2 BAC-GFP reporters to faithfully reflect the UPR response[232,252,253]. By combining these reporters with high throughput live cell confocal microscopy the temporal dynamics of the UPR response at individual cell level can be determined. We first evaluated if the HepG2 CHOP-GFP reporter system allows for the identification of regulators of CHOP and ER stress signalling by an siRNA knockdown screen.

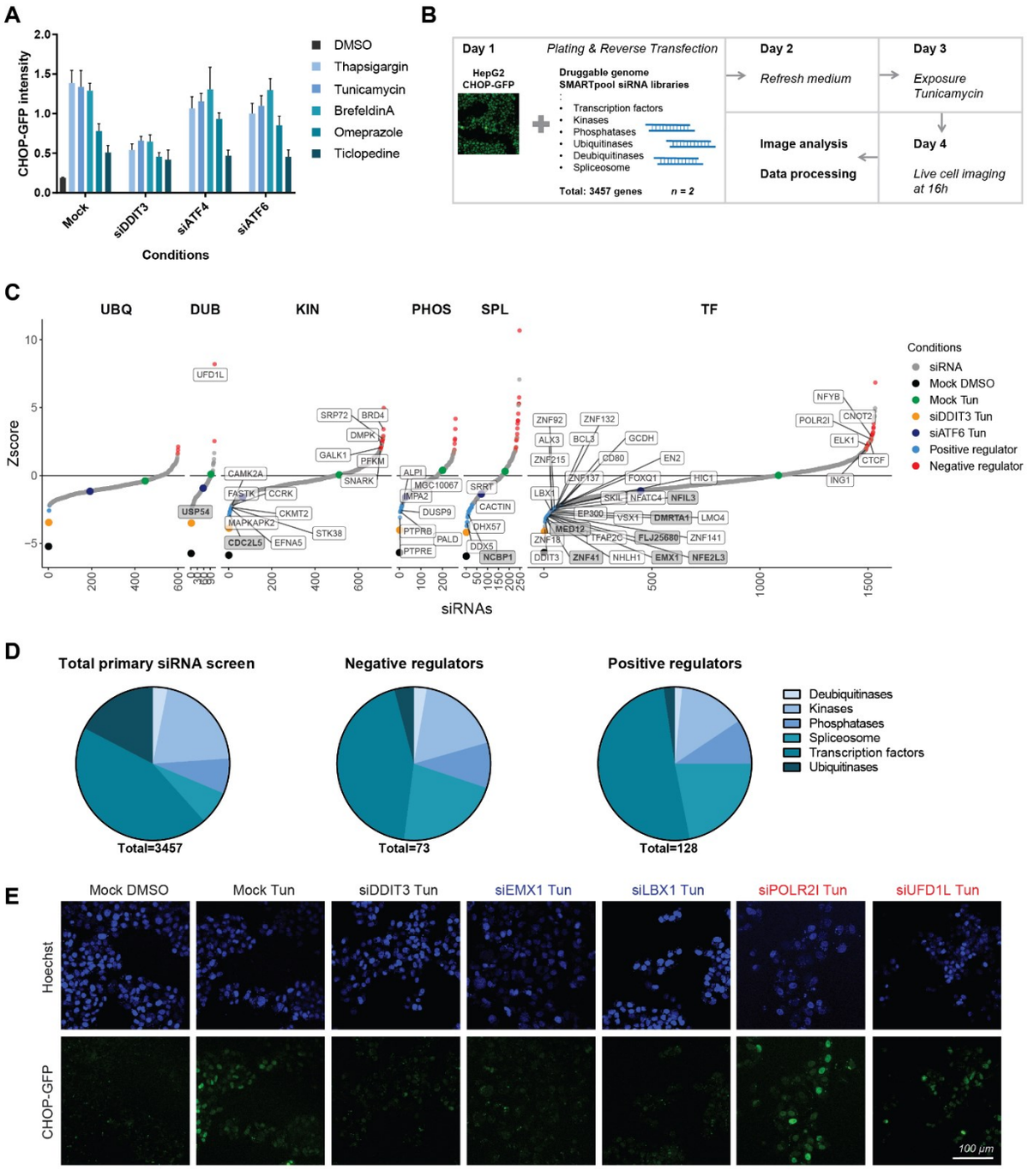

Fig. 1. High-throughput primary RNAi screening for the identification of CHOP regulators during ER stress. A) CHOP-GFP expression in HepG2 cells upon siRNA-mediated knockdown of UPR components and 24 h exposure to ER stress inducers using confocal microscopy. B) Experimental setup of primary RNAi screen for the identification of CHOP regulators during ER stress. C) Z-score based on the CHOP-GFP intensity upon exposure to tunicamycin for 16 h and siRNA-mediated knockdown of individual genes (3457 genes in total) compared to no siRNA control (Mock). Genes are separated based on protein class. Data based on two biological replicates. D) Distribution of total screened genes (left), identified negative (middle) or positive (right) CHOP regulators among different protein classes. E) Confocal images using 20x objective of HepG2 CHOP-GFP cells stained with Hoechst for nuclei visualization upon exposure to tunicamycin for 16 h and siRNA-mediated knockdown.

CHOP/*DDIT3* expression was silenced and CHOP-GFP reporter activity was evaluated by confocal microscopy after exposure to various ER stress inducers (Fig. 1A). Thapsigargin, tunicamycin and

brefeldinA showed a strong induction of CHOP-GFP expression, which was reduced 2-fold by CHOP/*DDIT3* knockdown exemplifying reporter activity can be successfully manipulated by siRNA transfection.

Next, we performed an imaging-based siRNA screen of the druggable genome in HepG2 CHOP-GFP cells, targeting in total 3,457 genes: transcription factors, kinases, phosphatases, ubiquitinases, deubiquitinases and spliceosome components. Tunicamycin is the most specific ER stress inducer, inhibiting N-glycosylation leading to accumulation of misfolded glycoproteins inside the ER[254]. We silenced individual genes using SMARTpool siRNAs and evaluated the effect of silencing on CHOP-GFP induction using confocal microscopy after 16 hours of 6 µM tunicamycin exposure (Fig. 1B). We identified 201 genes that significantly altered CHOP induction during tunicamycin-induced ER stress, where 128 genes had an inhibitory effect and 73 genes showed upregulation of CHOP upon knockdown (Fig. 1C-D). Almost half of the identified genes were transcription factors. Interestingly, many spliceosome genes (18% of spliceosome sub-library) were identified as potential CHOP regulators.

To exclude off-target effects of the siRNAs, a secondary screen of the 201 identified hits was performed using 4 individual single siRNAs targeting the same gene. Hits were considered validated if a minimum of 2 single siRNAs showed a significant effect on CHOP induction during tunicamycin-induced ER stress (Fig. 2A and B). Using these criteria, 74 hits were validated consisting: 18 negative regulators including *UFD1L*, *POLR2I*, *UBA3*, *NARG1* and *PFKM*; and 56 positive regulators including *EMX1*, *POU5F2*, *USP54*, *NFE2L3* and *DMRTA1*. Most of these 74 genes were transcription factors such as *EMX1*, *POU5F2*, *NFE2L3* and *DMRTA1*, followed by kinases including *PFKM*, *GALK1*, *BRD4* and *CDC2L5*/*CDK13* and ubiquitinases *UFD1L*, *UBA3* and *USP54* (Fig. 2C-F and Suppl. Excel Table S1). Gene set enrichment analysis (GSEA) on GO biological processes based on Z-scores for all screened siRNAs flagging the validated 74 genes as hits identified general processes such as mRNA processing as well as ER associated processes were identified (Suppl. Table S2).

Impact of candidate CHOP regulators on ER stress signalling by various ER stress inducers

We further explored the consequences of silencing the 74 candidate regulators on the temporal dynamics of CHOP induction. Live confocal imaging was performed during 24 h tunicamycin treatment of the HepG2 CHOP-GFP reporter cells (Fig. 3A-B, Suppl. Excel Table S1 and Suppl. Movies 1). All candidate positive regulators showed a significant downregulation of CHOP upon knockdown over time. Some genes, such as *EMX1* and *LBX1*, showed almost complete inhibition of the temporal induction of CHOP-GFP expression. Silencing of other genes, such as *MAPKAPK2*, *NFATC4* and *TAF8,* showed a delayed response with a small peak at late time points. Most of the genes that upregulate CHOP upon knockdown significantly enhanced and/or sustained CHOP-GFP activation dynamics such as *BRD4, PFKM* and *UFD1L*.

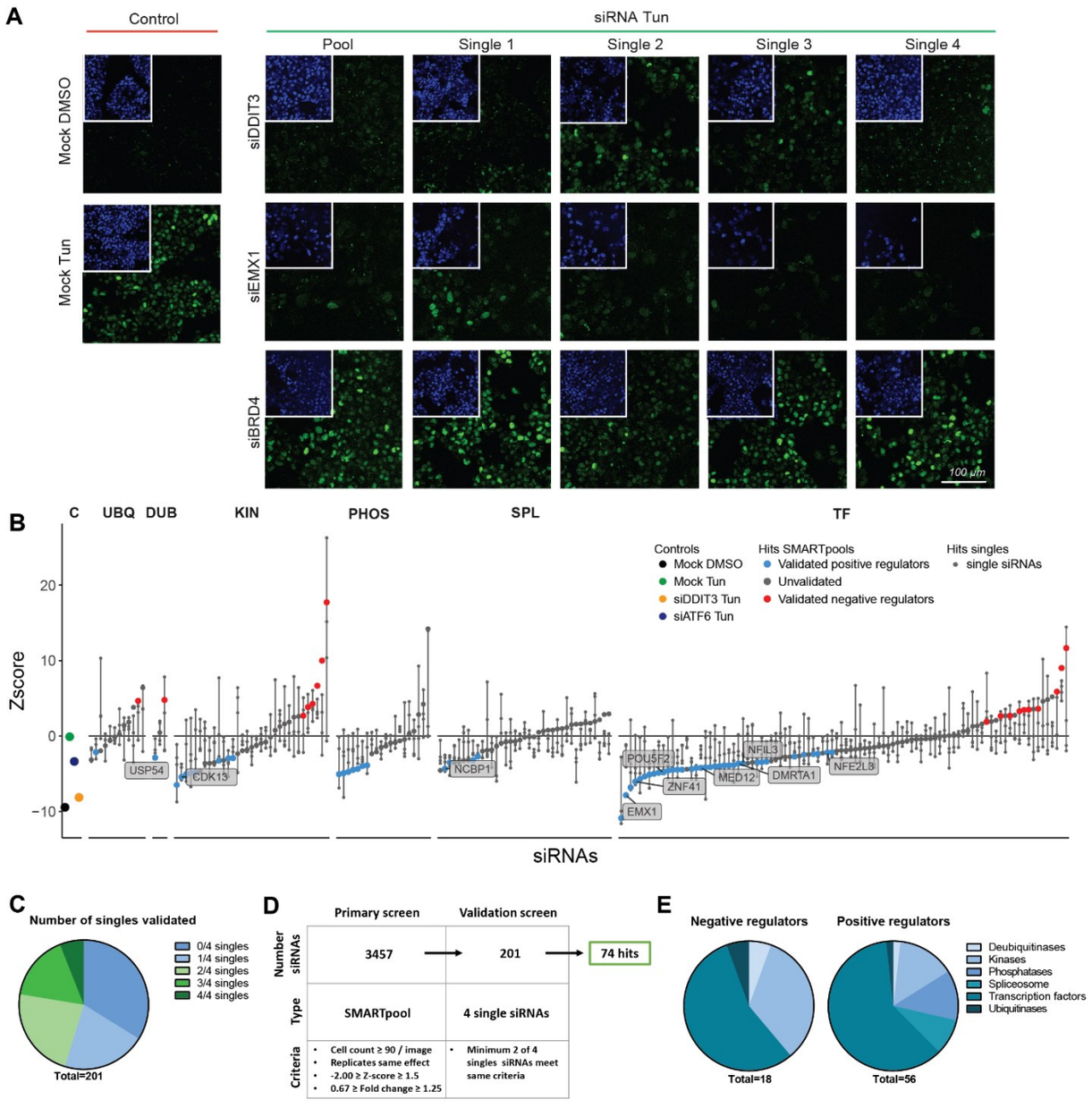

Fig. 2. Secondary RNAi screening for the validation of identified CHOP regulators. A) Confocal images using 20x objective of HepG2 CHOP-GFP cells stained with Hoechst treated with tunicamycin for 16 h after siRNA-mediated knockdown using pool or single siRNAs targeting CHOP/*DDIT3, EMX1*, or *BRD4*. B) Z-score based on the CHOP-GFP intensity in HepG2 cells upon exposure to tunicamycin for 16 h and knockdown using pool or single siRNAs for each identified regulator in primary screen. Data based on two biological replicates. C) Number of single siRNAs validated (having similar effect as the pool of 4 single siRNAs) for each regulator identified in primary screen (201 genes). D) Scheme of hit selection during primary and validation secondary siRNA screen and used selection criteria. E) Number of validated negative and positive regulators of CHOP during ER stress within each protein class.

To determine which of the 74 candidate genes also impact on the CHOP activation by other ER stressors, we treated HepG2 CHOP-GFP cells also with thapsigargin or omeprazole (Fig. 3C and E;

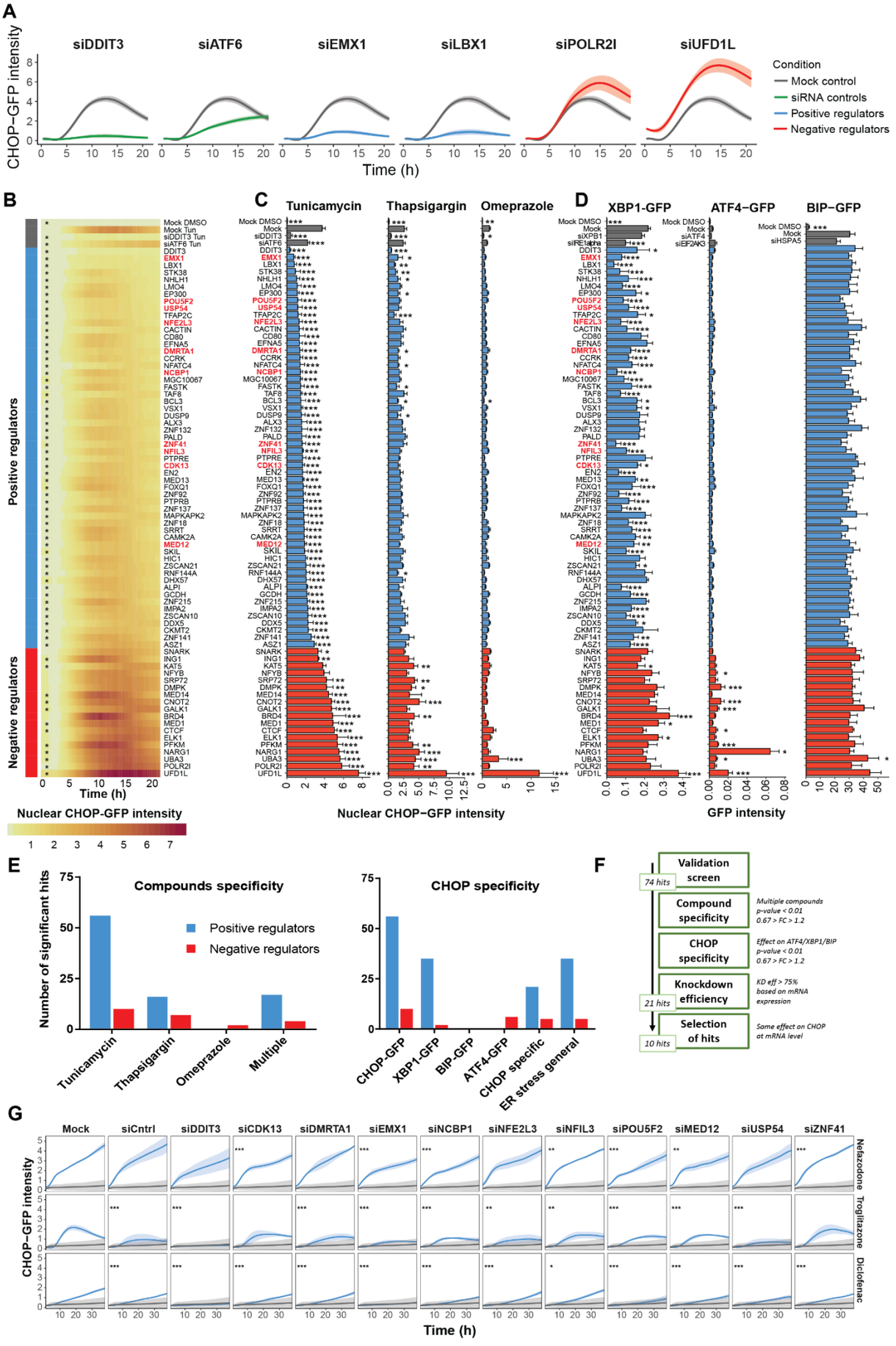
A
siDDIT3
siATF6
siEMX1
siLBX1
siPOLR2I
siUFD1L
CHOP−GFP intensity
Time (h)
Condition
Mock control
siRNA controls
Positive regulators
Negative regulators
B
Positive regulators
Negative regulators
Time (h)
Nuclear CHOP-GFP intensity
C
Tunicamycin
Thapsigargin
Omeprazole
Nuclear CHOP−GFP intensity
D
XBP1-GFP
ATF4−GFP
BIP−GFP
GFP intensity
E
Compounds specificity
Number of significant hits
Positive regulators
Negative regulators
Tunicamycin
Thapsigargin
Omeprazole
Multiple
CHOP specificity
CHOP-GFP
XBP1-GFP
BIP-GFP
ATF4-GFP
CHOP specific
ER stress general
F
Validation screen
74 hits
Compound specificity
Multiple compounds
p-value < 0.01
0.67 > FC > 1.2
CHOP specificity
Effect on ATF4/XBP1/BIP
p-value < 0.01
0.67 > FC > 1.2
Knockdown efficiency
KD eff > 75%
based on mRNA expression
21 hits
Selection of hits
Same effect on CHOP at mRNA level
10 hits
G
Mock
siCntrl
siDDIT3
siCDK13
siDMRTA1
siEMX1
siNCBP1
siNFE2L3
siNFIL3
siPOU5F2
siMED12
siUSP54
siZNF41
CHOP−GFP intensity
Nefazodone
Troglitazone
Diclofenac
Time (h)

← Fig. 3. Chemical-independent regulation of the UPR during ER stress by key hits. A-B) Live cell confocal imaging of CHOP-GFP in HepG2 cells upon 24 h exposure with tunicamycin after siRNA-mediated knockdown of 74 validated hits. C) CHOP-GFP intensity in HepG2 cells upon exposure to tunicamycin for 16 h, thapsigargin or omeprazole for 24 h after siRNA-mediated knockdown of 74 validated hits. D) GFP intensity in HepG2 XBP1, ATF4 or BIP-GFP cells upon exposure to tunicamycin for 24 h after siRNA-mediated knockdown of 74 validated hits. E) Left panel: Number of validated hits showing significant up- or downregulation of CHOP after knockdown upon exposure to a specific ER stress inducer or for multiple inducers. Right panel: Number of validated hits showing significant up- or downregulation of CHOP specifically or multiple UPR components after knockdown and tunicamycin treatment. F) Scheme of hit selection based on compound specificity and knockdown efficiency. G) Live cell imaging of CHOP-GFP upon exposure towards DILI-inducing compounds (blue) or solvent DMSO (grey) after knockdown of selected hits. All data represented as the mean ± standard deviation of three biological replicates with significance levels depicted as *p<0.05, **p<0.01 and ***p<0.001.

Suppl. Excel Table S1). 21 genes showed a significant effect on CHOP induction with thapsigargin, with several of the most effective suppressors (*EMX1, LBX, STK38*) but the majority of the enhancers showed the highest overlap (*UFD1L, UBA3, BRD4*). The proton-pump inhibitor drug omeprazole that induces a mild UPR in liver cells[27,255], showed less extensive CHOP induction and only several candidate genes significantly impacted on CHOP-GFP expression.

Next we determined whether these 74 candidate CHOP regulators also impacted on other ER stress signalling components. We screened our full panel of ER stress HepG2 reporters, involving ATF4, XBP1 and BIP-GFP HepG2 cells (Fig. 3D-E, Suppl. Excel Table S1). Interestingly, the majority of the 56 positive regulators, but only few of the 18 negative regulators of the CHOP-GFP induction also affected the XBP1-GFP induction by tunicamycin. In contrast, approximately 50% of the negative regulators impacted on the ATF4-GFP induction, with none of the positive regulators suppressing the ATF4-GFP induction upon their individual depletion. None of the candidate genes did impact on the induction of the BiP-GFP expression.

Finally, we determined the effect of candidate genes on the CHOP-GFP induction by drugs that have the probability to induce liver injury. As a further selection, we evaluated the knockdown efficiency for the candidate genes in HepG2 with a focus on 21 genes that showed overlap between tunicamycin, thapsigargin as well as different UPR reporters (Suppl. Fig S1). Ten genes were selected that showed more than 75% knockdown efficiency and had a similar effect on

Table 1. Overview of ten most critical modulators of ER stress signalling

Selected hits	*Entrez*	*Fold change CHOP induction*	*pvalue*	*Affects ER stress components*	*Protein class*	*Family*
EMX1	2016	0.195 (± 0.042)	1.81933E-58	CHOP, XBP1	Transcription Factor	EMX homeobox family
POU5F2	134187	0.31 (± 0.114)	1.60827E-45	CHOP	Transcription Factor	POU transcription factor family
USP54	159195	0.311 (± 0.126)	1.64279E-45	CHOP	Ubiquitinases	Peptidase C19 family
NFE2L3	9603	0.351 (± 0.089)	4.7918E-41	CHOP, XBP1	Transcription Factor	bZIP family
DMRTA1	63951	0.367 (± 0.077)	2.1758E-39	CHOP, XBP1	Transcription Factor	DMRT family
NCBP1	4686	0.386 (± 0.065)	1.34373E-37	CHOP	Spliceosome	NCBP1 family
ZNF41	7592	0.435 (± 0.097)	7.93636E-32	CHOP, XBP1	Transcription Factor	Krueppel C2H2-type zinc-finger protein family
NFIL3	4783	0.446 (± 0.026)	2.62321E-31	CHOP, XBP1	Transcription Factor	bZIP family
CDK13	8621	0.448 (± 0.055)	4.51695E-31	CHOP	Kinases	MGC Ser/Thr protein kinase family
MED12	9968	0.503 (± 0.058)	1.11462E-25	CHOP	Transcription Factor	Mediator complex subunit 12 family

CHOP mRNA levels as on protein CHOP-GFP levels (Table 1). We depleted these 10 genes again in HepG2 CHOP-GFP cells and evaluated the effect on the dynamics of CHOP induction by hepatoxic drugs nefazodone, troglitazone and diclofenac (Fig. 3G). *EMX1, NCBP1, NFIL3, POU5F2* and *TNRC11* significantly reduced the CHOP-GFP expression caused by these three liver toxicants. Overall *EMX1* depletion caused the most prominent effect CHOP demonstrating its central role in ER stress signalling during chemical exposure.

EMX1 is an UPR master regulator that defines the UPR in human liver cells.

To translate the importance of the ten genuine ER stress signalling modulators to human liver hepatocyte physiology, we systematically investigated the effect of silencing the ten candidate genes on the transcriptome in both primary human hepatocytes (PHH) and HepG2 cells during tunicamycin-induced ER stress. For transcriptome mapping, the targeted RNA sequencing technology TempO-seq was used in combination with a sentinel gene set enriched with UPR response genes[164,256]. As a first step, the change in mRNA expression of key components of the ER stress signalling was evaluated (Fig. 4). All ten candidate regulators showed significant reduction in *DDIT3* expression upon knockdown during tunicamycin treatment in HepG2 cells (Fig. 4B). In PHH, only knockdown of *EMX1* showed a significant reduction of *DDIT3* expression levels. *EMX1* silencing also downregulated *ATF4*, *ATF6* and *XBP1* expression in PHH suggesting a general role in ER stress signalling regulation in human liver cells. Other candidate genes did suppress tunicamycin-induced *ATF4* induction.

We further evaluated the overall impact of *EMX1* depletion on the UPR transcriptional program with a focus on tunicamycin-induced genes that were significantly affected by *DDIT3* depletion. In both HepG2 and PHH, *EMX1* silencing led to a similar expression profile as *DDIT3* depletion (Fig. 5A). When comparing the median log2 fold change of all *DDIT3* regulated genes after tunicamycin-induced ER stress, of all candidate genes, *EMX1* showed the lowest median log2 fold change almost similar to *DDIT3* knockdown in HepG2 and PHH and comparable to depletion of other UPR drivers including ATF4, ATF6 and ERN1 (Fig. 5B-C). Furthermore, *EMX1* knockdown led to a significant reduction in expression of most of the individual top CHOP-regulated genes in PHH and to a minor degree also in HepG2 (Fig. 5D).

We further identified critical pathways that are regulated by EMX1 during tunicamycin-induced ER stress. The most enriched GO biological processes or Reactome pathways showed many pathways related to protein processing exemplifying its key role in ER stress signalling (Fig. 5E, Suppl. Excel Table S3). When enriched pathways either by *DDIT3* or *EMX1* knockdown were clustered and annotated[246,248], key processes could be identified such as regulation of the unfolded protein response (genes *ATF4*, *ATF6*, *HSPA5*, *XBP1*), translation (*EIF2A*, *EIF2S2*), ER-Golgi trafficking (*KDELR1*, *SEC24C*) and proteosomal degradation (*UFD1*, *EDEM2*), all being part of protein processing (Fig. 5E). In all of these pathway clusters, both *DDIT3* and *EMX1* knockdown showed enrichment of individual pathways having a high overlap in pathway enrichment.

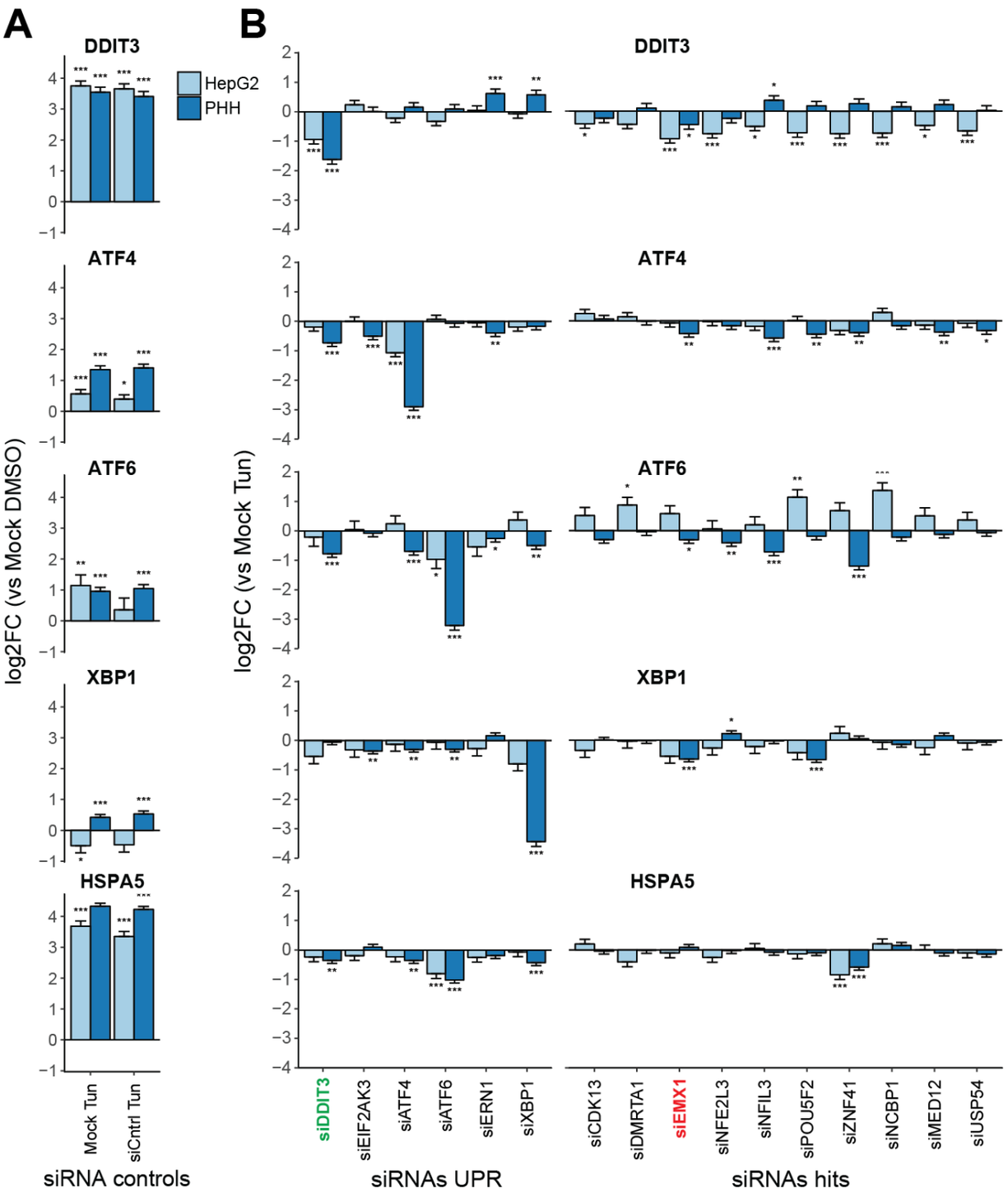

Fig. 4. Regulation of critical UPR components in HepG2 and primary human hepatocytes. Gene expression profile of critical UPR components upon tunicamycin treatment after siRNA-mediated knockdown in HepG2 and primary human hepatocytes (PHH) using TempO-seq analysis. A) Graphs of log2 fold change of gene expression upon tunicamycin treatment compared to solvent DMSO control after transfection without siRNA (Mock) or non-targeting siRNA (siCntrl). B) Graphs of log2 fold change of gene expression upon siRNA-mediated knockdown compared to no siRNA control (Mock) exposed to tunicamycin. Data represented as the mean ± standard deviation of three biological replicates with significance levels depicted as *p<0.1, **p<0.01 and ***p<0.001.

However, pathways related to ER-Golgi protein trafficking were mostly enriched by *EMX1* knockdown indicating a divergent role of EMX1 compared to CHOP in this process. Together this showed the crucial role of EMX1 in hepatocytes in regulating key protein processes during ER stress conditions.

Role of EMX1 in ER stress signalling during exposure to HCC chemotherapeutics

Given the importance of the regulation of the UPR during ER stress in HCC cells for survival, we evaluated the role of EMX1 in CHOP regulation and sensitivity for novel kinase inhibitors targeting HCC chemotherapeutic treatments in HepG2 cells (Fig. 6). A previous kinase inhibitor screen for modulators of CHOP induction identified the clinical approved HCC multi-kinase inhibitor sorafenib as modulators of CHOP expression (Fig. 6A). Both sorafenib as well as another HCC

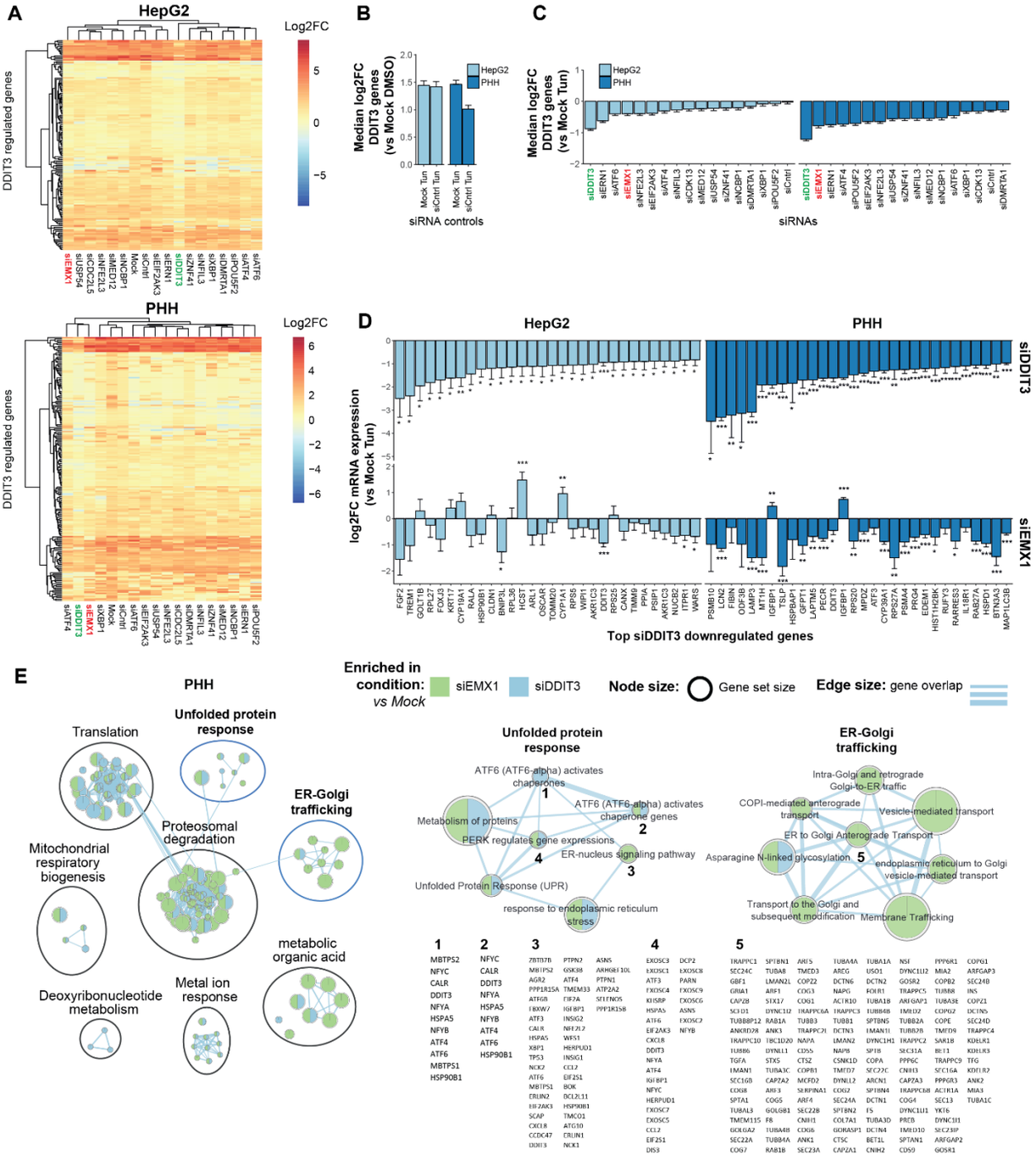

← Fig. 5. EMX1 strongly regulates CHOP and its downstream target genes in HepG2 and primary human hepatocytes. TempO-seq transcriptome analysis of HepG2 and primary human hepatocytes (PHH) upon siRNA-mediated knockdown and tunicamycin treatment. A) Hierarchical clustering of log2 fold change of mRNA expression of CHOP/*DDIT3* downstream target genes upon siRNA-mediated knockdown and tunicamycin treatment compared to solvent DMSO control. B) Graph of median log2 fold change of mRNA expression of CHOP downstream target genes upon tunicamycin treatment compared to solvent DMSO control after transfection without siRNA (Mock) or non-targeting siRNA (siCntrl). C) Graph of median log2 fold change of mRNA expression of CHOP downstream target genes upon tunicamycin treatment after siRNA-mediated knockdown compared to Mock control. D) Graph of log2 fold change of mRNA expression of CHOP target genes upon tunicamycin treatment and knockdown of *DDIT3* or *EMX1* compared to Mock control. E) Visualization of significantly enriched pathways with $p_{adj} < 0.05$ for siRNA-mediated knockdown of *EMX1* (green) or *DDIT3* (blue) vs transfection without siRNA (Mock) in PHHs upon tunicamycin treatment and clustered using WordCloud[248] in Cytoscape[246]. Data represented as the mean ± standard deviation of three biological replicates with significance levels depicted as *p<0.1, **p<0.01 and ***p<0.001.

kinase inhibitor regorafenib led to a sustained induction of CHOP-GFP expression in HepG2 cells at least up to 48 h of exposure (Fig. 6B-C). To evaluate the influence of EMX1 on the sensitivity, HepG2 cells were stained with propidium iodide (PI) and annexinV (AnV) as markers for necrosis and apoptosis, respectively in combination with live cell confocal imaging (Fig. 6D-E). Induction of cell death upon treatment with regorafenib and sorafenib was reduced by *EMX1* knockdown leading to approximately 2-fold lower PI or AnV positive cells. This protective role of *EMX1* silencing was confirmed by measuring cellular ATP content with the strongest effect for sorafenib (Fig. 6F), indicating that the cytotoxicity induced by sorafenib in this HCC cell line is fully dependent on EMX1 expression. To further assess the involvement of *EMX1* in HCC patients, mutation status and mRNA expression in relation to survival was evaluated using the TCGA PanCancer Atlas database (Fig. 6G-H)[251]. 65% of the 372 HCC patients showed alterations for *EMX1* where mRNA upregulation or downregulation was seen for 196 and 46 patients, respectively. Approximately a third of these patients showed also upregulation of *DDIT3* (Fig. 6G). Overall, patients having altered *EMX1* showed lower probability for survival compared to patients with unaffected *EMX1* (Fig. 6H). Together this highlights the importance of EMX1 in CHOP regulation in relation to HCC progression and treatment.

Discussion

To obtain better understanding of the regulation of ER stress signalling, we identified novel key regulators of ER stress signalling by combining the HepG2 CHOP-GFP reporter system with live cell imaging-based high-throughput arrayed RNAi screening targeting the druggable genome. 74 genes were identified that regulate tunicamycin-induced CHOP expression of which *EMX1, NCBP1, NFIL3, POU5F2* and *TNRC11* are genuine modulators of CHOP expression across different stress conditions. Transcriptomic profiling demonstrated that EMX1 is critically impacting on the full UPR program in both HepG2 and primary human hepatocytes, largely mimicking the effect of *DDIT3* silencing. Additionally, EMX1 affected ER-Golgi protein trafficking in liver cells during ER

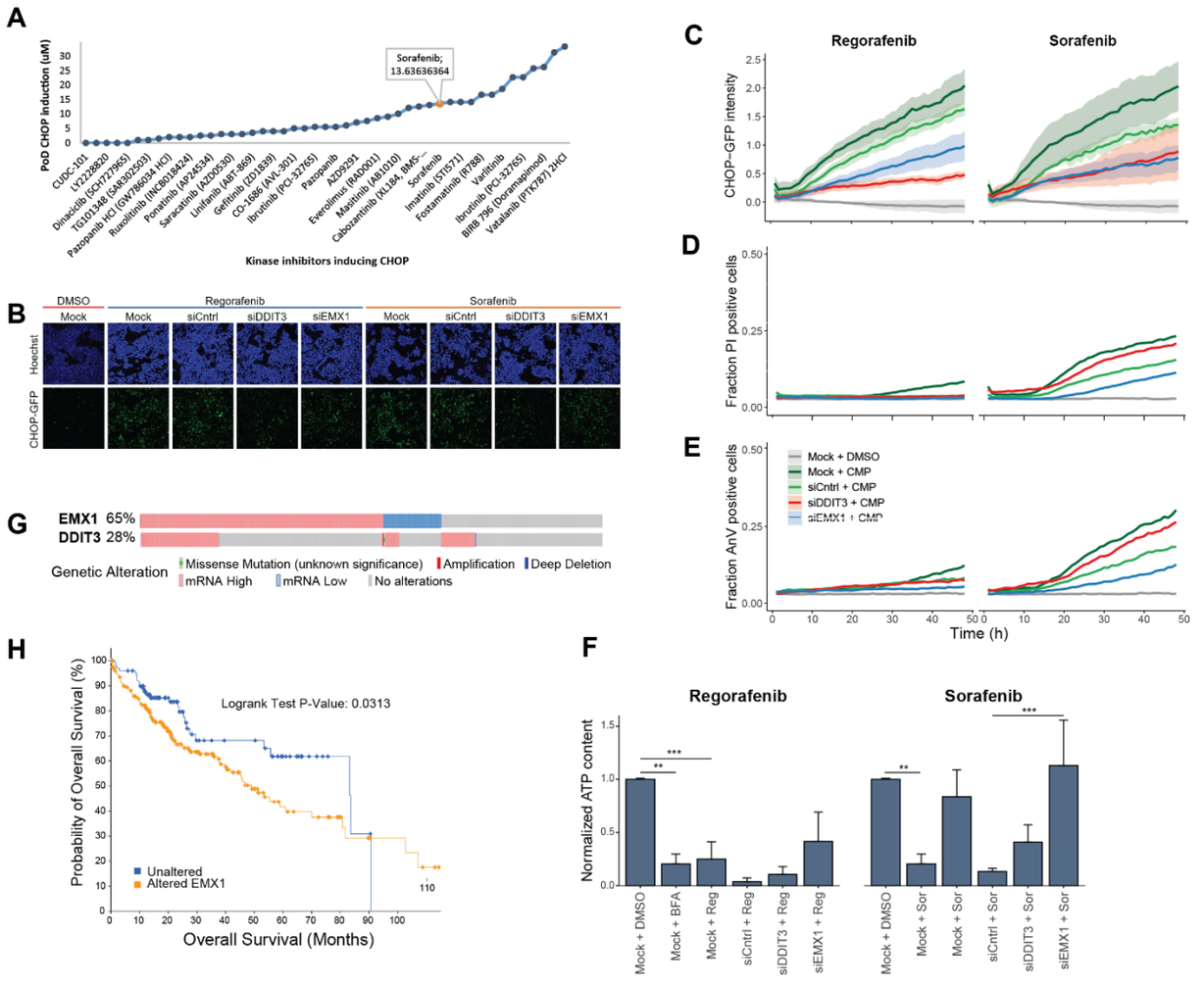

Fig. 6. EMX1 acts as positive regulator of CHOP and stimulates cell death upon exposure to HCC chemotherapeutics in HepG2. A) Point of departure of CHOP induction upon 24 h treatment with kinase inhibitors inducing CHOP in HepG2 cells. B-C) Live cell confocal imaging using 20x objective of HepG2 CHOP-GFP stained with Hoechst for nuclei visualization upon exposure for 48 h to hepatocellular carcinoma (HCC) chemotherapeutics regorafenib or sorafenib after siRNA-mediated knockdown of *DDIT3* or *EMX1* represented as images at 48 h (B) or in graphs (C). D-E) Graphs of fraction of propidium iodide (PI) (D) or annexinV (AnV) (E) positive HepG2 cells upon treatment with HCC chemotherapeutics after siRNA-mediated knockdown. F) ATP content of HepG2 cells treated with HCC chemotherapeutics or positive control brefeldinA (BFA) after siRNA-mediated knockdown. Data represented as the mean ± standard deviation of three biological replicates with significance levels depicted as *p<0.05, **p<0.01 and ***p<0.001. G) Overview of mutations known for *EMX1* in cancer where R209C was found in HCC tissue (upper panel). Among liver HCC tissue from 372 patients, genetic alterations in *EMX1* or *DDIT3* is shown (lower panel). H) Probability for overall survival among HCC patients having genetically unaltered or altered *EMX1*. G-H) Data derived from the TCGA PanCancer Atlas database using cBioPortal[249–251].

stress. EMX1 is essential for the killing of HCC cells by clinically approved HCC multi-kinase inhibitors regorafenib and sorafenib. Our findings have identified a clinically relevant novel master regulator of the UPR that controls the UPR transcriptional program.

The UPR is critical in drug-induced liver injury. Large transcriptional profiling efforts demonstrated that many drugs with the liability to cause hepatotoxicity in the clinical setting

activate the UPR pathway in various different human liver test systems involving induction of ATF4 and CHOP[20]. CHOP induction is causally associated with the onset of liver cell death[255]. In this study, we uncovered a landscape of the signalling components that modulate CHOP expression. Interestingly, several genes that upon depletion enhanced CHOP expression by both tunicamycin and thapsigargin are involved in direct gene transcription including *POLR2L* and *BRD4*. Depletion of CDC2L5/CDK13, a transcriptional cyclin-dependent kinase family member[257], suppressed CHOP induction. Together, this indicates a tight control of the transcriptional machinery in determining CHOP expression. Also depletion of several kinases including *SNARK/NUAK2*, *GALK1*, *PFKM*, *DMPK,* enhanced CHOP induction. While mutations in some of these kinases have been linked to genetic disorders[258–260], none of these kinases have been linked with UPR regulation. The majority of modulators of CHOP expression were transcription factors of which the majority co-operate with CHOP expression under normal conditions. Further selection criteria for modulation of CHOP induction by other stimuli and/or also affect activation of other UPR target genes revealed a set of seven robust transcription factors for which modulation of CHOP-GFP also correlated with *DDIT3/*CHOP expression, including *EMX1, POU5F2, NFEL2F3, DMRTA1, ZNF41, NFIL3, MED12*. These transcription factors also affected the CHOP-dependent transcriptional program in primary human hepatocytes, indicating a role in control of UPR untransformed cells. Moreover, they inhibited the CHOP activation by DILI-inducing compounds nefazodone, diclofenac and troglitazone, suggesting a role for these transcription factors in mediating the UPR adaptive responses upon exposure to drugs with DILI liabilities.

EMX1 was the most potent and consistent modulator of the CHOP-GFP induction by various stimuli. Moreover, from all candidate genes, EMX1 showed the highest similarity with CHOP in the control of ER stress downstream target genes. This was most significant for the primary human hepatocytes. In vivo, EMX1 is strongly expressed in the developing brain[261]. Loss of EMX1 is not lethal in mice but leads to neural developmental defects[262,263]. So far, EMX1 has not been linked to ER stress signalling or protein processes. EMX1 depletion did not fully phenocopy the transcriptional response of *DDIT3* depletion, indicating that EMX1 has other effects that go beyond the suppression of *DDIT3* transcription regulation. Therefore, future studies should focus on unravelling the mechanism how EMX1 influence ER stress signalling. Of relevance, recent work identified EMX1 among five other genes as methylated DNA markers for HCC detection via plasma testing[264]. Also others have shown the association of DNA methylation of EMX1 with HCC and gastric cancer[265,266]. Together, this suggests a role of EMX1 in the development of liver cancer or anti-cancer drug resistance through altered regulation of ER stress signalling by silencing EMX1 through hypermethylation or altered gene expression. In a panel of 50 different primary human hepatocyte donors, we have identified a major difference in the tunicamycin-induced UPR response[267]. Given that EMX1 is a UPR master regulator in hepatocytes, this high inter-individual variability is related to differential activity of EMX1 or other factors that we here identified. Given the importance ER stress in drug-induced liver injury, differential activity of EMX1 would also

impact on the inter-individual susceptibility for liver injury. Thus, patients having altered expression of EMX1, through for instance having certain SNPs, may react differently towards drug-induced ER stress. Indeed, SNPs, for instance in HLA region, have been associated with risk for the development of DILI for certain drugs[268]. Therefore it is of great interest to study the effect of specific mutations in EMX1, as observed in HCC, on the sensitivity towards the development of DILI mediated by ER stress.

In conclusion, using an arrayed high-throughput confocal imaging-based RNAi screen, we uncovered the signalling landscape of the ER stress response. Given the critical role of the unfolded protein response in diverse pathophysiological conditions, we anticipate that some of our candidate genes could be interesting targets for drug discovery to inhibit CHOP-mediated adverse outcomes.

Acknowledgements

This work was supported by the EU-ToxRisk project funded by the European Union under the Horizon 2020 programme (grant agreement 681002) and IMI MIP-DILI project (grant agreement 115336).

Supplemental figures

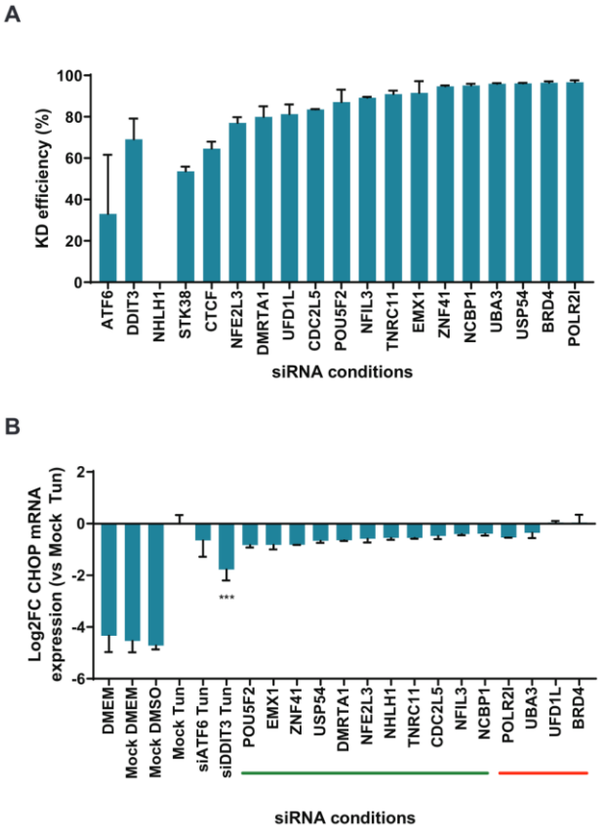

Fig. S1. Knockdown efficiency upon siRNA-mediated silencing of selected gene candidates.

Supplemental Table S2. Top enriched GO terms using gene set enrichment analysis based on the Z-scores for all genes screened in the primary siRNA screen

GO accession	*GO name*	*Observed Zscore*	*p-value*	p_{adj}	*FDR*	*Nr of genes*	*Nr of hits*	*Hits in GO term*
GO:0000381	regulation of alternative mRNA splicing, via spliceosome	0.605125909	0.00000	0.00000	0.04758	41	5	*DDX5, THRAP3, SAP18, DDX17, RBM25*
GO:0016567	protein ubiquitination	-0.363372581	0.00000	0.00000	1.00000	436	3	*MED1, RNF144A, MED12*
GO:0000398	mRNA splicing, via spliceosome	0.270534932	0.00010	0.05963	1.00000	236	33	*DDX5, DHX15, HNRNPD, HNRNPH2, NCBP1, PNN, …*
GO:0032735	positive regulation of interleukin-12 production	0.906572916	0.00010	0.05963	0.33954	25	1	*ISL1*
GO:0045540	regulation of cholesterol biosynthetic process	0.855909536	0.00010	0.05963	0.05419	34	1	*NFYB*
GO:0010875	positive regulation of cholesterol efflux	0.945876234	0.00020	0.09540	0.51800	14	1	*PON1*
GO:0050684	regulation of mRNA processing	-0.831514265	0.00030	0.13416	0.74066	11	0	*NA*
GO:0071712	ER-associated misfolded protein catabolic process	0.961225571	0.00070	0.22766	0.68978	13	1	*UFD1*
GO:0097190	apoptotic signaling pathway	-0.685176858	0.00070	0.22766	0.81830	69	2	*DAPK3, FASTK*
GO:0007099	centriole replication	0.944967541	0.00100	0.24672	0.68160	15	0	*NA*
GO:0046835	carbohydrate phosphorylation	0.590897246	0.00100	0.24672	0.37811	23	2	*GALK1, PFKM*
GO:0050776	regulation of immune response	0.955836942	0.00080	0.24672	0.69900	186	1	*IRF7*
GO:0070987	error-free translesion synthesis	0.87139437	0.00100	0.24672	0.54521	19	1	*UFD1*
GO:0006614	SRP-dependent cotranslational protein targeting to membrane	0.943017881	0.00140	0.27825	0.69800	89	1	*SRP72*
GO:0043044	ATP-dependent chromatin remodeling	-0.652257677	0.00170	0.31188	0.68213	23	3	*SMARCA1, MBD2, MTA2*

Chapter 7

Systematic transcriptome-based comparison of cellular adaptive stress response activation networks in hepatic stem cell-derived progeny and primary human hepatocytes

This chapter has been published as:

M. Niemeijer*, B. ter Braak*, R. Boon, C. Parmentier, A. Baze, L. Richert, S. Huppelschoten, S. Wink, C. Verfaillie and B. van de Water

*Both authors contributed equally

Systematic transcriptome-based comparison of cellular adaptive stress response activation networks in hepatic stem cell-derived progeny and primary human hepatocytes

Toxicol In Vitro. 2021 Jun;73:105107. doi: 10.1016/j.tiv.2021.105107.

Abstract

Various adaptive cellular stress response pathways are critical in the pathophysiology of liver disease and drug-induced liver injury. Human-induced pluripotent stem cell (hiPSC)-derived hepatocyte-like cells (HLCs) provide a promising tool to study cellular stress response pathways, but in this context there is limited insight on how HLCs compare to other *in vitro* liver models. Here, we systematically compared the transcriptomic profiles upon chemical activation in HLCs, hiPSC, primary human hepatocytes (PHH) and HepG2 liver cancer cells. We used targeted RNA-sequencing to map concentration transcriptional response using benchmark concentration modelling for the various stress responses in the different test systems. We found that HLC are very sensitive towards oxidative stress and inflammation conditions as corresponding genes were activated at over 3 fold lower concentrations of the corresponding pathway inducing compounds as compared to PHH. PHH were the most sensitive model when studying UPR related effects. Due to the non-proliferative nature of PHH and HLC, these do not pose a good/sensitive model to pick up DNA damage responses, while hiPSC and HepG2s were more sensitive in these conditions. We envision that this study contributes to a better understanding on how HLCs can contribute to the assessment of cell physiological stress response activation to predict hepatotoxic events.

Key words: Induced Pluripotent Stem Cell derived hepatocytes, Oxidative Stress, DNA Damage, Unfolded Protein Response, Inflammation, Transcriptomics

Introduction

Drug-induced liver injury (DILI) is one of the most frequent causes for drug withdrawal and the leading cause for compound attrition in drug development[269]. Current models that are used in drug safety screening include hepatoma cell lines and PHH, but these models have their limitations. The gold standard for toxicity testing, PHH, have a lack in bioavailability, high cost, high inter-donor variability and tendency to quickly dedifferentiate upon plating. Moreover, they can only provide limited mechanistic information[270]. HepG2, a liver carcinoma cell line, displays many phenotypic features of normal liver cells, but has a low metabolic capacity compared to PHH. On the other hand, current models that possess relatively high metabolic capacity such as HepaRG and Upcyte, show lower hepatotoxicity predictivity than HepG2 cells in comparison to PHH[45].

A new and very promising source for unlimited, stabile cells with potentially improved predictivity for hepatotoxicity are stem cell-derived hepatocyte models[271,272]. Ethical issues with embryonic stem cell-derived hepatocytes were resolved when reprogramming techniques made it possible to generate hiPSC from fibroblasts or any other nucleated somatic cell[47]. This procedure also makes it possible to study hepatotoxicity in patient-derived hiPSC-derived HLCs having specific genetic mutations and drug sensitivity backgrounds[273]. To understand the application value of hiPSC-HLCs as compared to PHH, most studies have measured the expression

and activity of biotransformation enzymes, including both phase I, phase II and phase III metabolism, as these are critical components for onset of DILI[16]. However, also other cell physiological responses that determine the ultimate fatal outcome for onset of hepatotoxicity are critical to evaluate, including cellular stress response pathways related to either internal or external cues and specific cell injury or inflammatory cytokines. The main cellular stress responses include oxidative stress-mediated NRF2 activation, unfolded protein response (UPR) through ATF4, ATF6 and XBP1 transcriptional responses, DNA damage responses through P53 signalling and inflammatory cytokine-mediated NF-κB activation[28]. Most likely, the dynamics and amplitude of these responses differ between cell types and will determine the ultimate cellular outcome. Since various drugs with DILI liability activate these stress pathways[28], it is of major interest to compare the cellular stress response pathways between hiPSC-HLCs and PHH. However, so far a systematic analysis of the response of hepatic hiPSC-progeny towards chemically-induced stress is lacking.

Omics approaches, such as transcriptomic profiling, enable a thorough comparison of different liver *in vitro* models and assess the resemblance to primary hepatocytes or liver tissue. Some studies describe a transcriptomic comparison between HLCs and other models like PHH and hepatoma lines[111,274], but a comparison of cellular stress responses has not been performed. Recent advances in higher throughput targeted RNA-sequencing technology, such as TempO-seq, enables a snapshot of the transcriptomic profiles of thousands of genes for various conditions[30,275]. This allows for detailed concentration response evaluation of chemical-induced cell injury responses in various cell types. Using the TempO-seq technology, a cost-effective technique allowing for the evaluation of the expression of a targeted set of genes only needing a small amount of sample, here we compared the chemically-induced cellular stress response activation in hiPSC-HLCs with cryopreserved PHH and HepG2 cells. We used diethyl maleate to induce an oxidative stress response, tunicamycin to induce unfolded protein stress response, cisplatin to induce the DNA damage response and tumor necrosis factor alpha (TNFα) to initiate inflammatory cytokine signalling for 8 hours to capture the primary stress response activation. The goal of this study is to compare specific stress pathway activation sensitivities to evaluate the suitability of each model in a hepatotoxicity assay. To our knowledge, this is the first systematic study that focusses on the transcriptomic effect of chemically-induced cellular stress responses in hiPSC-derived hepatocytes.

Materials and Methods

Cell Culturing

The hiPSC BJ-1 line (generated at KU Leuven) was cultured on Matrigel (Corning) coated plates. Medium (mTeSR1) was refreshed daily. Full description of the characteristics of the hiPSC BJ-1 line can be found in Helsen *et al.*[272]. The human liver carcinoma cell line, HepG2, obtained from American Type Culture Collection (ATCC) were cultured as described in Wink *et al.*[79]. Cryo-

preserved PHH derived from three different individuals (S1295T: 86-year-old male Caucasian patient with hepatocellular carcinoma; S1307T: male Caucasian 75-year-old patient with colorectal carcinoma; and S1423T: male Caucasian 68-year-old patient with colorectal adenocarcinoma) were provided by KaLy-Cell (Plobsheim, France) and selected based on their plateability. PHH were thawed, transferred to pre-warmed thawing UCRM medium (IVAL, Columbia, USA), transferred to pre-warmed seeding UPCM medium (IVAL). Viability was assessed using the Trypan Blue, cells were seeded at a density of 70.000 viable cells per well in 96 wells Biocoat Corning Collagen I Cellware plates from Corning (Wiesbaden, Germany). Medium was refreshed using seeding UPCM medium 6 hours after plating. Compound exposures were done 24 hours after plating in William's E medium supplemented with 100 U/mL penicillin and 100 µg/mL streptomycin.

Differentiation of hiPSCs towards hepatocytes

HiPSCs were differentiated to HLCs as described by Tricot et al[276]. In short, BJ1 hiPSC cells were seeded in mTeSR, supplemented with 1:100 Revitacell (Thermofisher), with 100.000 cells per 48-well. During differentiation, the cells were cultured on liver differentiation medium (LDM). In addition to the growth factors Activin-A (100 ng/ml), Wnt3a (50 ng/ml), BMP4 (50 ng/ml), FGF1 (50 ng/ml), and HGF (20 ng/ml) (Fig 1a), 0.6% DMSO (Sigma-Aldrich) was added from day 0 until day 11, from day 12 until day 25 2% DMSO was added to the LDM (Tricot et al., 2018). It was shown that DMSO improves the hepatic differentiation by downregulation of pluripotency genes[277]. Medium was refreshed daily. All growth factors were purchased from PeproTech. For the biological replicates three different stem cell culture flasks were used, which were differentiated separate from each other.

Cell treatment

Model compounds for oxidative stress (diethyl maleate; DEM) and unfolded protein response (tunicamycin; TUN) were purchased from Sigma-Aldrich, the cytokine to induce an inflammation response (tumor necrosis factor α; TNF) was purchased from R&D systems and the DNA damage response compound (cisplatin; CPT) from Ebewe. For each compound a dose range was chosen that is known to induce the corresponding stress pathway without inducing cytotoxicity[20,28,278]. Prior to exposure, 1000 times concentrated stock solutions were made in DMSO (DEM, TUN) or PBS (TNF, CPT). Exposures were performed by adding 100 µL two times concentrated exposure medium (with 0.2% DMSO independent of compound exposure) to each well already containing 100 µL maintenance medium. Cells were exposed for 8 hours in a 5% CO_2 humidified incubator at 37 °C. Thereafter, cells were washed with PBS, lysed with 1x TempO-Seq lysis buffer, stored at -80°C and shipped for targeted sequencing. All exposure experiments have been performed with three independent biological replicates using different compound stock solutions.

Immunofluorescence

Maturity status of the HLC differentiation was assessed with immunofluorescence using hepatocyte markers HNF4α (1:200, Abcam, ref#ab41898) and AAT (1:200, Dako, ref#A0012) following the protocol described in Boon et al [53].

Targeted sequencing

Gene expression profiles were analysed using a targeted RNA sequencing technology, TempO-Seq (Biospyder Technologies, Inc., Carlsbad, CA, USA). A set of genes was selected based on the S1500+ gene list of NIEHS[164]. This list contains 2736 genes that provide maximal toxicogenomic information on chemical perturbations that reflect general cellular responses. We supplemented this list with another 245 genes that are involved in hiPSC to hepatocyte differentiation, cellular stress pathways activated in PHH[97] and were missing in the S1500 list (for complete gene list see ESM_1.xlsx). A detailed description of the sample processing was described by Yeakley *et al*.[30]. In short, mRNA in the lysates was hybridized with detector oligo mix, and amplified using barcoded primer pairs to add a unique tag for each of the samples. Sample amplicons were pooled and purified. The libraries were sequenced using a HiSeq 2500 Ultra-High-Throughput Sequencing System (Illumina, San Diego, CA). De-multiplexing of the sequencing readouts resulted in FASTQ files.

Data processing

TempO-seq transcriptomics derived reads were aligned using the TempO-seqR package (done in-house by BioSpyder Technologies). Raw counts were normalized using the DESeq2 R package and log2 transformed. A library size (sum of reads within one sample) cut-off was used of 100.000 reads. Samples that did not meet this criterion were excluded for further analysis. Replicate Pearson correlation was calculated for each condition and model (supplemental figure ESM5). Data has been uploaded to the Gene Expression Omnibus (GEO) with series accession number GSE155771. Benchmark concentration (BMC) modelling was done using the BMDExpress 2 software (developed by Sciome LCC and NIEHS/NTP/EPA) to assess difference in sensitivity[32]. Here, the dose responses were fitted with various continuous models (exponential, linear, polynomial, hill and power model) for each gene and sample. Best model was selected which had the lowest Akaike's information criterion (AIC)[279] and a p-value of >0.05. The BMC was defined as the concentration at 1 standard deviation increase of gene expression. Genes were considered significant differentially expressed across dose-response when the adjusted p-value was <0.05 using a Williams trend test and Benjamini & Hochberg post-hoc test. Principal Component Analysis (PCA) of the log2 normalized counts or fold changes was done using the prcomp function from the Stats R package. Besides BMDExpress 2, Rstudio version 1.0.153 (Boston, USA) in combination with R 3.4.1 was used for data analysis including the following R packages: DESeq2, AnnotationDbi, pheatmap, ggplot2, data.table, dplyr, tidyr, reshape2, scales and stats[131–

[133,135,137,165,210,280]. Using R package pheatmap, hierarchical clustering of pathway-related genes was done based on Euclidean distance of log2 fold changes using Wards method.

Retrieving pathway specific gene list

To examine stress response perturbations by each compound using PCA, genes were selected when the mean maximal fold change across the dose response for the three PHH donors was higher than 4 for DEM, TUN and CPT, and 3.5 for TNF treated cells (for gene lists see ESM_2.xlsx). For hierarchical clustering and BMC distribution plots, stress response pathway-related genes were based on target genes of stress response specific transcription factors (UPR: *ATF4*, *ATF6*, *XBP1* and *DDIT3*; OX: *NFE2L2*; DDR: *TP53*; Inflammation: *RELA*, *REL* and *NFKB1*) defined by DoRothEA v2[209] with confidence level of A to D which were present in the S1500+ gene set. Of these genes, the top 30 were selected based on the rank of both maximal fold change

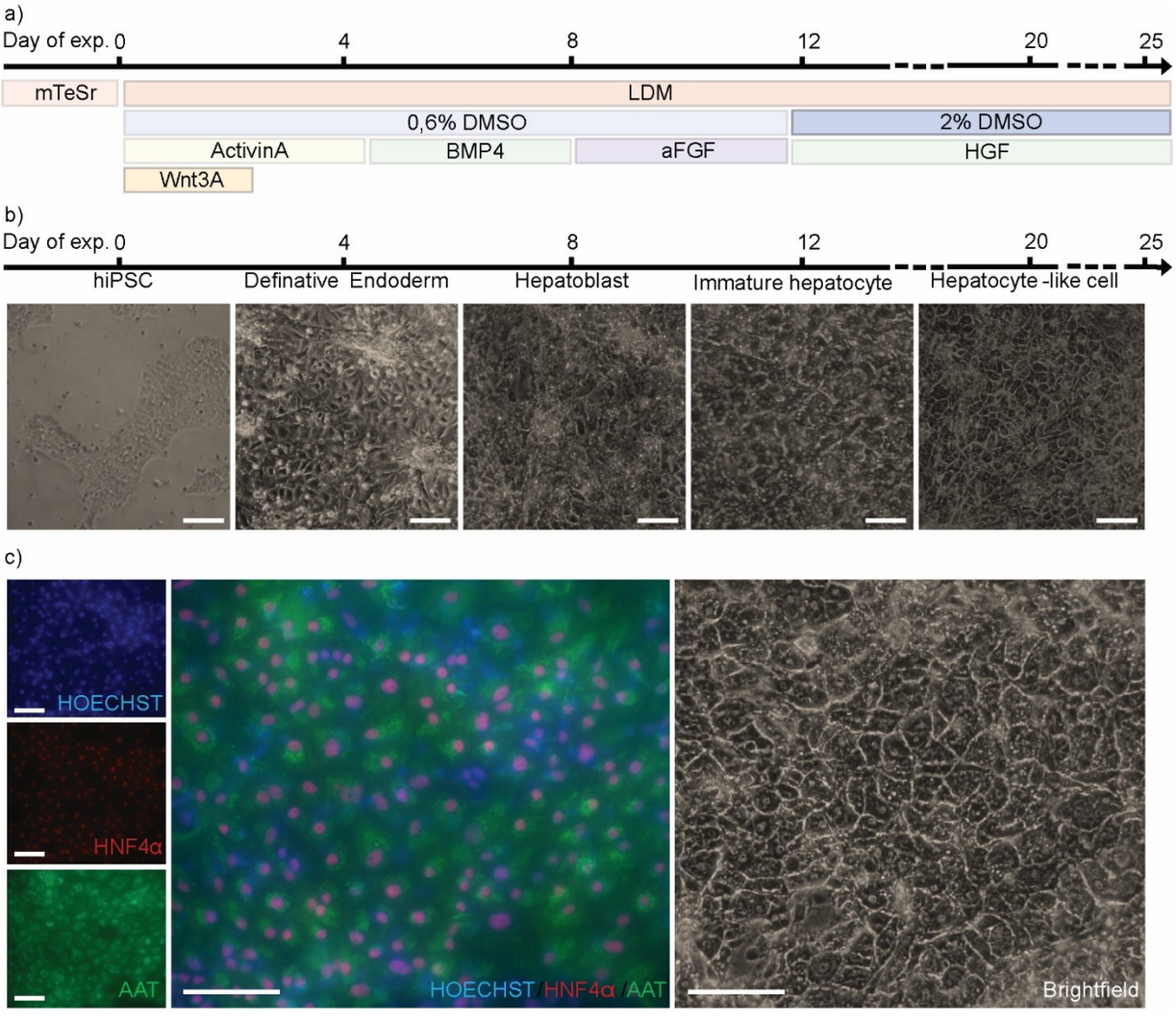

Fig. 1. HiPSC-hepatocyte differentiation process and differentiation quality. A) The 25-day hiPSC-HLC differentiation mTeSR based protocol. Compound exposures were performed at the indicated days during differentiation (0, 4, 8, 12, 20 and 25 days). B) Brightfield image overview of the differentiation process, in which several intermediate cell types can be identified. C) Immunofluorescence (HNF4α and AAT) and brightfield imaging of hepatocyte-like cells (day 25). Scale bars represent a size of 100 µm.

across dose and BMC having at least a fold change of 2.5 for one of the cell types (for gene lists see ESM_3.xlsx). These genes were used for hierarchical clustering and BMC distribution comparison to assess sensitivity for pathway activation. To evaluate the specificity of the compounds activating the stress responses of interest, we have performed transcription factor activity analysis using gene set enrichment analysis using the viper R package of the transcription factor regulons defined by DoRothEA v2 with a confidence level A to D present in the S1500+ gene set. Transcription factors were filtered based on FDR < 0.05 and the top 20 were selected based on ranking of the minimum FDR across concentration range having a positive NES.

Results

HiPSC differentiation to hepatocyte-like cells

A twenty day hiPSC-hepatocyte differentiation protocol[276] was followed (Fig 1a), in which growth factors ActivinA and Wnt3A started the hiPSC differentiation process towards a definitive endoderm cell stage (Fig 1b). At this point the cells showed a typical epithelial morphology and stopped proliferating. Addition of bone morphogenetic protein 4 (BMP4) differentiated these cells further towards hepatoblasts followed by a 4-day long stimulation with acidic fibroblast growth factor (aFGF) which resulted in immature hepatocytes. In the last phase of the differentiation protocol, hepatocyte growth factor (HGF) was added to the LDM which resulted in cells with a typical cuboidal morphology[281], that stained positive for anti-alpha trypsin (AAT) and hepatocyte nuclear factor 4 alpha (HNF4α) (Fig 1c).

Transcriptomic overview of the differentiation process and comparison to PHH and HepG2

To assess the shift in the gene expression profile during the differentiation process, gene expression levels of undifferentiated hiPSC were compared with the different hepatocyte-differentiation stages and compared to HepG2 and the gold standard PHH, all in basal/unexposed conditions. General transcriptomic profiles between different cell types were compared using a principle component analysis (PCA). A relatively small difference was seen when hiPSCs were differentiated towards HLCs compared to PHH in the first principal component (PC) explaining 54.3% of the variance (Fig 2a), and they remained co-localized with HepG2 cells but not PHH. The liver associated genes, such as Haptoglobin (*HP*), Albumin (*ALB*) and Orosomucoid 1 (*ORM1)*, were chiefly responsible for the relatively small shift towards PHH. In PC2, a significant difference could be seen between hiPSC and HLCs, which was mostly accounted for by the enormous upregulation of both immature liver specific genes during differentiation, including alpha-fetoprotein (*AFP*), and mature liver specific pre-albumin Transthyretin (*TTR*), Fibrinogen Beta Chain (*FGB*) and Fibrinogen Gamma Chain (*FGG*). The biological variation between the different hiPSC progeny steps was relatively small as a clear separation of the different cell differentiation stages and cell types could be observed. hiPSC-hepatic progeny moved along the axis of PC4 and addition of BMP4 in the first 8 days of differentiation induced a strong *BMP6* expression, which was lost from day 9 onward. In addition, expression of Hemoglobin Subunit Gamma 2 (*HBG2*), a

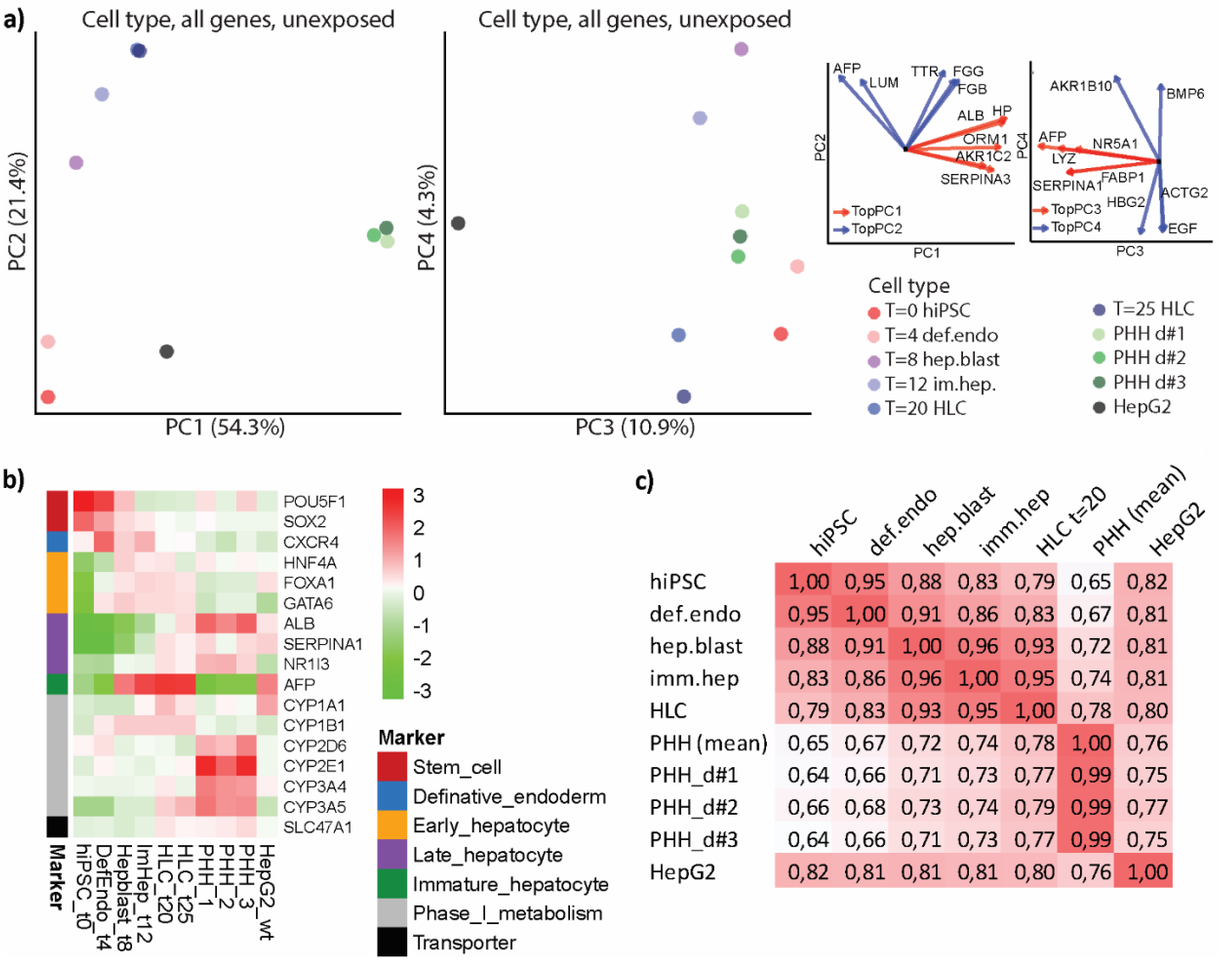

Fig. 2. Transcriptomic analysis of the hiPSC-hepatocyte differentiation process benchmarked to PHH and HepG2. A) Principle component analysis (PCA) of all genes at basal conditions of the different cell types using log2 transformed counts. The top 5 genes most determining the corresponding principle components are depicted on the right, where red arrows represent genes most affecting the principle component on the x-axis and blue on the y-axis. B) Heat map of the log10 FC expression levels of differentiation markers during hiPSC-hepatocyte differentiation process, the fold changes are compared to the median expression of each gene. C) Pearson correlation matrix on normalized gene expression counts of the different cell types. N=3

gene highly expressed in immature hepatocytes, was significantly upregulated. The variation between the different PHH donor populations was relatively small in all PCs. Interestingly, in PC3, a clear separation of HepG2 from all other cells became evident, primarily driven by high expression of *AFP* and Lysozyme (*LYZ*) in this cell line.

Next, we evaluated the expression of well-known markers for each hiPSC differentiation stage. The stem cell markers *POU5F1* and *SOX2* were highly expressed in undifferentiated hiPSC stage, but as expected were downregulated by >1000-fold upon differentiation towards HLCs (Fig 2b). At step 1 of differentiation, the definitive endoderm marker *CXCR4* was more than 50-fold increased. Early hepatocyte markers *FOXA1* and *HNF4α* were highly induced in the HLC stage and reached expression levels similar to those in PHH[274,282]. *AFP*, a gene that is associated with fetal hepatocytes, was highly expressed in HLCs suggesting an immature hepatocyte phenotype. Late

hepatocyte markers, such as *ALB, NR1I3* and *SERPINA1* were strongly induced during the differentiation process, where transcript levels for *NR1I3* and *SERPINA1* levels were comparable to PHH. However, *ALB* gene expression levels remained still >10-fold lower compared to PHH. A key feature of hepatocytes is their ability to metabolize drugs. Phase 1 metabolism is mainly regulated by CYP enzymes. During differentiation some of these enzymes (e.g. *CYP1A1, CYP1B1,* and *CYP3A5*) were strongly induced and reached similar or higher expression levels as compared to PHH. Several other enzymes including *CYP2D6, CYP2E1* and *CYP3A4* remained significantly less expressed in HLCs as compared to PHH, indicating the immaturity of the HLCs. For metabolically functional hepatocytes, expression of transporters is necessary, especially *SLC47A1* plays an important role in xenobiotic clearance[283]. In contrast to HepG2, the SLCs were expressed at a similar level in HLCs as compared to PHH. Thus, as summarized in Figure 2C, the gene expression profiles of the differentiated hiPSCs correlated increasingly stronger with PHH, with hiPSC:PHH correlation of 0.65 and HLC:PHH correlation of 0.78. The correlation of HepG2:PHH was 0.76. The variation along the different donors of PHH was relatively small as all had a correlation of 0.99 with the mean of the PHH.

Transcriptomic space of HLCs and other models in oxidative stress conditions

Diethyl maleate (DEM) is an electrophilic compound which conjugates with cysteine residues in KEAP1 thus activating the activation of the NRF2 pathway, and at higher concentration also affecting the levels of reduced glutathione, thereby disturbing the cellular redox balance and allowing oxidative stress[126]. DEM was used as a model compound to induce an overall cellular oxidative stress response. A selection of DEM upregulated genes was based on having a minimum fold change of 4 across dose response of DEM in PHH (see ESM_2.xlsx for complete list). We performed a PCA analysis on the fold changes DEM vs DMSO to examine the effect on gene expression of the DEM responsive genes (Fig 3a). Interestingly, at the lowest DEM concentrations all cell types co-localized in the PCA plot, indicating similar behaviour between cell types under mild oxidative stress conditions. A very clear DEM concentration-dependent shift in PC1 could be detected for PHH and HLCs, and to a lesser extent hiPSC and HepG2. This effect was predominantly caused by increasing expression of heat shock proteins (secondary response after oxidative stress) or one of the downstream targets of the NRF2 pathway (*MAFF*). Interestingly, at the highest DEM concentration the samples shifted up again on the PC2 axis indicating a downregulation of the NRF2 pathway. The DEM concentration-dependent shift of PHH moved along the PC1 axis which was mainly related to the high expression of the NRF2 target gene oxidative stress induced growth inhibitor 1 (*OSGIN1*) gene.

Next, we investigated the top 30 most responding oxidative stress genes after DEM exposure. Genes were selected on the basis of direct targets of NRF2 as defined by DoRothEA v2[209]. Activation of transcription factors was evaluated by gene set enrichment analysis of the transcription factor downstream targets (supplemental table ESM4), where among *NFE2L2* also

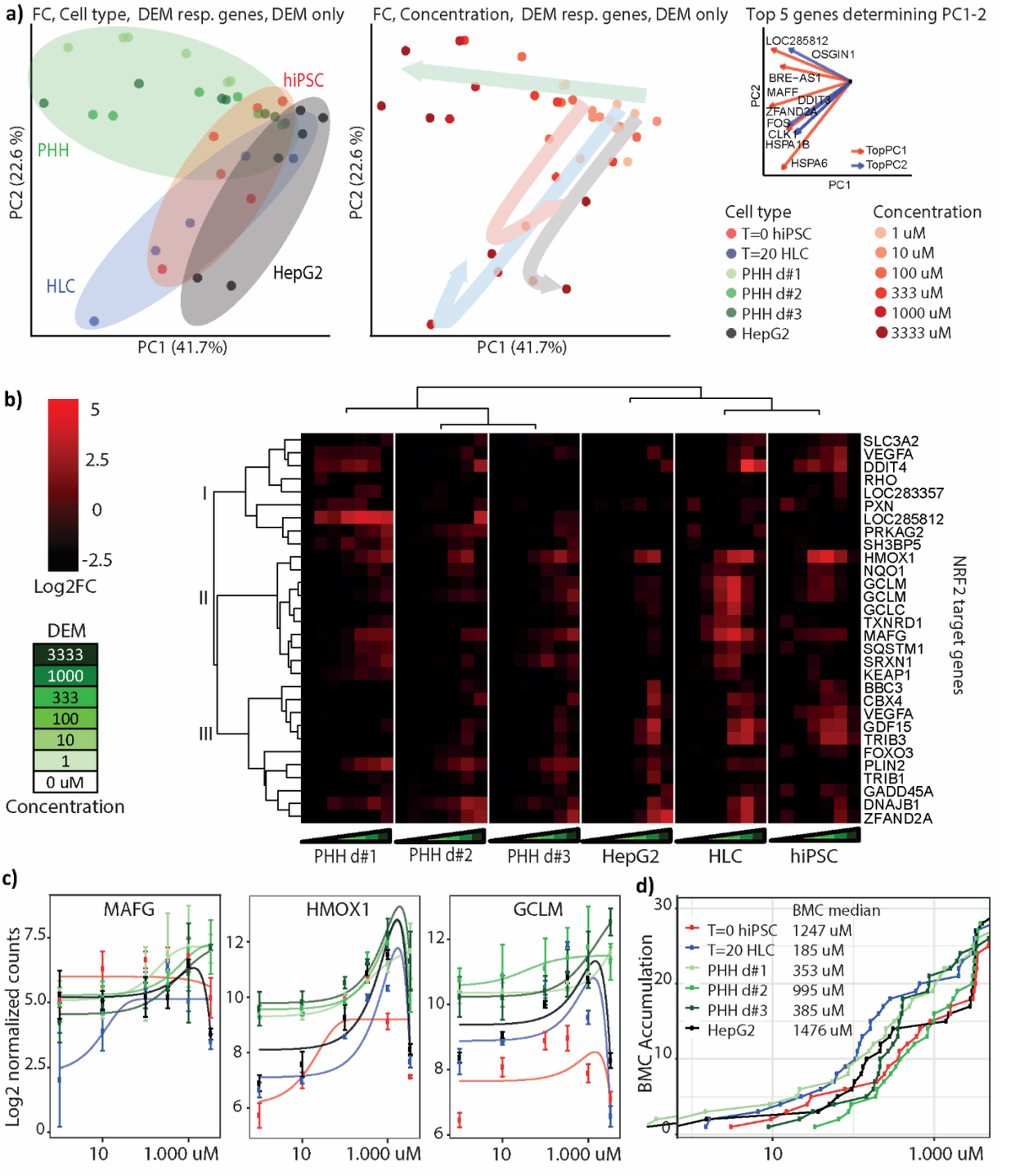

Fig. 3. Effect of oxidative stress on the transcriptomic space of hiPSC, HLC, PHH and HepG2. A) Left panel: PCA of log2 normalized counts of DEM responsive genes with all treatments. Right panel: PCA of log2 fold changes of the DEM responsive genes after DEM exposure. The vector plots on the right represent the top 5 most determining genes of PC1 (red) or PC2 (blue). The size and orientation of the vector represent the contribution and PC-orientation of the 10 genes. B) Hierarchical clustering of the log2 fold changes of the top 30 responding oxidative stress genes after DEM exposure. C) Concentration response curves of log2 normalized counts for three oxidative stress genes after DEM exposure. Dots and error bars (SE) represent gene expression data, lines represent best BMC model. D) BMC accumulation plots of the top 30 responding oxidative stress genes after DEM exposure. Median BMC were extracted from these plots. N=3

ATF4, important in the UPR, was activated among the models. Hierarchical clustering of NRF2 genes based on Euclidean distance identified genes involved in secondary cell stress responses (e.g. *FOXO3, DNAJB1, TRIB3*) in cluster III and genes involved in the NRF2 mediated oxidative stress response (e.g. *HMOX1, SRXN1, KEAP1, MAFG, GCLM, GCLC, NQO1*) in cluster II (Fig 3b). Especially in cluster II, HLCs appeared to be more responsive towards DEM as compared to the hiPSC, PHH and HepG2. Clustering of the models indicated that the oxidative stress gene expression profiles of HLCs are similar to hiPSC having higher induction at lower concentrations as compared to PHH.

To further investigate the pathway specific sensitivity of each model, a BMC analysis was performed (Fig 3c) where the BMC was defined as the concentration at which the target gene expression increases by 1 standard deviation above baseline levels. For this analysis, the same pathway specific top 30 oxidative stress genes were selected. The cumulative BMC plots indicated that hiPSC-derived HLCs were most sensitive towards DEM exposure, having a median BMC of 185 µM (Fig 3d). PHH were in general less sensitive than HLCs having a median BMC of 353, 385 or 995 µM, and there were significant differences between donors. HepG2 and undifferentiated hiPSCs appeared to be the least sensitive (1476 and 1247 µM, respectively).

Transcriptomic space of different liver test systems for the unfolded protein stress response.

Tunicamycin (TUN) was used to induce the UPR as it inhibits N-linked glycosylation thereby disturbing protein folding of glycoproteins leading to ER stress[284]. A PCA analysis was performed to visualize the transcriptomic changes at the different concentrations of TUN of the different models. We focused the analysis on TUN responsive genes that changed in expression by > 4-fold in PHH across the dose response (Fig 4a; ESM_2.xlsx for list of genes). The PCA analysis, based on log2 fold changes TUN vs DMSO control, showed that with lower TUN concentrations all models did behave similar (Fig 4a). Upon increasing concentrations of TUN, all cell types moved up in PC2, which was mainly caused by high levels of expression of *DDIT3, HERPUD1* and *MANF* at increasing concentrations of TUN. These genes are all well known to have a role in the adaptive response against ER stress. Interestingly, four samples moved to the right on the PC1 axis at the highest TUN concentration (100 µM) (HLCs and all three donors of the PHH). This shift was caused by, among others, a downregulation of UPR responding genes and upregulation of early stress response genes (e.g. *FOS* and *EGR1*), indicating that HLCs and PHH were more sensitive towards ER stress than HepG2 and hiPSC. This illustrated a similar TUN dose-response behaviour of HLCs and PHH. We also performed hierarchical clustering (Fig 4b) analysis, including the 30 UPR related genes most affected by TUN exposure. In general, UPR genes were stronger upregulated in HLCs. In HLCs and hiPSCs there was a threshold concentration of TUN when the UPR was started to be induced. Below 1 µM the pathway was inactive but at 1, 10 and 100 µM there was a very pronounced induction. However, for PHH, this effect seemed to be more gradual, starting already at 0.001 µM TUN where there is some upregulation of UPR related genes. Dose response curves

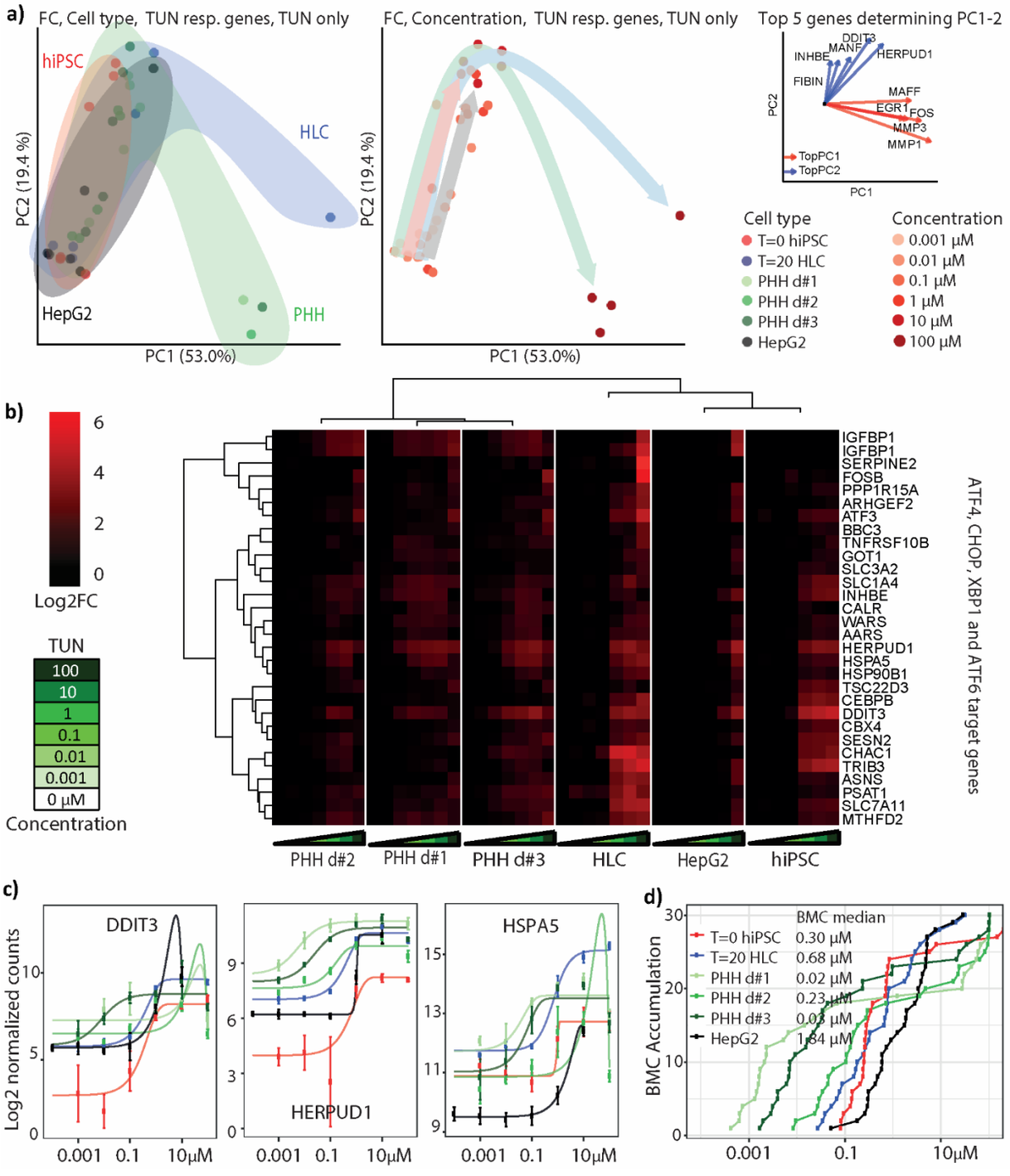

Fig. 4. Effect of the unfolded protein response on the transcriptomic space of hiPSC, HLC, PHH and HepG2. A) Left panel: PCA of the unfolded protein genes (log2 normalized counts) with all treatments. Right panel: PCA of log 2-fold changes of the TUN responsive genes after TUN exposure. The vector plots on the right represent the top 5 most determining genes of PC1 (red) or PC2 (blue). The size and orientation of the vector represent the contribution and PC-orientation of the 10 genes. B) Hierarchical clustering of the log2 fold changes of the top 30 UPR related genes after TUN exposure. C) Concentration response curves of log2 normalized counts for three UPR genes after TUN exposure. Dots and error bars (SE) represent gene expression data, lines represent best BMC model. D) BMC accumulation plots of the top 30 responding UPR related genes after TUN exposure. Median BMC were extracted from these plots. N=3

of three example and well-known targets of the UPR response (*DDIT3, HERPUD1* and *HSPA5*) demonstrated that basal expression of UPR downstream targets was lower in the HepG2 and hiPSC (Fig 4c). Transcription factor activity analyses revealed the activation of both UPR related transcription factors, but also NF-κB related transcription factors such as *RELA* and *NFKB1* (supplemental table ESM4). The BMC accumulation plot of the 30 most affected TUN modulated genes showed that PHH are the most sensitive for UPR with considerable variation between different donors (median BMC of 0.02 – 0.23 µM) (Fig 4d). Undifferentiated hiPSCs and their differentiated HLC progeny were less sensitive than PHH (median BMC 0.3 and 0.68 µM, respectively). Of note, UPR target genes were only upregulated at much higher concentrations of TUN in HepG2 cells (median BMC of 1.84 µM).

Transcriptomic space of hiPSC-HLCs and other models in DNA damage conditions

CPT, a clinically relevant anticancer agent, was used to induce a DNA damage response (DDR). CPT induces intra and inter-strand DNA adducts, eventually resulting in single and double stranded DNA breaks and subsequent induction of a DDR[285]. Selection of CPT upregulated genes was based on PHH-gene expression after CPT exposure having a minimal fold change of 4 across dose response (see gene list ESM_2.xlsx). PCA analysis of the log2 fold change of CPT vs DMSO showed that the response of HLCs was most similar to PHH (Fig 5a). A clear dose response shift could be observed towards high PC2 and low PC1 values. High expression of typical TP53 downstream targets (*MDM2* and *BTG2*) contributed to this shift. The concentration response shift of HLCs and PHH moved more along the PC1 axis compared to hiPSC and HepG2, predominantly caused by increased expression of ATM dependent genes (e.g. *CDK5R1* and *H2AFX*). Interestingly, at the highest concentration of CPT, all 3 PHH donor samples showed a major shift in the PC2 transcriptomic space. A reduction of the typical DNA damage response genes was observed. This indicates a clear tipping point where PHH switch from adaptation to DNA damage towards adverse regulated cell death programs. Apparently, this tipping point is only reached at higher concentrations of CPT in the other models. The hierarchical clustering on the 30 most responsive downstream targets of TP53 after CPT exposure revealed that the gene induction pattern of HLCs, HepG2 and PHH were similar (Fig 5b), while hiPSC were most distinct. The log2 normalized counts of three DDR genes, *BTG2, GADD45A* and *MDM2*, demonstrated that although the expression profiles were similar for HLCs and PHH, basal expression levels of TP53 downstream targets were much lower in HLCs (Fig 5c). Furthermore, the tipping point at which PHH switch from adaptive to adverse signalling is clearly visible at the highest concentrations. As expected, transcription factor activity analysis revealed *TP53* activity for primarily the hiPSCs and to a lesser extend in the other non-dividing models (supplemental table ESM4). The BMC accumulation plot of the 30 TP53 downstream target genes demonstrated that cells with high proliferative potential (hiPSC and HepG2) respond already at lower CPT (Fig 5d), likely related to replicative stress in the proliferating cells caused by CPT-induced DNA damage.

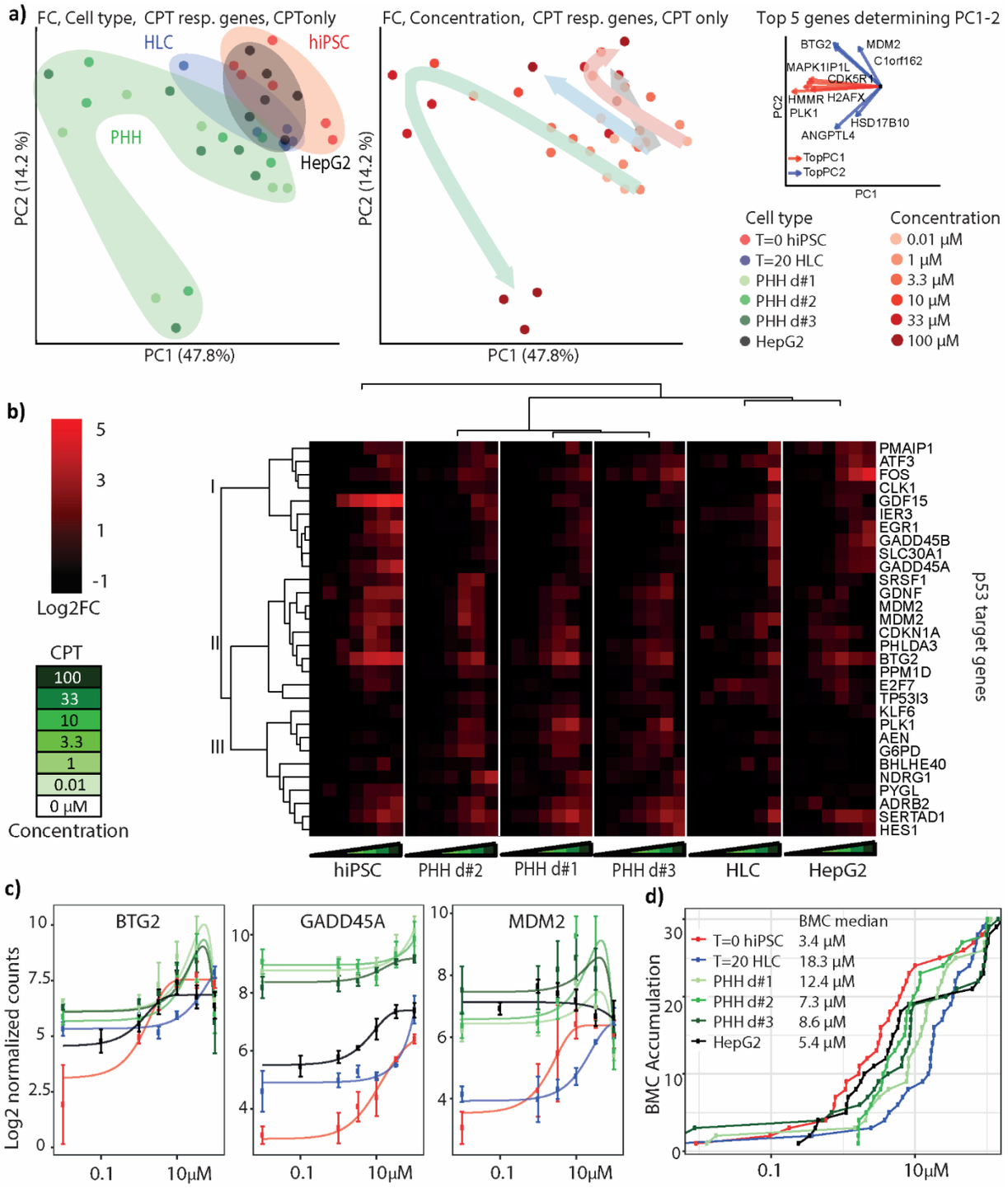

Fig. 5. Effect of the DNA damage response on the transcriptomic space of hiPSC, HLC, PHH and HepG2. A) Left panel: PCA of the CPT responsive genes (log2 normalized counts) with all treatments. Right panel: PCA of log2 fold changes of the CPT responsive genes after CPT exposure. The vector plots on the right represent the top 5 most determining genes of PC1 (red) or PC2 (blue). The size and orientation of the vector represent the contribution and PC-orientation of the 10 genes. B) Hierarchical clustering of the log2 fold changes of the top 30 DNA damage response (DDR) related genes after CPT exposure. C) Concentration response curves of log2 normalized counts for three DDR genes after CPT exposure. Dots and error bars (SE) represent gene expression data, lines represent best BMC model. D) BMC accumulation plots of the top 30 responding DDR related genes after CPT exposure. Median BMC were extracted from these plots. N=3

Transcriptomic space of HLCs and other liver test systems in TNFα-mediated inflammatory signalling.

TNF is a natural ligand of p55, TNF receptor I, and involved in the acute phase reaction of the systemic inflammation response. Here, we used TNF to induce an inflammation NF-kB signalling response in our test systems. A PCA analysis on a set of the TNF responsive genes (see ESM_2.xlsx) across all test system showed a very distinct TNF response of the HLCs as compared to PHH, HepG2 and hiPSC (Fig 6a). For HLCs (and to a lesser extent, HepG2), there was a concentration-dependent shift along the PC2 axis, mainly caused by increased expression of typical inflammation markers like *TNFAIP2, ICAM1* and *CCL2*. TNF exposure only led to a mild transcriptomic shift in the HepG2 and hiPSC. For PHH, a concentration-dependent shift along the PC1 axis was found which was mostly determined by *JUNB, DDIT4* and *CSK*. These genes are known to play a role in stress response signalling but not necessarily inflammation or NF-κB signalling pathway. The unique TNF response of every model was also evident from the hierarchical clustering of the log2 fold changes of the 30 most responsive NF-κB targets after TNF exposure (Fig 6b). It was evident that HLCs were by far the most sensitive to TNF exposure, as already at low concentrations a strong upregulation of typical inflammatory genes including *ICAM1, CCL2/20, CXCL1/2, TNFAIP3, CXCL5, VCAM1* and *SOCS3* was seen. Surprisingly, this change was not caused by an increased expression of the TNF-receptor family members. Only expression of *TNFRSF21* (associated with the fetal liver) was significantly increased in the HLCs model as compared to PHH. TNF concentration responses of three proto-typical NFκB downstream target genes (*ICAM, RELB* and *TNFAIP3*) demonstrated that while the basal expression levels of these genes in HLCs was low, there was a very strong induction after TNF exposure (Fig 6c). This effect was virtually absent in the undifferentiated hiPSCs. In HepG2 and PHH, there was higher basal gene expression of inflammatory targets, but only a mild induction after exposure to TNF. Besides, variation was seen in upregulation of inflammatory genes between the different PHHs, where for instance *CCL2* was dose-dependent upregulated in two of the PHHs but not in the third PHHs potentially due to the difference in initial inflammation state. Transcription factor activity analysis showed the activation of various NF-κB subunits among all models except for hiPSCs (supplemental table ESM4). The BMC accumulation plot for the 30 most responsive NF-κB targets indicated that both HepG2 and HLCs were very sensitive towards TNF exposure but hiPSC not at all (Fig 6d).

Discussion

PHH are regarded as the gold standard for hepatotoxic liability testing, but suffer from lack of availability, poor *in vitro* metabolic stability, and variability. Therefore, hiPSC-hepatic progeny is being evaluated as an alternative for chemical safety testing. Given that chemicals cause cell injury that triggers cellular stress response pathways, a question that has yet to be answered is how hiPSC-hepatic progeny compares to PHH in the context of cellular stress response activation. Using transcriptomic approaches, here we systematically assessed four critical stress pathways

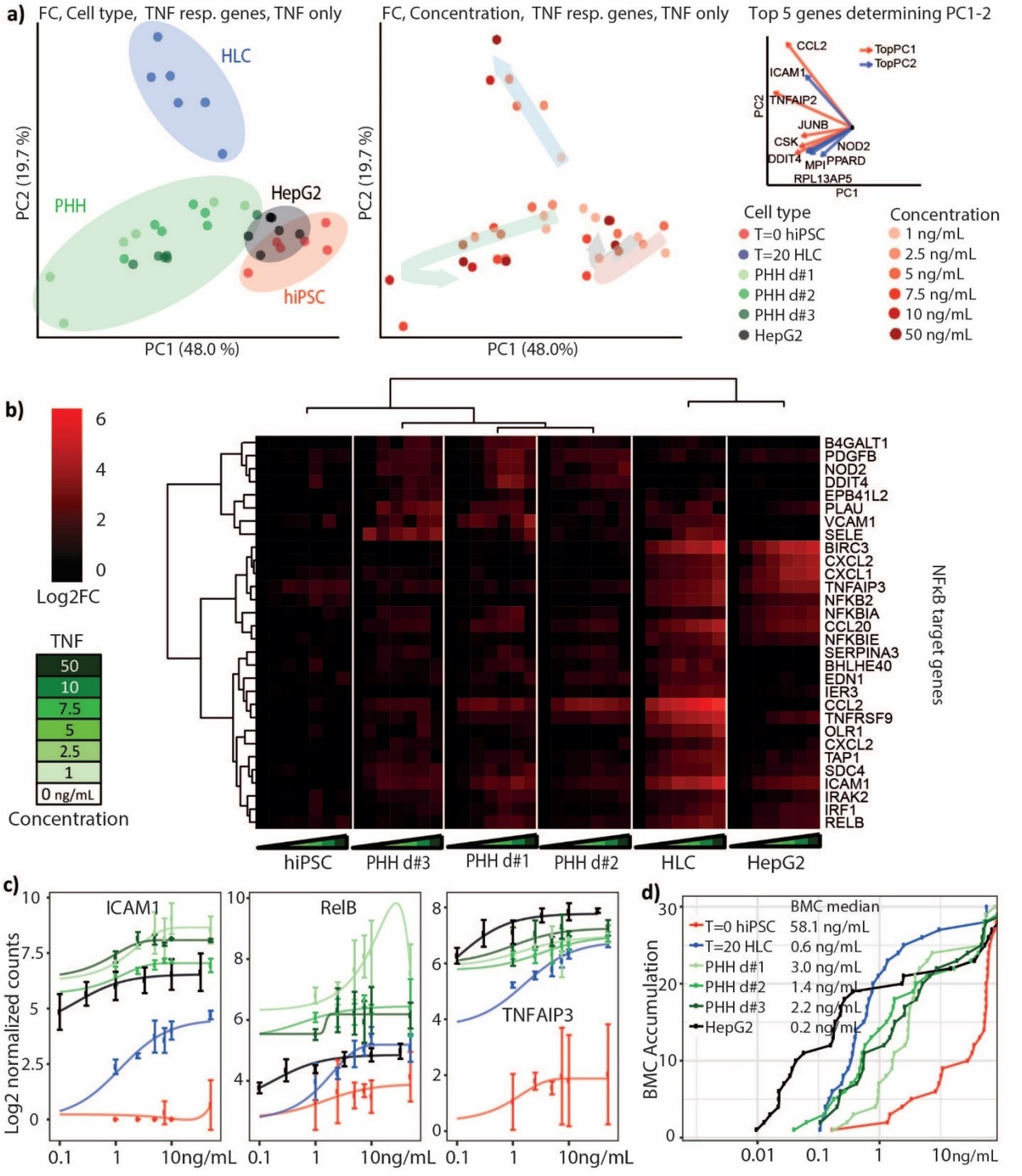

Fig. 6. Effect of the inflammation response on the transcriptomic space of hiPSC, HLC, PHH and HepG2. A) Left panel: PCA of the TNF responsive genes (log2 normalized counts) with all treatments. Right panel: PCA of log2 fold changes of the TNF responsive genes after TNF exposure. The vector plots on the right represent the top 5 most determining genes of PC1 (red) or PC2 (blue). The size and orientation of the vector represent the contribution and PC-orientation of the 10 genes. B) Hierarchical clustering of the log2 fold changes of the top 30 NFκB related genes after TNF exposure. C) Concentration response curves of log2 normalized counts for three NFκB target genes after TNF exposure. Dots and error bars (SE) represent gene expression data, lines represent best BMC model. D) BMC accumulation plots of the top 30 responding NFκB related genes after TNF exposure. Median BMC were extracted from these plots. N=3

involved in cell injury repair in hiPSC, hiPSC-HLCs, PHH and HepG2 cells. Our data indicate that the cellular stress response of HLCs is clearly different from undifferentiated hiPSC and more resembles that of liver (PHH and HepG2) cell type responses. The sensitivity score, which was calculated as an EC50 over the stress pathway BMC accumulation plot, was within a 3-fold difference compared to PHH donors, HLCs being more sensitive to oxidative stress and cytokine signalling, and PHH being more sensitive for ER stress.

We found that untreated HLCs were transcriptionally quite distinct from PHH. The overall transcriptomic similarity between HLC and PHH was as close to that of HLC and undifferentiated hiPSC, an observation that was previously also reported by another group[286]. However, HLCs are remarkably similar to PHH when comparing cellular stress response pathway activation. This suggests that HLCs have gained a differentiation status that reflects the responses observed in PHH. This is consistent with a previous proteomic study that compared the proteomic profiles of HLCs and PHH[287] and also sensitivity to hepatotoxic drugs[53,288]. This indicates that despite their relative immaturity, HLCs respond similarly to liver toxicants as gold standard *in vitro* models like PHH. Therefore, at least for compounds that do not require bioactivation, HLCs might be a predictive model for hepatotoxicity.

For this study we included one model compound per stress pathway to activate either an oxidative stress, DNA damage ER stress or inflammation conditions. Our study demonstrates clear dose response differences at the individual gene level between the different cell models. PHH were in particular sensitive for the onset of the UPR genes as a consequence of ER stress when compared to the other models. While the three individual donors showed average BMCs for UPR genes of around 0.1 µM, this was seven times higher for HLCs. Overall, individual UPR genes were activated throughout all model systems, although at different concentration levels. *HERPUD1*, *DDIT3*, *HSPA5*, three bona fide UPR genes, were already activated at around 0.1 µM in PHH being most sensitive, while HLCs showed activation starting at 1 µM. Despite difference in sensitivity, HLCs showed in general higher upregulation of UPR specific genes compared to PHH. The UPR is of prominent importance in both DILI responses in PHH as well as in the rat liver *in vivo*[97] and in liver disease settings[234].

In contrast to the UPR pathway, HLCs were more sensitive to TNF-mediated NF-kB target gene expression than the three PHH donors and more comparable to HepG2 cells. Clearly, differentiated HLCs were distinct from hiPSCs, as only very minimal TNF-mediated NF-kB target gene activation was observed in hiPSCs. As various liver diseases involve inflammatory signalling through NF-kB, including non-alcoholic fatty liver disease (NAFLD), liver fibrosis and cancer[289] as well as DILI[25], HLCs can be a good model to study TNF-mediated signalling responses, although this does not reflect the multicellular system including Kupffer and stellate cells mediating inflammatory signalling. If HLCs are combined with multiple liver-specific cell types in a 3D structure this may further improve its relevance for the study of inflammatory signaling[56]. The

limited sensitivity of the PHH to TNF could be related to the prior disease status, and that for instance the colon metastases had already affected the level of local or systemic cytokine levels that influence the PHH prior to isolation. On top of that, it is likely that the hepatocyte harvesting method also contributes to a pre-inflammatory state of the PHH.

Similarly, HLCs were also more sensitive for DEM-induced oxidative stress compared to PHH, and even more so than hiPSCs and HepG2, which showed an 8-fold lower sensitivity for NRF2 target gene induction. A study by Kang et al. showed similar differences where HLCs were more comparable to PHH in oxidative stress induction by acetaminophen than the less sensitive HepG2 model[288]. In the liver, high metabolic activity of hepatocytes results in elevated levels of ROS due to biotransformation and xenobiotic metabolism and therefore the necessity of a cellular defence mechanism through strong activation of the NRF2-mediated anti-oxidant response[290]. In that respect, the differentiation of hiPSCs towards HLCs lead to a sensitivity towards oxidative stress comparable to PHH making them suitable for the evaluation of chemical-induced oxidative stress response signalling.

On the other hand, HLCs were the least sensitive cell type for CPT-induced DDR-mediated P53 activation. While for all three PHH donors, the activation of P53 target genes, such as *MDM2*, *CDKN1A* and *BTG2* was initiated at around 10 µM, in HLCs this was about 2 times higher. These HLC responses are in sharp contrast to the high sensitivity of undifferentiated hiPSCs, responding already at 3 µM, and therefore illustrates the strong difference of the DDR in hiPSCs and differentiated liver progeny. Indeed, a study by Shimada *et al*. showed strong sensitivity towards DNA damage in hiPSCs compared to a differentiated state indicating a shift in the regulatory network of DNA damage signalling during differentiation[291].

Sensitivity towards the analysed stress pathways is an important feature for a hepatotoxicity model. We believe that in this respect a model cannot be too sensitive. Especially for DNA damage as a mutagenic effect will always increase the chance for a malignancy and sensitive models have in this respect less false negatives. For the *in vitro* to *in vivo* translation, the retrieved BMCs should be benchmarked to the BMCs of compounds of which the pathological outcome is known. Besides stress pathway sensitivity, metabolism is another important feature for a hepatotoxicity model. HepG2 cells as cultured in a 2D monolayer have a very low phase I and phase II drug metabolism. Bioconversion characteristics can therefore not be studied in this simple model[29], and PHHs and HLCs are in this case the preferred model.

In conclusion, despite limitation in full hepatocyte maturation, which caused a quite distinct overall basal transcriptomic space of HLC in comparison to PHH, HLCs did gain specific adaptive cellular stress response networks that mimic those of PHHs. We envision that the use of HLCs in hepatotoxicity screening will steadily increase and when differentiation protocols are further optimized, HLCs might be more reliable to uncover stress response activation to assess chemical

safety as well as to understand the modulation of cellular stress responses in hiPSC-derived liver disease models.

Acknowledgments

This work was supported by the EU-ToxRisk project funded by the European Commission under the Horizon 2020 programme (grant agreement number 681002), the Belgium IWT project HILIM-3D (project 140045) and the IMI MIP-DILI project (grant agreement number 115336).

Conflicts of interest: Lysiane Richert is founder and CSO of KaLy-Cell.

Chapter 8

Mapping inter-individual variability of toxicodynamics using high throughput transcriptomics and primary human hepatocytes from 50 donors

---

This chapter has been submitted as:

M. Niemeijer, W. Wiecek, S. Huppelschoten, P. Bouwman, A. Baze, C. Parmentier, L. Richert, R.S. Paules, F.Y. Bois and B. van de Water

Mapping inter-individual variability of toxicodynamics using high throughput transcriptomics and primary human hepatocytes from 50 donors.

Under review, 2022, Environmental Health Perspectives

Abstract

Understanding the variance across the human population with respect to toxicodynamic responses after exposure to chemicals is essential to define safety factors for risk assessment to protect the entire population. Activation of cellular stress response pathways are early AOP key events of chemical-induced toxicity and would elucidate the estimation of population variability of toxicodynamic responses. We aimed to map the inter-individual variability in cellular stress response activation in a large panel of primary human hepatocyte (PHH) donors to quantify toxicodynamic variability to derive safety uncertainty factors. High-throughput transcriptomics of over 8,000 samples was performed in panel of 50 individual PHH donors upon 8 to 24 h exposure to broad concentration ranges of four different toxicological relevant stimuli: tunicamycin for the unfolded protein response (UPR), diethyl maleate for the oxidative stress response (OSR), cisplatin for the DNA damage response (DDR) and TNFα for NF-κB signalling. Using a population mixed-effect framework, the distribution of benchmark concentrations (BMCs) and maximum fold change were modelled to evaluate the influence of PHH donor panel size on the correct estimation of inter-individual variability for the various stimuli. Transcriptome mapping allowed the investigation of the inter-individual variability in concentration-dependent stress response activation, where the average of BMCs had a maximum difference of 864, 13, 13 and 259-fold between different PHHs for UPR, OSR, DDR and NF-κB signalling-related genes, respectively. Population modelling revealed that small PHH panel sizes systematically under-estimated the variance and gave low probabilities in estimating the correct human population variance. Estimated toxicodynamic variability factors were up to 2-fold higher than the standard uncertainty factor of $10^{1/2}$ to account for population variability during risk assessment, exemplifying the need of data-driven variability factors. Overall, by combining high throughput transcriptomics and population modelling, improved understanding of interindividual variability in stress response activation across the human population was established, thereby contributing towards increasing the confidence of in vitro-based prediction of adverse responses, in particular hepatotoxicity.

Key words: inter-individual variability, uncertainty factors, stress response pathways, primary human hepatocytes, high throughput transcriptomics, population modelling

Introduction

For safety assessment a default uncertainty factor (UF) of 10 is used, with the goal to equally cover toxicokinetic and toxicodynamic variance[59]. Whether this UF of 10 is enough to capture the full human population variance is unclear and this hampers a reliable risk assessment. Therefore, there is a need for data-driven UFs which are both chemical and endpoint specific and accurately account for inter-individual variability. While the variability of toxicokinetic properties has received much investigation, the inter-individual variability of toxicodynamics is poorly understood.

The development of chemical-induced liver injury is one of the main reasons for drug withdrawal from the market[269] and also one the most frequent adverse outcome in in vivo chemical safety testing[1,292]. Therefore, it is key to improve prediction of hepatotoxicity at an early stage in research and development. For the evaluation of liver injury by chemicals or drugs, primary human hepatocytes (PHHs) are currently considered to be the gold standard of tissue culture models for human liver toxicity. Despite their disadvantages, such as dedifferentiation and source limitations, they closely resemble human hepatocytes *in vivo*, allowing for the study of chemical-induced liver injury[293]. Therefore, PHHs from different donors form an excellent basis to get deeper understanding of inter-individual variability in toxicodynamics responses.

During chemical-induced stress, cellular defensive mechanisms are activated to restore homeostasis. Well known stress responses are the oxidative stress response in reaction to accumulation of reactive oxygen species (ROS) regulated by nuclear factor, erythroid 2 like 2 (*NFE2L2*/NRF2), the unfolded protein response (UPR) activated upon accumulation of misfolded proteins in the endoplasmic reticulum (ER) regulated by three sensors endoplasmic reticulum to nucleus signalling 1 (*ERN1*/IRE1α), activating transcription factor 6 (ATF6) and eukaryotic translation initiation factor 2 alpha kinase 3 (*EIF2AK3*/PERK), DNA damage response mediated by tumor protein P53 (*TP53*/P53) signalling upon DNA damage and NF-κB signalling upon inflammatory conditions. Monitoring the activation of these adaptive stress responses upon chemical exposure can give insight into liver injury liabilities of chemicals as well as the underlying modes-of-action[27,28]. Because of the protective functions of adaptive stress responses, inter-individual variations in their activities affect adverse outcomes such as liver injury. Quantitative insight in these variations among the human population would allow the derivation of data-driven toxicodynamic UFs specifically for each type of stress response, thereby enabling better predictions of liver injury liabilities.

Omics approaches such as transcriptomics, are powerful tools to fully map differences in adaptive stress response signalling networks across different patients. Several studies have already used transcriptomics approaches to compare differences between chemical-induced stress responses in different liver cell culture models[274,294]. Due to advances in this area, novel approaches such as targeted TempO-Seq technology can now be used, which allow for transcriptome mapping of gene sets of interest in a high-throughput fashion[29,30]. This allows large-scale population studies and accurate analyses of inter-individual variance in transcriptomic perturbations for the improvement of DILI liability assessment. When combining experimental transcriptomic data with population modelling, an estimate of the variance across the entire population can be derived, an approach taken by Blanchette *et al.* for the evaluation of the variance in chemical-induced cardiotoxicity[54,295].

Here, to map the inter-individual variability in stress response activation upon chemical exposure, we profiled the transcriptome for over 8,000 samples of a large panel of 50

cryopreserved PHHs derived from different individuals and exposed to a broad concentration range of specific stress response inducing compounds, namely diethyl maleate, tunicamycin, cisplatin and TNFα to induce the oxidative stress, UPR, DNA damage and NF-κB signalling, respectively. Chemical-induced perturbation of the transcriptome was evaluated upon 8 and 24h of exposure using TempO-Seq technology[30]. In combination with population modelling, these data allows to evaluate the influence of PHH panel sizes on the correct estimation of inter-individual variance in chemical stress responses and exemplify the need of data-driven toxicodynamic UFs, which will contribute to improved prediction of chemical-induced liver injury liabilities.

Methods

Cell culture

Plateable cryopreserved PHHs[296] were derived from 54 different individuals (KaLy-Cell, Plobsheim, France) with permission of the national ethics committees and regulatory authorities (Excel Table S1). For plating, PHHs were thawed in warm water bath at 37°C and diluted in pre-warmed thawing UCRM medium (IVAL, Columbia, USA) followed by centrifugation at 170g for 20 min at RT. Thereafter, cell pellet was diluted in seeding UPCM medium (IVAL) and viability was assessed using the Trypan blue exclusion method. Cells were plated at a density of 70.000 cells in 100 µL per well in 96 wells BioCoat Collagen I Cellware plates from Corning (Wiesbaden, Germany). After 6 hours, medium was refreshed with seeding UPCM medium. PHHs showing less than 70% confluency 24 h after plating were discarded for further analysis leading to a panel of PHHs derived from in total 50 individuals. Characteristics of these PHHs are depicted in Supporting Fig. S1. To evaluate variability in dedifferentiation upon culturing of PHHs, samples were also generated from PHHs directly upon thawing or from snap-frozen liver tissue derived from 8 individuals (Excel Table S1).

Cell treatment

Prior to compound exposure, PHHs were first washed after 24 h of attachment using 1x PBS to remove unattached cells. Exposures were done using William's E medium supplemented with 100 U/mL penicillin and 100 µg/mL streptomycin. PHHs were exposed to four reference compounds in a broad concentration range known to induce specific stress response pathways (Supporting Table S1), namely tunicamycin and diethyl maleate from Sigma, TNFα from R&D systems and cisplatin from Ebewe. To evaluate variability in stress response activation by DILI compounds, PHHs were exposed to a broad concentration range of acetaminophen, propylthiouracyl, nitrofurantoin, ticlopidine, nefazodone and diclofenac (Supporting Table S1) from Sigma. All compound stocks, except for TNFα and cisplatin, were prepared using dimethylsulfoxide (DMSO) from BioSolve and stored at -20°C. End concentration of DMSO in all conditions were kept identical at 0.2%.

Cell viability

To evaluate cytotoxicity, LDH release was evaluated after 24 h of exposure in supernatants using cytotoxicity detection kit from Roche according to instructions by provider. As positive control, supernatant of PHHs incubated for 5 minutes with 1% triton was taken along. Collected supernatants were stored at 4°C for a maximum of 3 days before analysis. Upon analysis, supernatants were diluted 10x and measured in triplicate. Absorbance was measured at 490 nm with a VICTOR plate reader (PerkinElmer). Cell viability was determined for three biological replicates for each condition for each PHH.

Targeted sequencing

After exposure for 8 or 24 h, the transcriptome was analysed using the targeted TempO-Seq technology (BioSpyder Technologies, Inc., Carlsbad, CA, USA). First, cells were washed with 1x PBS and lysed with 50 µL 1x BNN TempO-Seq lysis buffer per well (BioSpyder). Lysates were incubated for 15 min at RT and stored at -80°C. Samples were shipped for TempO-Seq analysis(Yeakley et al. 2017) using the S1500+ gene set of NIEHS[164] supplemented with additional stress response relevant genes (Excel Table S2) at BioSpyder (Carlsbad, CA, USA) and sequenced using a HiSeq 2500 Ultra-High-Throughput Sequencing System (Illumina, San Diego, CA, USA). For each PHH, three biological replicates were analysed. To evaluate variance in dedifferentiation, samples from PHHs in suspension directly upon thawing, snap-frozen liver tissue or PHHs grown in 2D for 24 h derived from 8 individuals were analysed using the targeted whole transcriptome panel in combination with TempO-Seq technology (BioSpyder) (Excel Table S2).

Transcriptomics dose-response analysis and statistics

For the analysis of TempO-Seq transcriptome data, as a first step reads were aligned by BioSpyder technologies using the TempO-Seq R package. Derived raw counts were normalized using the DESeq2 R package[165] and log2 transformed. For each PHH and condition, three biological replicates were analysed and represented as the mean. A library size cut-off was used of 100,000 counts to eliminate samples having low amount of total counts (Supporting Fig. S2). To evaluate variability in sensitivity for stress response activation, benchmark concentration (BMC) modelling was done using the BMDExpress 2 software developed by Sciome LCC and NIEHS/NTP/EPA[31,32]. Dose response modelling was done for each gene and sample using various models (exponential, linear, polynomial, hill and power model). The BMC was defined as the concentration at which 1 standard deviation of increase in gene expression was seen. For each reference compound, the top 50 activated genes across the PHH panel were defined based on both the BMC and the maximal fold change across concentration range (maxFC) (Excel Table S2). The median BMC and maxFC were calculated based on these top 50 genes for each PHH. To classify PHHs for their sensitivity, a sensitivity score was calculated based on the sum of the ranking of the median BMCs and maxFC at both time points for the top 50 genes for each reference compound. Principal component analysis (PCA) was done using prcomp from the Stats Rpackage. Hierarchical

clustering based on Euclidean distance and Wards method was done using Rpackage pheatmap. Significant differences between PHHs with certain disease background were calculated using unpaired Student's t test represented as *p < 0.1, **p < 0.05, ***p < 0.01. Data analysis and visualization was done using R 3.4.1 and Rstudio (Boston, USA) with the following Rpackages: DESeq2, pheatmap, ggplot2, data.table, dplyr, reshape2, stats. To evaluate difference in pathway activation between different PHHs, gene set enrichment analysis (GSEA) in combination with Gene Ontology (GO) gene sets v7.1[244] retrieved from the MSigDB was performed using the maxFC as input in the GSEA software (derived from joint project of UC San Diego and Broad Institute)[297,298]. Visualization of GSEA results was done using Cytoscape 3.8.1 software[246] in combination with EnrichmentMap[247] and WordCloud[248].

Population statistical modelling

The BMC-maxFC values distributions were modelled in a Bayesian hierarchical framework. We were interested a priori by inter-subject variability; therefore, our primary observational unit was the individual donor. Genes were considered as exchangeable; independent and identically distributed.

At the level of the i^{th} subject, we assumed that the counts n_{ik} of genes falling in the k^{th} of the K (equal to either two or four) pre-defined clusters followed a multinomial distribution:

$$\boldsymbol{n}_{\mathrm{i}} = (n_{i1}, \dots, n_{iK}) \sim Multinomial\,(p_{i1}, \dots, p_{iK}) \quad (1)$$

At the population level, the subjects' multinomial probabilities were softmax-transformed and the corresponding parameters $\boldsymbol{\beta}$ were assumed to be multivariate-normal-distributed around a population mean $\boldsymbol{\mu}$ with covariance matrix $\boldsymbol{\Omega}$.

$$p_{ik} = \frac{\exp(\beta_{ik})}{\sum_{j=1}^{K} \exp(\beta_{ij})} \quad (2)$$

$$\beta_{i1} = 0 \quad (3)$$

$$(\beta_{i2}, \dots, \beta_{iK}) \sim N_{K-1}(\boldsymbol{\mu}, \boldsymbol{\Omega}) \quad (4)$$

The prior on each element of $\boldsymbol{\mu}$ was a vague normal distribution:

$$\mu_k \sim N\,(0, 5) \quad (5)$$

The prior on $\boldsymbol{\Omega}$ was a Cauchy-LKJ (Lewandowski-Kurowicka-Joe) distribution with a Cauchy-distributed diagonal vector of standard deviations $\boldsymbol{\vartheta}$:

$$\theta_k \sim Cauchy\,(0, 2.5) \quad (6)$$

and a LJK-distributed prior on the correlation matrix $\boldsymbol{L}$:

$$\mathbf{L} \sim LKJ\,(3) \quad (7)$$

The *Stan* statistical software was used to obtain a posterior sample of $\boldsymbol{\mu}$, $\boldsymbol{\vartheta}$, and $\boldsymbol{L}$ values by Hamiltonian Monte Carlo simulations.

Still at the i^{th} subject level, we modelled independently for each cluster the joint distribution of genes' BMCs (noted x in the following) and maxFCs (noted y) values as a bivariate lognormal distribution. We took the absolute value of negative maxFC values before log-transformation:

$$(\log(\boldsymbol{x}_i), \log(abs(\boldsymbol{y}_i))) \sim N_2\left((\upsilon_{xi}, \upsilon_{yi}), \boldsymbol{\Delta}_i\right) \quad (8)$$

with **Δ** defined as

$$\boldsymbol{\Delta}_i = \begin{pmatrix} \sigma_{xi} & \rho_i \\ \rho_i & \sigma_{yi} \end{pmatrix} \quad (9)$$

At the population level, we modelled the distributions of subjects' means υ_{xi} and υ_{yi}, of the standard deviations σ_{xi} and σ_{yi}, and of the correlation coefficient ρ_i as normal around their population counterparts:

$$\upsilon_{xi} \sim N(\upsilon_x, \sigma_a) \quad (10)$$

$$\upsilon_{yi} \sim N(\upsilon_y, \sigma_b) \quad (11)$$

$$\sigma_{xi} \sim N(\sigma_x, \sigma_c) \quad (12)$$

$$\sigma_{yi} \sim N(\sigma_y, \sigma_d) \quad (13)$$

$$\rho_i \sim N(\rho, \sigma_e) \quad (14)$$

The standard deviations σ_a, σ_b, σ_c, σ_d, σ_e, were all assigned a half normal prior with SD 0.2. The other priors were:

$$\upsilon_x \sim Uniform(-5,7) \quad (15)$$

$$\upsilon_y \sim Uniform(-11.5,5) \quad (16)$$

$$\sigma_x \sim Halfnormal(1) \quad (17)$$

$$\sigma_y \sim Halfnormal(1) \quad (18)$$

$$\rho \sim Uniform(-1,1) \quad (19)$$

All model parameters (265 parameters in total for each chemical exposure) were jointly estimated from the data with Metropolis-Hastings Markov chain Monte Carlo simulation, using the *GNU MCSim* software V6.1.0.

Predictive simulations

For predictions of inter-subject variability, the transformed BMC and maxFC values were restored to natural space using the suitable inverse transformations. First, large sample reference median coefficients of variation (CVs) were obtained for BMC and maxFC values by simulating of 1,000 assays with hepatocytes from 2,000 individuals each. For each simulated individual, BMC and maxFC values were simulated by Monte Carlo sampling using the average posterior estimates of the population parameters obtained by calibration of the model with the experimental data on 50 individuals. Those can therefore be considered as "true CV values", conditionally on the BMC-

maxFC values being correctly modelled. Similar assay simulations were performed for smaller, realistic, donor panel sizes (N = 3, 4, 5, 6, 7, 8, 10, 12, 14, 16, 20, 24, 28, 32, 36, 40, 50). CVs for BMC and maxFC values were obtained for each case.

Results

Variability in basal gene expression across PHH panel

Since PHH show dedifferentiation in cell culture, as an initial step, the variance in dedifferentiation of PHHs derived from different individuals during culture was evaluated (Fig. 1A-B). For this purpose, we used whole transcriptome targeted TempO-Seq analysis of liver tissue and derived cryopreserved PHHs upon thawing or cultured in 2D for 24 h for eight different individuals. Principal component analysis (PCA) showed greatest variability between individuals for freshly thawed PHHs (Fig. 1A-B). Noticeably, the transcriptome of PHHs cultured in 2D was more alike liver tissue compared to freshly thawed PHHs for principal component 1, representing 60.9% of the total variance (Fig. 1A). However, when only considering liver-related genes, both PHHs cultured in 2D or freshly thawed were similarly distinct from liver tissue for both principal components, although the latter being more variable (Fig. 1B). Genes involved in metabolism, such as *CYP3A4*, *CYP2C8* and *UGT2B7* were mostly differently expressed between liver tissue and PHHs, either cultured in 2D or freshly thawed.

Next, we evaluated differences in gene expression for a panel of PHHs derived from 50 individuals cultured for 24 h in 2D for all genes (Fig. 1C), liver-related genes (Fig. 1D) or stress response-related genes (Supporting Fig. S3). PHHs from some individuals showed altered expression for genes dominating the variance across the first principal component based on all genes, such as *DDIT4,* a regulator of mTOR activity induced upon various stress conditions (Fig. 1C). In addition, variability in various phase-I enzymes such as *CYP3A4* was seen across the panel of PHHs mostly affecting the second principal component for liver-related genes (Fig. 1D and Supporting Fig. S4). Also, large variation was seen in the expression of *CCL2*, a chemokine involved in the recruitment of monocytes and basophils, affecting the principal components for all genes (Fig. 1C) but also more specifically UPR and NF-κB signalling related genes (Supporting Fig. S3).

Difference in sensitivity towards chemical-induced cell death

To evaluate the inter-individual variability in chemical-induced cellular stress responses across the panel of 50 PHH cultures, PHHs were exposed for 8 or 24 h to broad concentration ranges of specific stress inducers: diethyl maleate (DEM) to induce the oxidative stress response, tunicamycin (TUN) for the unfolded protein response, cisplatin (CPT) for the DNA damage response and TNFα for inflammatory NF-κB signalling (Fig. 1E). Great difference in viability, measured by LDH release, was only seen between PHHs from different individuals following 24 h exposure at the highest concentration of DEM, where significant induction of cell death was seen for a subset of PHHs while other PHHs did not show viability loss at all (Fig. 1F). The other compounds did not lead to significant loss of viability upon 24 h of exposure, although some PHHs

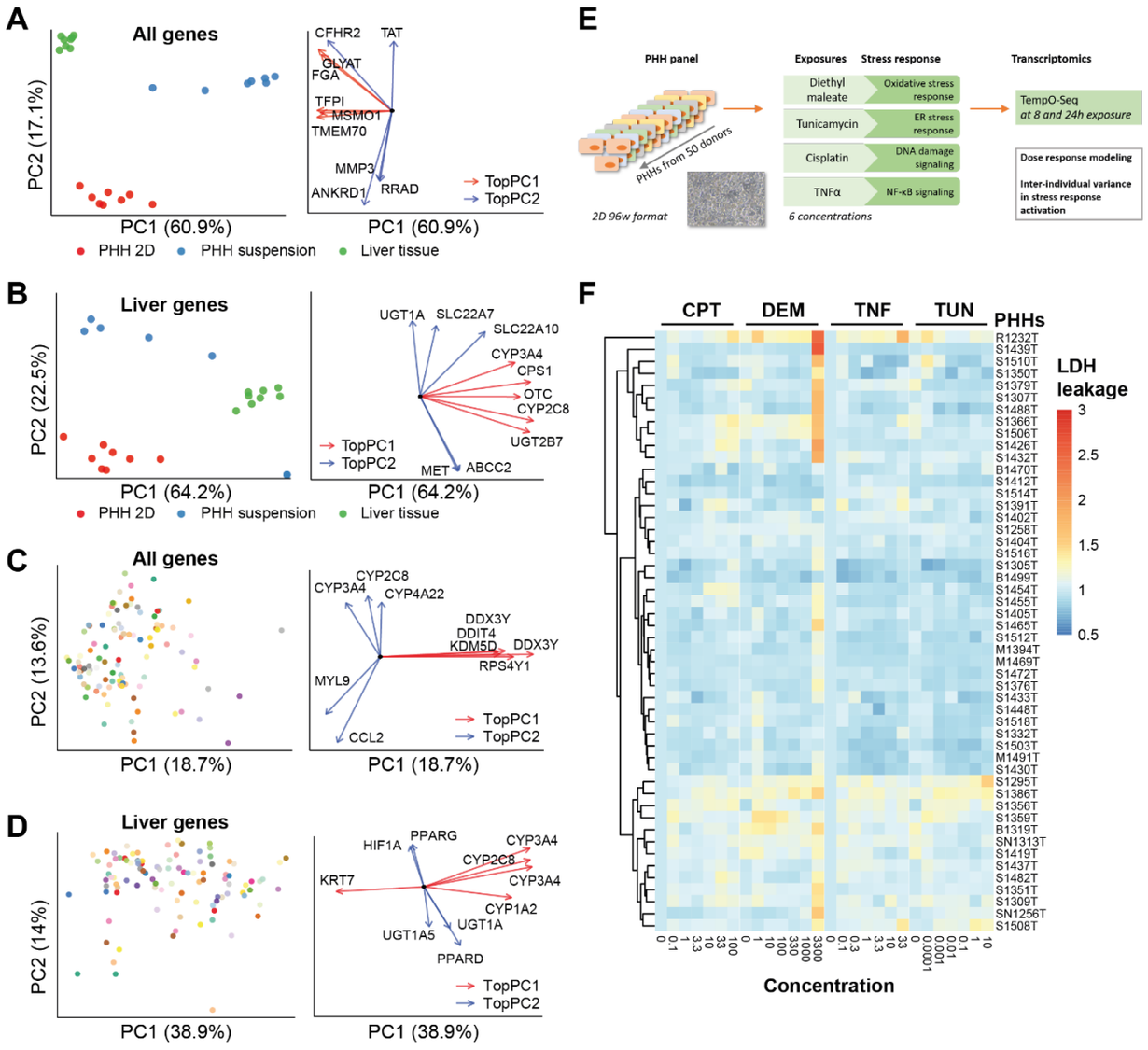

Fig. 1. Characterization of the inter-individual variability utilizing a large panel of primary human hepatocytes derived from 50 individuals. A-D) Left panel: Principle component analysis (PCA) based on gene expression as log2 normalized counts. Right panel: Top 5 genes mostly determining PC1 or 2 depicted as vectors representing contribution and PC orientation. A-B) PCA of liver, PHHs in suspension or grown as 2D based on all genes (A) or liver-related genes (B) in whole transcriptome panel. C-D) PCA of panel of 50 PHHs depicted in different colours based on all genes (C) or liver-related genes (D) of S1500+ gene set. E) Schematic representation of experimental setup. F) LDH leakage upon exposure to DEM, TUN, CPT and TNFα in wide concentration range for 24 h across panel of PHHs. N = 3.

were more sensitive, such as R1232T and S1295T, resulting in a minor LDH release at the highest concentrations.

Inter-individual variability in chemical-induced stress response activation

Next, the effects of 8 or 24 h of chemical exposure on the PHH transcriptomes were analysed. Exposure to the oxidative stress-inducing compound DEM resulted in clear upregulation of NRF2 target genes *HMOX1* and *SRXN1* at concentrations ranging from 330 µM to 3300 µM for both time points (Fig. 2A). Cisplatin-induced DNA damage signalling in the panel of PHHs was most

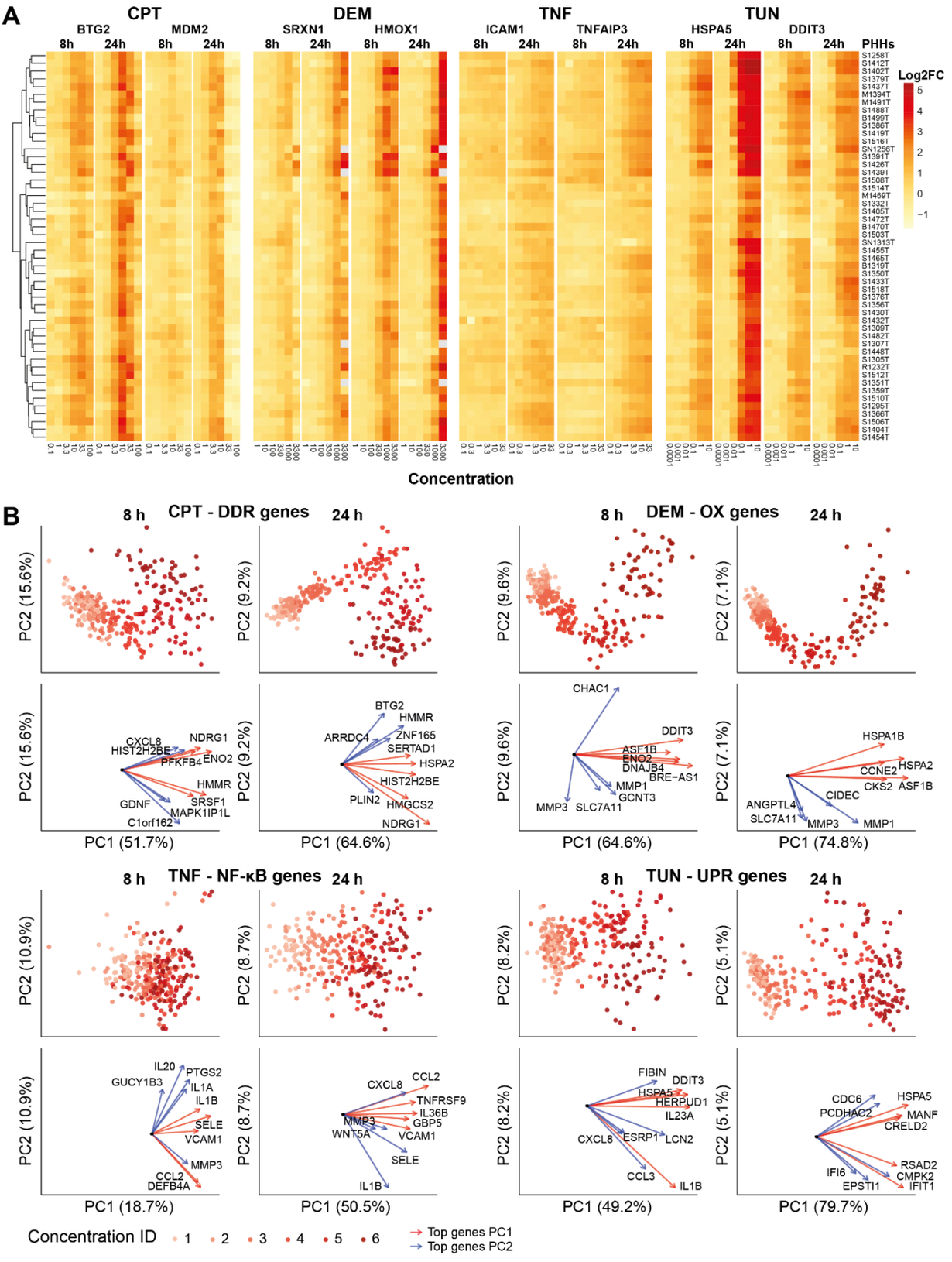

Fig. 2. Inter-individual variability in concentration-dependent stress response activation. A) Hierarchical clustering of log2 fold change gene expression of key genes for each evaluated stress response pathway of panel of PHHs exposed to reference compounds. B) Principle component analysis (PCA) based on log2 fold changes of stress responsive genes of panel of PHHs exposed to DEM, TUN, CPT and TNFα. Top 5 genes mostly determining PC1 or 2 depicted as vectors representing contribution and PC orientation. N=3.

profound at a concentration of 10 µM upon 24 h of exposure, where in general the highest upregulation of P53 target genes *BTG2* and *MDM2* was seen. PHHs showed variable responses, where some showed *BTG2* or *MDM2* upregulation already at a cisplatin concentration of 1 µM, while others required higher amounts of this compound. Regarding the UPR induced by TUN, activation of both the adaptive gene *HSPA5* and pro-apoptotic related gene *DDIT3* was seen at a concentration of 0.01 µM or higher at the 24 h time point. Some PHHs showed already strong upregulation of both genes at 0.01 µM of TUN, while other PHHs only showed upregulation at 1 µM or higher, suggesting particularly large differences in the UPR response of different individuals. Upon TNFα exposure to study variance in inflammation signalling, NF-κB target genes *ICAM1* and *TNFAIP3* were activated in a concentration-dependent manner. For most of the PHHs, activation was seen at 1 ng/mL and higher when exposed for 24 h. Some PHHs showed activation at the lowest concentration of 0.1 ng/mL, while other PHHs were completely unresponsive to TNFα exposure.

Subsequently, we selected the top 50 most strongly activated genes at the lowest effective concentration (Excel Table S2) of each stress response reference compound. The inter-individual variability in the concentration-dependent activation of these top 50 genes for each stress response was evaluated by PCA (Fig. 2B). In general, for all compounds a clear concentration-dependent shift was seen for all PHHs. Most variability was observed between different PHHs for TUN-induced UPR genes and TNFα-induced NF-κB related genes, mainly driven by variable expression of cyto- or chemokines such as *IL1B*.

Inter-individual differences in points-of-departure of stress response activation

To evaluate the inter-individual variability in sensitivity to chemical-induced stress response activation, we defined benchmark concentrations (BMCs) at which the top 50 most strongly activated genes for each specific compound showed an increase of 1 standard deviation in gene expression (Excel Table S3). Upon dose response modelling, we observed large differences in the gene-specific BMCs between different PHHs (Fig. 3A). In general, most variability was seen at 8 h of exposure, while at 24 h the response was more stable across the PHH panel. Large shifts in the BMC distribution could be seen especially at the 8 h time point, with medians varying 864, 259, 13 and 13-fold for TUN, TNFα, DEM and CPT, respectively (Table 1). This means that BMC estimations can shift significantly depending on which PHHs are taken along in chemical toxicity testing at early time points. Variability could also be observed in the distribution of the maxFC of the top 50 most strongly activated genes among the different PHHs, where compound sensitivity correlated positively with levels of upregulation (Supporting Fig. S6).

To further assess differences in PHH sensitivity, sensitivity scores were determined based on both the median BMC and maxFC for the top 50 activated genes for each compound for both time points (Supporting Fig. S5B and Data S4). A subset of PHHs (cluster I-II) showed high sensitivity scores for all stress responses induced by the reference compounds and also showed higher cell

Table 1. Median benchmark concentrations for each PHH based on top 50 stress responsive genes for each compound and time point.

	CMP	*Median BMC ± SD (min-max)*	*FC min-max Median BMC*	*$TDVF_{0.01}$ Exp data*	*$TDVF_{0.01}$ Model**	*SD $TDVF_{0.01}$ Model**
8 h	TUN	0.534 ± 1.320 (0.009 - 7.768)	864.1	**6.545**	**6.317**	0.582
	DEM	352.486 ± 243.643 (111.726 - 1405.220)	12.6	2.517	1.828	0.066
	CPT	9.488 ± 5.867 (2.640-35.447)	13.4	2.786	**3.241**	0.202
	TNF	12.447 ± 13.310 (0.157 - 40.633)	258.8	**26.524**	**5.315**	0.423
24 h	TUN	0.023 ± 0.061 (0.002 - 0.447)	223.5	**4.950**	**4.811**	0.386
	DEM	315.597 ± 108.883 (176.656 - 623.096)	3.5	1.701	1.624	0.047
	CPT	3.083 ± 1.022 (1.471 - 6.401)	4.4	1.847	2.184	0.090
	TNF	0.926 ± 2.252 (0.137 - 15.263)	111.4	2.516	2.556	0.128

**Based on population modelling of 2000 virtual donors for 1000 assays*

death induction at the highest concentration of DEM (Fig. 3B). In addition, a subpanel of PHHs (cluster III) was highly sensitive towards TNFα, while being insensitive towards all other chemical induced stress responses. Thus, PHHs can be sensitive to chemical compounds in general, but also selectively sensitive for specific types of stress-inducing chemicals. In addition, positive correlations could be seen between cell death induction as measured by LDH release and the sensitivity scores, where in general PHHs with high LDH release were more sensitive for stress response activation (Fig. 3B, Supporting Fig. S7). This indicates that for the most sensitive PHHs the switch towards adverse signalling was already reached at lower concentrations of stress-inducing chemicals.

Next, we calculated a data-driven toxicodynamic variability factor ($TDVF_{0.01}$), which is the ratio between the median population point-of-departure (PoD) and the 1% quantile individual PoD. This $TDVF_{0.01}$ accounts for underestimation of the variance within the human population when estimating the PoDs for cellular stress response activation upon chemical exposures (Table 1). For DEM-mediated oxidative stress and cisplatin-induced DNA damage, the commonly used uncertainty factor[59] of 3.16 would be enough since data-based $TDVF_{0.01}$s were all lower at both 8 and 24 h timepoint. However, for 8 h TUN-induced UPR activation and TNFα-mediated NF-κB signalling, the defined $TDVF_{0.01}$ was higher than the uncertainty factor of 3.16, namely 6.5 and 26.5, respectively. At the 24 h timepoint, which showed in general less variability across the panel of PHHs than the 8 h timepoint, TUN-induced UPR had a $TDVF_{0.01}$ of 5, which is also higher than the standard factor. These examples show that the standard uncertainty factor is not enough to capture the variation in all chemical-induced stress responses within the human population.

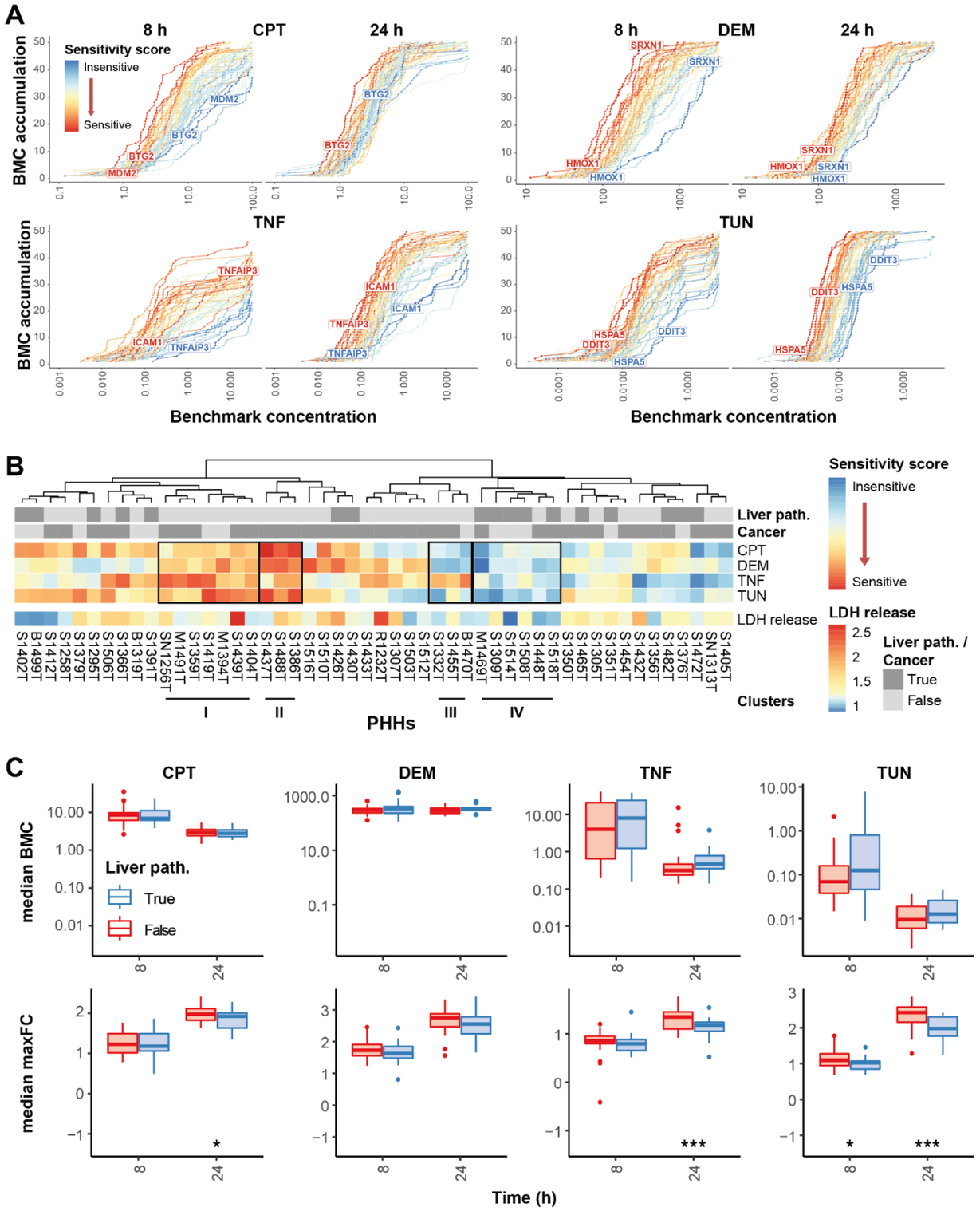

Fig. 3. Benchmark concentration distributions across panel of primary human hepatocytes (PHHs) and influence of liver disease status. A) Distribution of bench mark concentrations (BMC) of top 50 stress responsive genes for each compound. Lines represent the different PHHs within panel. B) Hierarchical clustering of sensitivity score for panel of PHHs for each treatment. The LDH leakage is shown of 3300 µM DEM at 24 h and the disease status. C) Boxplots of median BMC or maxFC of top 50 stress responsive genes of exposure for each treatment for PHHs with or without liver disease status. Significance levels represented as * $p < 0.1$, ** $p < 0.05$, *** $p < 0.01$. N = 3.

Influence of pathology on stress response activation

Inter-individual variability could be based on liver pathology background of donors. Therefore, next, the influence of the disease status, such as cancer or different types of liver pathology, on stress response activation upon chemical exposure in PHHs was evaluated. In general, the presence of any type of cancer did not have an obvious influence on the sensitivity of the PHHs towards chemical-induced stress, since clear clustering of sensitivity scores of PHHs derived from patients with cancer was not seen (Fig. 3B). In addition, presence of cancer only mildly influenced the distribution of median maxFC and BMC for the top 50 stress responsive genes (Supporting Fig. S8B). In contrast, PHHs from patients having any type of liver pathology were in general less sensitive towards chemical-induced stress, especially for TUN-induced UPR and TNFα-induced NF-κB signalling (Fig. 3B). When we evaluated the distribution of the median maxFC, a significant difference could be seen between PHHs derived from patients with or without liver pathology when exposed to TUN or TNFα for 24 h (Fig. 3C). The same trend was seen for DEM and CPT, although this was not significant. Possibly, PHHs from patients with a certain liver pathology were already at a higher level of stress leading to lower fold changes upon chemical-induced stress. Indeed, these PHHs showed in general significant slightly higher basal expression of the top 50 stress responsive genes compared to PHHs without liver pathology (Supporting Fig. S8C, Excel Table S3). Variability in differentiation status did not have an effect on BMC and maxFC distribution (Supporting Fig. S9).

Variance in pathway enrichment upon chemical exposure

To get more insight in chemical-induced stress pathway activation, gene set enrichment analysis of gene ontology terms was performed using the maxFC as input for ranking of the genes. In general, upon exposure to each reference compound, expected terms were enriched related to anticipated chemical-induced stress response pathways (Fig. 4A, Supporting Fig. S10). For instance, TUN treatment led to the strong enrichment of ER stress and UPR-related terms, TNFα resulted in chemotaxis and chemokine-related terms, DEM gave enrichment of heat shock or ion response-related terms and CPT treatment led to enrichment of ion or metabolic-related terms. All chemicals led to enrichment for both sensitive and insensitive PHHs, although some terms were more specific for either sensitive or insensitive PHHs, e.g. terms related to response to ions were more enriched for insensitive PHHs upon DEM exposure (Fig. 4A). Clustering of enriched terms for at least three PHHs showed specific enrichment of terms related to ribosomal localization or subunits for insensitive PHHs upon TUN or CPT exposure, while terms related to response to virus or interferon were enriched for specifically sensitive PHHs upon TNFα treatment (Fig. 4B).

Inter-individual variability in stress response activation by hepatotoxicants

The inter-individual difference in sensitivity towards chemical-induced oxidative stress response and UPR activation was further analysed by screening the three most sensitive and insensitive

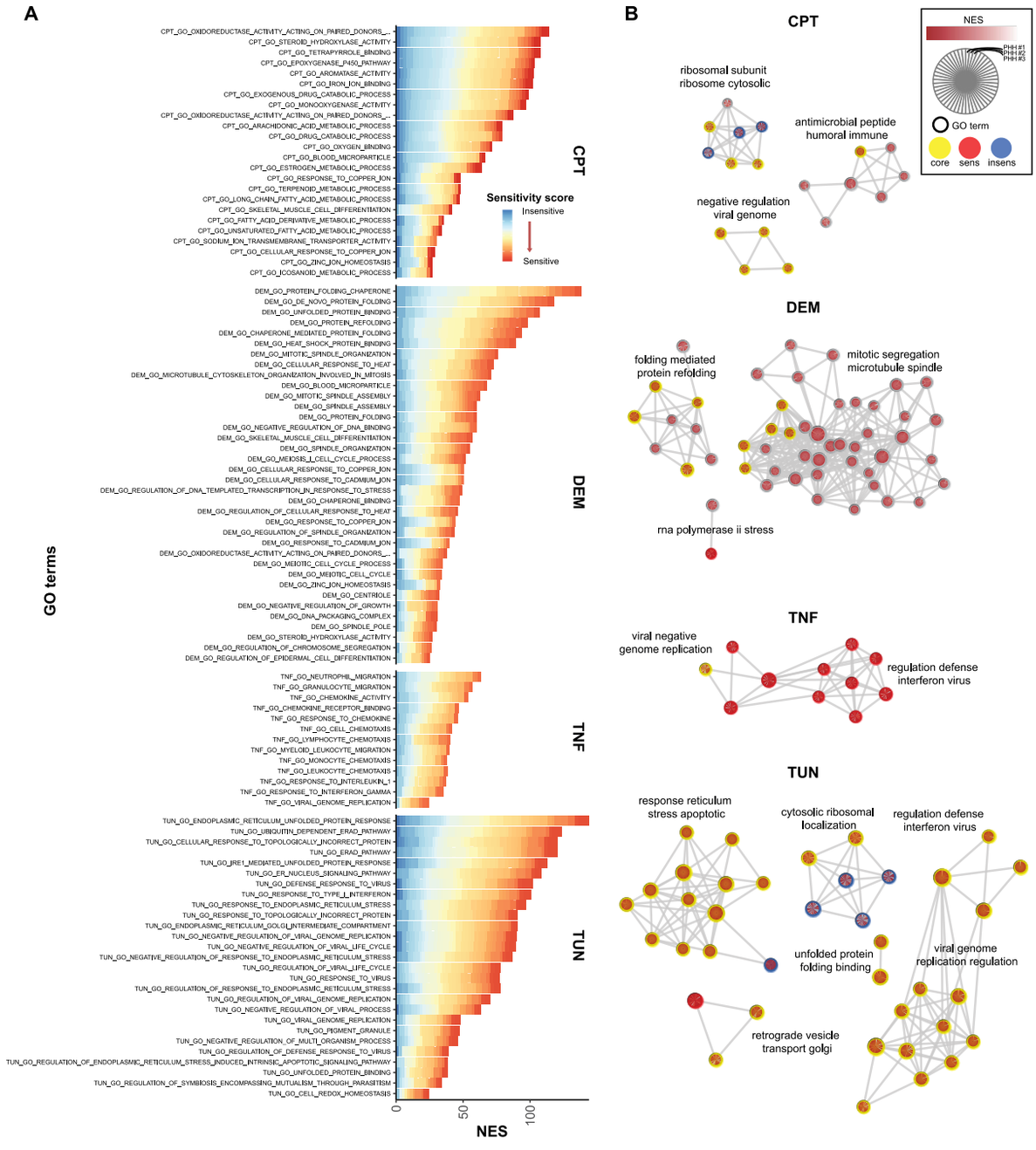

Fig. 4. Variance in gene set enrichment upon chemical-induced stress. Gene set enrichment analysis (Subramanian et al. 2005) was done using gene ontology terms v7.1 and the maximal fold change across concentration range (maxFC) of measured S1500+ genes as input for each PHH and treatment for 24h with each reference compound. A) Bar plots of normalized enrichment scores (NES) of significantly enriched GO terms with a cut-off of adjusted FDR of < 0.05 for at least 10 different PHHs. NES were stacked for all PHHs showing significantly enrichment for each term. B) Significantly enriched terms in which one or more terms within cluster showed specific enrichment in either most sensitive (red circle) or insensitive (blue circle) PHHs, or both defined as core (yellow circle) using Cytoscape[246] and EnrichmentMap[247]. Within each term, NES for each PHH is depicted in grey to red scale from low to high. Enriched terms were clustered and summarized with 3 to 4 keywords using WordCloud[248].

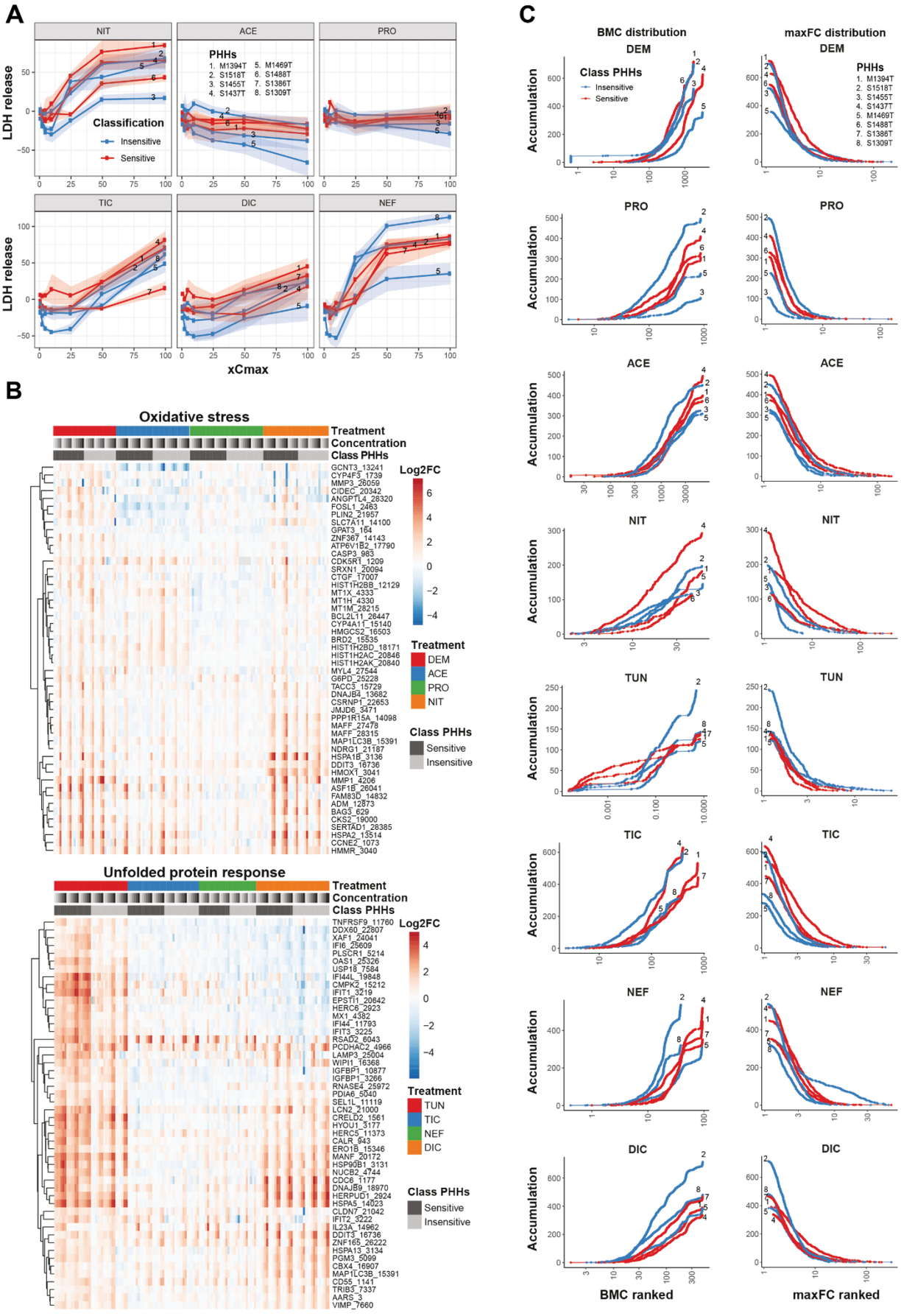
A
NIT
ACE
PRO
TIC
DIC
NEF
LDH release
xCmax
Classification
Insensitive
Sensitive
PHHs
1. M1394T
2. S1518T
3. S1455T
4. S1437T
5. M1469T
6. S1488T
7. S1386T
8. S1309T
B
Oxidative stress
Unfolded protein response
Treatment
Concentration
Class PHHs
Log2FC
DEM
ACE
PRO
NIT
TUN
TIC
NEF
DIC
Sensitive
Insensitive
C
BMC distribution
maxFC distribution
Accumulation
BMC ranked
maxFC ranked

← Fig. 5. Difference in sensitivity towards hepatotoxicants within a subpanel of primary human hepatocytes (PHHs). A) LDH release upon treatment with hepatotoxicants for 24 h in 6 defined most sensitive or insensitive PHHs. B) Hierarchical clustering of log2 fold changes of top 50 stress responsive genes for the oxidative stress and unfolded protein of PHHs exposed to various hepatotoxicants (acetaminophen; ACE, propylthiouracyl; PRO, nitrofurantoin; NIT, ticlopidine; TIC, nefazodone; NEF, diclofenac; DIC) for 24 h. C) Distribution of benchmark concentration (BMC) and maximal fold change across concentration range (maxFC) for all responsive genes of PHHs exposed to various hepatotoxicants for 24 h. N = 3.

Table 2. Median maximal fold change across concentration range (maxFC) and benchmark concentration (BMC) for most sensitive and insensitive PHHs based on all responsive genes for each treatment.

	Median maxFC						***Median BMC (µM)***					
CMP	***Insensitive PHHs***			***Sensitive PHHs***			***Insensitive PHHs***			***Sensitive PHHs***		
OX	*M1469T*	*S1455T*	*S1518T*	*M1394T*	*S1437T*	*S1488T*	*M1469T*	*S1455T*	*S1518T*	*M1394T*	*S1437T*	*S1488T*
DEM	2.94	2.51	2.25	2.33	3.48	2.53	1024.47	580.07	629.48	672.95	1051.43	375.30
ACE	3.14	2.95	3.59	2.93	3.61	3.68	1528.25	1331.12	1069.92	1761.77	1993.41	1379.58
NIT	1.92	3.10	3.17	6.31	2.86	3.80	20.65	11.60	24.03	29.02	17.37	22.12
PRO	1.96	1.54	2.16	1.78	2.03	2.22	293.33	345.93	193.57	312.23	311.24	235.90
UPR	*M1469T*	*S1309T*	*S1518T*	*M1394T*	*S1386T*	*S1437T*	*M1469T*	*S1309T*	*S1518T*	*M1394T*	*S1386T*	*S1437T*
TUN	1.84	1.98	1.78	1.73	1.89	1.78	0.07	0.21	0.19	0.004	0.19	0.04
DIC	3.08	2.68	2.88	5.02	2.90	3.70	122.25	72.45	68.45	137.28	99.12	137.80
NEF	3.33	2.13	2.09	2.92	2.61	2.42	37.31	18.24	19.01	37.25	25.66	40.28
TIC	1.97	2.20	2.21	3.63	2.67	2.48	103.17	141.57	96.00	229.69	210.65	151.71

**Diethyl maleate; DEM, acetaminophen; ACE, propylthiouracyl; PRO, nitrofurantoin; NIT, tunicamycin; TUN, ticlopidine; TIC, nefazodone; NEF, diclofenac; DIC.*

PHHs with various hepatotoxicants known to induce oxidative stress (acetaminophen, propylthiouracyl and nitrofurantoin) or ER stress (ticlopidine, nefazodone and diclofenac) (Fig. 5). Upon evaluation of differences in cell death induction, a concentration-dependent increase in LDH release was seen for all tested hepatotoxicants, except for acetaminophen and propylthiouracil (Fig. 5A). Both nitrofurantoin and nefazodone already showed cell death induction at 25x Cmax or higher. The most sensitive PHHs showed higher cytotoxicity when exposed to nitrofurantoin and diclofenac than the most insensitive PHHs. For the other hepatotoxicants, no difference was seen. Next, the expression of the top 50 activated genes was evaluated for both the oxidative stress response and UPR, where in particular nitrofurantoin showed higher induction in sensitive PHHs compared to insensitive (Fig. 5B). Other hepatotoxicants did not show clear distinction when only evaluating these genes. Thereafter, the difference in the distribution of BMCs and maxFC of all responsive genes was evaluated between the most sensitive and insensitive PHHs for each tested DILI compound. The hepatotoxicants propylthiouracyl, acetaminophen and ticlopedine showed clear separation for most of the sensitive and insensitive PHHs, but not all, in BMC and maxFC distribution (Fig. 5C, Table 2). For all other hepatotoxicants, differences in BMCs and maxFCs were more variable.

Influence of PHH panel size on estimating variance

To check the inter-individual variability model for the entire human population in chemical-induced stress response activation, both the BMC and maxFC for the top 50 stress responsive genes for each compound was simulated for 500 virtual PHHs. The distribution of the simulated BMCs and maxFCs were in concordance with the experimental data based on the panel of 50 PHHs showing similar distributions (Supporting Fig. S11-12).

To evaluate the effect of the number of PHHs from different individuals used to obtain the correct population CVs in stress response activation, reference (large sample size) population variances of BMC and maxFC values for the top 50 stress responsive genes were first estimated by simulating 1,000 assays with a panel of PHHs from 2,000 virtual individuals (Fig. 6A-B). Next, inter-individual CV estimates were simulated when using different panel sizes of PHHs derived from 3 to 50 individuals for each reference compound (Fig. 6A-B). When the PHH panel size was increased, the CV estimates became increasingly precise and converge to the true human population variability. For small PHH panel sizes which are commonly used during hepatotoxicity testing, the imprecision is very large, leading to consistent underestimation of the inter-individual variance in stress response activation upon chemical exposure.

Next, the probability of obtaining a CV which is close to the true human population CV was evaluated when using different PHH panel sizes (Fig. 6C-D). Overall, when using a PHH panel size of 10 or less the probability to estimate the correct CV of the BMC is very low, namely smaller than ~ 0.3, 0.05, 0.15 and 0.2 for DEM, CPT, TUN and TNFα, respectively (Fig. 6C). When using a PHH panel size of 50, the maximal probability that could be reached to estimate the correct CV of the BMC is ~ 0.45, 0.3, 0.4 and 0.4 for DEM, CPT, TUN and TNFα, respectively, still resulting in quite some uncertainty. For estimating the correct CV of the maxFC, a maximal probability of 0.3 was reached for all compounds when using a PHH panel size of 50, which is also still quite low (Fig. 6D). Therefore, we propose to use an additional uncertainty factor to account for the uncertainty in estimating the true median population PoD and variance of stress response activation upon chemical exposure during hepatotoxicity testing in PHHs. Indeed, simulation of 2,000 virtual donors for 1,000 assays resulted in $TDVF_{0.01}$s that were up to 2-fold higher than the standard used UF of 3.16 for TUN, CPT and TNFα for 8 h and TUN for 24 h (Table 1).

Discussion

Human tissue-culture based methods hold great promise for the prediction of chemical-induced adversities[299–301]. Here, we evaluated the effects of inter-individual differences in sensitivity to chemical-induced stress in PHHs, to determine data-driven toxicodynamic uncertainty factors for specific types of relevant stress responses that are critical in chemical-induced toxicity. In our analysis, we focused on compounds inducing the UPR, the oxidative stress response, the DNA damage response and cytokine-mediated NF-κB signalling. The activation of each of these stress responses is considered a key event leading to the development of chemical-induced liver

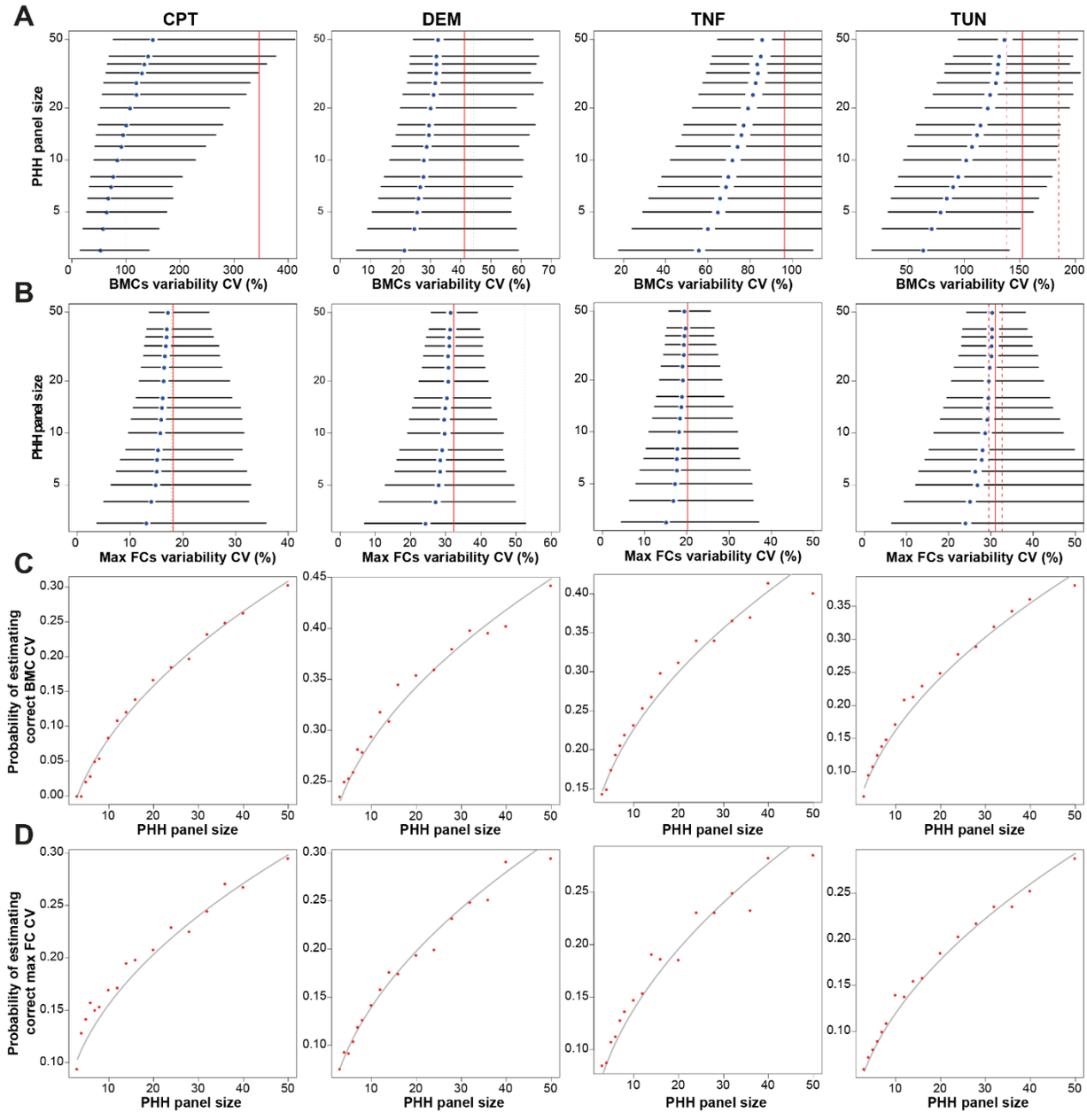

Fig. 6. Influence of primary human hepatocyte (PHH) panel size on probability to capture correct variance in stress response activation. A-B) Forest plots of simulated distributions (medians ± 5th / 95th percentiles) of the estimated coefficients of variation (CVs) of benchmark concentrations (BMC) (A) and maximal fold changes across concentration range (maxFC) (B) based on top 50 stress responsive genes for each reference compound as a function of PHH panel size. As reference, 1,000 assays with a panel of PHHs from 2,000 individuals was simulated depicted as red lines (median: solid ± 5th / 95th percentiles: dashed). C-D) Probability of reporting a correct CV falling between the 5th and 95th percentile of the reference CVs as a function of PHH panel size for BMC (C) and maxFC (D). Red dots resemble Monte Carlo simulation estimates and grey lines resemble visually fitted smoothing curves.

injury[16]. Moreover, the consequent upregulation of a specific set of gene transcripts that represents these stress response pathways can be used to qualify and quantify the mode-of-action for the evaluation of hepatoxicity[16,28]. Our results indicate that large differences in the distribution of BMCs are observed between different PHHs. Moreover, standard uncertainty

factors for toxicodynamic responses for risk assessment are insufficient for toxicity responses that would involve UPR and NF-κB signalling.

Our data exemplify the need of accurately determined data-driven uncertainty factors during risk assessment to improve the prediction of liabilities for chemical-induced liver injury. Our results indicate that these uncertainty factors can be at least 2-fold higher than the standard toxicodynamic uncertainty factor of $10^{1/2}$. In concordance, Blanchette *et al.* characterized the human population variance of chemical-induced cardiotoxicity using hiPSC-derived cardiomyocyte panel together with population modelling and also showed higher TDVFs than the standard $10^{1/2}$[54,295.] Likewise, Abdo *et al.* found that some of the 179 screened chemicals led to TDVFs higher than 10 when evaluating cytotoxicity in 1,086 lymphoblastoid cell lines[302].

Potentially, several factors may influence PHH sensitivity to chemical-induced stress, including differences in health characteristics of PHH donors. We found that PHHs from patients with any type of liver disease showed less induction of stress responses upon exposure, especially for TNFα-induced NF-κB signalling and TUN-induced UPR. These PHHs showed already higher expression of stress response-related genes in control conditions, thereby leading to less capacity to further induce protective stress responses upon chemical exposure. Indeed, there are strong correlations between liver diseases, such as non-alcohol fatty liver disease, non-alcohol steatohepatitis and liver cancer, increased activation of e.g. the UPR and the inflammatory response[234,303–305], and increased DILI susceptibility[306,307]. Thus, the liver disease background of PHHs can have a significant impact on their sensitivity to DILI compounds. In this respect, special attention should be given to the inflammatory state of the liver prior to the isolation of PHHs. Large differences were seen in basal expression of chemokines, such as *CCL2*, possibly affecting their sensitivity towards chemical exposure. Indeed, the presence of inflammation is one of the susceptibility factors for development of DILI[308,309]. In addition, large variability was also seen in the expression of inflammatory genes upon chemical exposure across panel of PHHs. Inflammatory genes such as *IL1B* and *CCL3* were most differently expressed across panel of PHHs upon TUN treatment. Several studies have shown the relation between UPR activation and inflammatory signalling through activation of NF-κB and the NLRP3 inflammasome, leading to induction of *IL1B* expression[310].

In conclusion, we demonstrated that chemical-induced liver injury associated stress response activation is highly variable between different individuals. This highlights the need to use toxicodynamic uncertainty factors for safety evaluation. We show that the currently used standard uncertainty factor of $10^{1/2}$ is not sufficient to capture all variance for every chemical or endpoint measured in PHHs. For activation of the UPR and NF-κB signalling the defined TDVF was up to 2-fold higher than this standard. This exemplifies a general need for the use of data-driven mechanism-specific uncertainty factors to accurately correct for toxicodynamic variance across

the human population to improve assessment of liabilities for development of chemical or drug-induced liver injury.

Author Contributions

MN, SH, LR, RSP, FYB and BW designed research work. MN, SH, AB and CP performed experiments. MN, WW and FYB performed data analysis. MN, PB, FYB and BW wrote and edited manuscript. All authors revised and approved final manuscript.

Acknowledgements

This work was supported by the EU-ToxRisk project funded by the European Union under the Horizon 2020 programme (grant agreement 681002), IMI MIP-DILI project (grant agreement 115336) and Division of the National Toxicology Program at NIEHS, NIH, USA (ZIA ES103318-03).

Supplemental figures

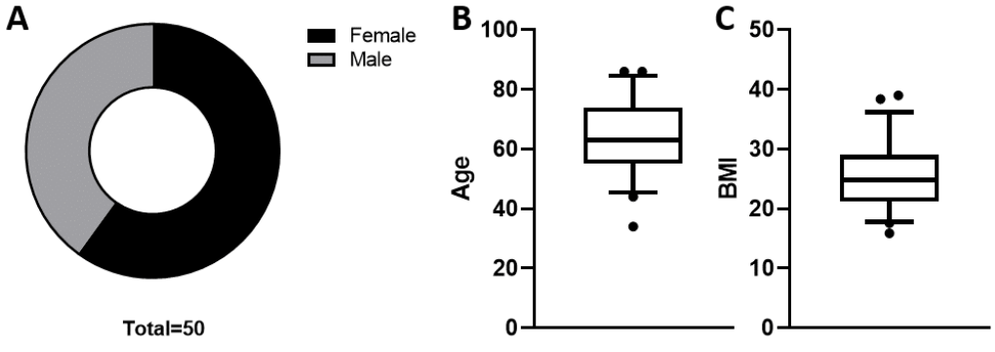

Fig. S1. Characteristics of large panel of primary human hepatocytes derived from 50 individuals. Distribution of gender (A), age (B) and BMI (C) within panel of primary human hepatocytes derived from 50 individuals.

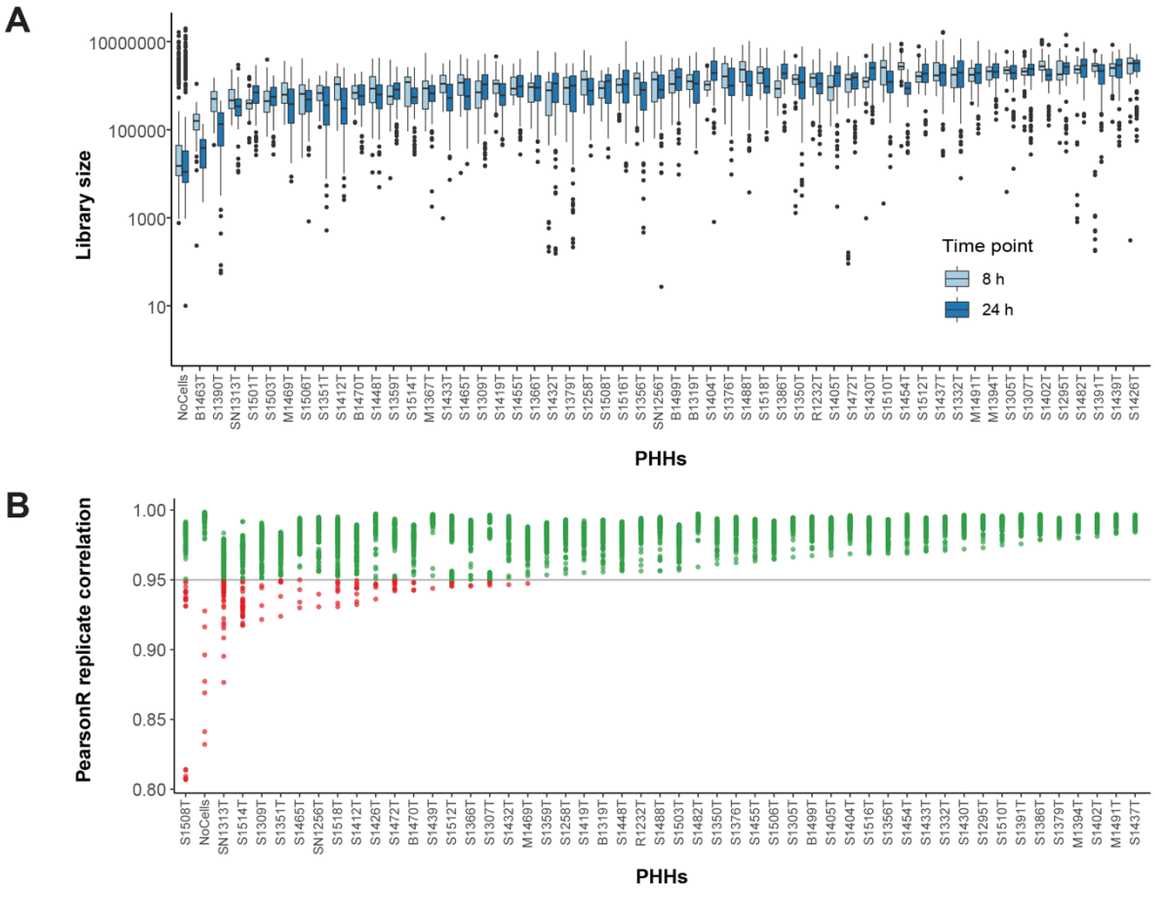

Fig. S2. Quality controls of TempO-seq data for each PHH donor. A) Distribution of total library size for each sample across PHH panel. B) Pearson's R correlation of each biological replicate compared to mean for each sample across PHH panel. N=3.

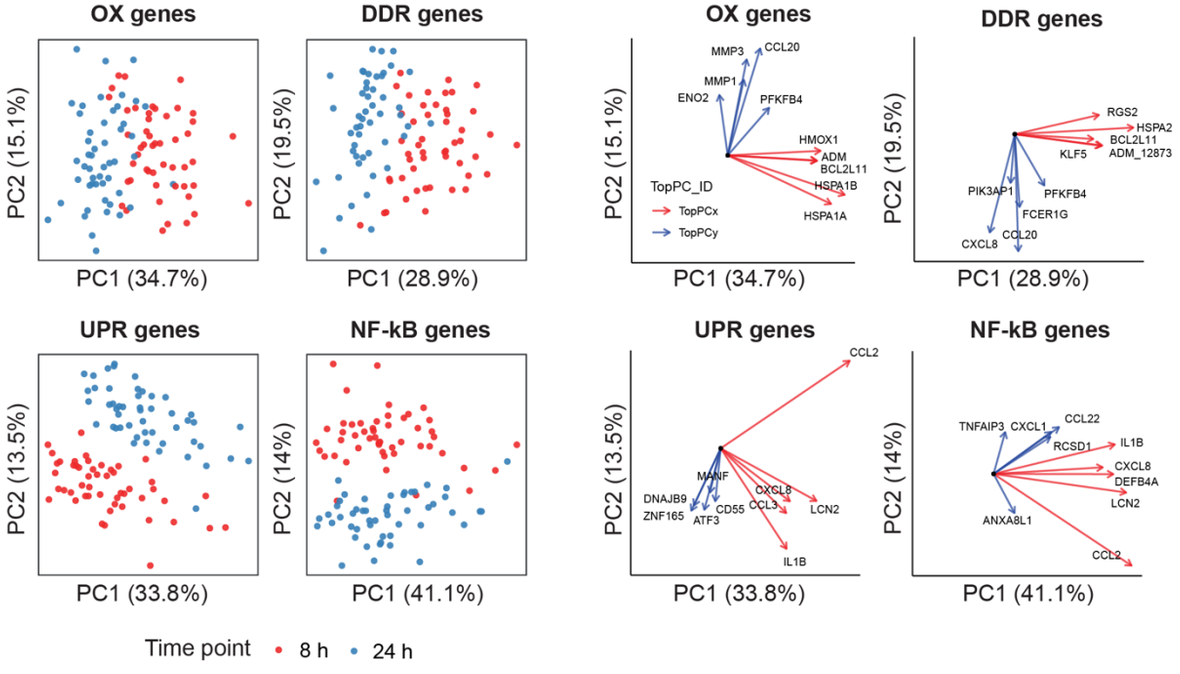

Fig. S3. Principal component analysis (PCA) of stress responsive genes at basal conditions across panel of PHHs. A) PCA based on log2 normalized counts of stress responsive genes of panel of PHHs at basal medium conditions at identical timepoints of compound exposure for 8 and 24 h. B) Top 5 genes mostly determining PC1 or 2 depicted as vectors representing contribution and PC orientation. N=3.

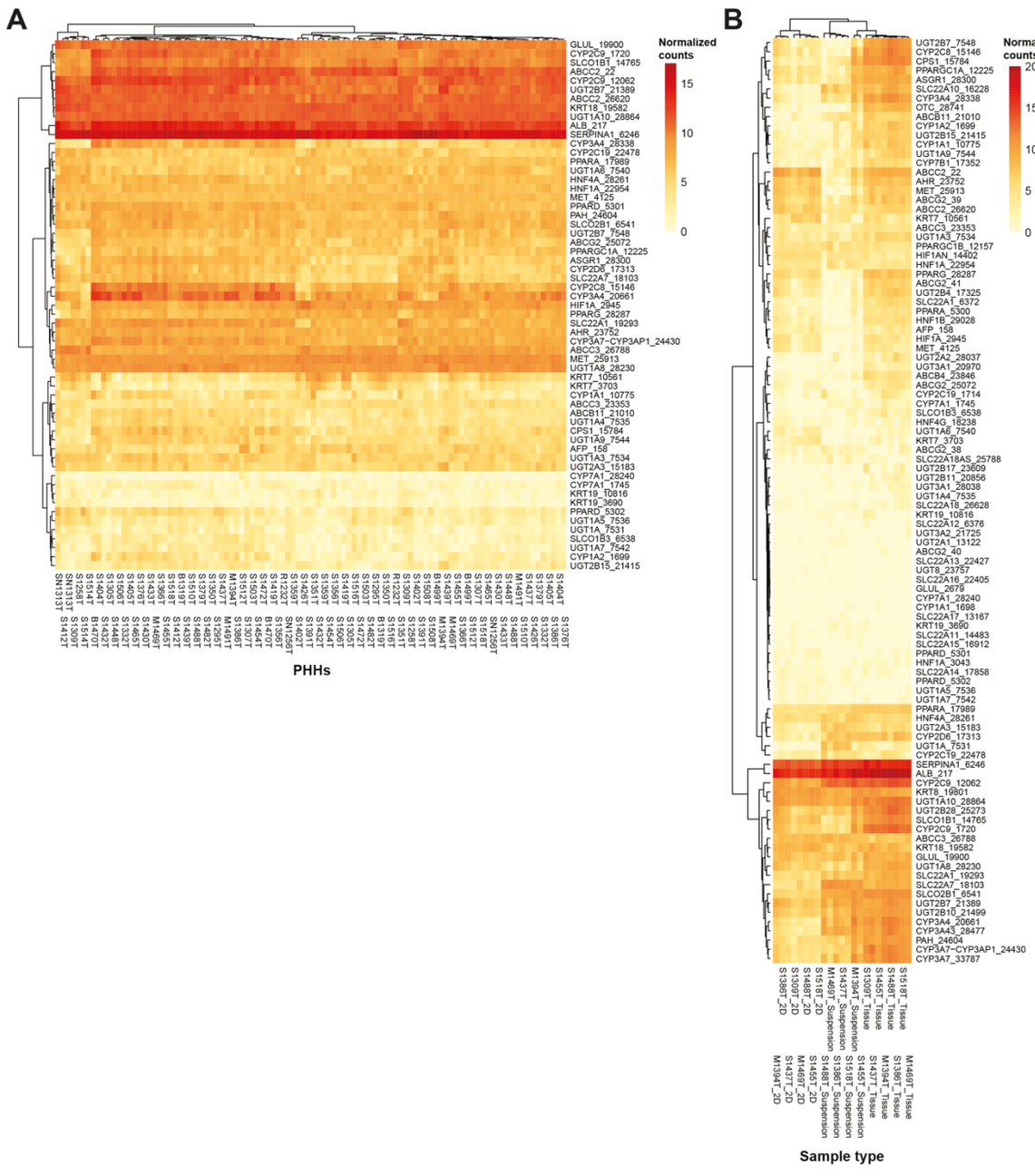

Fig. S4. Variability in expression of liver-related genes across PHH panel. A) Hierarchical clustering of log2 normalized counts of liver-related genes within the S1500+ gene set across PHH panel derived from 50 individuals cultured as 2D for 24 h upon thawing. B) Hierarchical clustering of log2 normalized counts of liver-related genes within the targeted whole transcriptome gene set for liver tissue (N=1), freshly thawed PHHs in suspension (N=3) or PHHs cultured as 2D for 24 h (N=3) derived from 8 individuals.

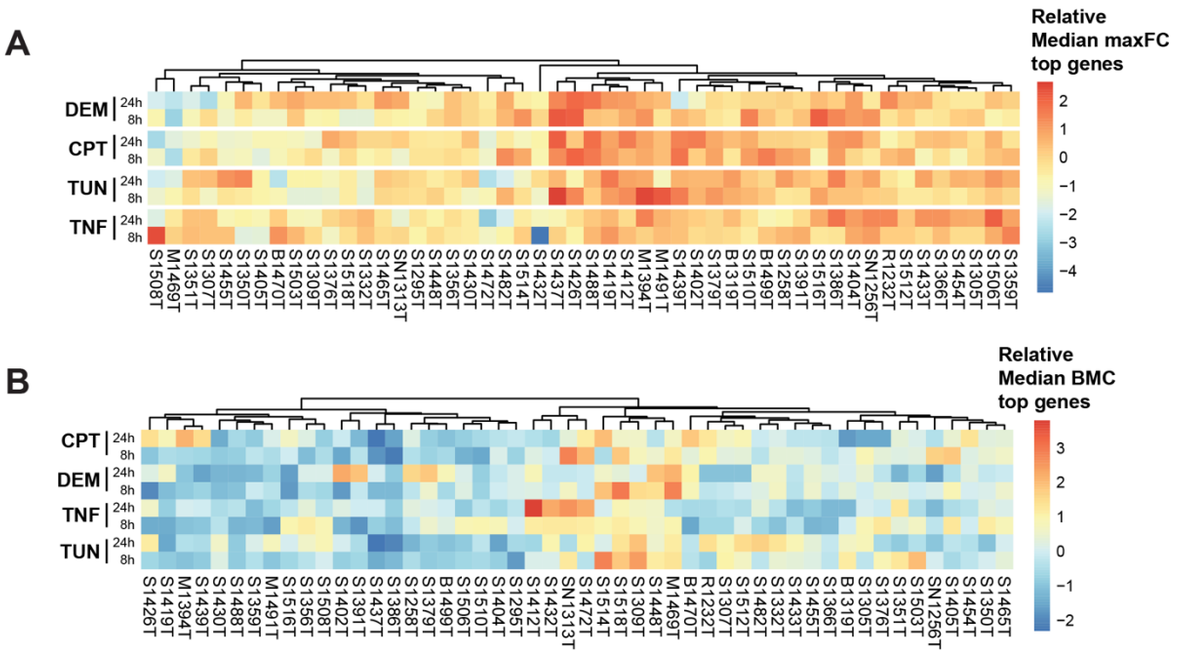

Fig. S5. Inter-individual variability of median maximal fold change and benchmark concentration of most responsive genes upon chemical exposure. A) Hierarchical clustering of relative median maximal fold change (maxFC) across concentration range for top 50 stress responsive genes for each compound across PHH panel at 8 and 24 h exposure. B) Hierarchical clustering of relative median BMC of top 50 stress responsive genes for each compound and timepoint across PHH panel. N=3.

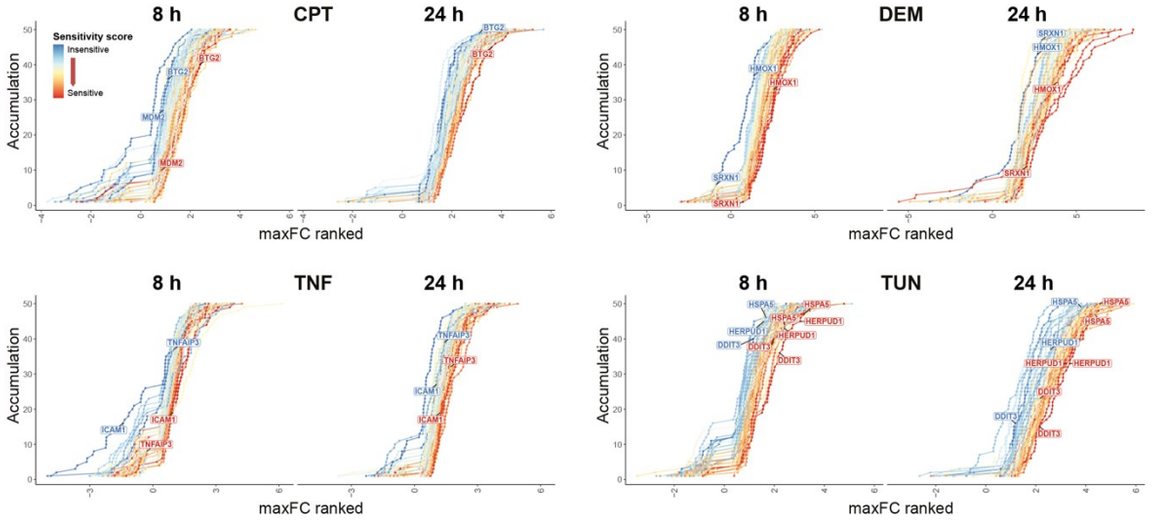

Fig. S6. Variability in the distribution of maximal fold change of most responsive genes upon exposure. Distribution of maximal fold change across concentration range (maxFC) of top 50 stress responsive genes for each compound (diethyl maleate; DEM, cisplatin; CPT, tunicamycin; TUN, TNFα; TNF) and time point 8 and 24 h. Lines represent each PHH where colour reflects the sensitivity score based on rank of median maxFC and benchmark concentration (BMC) of top 50 genes.

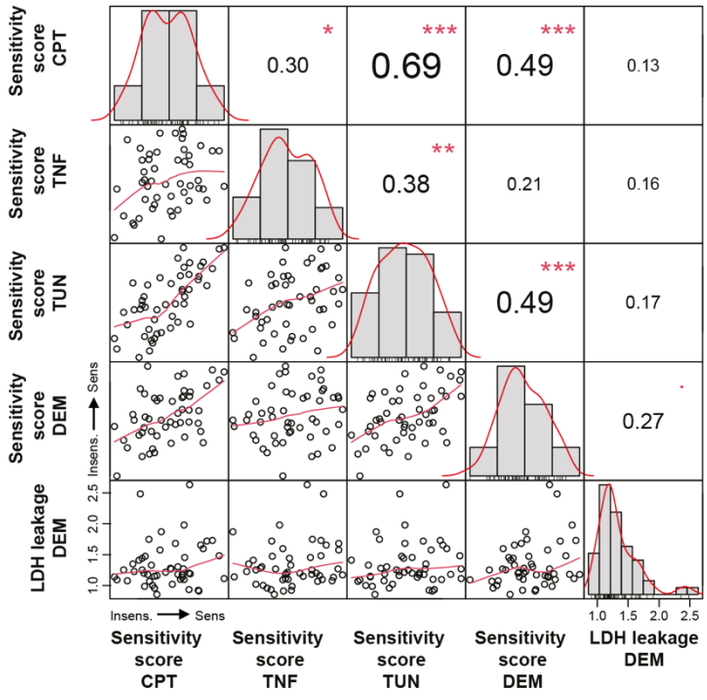

Fig. S7. Correlation cell viability and sensitivity scores for PHH panel. Correlation between the sensitivity scores for each compound and LDH leakage as a measure of cell viability at 3300 µM diethyl maleate (DEM). The sensitivity scores were based on rank of median maxFC and benchmark concentration (BMC) of top 50 stress responsive genes for each compound (diethyl maleate; DEM, cisplatin; CPT, tunicamycin; TUN, TNFα; TNF) ranging from 0 (most sensitive) to 200 (most insensitive). Left bottom represents the scatter plots, in the middle histograms and upper right the Pearson correlation. Significant correlations depicted as * $p < 0.05$, ** $p < 0.01$, *** $p < 0.001$. N = 3.

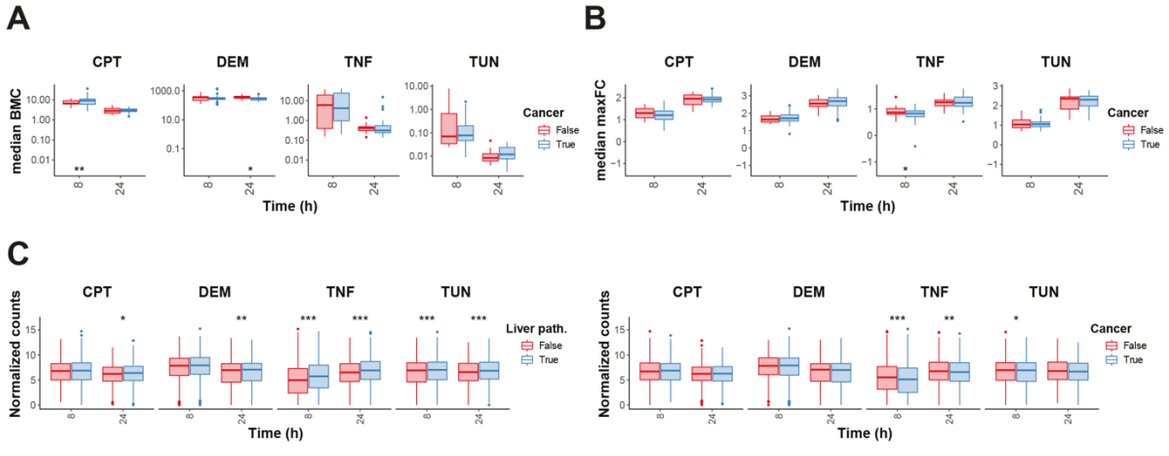

Fig. S8. Effect of pathology background on sensitivity of chemical-induced stress response activation. Distribution of median benchmark concentration (BMC) (A) or median maximal fold change across concentration range (maxFC) (B) of top 50 stress responsive genes for each compound (diethyl maleate; DEM, cisplatin; CPT, tunicamycin; TUN, TNFα; TNF) and time point 8 and 24 h across PHH panel from 50 individuals with or without cancer. C) Distribution of normalized counts in baseline medium condition of top 50 stress responsive genes for each compound and time point across PHH panel from 50 individuals with or without liver pathology (left panel) or cancer (right panel). Significance levels represented as * $p < 0.1$, ** $p < 0.05$, *** $p < 0.01$. N = 3.

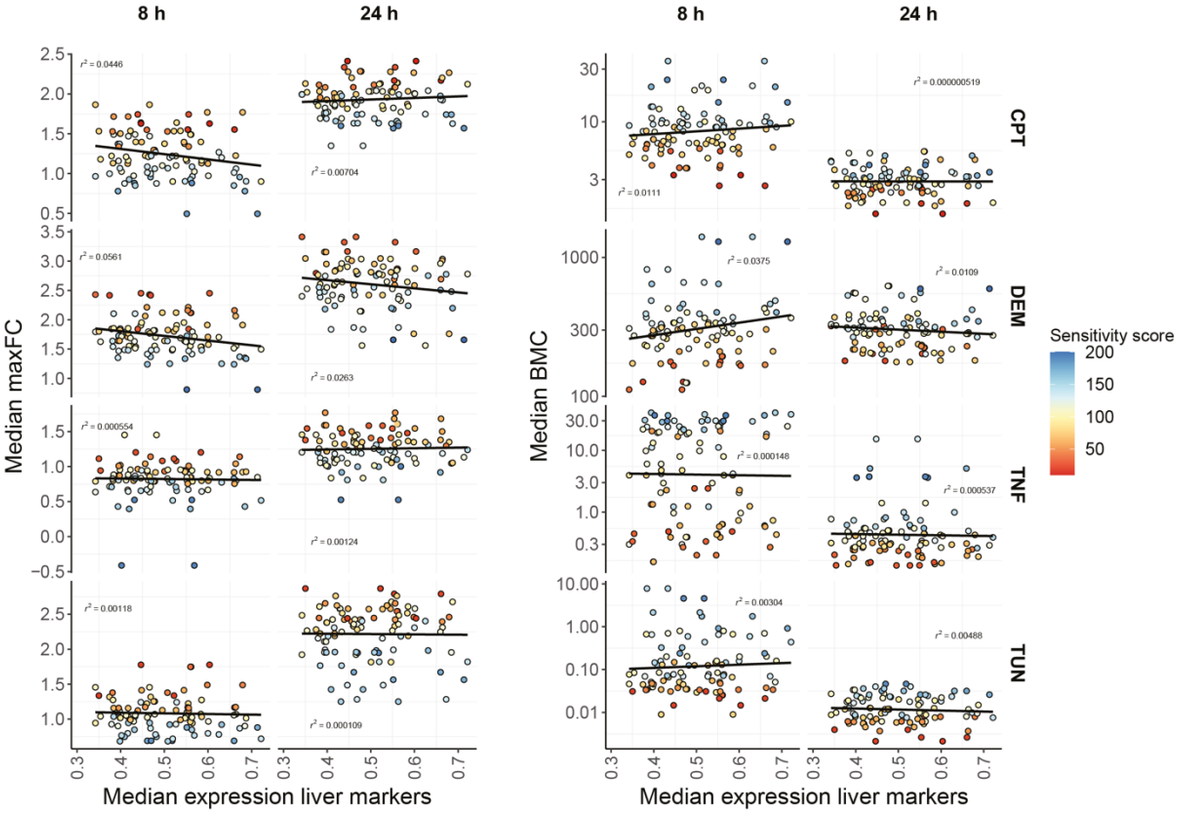

Fig. S9. Correlation hepatic phenotype with sensitivity of chemical-induced stress response activation. Scatter plots of the median expression of liver-related genes vs median maximal fold change across concentration range (maxFC) (left panel) or median benchmark concentration (BMC) (right panel) of top 50 stress responsive genes for each compound (diethyl maleate; DEM, cisplatin; CPT, tunicamycin; TUN, TNFα; TNF) and time point 8 and 24 h for each PHH across panel of 50. Sensitivity scores for each PHH is depicted in colour scale from red to blue, sensitive to insensitive. The correlation is given as r^2.

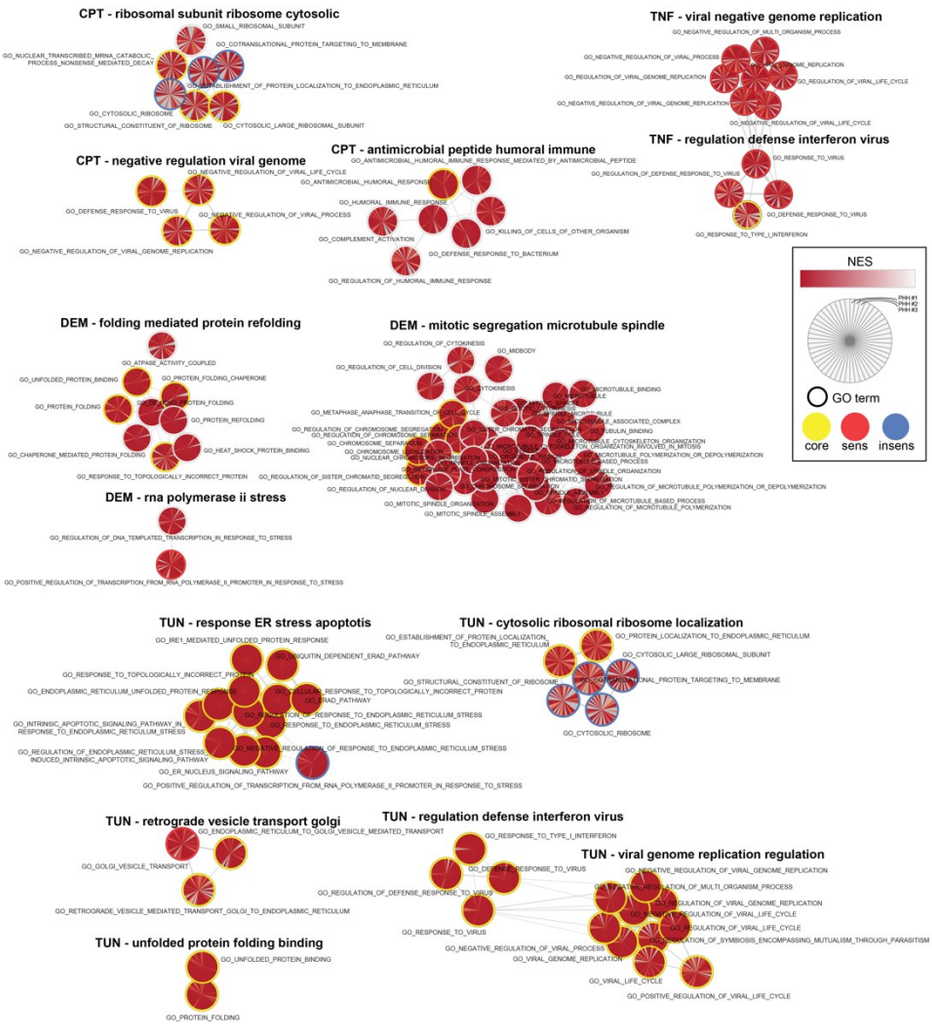

Fig. S10. Evaluation of variance in pathway activation by gene set enrichment analysis (GSEA) of gene ontology (GO) terms. Gene set enrichment analysis (GSEA)[298] was done using gene ontology (GO) terms v7.1 and the maximal fold change across concentration range (maxFC) of measured S1500+ genes as input for each PHH and treatment for 24h with cisplatin (CPT), diethyl maleate (DEM), TNFα (TNF) or tunicamycin (TUN). Detailed representation of significantly enriched GO terms in which one or more terms within cluster showed specific enrichment in either most sensitive (red circle) or insensitive (blue circle) PHHs, or both defined as core (yellow circle) using Cytoscape[246] and EnrichmentMap[247]. Within each term, the NES for each PHH is depicted in grey to red scale from low to high. Enriched GO terms were clustered and summarized with 3 to 4 keywords using WordCloud[248].

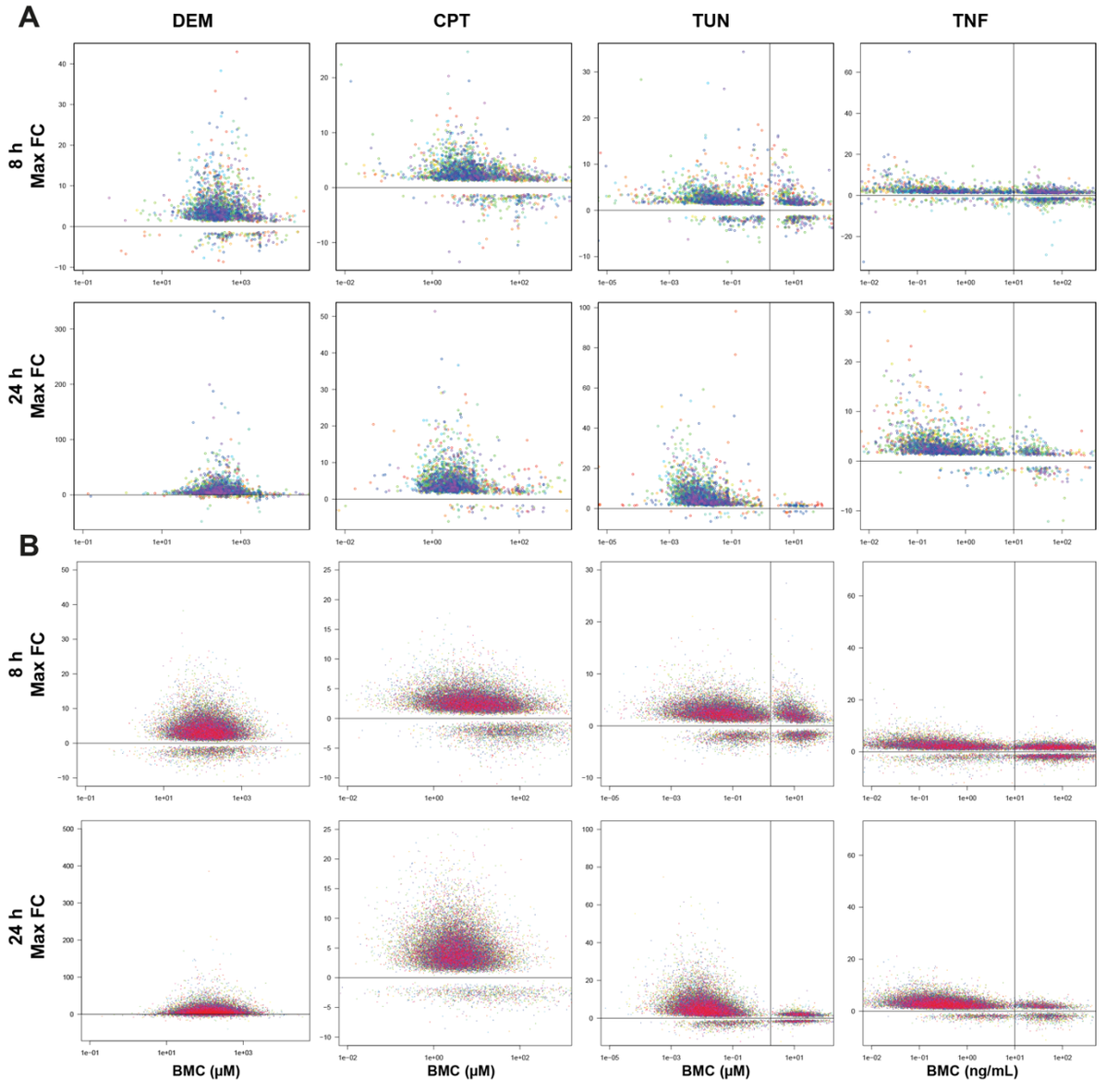

Fig. S11. Simulation of the distribution of benchmark concentration (BMC) and maximal fold change across concentration range (maxFC) of top 50 stress responsive genes across extended panel of PHHs. A) Experimental observation of distribution of BMC and maxFC of top 50 stress responsive genes for diethyl maleate (DEM), cisplatin (CPT), tunicamycin (TUN) and TNFα (TNF) across panel of PHHs depicted in different colours at 8 and 24 h timepoint. N = 3. B) Computer simulated sample for a panel of 500 PHHs depicted in different colours. The vertical and horizontal lines delimit the observed cluster of BMC and maxFC values.

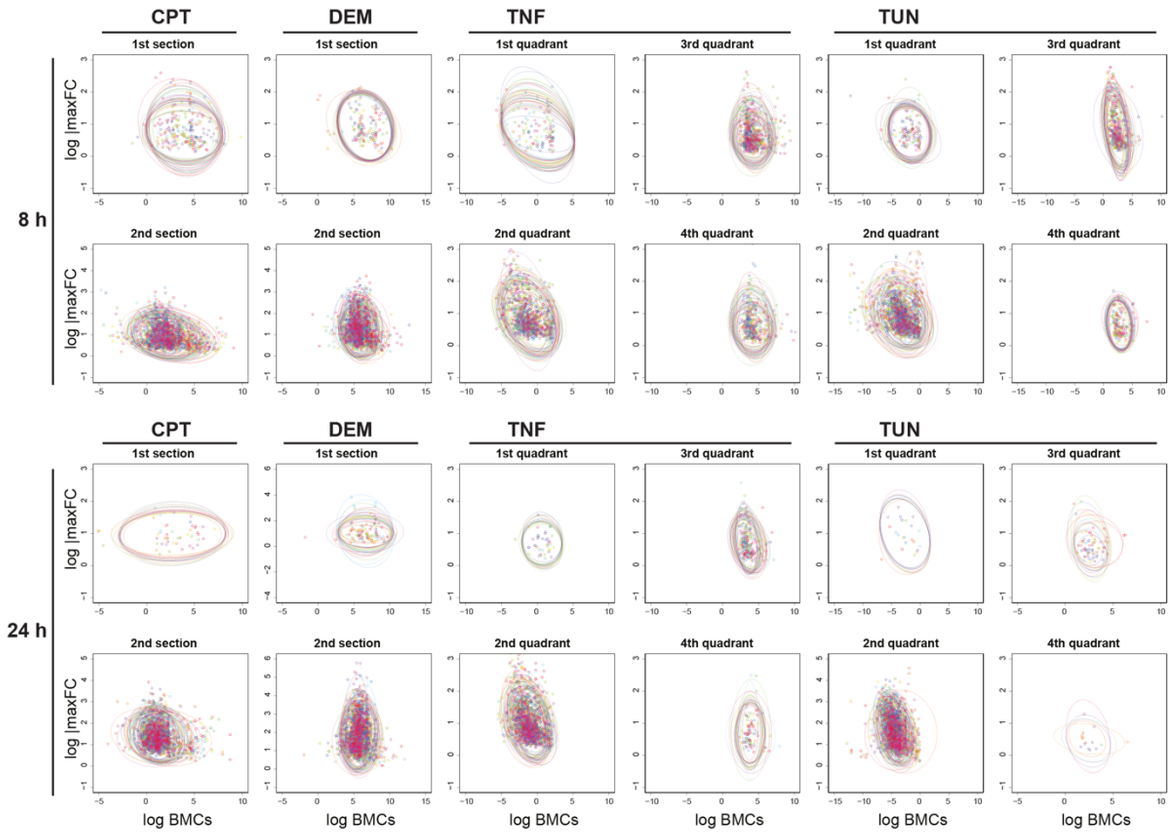

Fig. S12. Simulation of the confidence intervals of the lognormal bivariate distributions of benchmark concentration (BMC) and maximal fold change across concentration range (maxFC) of top 50 stress responsive genes across panel of PHHs. Experimental observation of the distribution of BMC and maxFC of top 50 stress responsive genes for diethyl maleate (DEM), cisplatin (CPT), tunicamycin (TUN) and TNFα (TNF) across panel of PHHs depicted as dots in different colours at 8 (upper panel) and 24 h (lower panel) timepoint for each observed section or quadrant. N = 3. Computer simulated confidence intervals indicated as eclipses for a panel of 500 PHHs depicted in different colours.

Supplemental materials

Table S1. Overview of concentration ranges used for each compound tested in panel of PHHs.

ID	***Reference compounds***			
	DEM	**CPT**	**TUN**	**TNF**
1	1	0.1	0.0001	0.1
2	10	1	0.001	0.3
3	100	3.3	0.01	1
4	330	10	0.1	3.3
5	1000	33	1	10
6	3300	100	10	33
	µM	µM	µM	ng/mL

xCmax	***DILI compounds***					
	NIT	**ACE**	**PRO**	**TIC**	**DIC**	**NEF**
1	6	139	9.1	8.1	10.1	4.0
2.5	15	347.5	22.75	20.2	25.25	9.9
5	30	695	45.5	40.4	50.5	19.8
10	60	1390	91	80.7	101	39.5
25	150	3475	227.5	201.9	252.5	98.8
50	300	6950	455	403.7	505	197.5
100	600	13900	910	807.5	1010	395.0
	µM	µM	µM	µM	µM	µM

Diethyl maleate; DEM, Cisplatin; CPT, tunicamycin; TUN, TNFα; TNF, acetaminophen; ACE, propylthiouracyl; PRO, nitrofurantoin; NIT, ticlopidine; TIC, nefazodone; NEF, diclofenac; DIC

Chapter 9

Summary and discussion

Improved insight in the regulation of stress response activation upon chemical exposure for improved predictivity of hepatotoxicity is the common thread within this thesis. The activation of stress response pathways is one of the early key events, close to the molecular initiation event (MIE), leading to the development of DILI[311]. The activation of stress response pathways allows cells to cope with chemical-induced stress trying to restore homeostasis. However, upon prolonged stressed conditions, activation of these stress responses may not be enough leading to irreversible cellular injury and eventually injury at organ level. Adaptive stress response pathways are typically activated at lower concentrations in response to chemical toxicity compared to more general cytotoxicity endpoints and are preserved across all cell types making it highly suitable for drug toxicity screening[311].

BAC-GFP reporter panel

To monitor the activation of these stress response pathways, a panel of HepG2 BAC-GFP reporters has been build which can be combined with high-throughput confocal microscopy allowing to capture temporal dynamics at single cell level in both 2D and 3D setup[27–29]. The reporter panel consists of reporters for the sensor, transcription factor and downstream target genes to capture different levels within each stress response pathway. These stress response reporters are suitable to identify hepatotoxic drugs and allow to combine with genomic screening methods such as RNAi screening to increase understanding of stress response regulation. Therefore, in **chapter 2** an overview has been given in the development and application of these BAC-GFP reporters followed by **chapter 3, 4, 5 and 6** where we used these reporters to improve understanding of the regulation of these stress response pathways and their context of use.

Since these reporters rely on the BAC recombineering technique, additional copies of the reporter gene are added to the genome of the cell. We do not have an exact insight in the number of copies of the BAC-GFP reporter constructs in the various reporters, but likely several copies are integrated. This can be advantageous with respect to sensitivity of the GFP signal, but could also provide an overestimation of the response. Moreover, we cannot exclude that the reporter activity might be influenced in the context of the location of the genomic integration, which is likely in active regions of the genome in the HepG2 cells. This different integration sites may affect downstream signalling and overall adaptation responses upon chemical exposure. Therefore, stress response reporter lines that take advantage of the CRISPR/Cas9 technology may overcome these limitations. This technology allows endogenous gene tagging with the fluorophore of interest in a scarless manner in cell lines but also in hiPSCs[312]. The latter approach will then allow differentiation of the reporter hiPSC into different lineages and create a broader application of the same reporter for different target organs. Yet, if the fluorophore fusion product affects functionality of the endogenous protein, downstream signalling can also be affected. Likely, heterozygous tagging only one allele has a preference when using CRISPR/Cas9 mediated fluorophore tagging, although this would also impact on overall reporter sensitivity. Besides,

building reporters in hiPSCs instead of HepG2 cells allows to evaluate stress response pathway activation in multiple cell types upon differentiation. In this way, difference in sensitivity between different cell types from different organs can be compared, but also stress response activation within co-cultures with multiple cell types can be evaluated. This opens up numerous possibilities in the application of these reporters, both in chemical screening as well as in disease modelling and improved mechanistic understanding. We have already assessed the functionality of an HMOX1-GFP hiPSC reporter that was differentiated into different lineages, including hepatocytes, cardiomyocytes, renal proximal tubular cells and neuronal cells and established the success of such reporters[312]. In our laboratories in Leiden we have established a series of reporters in hiPSC for different cellular stress response pathways and are currently assessing the functionality of these reporters. We anticipate that such hiPSC-based reporters will find broader application for different target organ toxicities, with the disadvantage of the typically costly and more lengthy differentiation programs involved.

Influence of oxidative stress response on DNA damage signalling

One of the critical cellular stress response pathways is the oxidative stress response pathway which is regulated by the transcription factor NRF2 and sensor KEAP1. It is activated upon oxidative stress due to ROS formation leading to a conformational change of KEAP1 and stabilization of NRF2 translocating to the nucleus[313]. Here it can activate its downstream target genes such as anti-oxidant genes trying to restore homeostasis[17]. During chemical-induced oxidative stress, other stress response pathways may influence the NRF2 response, such as the DNA damage response since ROS can lead to DNA damage affecting cellular outcome[314]. Therefore, in **chapter 3** we evaluated the crosstalk between the oxidative stress response and DNA damage signalling upon chemical exposure.

As a first step, the concentration-dependent activation dynamics of both the oxidative stress and the DNA damage response was evaluated using oxidative stress inducer diethyl maleate and DNA damage inducer etoposide in a wide concentration range in HepG2 BAC-GFP reporters in combination with confocal imaging. Both compounds could activate both pathways, suggesting the presence of crosstalk. Silencing of NRF2 led to the inhibition of the DNA damage response, while silencing of KEAP1 led to enhancement of the DNA damage response during etoposide treatment. Silencing of both led to restoration, suggesting the activating role of NRF2 in p53 signalling possibly mediated by NQO1. Our data demonstrate the overall application of the reporter platform to map the concentration temporal responses using high throughput confocal microscopy in combination with RNA interferences approaches to qualify and quantify systematically the interactions between different stress pathways. Obviously, our results are based on HepG2 cells, and if similar interactions occur in normal human hepatocytes should be further explored and validated in multiple test systems. Optimally, the activation of both stress response pathways could be followed in the same cell to accurately follow activation dynamics

of both at the same time, yet, current comparison in the temporal responses can now only be made with different reporters. Exploration of dual-fluorescent reporter systems could be applied where e.g. one channel would involve the GFP reporter for the NRF2 pathway and another channel would involve a mScarlet reporter for the p53 pathway. This would allow the temporal dynamics of both pathways with the same cell.

Identification of DNA damaging agents using BAC-GFP reporters

To evaluate DNA damage upon chemical exposure, test systems such as the Ames test, Comet assay or the micronucleus test are being used[143,144,147]. However, still improvements in the predictivity is needed. Therefore, in **chapter 4** we evaluated the suitability of the DNA damage HepG2 BAC-GFP reporters in different culture setups for identifying genotoxicants. HepG2 cells were either cultured in 2D as a monolayer or in 3D as spheroids within a Matrigel layer. They were cultured with standard medium or with AAGLY medium increasing maturation status of hepatocytes[53]. The AAGLY medium enhanced the cytochrome P450 expression making it more suitable for evaluation of metabolite-mediated toxicity. HepG2 cells also stop proliferating when cultured using the AAGLY medium, also making them more suitable for repeated exposure scenarios[53]. In general, HepG2 cells that still proliferate, cultured in 2D with standard medium, are most sensitive towards genotoxicants not requiring metabolism for bioactivation, i.e. cisplatin and mitomycin C, to induce toxicity. Genotoxicants where the metabolites are responsible for the genotoxic effects, e.g. aflatoxin B1, are best recognized in the HepG2 3D setup or cultured with AAGLY medium having higher metabolic capacity[29]. Again, here the reporter readout is more sensitive than the cytotoxicity endpoints exemplifying the suitability of the reporter system for chemical screening. Furthermore, here the activation of the DNA damage response is evaluated being more sensitive than measuring DNA damage itself as with the traditional endpoints for DNA damage. However, this should be further evaluated by testing the reporters with a larger genotoxicant screen alongside the traditional readouts such as the comet assay for comparison. Most optimally, also the oxidative stress reporter should be taken along to discriminate indirect activation of DNA damage response through ROS formation. These results clearly demonstrate that the same test method that is cultured under different culture conditions can have different outcomes. Any substance could be a false negative in the same test systems depending on the culture condition. This illustrates the requirement for systematic evaluation of the test system under different culture conditions to determine precisely the fit-for-purpose. This is however often overlooked.

Tight control of unfolded protein response activation

Activation of the unfolded protein response (UPR), controlled by the sensors ATF6, PERK and IRE1 upon ER stress, plays a role in the development of DILI for some DILI-inducing drugs, such as diclofenac and nefazodone[97]. Regulation of the UPR is tightly controlled to eliminate the accumulation of misfolded proteins within the ER. To fully understand this tight regulation and

how it affects cell fate upon chemical exposure, we aimed to identify key regulators of CHOP, a pro-apoptotic transcription factor within the UPR, during ER stress in **chapter 5 and 6**.

By combining ODE-modelling and confocal imaging of HepG2 BAC-GFP UPR reporters for ATF4, XBP1, CHOP and BIP exposed to a broad concentration range of tunicamycin in **chapter 5**, it allowed us to dissect the contribution of each UPR signalling branch in activating CHOP. Here, the transcription factor ATF6 predominantly regulates CHOP during the initial phase. Upon silencing of ATF6, CHOP was blocked during the initial phase, however at later timepoints CHOP was further induced. This indicates a significant role for ATF6 in cell fate outcomes during stressed conditions. However, the relationship of ATF6 signalling and cell fate was not yet evaluated here and should be included within the model. Also, it would be of great value to have a reporter for ATF6 to fully capture the activation dynamics and translocation during chemical exposure which could feed into the model now only based on selected time points and western blot data of uncleaved form of ATF6. Furthermore, the regulation of CHOP by ATF6 should be further validated in other cell types such as PHHs and extended with other ER stress inducing compounds. This clearly illustrates the value of the fluorescent reporters for defining the temporal dynamics of their activity at the individual cell level. Such datasets are of incredible value to computational biologist to establish mathematical models for cellular stress response pathways. While here we used the HepG2 reporters to establish models for the ER stress pathway, the ultimate challenge will be whether the same model can be applied for the hiPSC reporters that are differentiated into different lineages. This will allow to establish the variability of the models. At Leiden we have also established mathematical models based on the DNA damage response reporters and the NRF2 antioxidant response[313,315]. The future challenge will also be to integrate the different models together and determine the application for the overall prediction of adversity.

To identify novel regulators of CHOP in **chapter 6**, besides the known UPR components, we have performed a large RNAi screen consisting of 3,457 genes in HepG2 CHOP-GFP cells upon tunicamycin treatment to evaluate the role of individual genes in CHOP upregulation during ER stress. A secondary screen led to the validation of a total of 74 novel regulators of CHOP: 18 potential negative regulators and 56 potential positive regulators. One of the key hits, transcription factor EMX1, reduced CHOP significantly upon silencing upon treatment with various ER stress inducers in HepG2 cells. The role in CHOP regulation could also be confirmed in PHHs besides HepG2 cells evaluated by transcriptomic analysis. The UPR plays also a pivotal role in carcinogenesis where activating the UPR extensively is advantageous for cancer cells to minimize ER stress[240]. Here, silencing of EMX1 could also block CHOP and enhance survival during exposure with HCC treatments regorafenib and sorafenib in HepG2 cells. To elucidate the role of EMX1 during HCC development, other HCC lines besides HepG2 should be tested. Furthermore, CRISPR/Cas9 KO strategy could be applied to establish a stable knockout cell line for EMX1 to

further validate and unravel its precise role in regulating CHOP[316]. Since EMX1 is a transcription factor, identifying to which DNA regions and other factors EMX1 binds to would aid in dissecting the mechanism in how EMX1 controls the UPR during ER stress. While we demonstrated a role for different modulators of the ER stress response in hepatocytes, our results could also hint for candidate novel drug targets that could be exploited for either protection against liver injury and/or sensitization of cancer cells to anticancer therapeutics.

hiPSCs-HLCs as a model to recognize stress response activation

Over the years major improvements have been made in establishing hiPSC-derived hepatocyte-like cells (HLCs) using differentiation protocols mimicking the fetal liver development[49,50,317]. However, it has not been characterized how they respond towards chemical-induced stress in terms of stress response activation. Therefore, in **chapter 7** we compared the behaviour of hiPSC-HLCs with HepG2 and PHHs using transcriptomics upon exposure towards specific stress response inducers in a broad concentration range. Here, we found that HLCs were very sensitive towards oxidative stress and inflammatory signalling. However, PHHs were the most sensitive for chemical-induced UPR activation. DNA damage signalling was mostly picked up in HepG2 and undifferentiated hiPSCs as expected since these cell types proliferate. In general, hiPSCs-HLCs behaved more similarly as PHHs and HepG2 than hiPSCs, therefore also serve as a good model to study hepatotoxicity and for building a reporter panel for drug screening purposes. Besides, HLCs express higher levels of metabolizing enzymes therefore also suitable for studying metabolite-specific hepatotoxicity[49,50,317]. Interestingly, gene patterns that were active for the different stressors were different between the different cell types. This illustrates the complexity when translating gene responses from hiPSCs-HLCs systems to more human relevant test systems and highlights the need for other methodologies to compare the activity of genes. We have established a weighted gene co-regulation network analysis (WGCNA) approach to define the activation of biological responses in PHH[318]. Qualifying and quantifying the activity of gene networks might be a better approach to compare different test systems than individual gene level approaches.

Inter-individual variability in stress response activation

During risk assessment to account for inter-individual variability within the human population, standard safety factors are used for both pharmacokinetic as well as pharmacodynamics[59]. These standard factors are not data-driven, endpoint or chemical specific. Therefore it is crucial to map the variability that exists within the human population in activating stress response pathways to enable to define data-driven safety factors. To study inter-individual variability in stress response activation in **chapter 8**, the transcriptome was analysed of a panel of PHHs from 50 donors upon exposure towards specific stress inducers. Here, the variability could be mapped of the concentration-dependent stress response activation. Upon dose-response modelling to define benchmark concentrations (BMCs)[31,32], a maximum difference of the BMCs could be observed of

864-fold for tunicamycin exemplifying the great variability among donors. When combining with computational modelling, small panel sizes under-estimated the inter-individual variability and lowered the probability in estimating the correct variability. Besides, estimated safety factors were twice as high than the standard factor. This highlights the need of using data-driven safety factors during risk assessment to account for inter-individual variability. Here, we assessed the variability that exists in these plated PHHs cultured as a 2D monolayer derived from different individuals. Potentially, additional variation in stress response activation is due to difference in the isolation, plating and dedifferentiation process. A study by Blanchette et al. has characterized inter-individual variability in cardiotoxicity using hiPSC-derived cardiomyocytes[54,295]. Using hiPSCs enables to study multiple cell types from the same donor, however the transformation into pluripotent cells could also affect the observed variability between different donors. While not represented in this thesis, we observed that HepG2 cells do not mimic the average PHH donor in sensitivity. For the NRF2 pathway, HepG2 cells are much more sensitive, while for the UPR pathway HepG2 cells are less sensitive than PHH. This variability in sensitivity between donors and cell lines underscores the overall need to understand for each liver test system where it stands with respect to sensitivity. This will be in particular relevant when such test systems will be used in next generation risk assessment approaches without the use of animals to define safety margins for risk assessment.

Future perspectives and conclusions

To improve risk assessment, it is of importance to associate stress response activation with liabilities for the development of specific adversities within the framework of adverse outcome pathways (AOPs). Ideally the liability for a certain outcome should depend on duration, magnitude and benchmark concentration of stress response pathway activation. High-throughput methods for transcriptome analysis, such as TempO-seq targeted RNAseq[30], allows for mapping of stress response network activation for larger number of samples enabling to study dose-response relationships and temporal activation dynamics in a drug screening fashion. When combining with weighted co-regulated gene network analysis (WGCNA), modules of co-regulated genes similarly activated upon chemical exposure can be identified in an unbiased fashion and annotated for stress response pathway enrichment[98,318,319]. Associating module activation related to certain stress response pathways with the liability for development of adverse outcomes when combined with in vivo transcriptome data can give us improved insight in the liabilities for development of DILI upon stress response activation. Ideally, mapping of these module networks and there association to adverse outcome liabilities is established for all liver in vitro test systems used for drug screening. Moreover, the activation of each co-regulated module and its association towards adversity upon drug exposure may have different degrees of variability that exist within the human population. Therefore as part of future work, specific safety factors for each co-regulated gene module should be identified based on whole transcriptomes of a large panel of cells derived from different individuals upon chemical

exposures reflecting population variability. In this way, variability can be accurately accounted for during risk assessment for the entire gene co-regulated network upon chemical exposure for each test system used.

The selection of reporter genes for stress response activation used for drug safety evaluation is critical. Here, it is essential to select for genes which are most predictive for the identification of drugs inducing adverse events also revealing its mode-of-action. By utilizing the WGCNA approach, genes most reflective for critical modules can be selected associated with certain adversities. In addition, genes could be selected based on their variability within the human population by either selecting for the most stable genes to minimize donor-to-donor variability during drug screening or on the other hand specific genes that reflect mostly the inter-individual variability. Future work should focus on expanding the reporter panel in hiPSCs to improve predictivity and allow for the evaluation of toxicity in different organ cell types. Ideally, multiple hiPSC lines from different donors are combined to reflect inter-individual variability in drug-induced stress.

Currently, the differentiation towards fully mature hepatocytes of hiPSCs is still lacking where the hiPSC-HLCs are in an immature state which may influence their predictivity for drug-induced adversity. Therefore, there is a need to further improve the differentiation process and mimic the 3D environment in vivo. Recent efforts led to the identification that overexpression of three transcription factors during differentiation and the usage of amino acid rich medium could improve the maturation status significantly of hiPSC-HLCs[53]. However, the differentiation takes up to 40 days being very time consuming and costly and do not yet fully reach the level of PHHs. The most optimal balance between maturation status and time needed for differentiation should be characterized for drug screening purposes. To further improve maturity, hiPSC-HLCs can also be grown in a 3D structure either scaffold-free or within a scaffold such as Matrigel or hydrogel, combined with other cell types and the inclusion of microfluidics[56,320–326]. Despite, these efforts still did not lead to fully mature hepatocytes and needs further improvement. Currently, comparing hiPSC-HLC differentiation strategies and culture methods is difficult since there is no homogenization of standard readouts for the assessment of the maturation status, making it more difficult to pinpoint most essential culture modifications for HLC maturation. Therefore, besides development of improved methods of HLC maturation, current approaches should be properly compared using identical readouts and references and further characterized regarding their sensitivity and specificity for identifying DILI-inducing drugs.

Often patients are exposed not only to one chemical or drug, but take multiple drugs and come into contact with a mixture of environmental toxicants which adds another layer of complexity for risk assessment[327]. Depending on exposure levels, frequency of exposure and route of administration, this may impact their sensitivity in the development of adverse events upon exposure to a single drug. Not only exposure to other substances, but also the presence of certain

diseases could influence the response towards drug exposures. Ideally, the influence of prerequisite presence of certain stress levels and stress response activation should be taken into account during drug safety testing and requires novel strategies for risk assessment. By systematically evaluating the response towards mixtures of certain chemical or drug classes with a specific mode-of-action in comparison with single exposures and combining with in silico approaches, the influence of multiple exposures and certain exposure levels on the liability for adverse event development can be predicted.

To conclude, in this thesis the improved insight in the regulation of stress response pathways such as the unfolded protein response and the crosstalk between oxidative stress and DNA damage response will aid in understanding and prediction of DILI. Comparing different liver test systems to identify genotoxicants or stress response activation allows for well-considered selection of models fit-for-purpose in a tiered fashion for drug screening. Lastly, by mapping of the inter-individual variability of stress response activation upon chemical exposure allows for accurate definition of data-driven safety factors which can be used during risk assessment.

Appendix

References

Abbreviations

Nederlandse samenvatting

About the author

References

1. Watkins, P. B. Drug safety sciences and the bottleneck in drug development. *Clin Pharmacol Ther* **89**, 788–790 (2011).
2. Hayashi, P. H. *et al.* Death and Liver Transplantation Within 2 Years of Onset of Drug-Induced Liver Injury. *Hepatology* **66**, (2017).
3. Jennings, P., Limonciel, A., Felice, L. & Leonard, M. O. An overview of transcriptional regulation in response to toxicological insult. *Arch Toxicol* **87**, 49–72 (2013).
4. Simmons, S. O., Fan, C. Y. & Ramabhadran, R. Cellular stress response pathway system as a sentinel ensemble in toxicological screening. *Toxicological Sciences* **111**, 202–225 (2009).
5. Hoofnagle, J. H. & Björnsson, E. S. Drug-induced liver injury - types and phenotypes. *N Engl J Med* **381**, 264–273 (2019).
6. Björnsson, E. S., Bergmann, O. M., Björnsson, H. K., Kvaran, R. B. & Olafsson, S. Incidence, presentation, and outcomes in patients with drug-induced liver injury in the general population of Iceland. *Gastroenterology* **144**, (2013).
7. Ostapowicz, G. *et al.* Results of a Prospective Study of Acute Liver Failure at 17 Tertiary Care Centers in the United States. *Annuals of Internal Medicine* **137**, 947–955 (2002).
8. Bernal, W. *et al.* Outcome after wait-listing for emergency liver transplantation in acute liver failure: A single centre experience. *J Hepatol* **50**, 306–313 (2009).
9. Thanapirom, K. *et al.* The incidence, etiologies, outcomes, and predictors of mortality of acute liver failure in Thailand: A population-base study. *BMC Gastroenterol* **19**, 1–7 (2019).
10. Robles-Díaz, M., Medina-Caliz, I., Stephens, C., Andrade, R. J. & Lucena, M. I. Biomarkers in DILI: One more step forward. *Front Pharmacol* **7**, 1–7 (2016).
11. Robles-Diaz, M. *et al.* Use of Hy's law and a new composite algorithm to predict acute liver failure in patients with drug-induced liver injury. *Gastroenterology* **147**, (2014).
12. Russo, M. W. *et al.* Profiles of miRNAs in serum in severe acute drug induced liver injury and their prognostic significance. *Liver Int* **37**, 757–764 (2017).
13. Antoine, D. J. *et al.* Mechanistic biomarkers provide early and sensitive detection of acetaminophen-induced acute liver injury at first presentation to hospital. *Hepatology* **58**, 777–787 (2013).
14. Church, R. J. *et al.* Candidate biomarkers for the diagnosis and prognosis of drug-induced liver injury: An international collaborative effort. *Hepatology* **69**, 760–773 (2019).
15. Watkins, P. B. The DILI-sim Initiative: Insights into Hepatotoxicity Mechanisms and Biomarker Interpretation. *Clin Transl Sci* **12**, 122 (2019).
16. Weaver, R. J. *et al.* Managing the challenge of drug-induced liver injury: a roadmap for the development and deployment of preclinical predictive models. *Nat Rev Drug Discov* **19**, 131–148 (2020).
17. Copple, I. M. *et al.* Characterisation of the NRF2 transcriptional network and its response to chemical insult in primary human hepatocytes: implications for prediction of drug-induced liver injury. *Arch Toxicol* **93**, 385–399 (2019).
18. Ramachandran, A. & Jaeschke, H. Oxidative Stress and Acute Hepatic Injury. *Curr Opin Toxicol* **7**, 17–21 (2018).
19. Burban, A., Sharanek, A., Guguen-Guillouzo, C. & Guillouzo, A. Endoplasmic reticulum stress precedes oxidative stress in antibiotic-induced cholestasis and cytotoxicity in human hepatocytes. *Free Radic Biol Med* **115**, 166–178 (2018).
20. Fredriksson, L. *et al.* Drug-induced endoplasmic reticulum and oxidative stress responses independently sensitize toward TNFα-mediated hepatotoxicity. *Toxicological Sciences* **140**, 144–159 (2014).
21. Lafleur, M. a, Stevens, J. L. & Lawrence, J. W. Xenobiotic perturbation of ER stress and the unfolded protein response. *Toxicol Pathol* **41**, 235–62 (2013).
22. Hartwig, A. *et al.* Mode of action-based risk assessment of genotoxic carcinogens. *Arch Toxicol* **94**, 1787–1877 (2020).
23. Hanson, R. L., Porter, J. R. & Batchelor, E. Protein stability of p53 targets determines their temporal expression dynamics in response to p53 pulsing. *Journal of Cell Biology* **218**, 1282–1297 (2019).
24. Hafner, A., Bulyk, M. L., Jambhekar, A. & Lahav, G. The multiple mechanisms that regulate p53 activity and cell fate. *Nat Rev Mol Cell Biol* **20**, (2019).
25. Fredriksson, L. *et al.* Diclofenac inhibits tumor necrosis factor-α-induced nuclear factor-κB activation causing synergistic hepatocyte apoptosis. *Hepatology* **53**, 2027–2041 (2011).

26. Beggs, K. M. *et al.* Trovafloxacin-induced replication stress sensitizes HepG2 cells to tumor necrosis factor-alpha-induced cytotoxicity mediated by extracellular signal-regulated kinase and ataxia telangiectasia and Rad3-related. *Toxicology* **331**, 35–46 (2015).
27. Wink, S., Hiemstra, S., Herpers, B. & van de Water, B. High-content imaging-based BAC-GFP toxicity pathway reporters to assess chemical adversity liabilities. *Arch Toxicol* **91**, 1367–1383 (2017).
28. Wink, S., Hiemstra, S. W., Huppelschoten, S., Klip, J. E. & van de Water, B. Dynamic imaging of adaptive stress response pathway activation for prediction of drug induced liver injury. *Arch Toxicol* **92**, 1797–1814 (2018).
29. Hiemstra, S. *et al.* High-throughput confocal imaging of differentiated 3D liver-like spheroid cellular stress response reporters for identification of drug-induced liver injury liability. *Arch Toxicol* **93**, 2895–2911 (2019).
30. Yeakley, J. M. *et al.* A Trichostatin a expression signature identified by TempO-Seq targeted whole transcriptome profiling. *PLoS One* **12**, (2017).
31. Yang, L., Allen, B. C. & Thomas, R. S. BMDExpress: A software tool for the benchmark dose analyses of genomic data. *BMC Genomics* **8**, 1–8 (2007).
32. Phillips, J. R. *et al.* BMD Express 2: Enhanced transcriptomic dose-response analysis workflow. *Bioinformatics* **35**, 1780–1782 (2019).
33. Ulvestad, M. *et al.* Drug metabolizing enzyme and transporter protein profiles of hepatocytes derived from human embryonic and induced pluripotent stem cells. *Biochem Pharmacol* **86**, 691–702 (2013).
34. Godoy, P. *et al.* Recent advances in 2D and 3D in vitro systems using primary hepatocytes, alternative hepatocyte sources and non-parenchymal liver cells and their use in investigating mechanisms of hepatotoxicity, cell signaling and ADME. *Arch Toxicol* **87**, 1315–1530 (2013).
35. Fu, G. B. *et al.* Expansion and differentiation of human hepatocyte-derived liver progenitor-like cells and their use for the study of hepatotropic pathogens. *Cell Res* **29**, 8–22 (2019).
36. Kim, Y. *et al.* Small molecule-mediated reprogramming of human hepatocytes into bipotent progenitor cells. *J Hepatol* **70**, 97–107 (2019).
37. Zhang, K. *et al.* In Vitro Expansion of Primary Human Hepatocytes with Efficient Liver Repopulation Capacity. *Cell Stem Cell* **23**, 806-819.e4 (2018).
38. Bell, C. C. *et al.* Characterization of primary human hepatocyte spheroids as a model system for drug-induced liver injury, liver function and disease. *Sci Rep* **6**, (2016).
39. Hu, H. *et al.* Long-Term Expansion of Functional Mouse and Human Hepatocytes as 3D Organoids. *Cell* **175**, 1591-1606.e19 (2018).
40. Garnier, D. *et al.* Expansion of human primary hepatocytes in vitro through their amplification as liver progenitors in a 3D organoid system. *Sci Rep* **8**, 1–10 (2018).
41. Proctor, W. R. *et al.* Utility of spherical human liver microtissues for prediction of clinical drug-induced liver injury. *Arch Toxicol* **91**, 2849–2863 (2017).
42. Tolosa, L. *et al.* Human Upcyte Hepatocytes: Characterization of the Hepatic Phenotype and Evaluation for Acute and Long-Term Hepatotoxicity Routine Testing. *Toxicological Sciences* **152**, 214–229 (2016).
43. Ashraf, M. N., Asghar, M. W., Rong, Y., Doschak, M. R. & Kiang, T. K. L. Advanced In Vitro HepaRG Culture Systems for Xenobiotic Metabolism and Toxicity Characterization. *Eur J Drug Metab Pharmacokinet* **44**, 437–458 (2019).
44. Gupta, R. *et al.* Comparing in vitro human liver models to in vivo human liver using RNA-Seq. *Arch Toxicol* **95**, 573–589 (2021).
45. Sison-Young, R. L. *et al.* A multicenter assessment of single-cell models aligned to standard measures of cell health for prediction of acute hepatotoxicity. *Arch Toxicol* **91**, 1385–1400 (2017).
46. Guillouzo, A. *et al.* The human hepatoma HepaRG cells: A highly differentiated model for studies of liver metabolism and toxicity of xenobiotics. *Chem Biol Interact* **168**, 66–73 (2007).
47. Takahashi, K. *et al.* Induction of Pluripotent Stem Cells from Adult Human Fibroblasts by Defined Factors. *Cell* **131**, 861–872 (2007).
48. Takata, A. *et al.* Direct differentiation of hepatic cells from human induced pluripotent stem cells using a limited number of cytokines. *Hepatol Int* **5**, 890–898 (2011).
49. Song, Z. *et al.* Efficient generation of hepatocyte-like cells from human induced pluripotent stem cells. *Cell Res* **19**, 1233–42 (2009).
50. Si-Tayeb, K. *et al.* Highly efficient generation of human hepatocyte-like cells from induced pluripotent stem cells. *Hepatology* **51**, 297–305 (2010).
51. Sancho-Bru, P. *et al.* Directed differentiation of murine-induced pluripotent stem cells to functional hepatocyte-like cells. *J Hepatol* **54**, 98–107 (2011).

52. Böhm, F., Köhler, U. A., Speicher, T. & Werner, S. Regulation of liver regeneration by growth factors and cytokines. *EMBO Mol Med* **2**, 294–305 (2010).
53. Boon, R. *et al.* Amino acid levels determine metabolism and CYP450 function of hepatocytes and hepatoma cell lines. *Nat Commun* **11**, (2020).
54. Burnett, S. D. *et al.* Population-based toxicity screening in human induced pluripotent stem cell-derived cardiomyocytes. *Toxicol Appl Pharmacol* **381**, 114711 (2019).
55. Sharma, A., Sances, S., Workman, M. J. & Svendsen, C. N. Multi-lineage Human iPSC-Derived Platforms for Disease Modeling and Drug Discovery. *Cell Stem Cell* **26**, 309–329 (2020).
56. Ouchi, R. *et al.* Modeling Steatohepatitis in Humans with Pluripotent Stem Cell-Derived Organoids. *Cell Metab* **30**, 374-384.e6 (2019).
57. Bircsak, K. M. *et al.* A 3D microfluidic liver model for high throughput compound toxicity screening in the OrganoPlate®. *Toxicology* **450**, (2021).
58. Harrison, S. P. *et al.* Liver Organoids: Recent Developments, Limitations and Potential. *Front Med (Lausanne)* **8**, (2021).
59. IPCS & WHO. *Chemical-specific adjustment factors for interspecies differences and human variability: guidance document for use of data in dose/concentration-response assessment. Harmonization project document No. 2. World Health Organization Geneva* (2005).
60. Wilke, R. A. *et al.* Identifying genetic risk factors for serious adverse drug reactions: current progress and challenges. *Nat Rev Drug Discov* **6**, 904–916 (2007).
61. Gu, X. & Manautou, J. E. Molecular mechanisms underlying chemical liver injury. *Expert Rev Mol Med* **14**, (2012).
62. Vinken, M. The adverse outcome pathway concept: A pragmatic tool in toxicology. *Toxicology* **312**, 158–165 (2013).
63. O'Brien, P. J. *et al.* High concordance of drug-induced human hepatotoxicity with in vitro cytotoxicity measured in a novel cell-based model using high content screening. *Arch Toxicol* **80**, 580–604 (2006).
64. Xu, J. J. *et al.* Cellular imaging predictions of clinical drug-induced liver injury. *Toxicol Sci* **105**, 97–105 (2008).
65. Persson, M., Løye, A. F., Mow, T. & Hornberg, J. J. A high content screening assay to predict human drug-induced liver injury during drug discovery. *J Pharmacol Toxicol Methods* **68**, 302–313 (2013).
66. Tolosa, L. *et al.* Development of a multiparametric cell-based protocol to screen and classify the hepatotoxicity potential of drugs. *Toxicological Sciences* **127**, 187–198 (2012).
67. Zhang, J. *et al.* Evaluation of multiple mechanism-based toxicity endpoints in primary cultured human hepatocytes for the identification of drugs with clinical hepatotoxicity: Results from 152 marketed drugs with known liver injury profiles. *Chem Biol Interact* **255**, 3–11 (2016).
68. Tolosa, L., Carmona, A., Castell, J. v., Gómez-Lechón, M. J. & Donato, M. T. High-content screening of drug-induced mitochondrial impairment in hepatic cells: effects of statins. *Arch Toxicol* **89**, 1847–1860 (2015).
69. Bauch, C., Bevan, S., Woodhouse, H., Dilworth, C. & Walker, P. Predicting in vivo phospholipidosis-inducing potential of drugs by a combined high content screening and in silico modelling approach. *Toxicology in Vitro* **29**, 621–630 (2015).
70. Germano, D., Uteng, M., Pognan, F., Chibout, S. D. & Wolf, A. Determination of liver specific toxicities in rat hepatocytes by high content imaging during 2-week multiple treatment. *Toxicology in Vitro* **30**, 79–94 (2015).
71. van de Water, F. M., Havinga, J., Ravesloot, W. T., Horbach, G. J. M. J. & Schoonen, W. G. E. J. High content screening analysis of phospholipidosis: Validation of a 96-well assay with CHO-K1 and HepG2 cells for the prediction of in vivo based phospholipidosis. *Toxicology in Vitro* **25**, 1870–1882 (2011).
72. Lechner, C., Reichel, V., Moenning, U., Reichel, A. & Fricker, G. Development of a fluorescence-based assay for drug interactions with human Multidrug Resistance Related Protein (MRP2; ABCC2) in MDCKII-MRP2 membrane vesicles. *Eur J Pharm Biopharm* **75**, 284–290 (2010).
73. de Bruyn, T. *et al.* Confocal imaging with a fluorescent bile acid analogue closely mimicking hepatic taurocholate disposition. *J Pharm Sci* **103**, 1872–1881 (2014).
74. Perlman, Z. E. *et al.* Multidimensional drug profiling by automated microscopy. *Science* **306**, 1194–8 (2004).
75. Shuhendler, A. J., Pu, K., Cui, L., Uetrecht, J. P. & Rao, J. Real-time imaging of oxidative and nitrosative stress in the liver of live animals for drug-toxicity testing. *Nat Biotechnol* **32**, 373–80 (2014).

76. Poon, K. L. *et al.* Transgenic Zebrafish Reporter Lines as Alternative in vivo Organ Toxicity Models. *Toxicological Sciences* **156**, 133–148 (2017).
77. Ray, P. D., Huang, B. W. & Tsuji, Y. Reactive oxygen species (ROS) homeostasis and redox regulation in cellular signaling. *Cell Signal* **24**, 981–990 (2012).
78. Hetz, C. The unfolded protein response: controlling cell fate decisions under ER stress and beyond. *Nat Rev Mol Cell Biol* **13**, 89–102 (2012).
79. Wink, S. *et al.* Quantitative high content imaging of cellular adaptive stress response pathways in toxicity for chemical safety assessment. *Chem Res Toxicol* **27**, 338–355 (2014).
80. Banin, S. *et al.* Enhanced phosphorylation of p53 by ATM in response to DNA damage. *Science (1979)* **281**, 1674–1677 (1998).
81. Varfolomeev, E. & Vucic, D. Intracellular regulation of TNF activity in health and disease. *Cytokine* **101**, 26–32 (2018).
82. Jaeschke, H., Mcgill, M. R. & Ramachandran, A. Drug Metabolism Reviews Oxidant stress, mitochondria, and cell death mechanisms in drug-induced liver injury: Lessons learned from acetaminophen hepatotoxicity. *Drug Metab Rev* **44**, 88–106 (2012).
83. Liu, J., Wu, K. C., Lu, Y.-F., Ekuase, E. & Klaassen, C. D. NRF2 Protection against Liver Injury Produced by Various Hepatotoxicants. *Oxid Med Cell Longev* **2013**, (2013).
84. Qu, Q., Liu, J., Zhou, H. H. & Klaassen, C. D. Nrf2 protects against furosemide-induced hepatotoxicity. *Toxicology* **324**, 35–42 (2014).
85. Enomoto, A. *et al.* High Sensitivity of Nrf2 Knockout Mice to Acetaminophen Hepatotoxicity Associated with Decreased Expression of ARE-Regulated Drug Metabolizing Enzymes and Antioxidant Genes. *Toxicological sciences* **59**, 169–177 (2001).
86. Puthalakath, H. *et al.* ER stress triggers apoptosis by activating BH3-only protein Bim. *Cell* **129**, 1337–1349 (2007).
87. Yamaguchi, H. & Wang, H. G. CHOP is involved in endoplasmic reticulum stress-induced apoptosis by enhancing DR5 expression in human carcinoma cells. *Journal of Biological Chemistry* **279**, 45495–45502 (2004).
88. Hur, K. Y. *et al.* IRE1alpha activation protects mice against acetaminophen-induced hepatotoxicity. *Journal of Experimental Medicine* **209**, 307–318 (2012).
89. Uzi, D. *et al.* CHOP is a critical regulator of acetaminophen-induced hepatotoxicity. *J Hepatol* **59**, 495–503 (2013).
90. Yu, J. & Zhang, L. No PUMA, no death: Implications for p53-dependent apoptosis. *Cancer Cell* **4**, 248–249 (2003).
91. Poser, I. *et al.* BAC TransgeneOmics: A high-throughput method for exploration of protein function in mammals. *Nat Methods* **5**, 409–415 (2008).
92. Igarashi, Y. *et al.* Open TG-GATEs: A large-scale toxicogenomics database. *Nucleic Acids Res* **43**, D921–D927 (2015).
93. Suter, L. *et al.* EU Framework 6 Project: Predictive Toxicology (PredTox)-overview and outcome. *Toxicol Appl Pharmacol* **252**, 73–84 (2011).
94. Chen, M. *et al.* FDA-approved drug labeling for the study of drug-induced liver injury. *Drug Discov Today* **16**, 697–703 (2011).
95. Jiang, X., Wink, S., van de Water, B. & Kopp-Schneider, A. Functional analysis of high-content high-throughput imaging data. *J Appl Stat* **44**, 1903–1919 (2017).
96. Herpers, B. *et al.* Activation of the Nrf2 response by intrinsic hepatotoxic drugs correlates with suppression of NF-κB activation and sensitizes toward TNFα-induced cytotoxicity. *Arch Toxicol* **90**, 1163–1179 (2016).
97. Fredriksson, L. *et al.* Drug-induced endoplasmic reticulum and oxidative stress responses independently sensitize toward TNFα-mediated hepatotoxicity. *Toxicological Sciences* **140**, 144–159 (2014).
98. Sutherland, J. J., Jolly, R. A., Goldstein, K. M. & Stevens, J. L. Assessing Concordance of Drug-Induced Transcriptional Response in Rodent Liver and Cultured Hepatocytes. *PLoS Comput Biol* **12**, 1–31 (2016).
99. Carreras Puigvert, J. *et al.* Systems biology approach identifies the kinase csnk1a1 as a regulator of the DNA damage response in embryonic stem cells. *Sci Signal* **6**, ra5 (2013).
100. Lecluyse, E. L., Witek, R. P., Andersen, M. E. & Powers, M. J. Organotypic liver culture models: Meeting current challenges in toxicity testing. *Crit Rev Toxicol* **42**, 501–548 (2012).
101. Ramaiahgari, S. C. *et al.* A 3D in vitro model of differentiated HepG2 cell spheroids with improved liver-like properties for repeated dose high-throughput toxicity studies. *Arch Toxicol* **88**, 1083–1095 (2014).

102. Hiemstra, S. *et al.* Comprehensive Landscape of Nrf2 and p53 Pathway Activation Dynamics by Oxidative Stress and DNA Damage. *Chem Res Toxicol* **30**, 923–933 (2017).
103. Jennen, D. G. J. *et al.* Comparison of HepG2 and HepaRG by Whole-Genome Gene Expression Analysis for the Purpose of Chemical Hazard Identification. *Toxicological Sciences* **115**, 66–79 (2010).
104. Wilkening, S., Stahl, F. & Bader, A. Comparison of primary human hepatocytes and hepatoma cell line HepG2 with regard to their biotransformation properties. *Drug Metabolism and Disposition* **31**, (2003).
105. Gómez-Lechón, M. J., Tolosa, L. & Donato, M. T. Metabolic activation and drug-induced liver injury: In vitro approaches for the safety risk assessment of new drugs. *Journal of Applied Toxicology* **36**, 752–768 (2016).
106. Amacher, D. E. The primary role of hepatic metabolism in idiosyncratic drug-induced liver injury. *Expert Opinion on Drug Metabolism & Toxicology* **8**, 335–347 (2012).
107. Leung, L., Kalgutkar, A. S. & Obach, R. S. Metabolic activation in drug-induced liver injury. *Drug Metab Rev* **44**, 18–33 (2012).
108. Jinek, M. *et al.* RNA-programmed genome editing in human cells. *Elife* **2**, (2013).
109. Cong, L. *et al.* Multiplex Genome Engineering Using CRISPR/Cas Systems. *Science (1979)* **339**, 819–823 (2013).
110. Gómez-Lechón, M. J. & Tolosa, L. Human hepatocytes derived from pluripotent stem cells: a promising cell model for drug hepatotoxicity screening. *Arch Toxicol* **90**, 2049–2061 (2016).
111. Gao, X. & Liu, Y. A transcriptomic study suggesting human iPSC-derived hepatocytes potentially offer a better in vitro model of hepatotoxicity than most hepatoma cell lines. *Cell Biol Toxicol* **33**, 407–421 (2017).
112. Asplund, A. *et al.* One Standardized Differentiation Procedure Robustly Generates Homogenous Hepatocyte Cultures Displaying Metabolic Diversity from a Large Panel of Human Pluripotent Stem Cells. *Stem Cell Rev and Rep* **12**, 90–140 (2016).
113. Chen, Y. F. *et al.* Rapid generation of mature hepatocyte-like cells from human induced pluripotent stem cells by an efficient three-step protocol. *Hepatology* **55**, 1193–1203 (2012).
114. Raju, R. *et al.* Cell Expansion During Directed Differentiation of Stem Cells Toward the Hepatic Lineage. *Stem Cells Dev* **26**, 274–284 (2017).
115. Ware, B. R., Berger, D. R. & Khetani, S. R. Prediction of drug-induced liver injury in micropatterned co-cultures containing iPSC-derived human hepatocytes. *Toxicological Sciences* **145**, 252–262 (2015).
116. Krewski, D. *et al.* Toxicity testing in the 21st century: a vision and a strategy. *J Toxicol Environ Health B Crit Rev* **13**, 51–138 (2015).
117. Shah, I. *et al.* Using ToxCast^{TM} data to reconstruct dynamic cell state trajectories and estimate toxicological points of departure. *Environ Health Perspect* **124**, 910–919 (2016).
118. Tong, K. I., Kobayashi, A., Katsuoka, F. & Yamamoto, M. Two-site substrate recognition model for the Keap1-Nrf2 system: A hinge and latch mechanism. *Biol Chem* **387**, 1311–1320 (2006).
119. Ogura, T. *et al.* Keap1 is a forked-stem dimer structure with two large spheres enclosing the intervening, double glycine repeat, and C-terminal domains. *PNAS* **107**, 2842–2847 (2010).
120. Chorley, B. N. *et al.* Identification of novel NRF2-regulated genes by ChIP-Seq: influence on retinoid X receptor alpha. *Nucleic Acids Res* **40**, 7416–7429 (2012).
121. FitzGerald, J. E., Grenon, M. & Lowndes, N. F. 53BP1: function and mechanisms of focal recruitment. *Biochem Soc Trans* **37**, 897–904 (2009).
122. Urso, L., Calabrese, F., Favaretto, A., Conte, P. F. & Pasello, G. Critical review about MDM2 in cancer: Possible role in malignant mesothelioma and implications for treatment. *Crit Rev Oncol Hematol* **97**, 220–230 (2016).
123. Hagemann, J. H., Thomasova, D., Mulay, S. R. & Anders, H.-J. Nrf2 signalling promotes ex vivo tubular epithelial cell survival and regeneration via murine double minute (MDM)-2. *Nephrol Dial Transplant* **28**, 2028–2037 (2013).
124. You, A. *et al.* Transcription factor Nrf2 maintains the basal expression of Mdm2: An implication of the regulation of p53 signaling by Nrf2. *Arch Biochem Biophys* **507**, 356–364 (2011).
125. Liu, K. *et al.* NQO1 Stabilizes p53 in Response to Oncogene-Induced Senescence. *Int. J. Biol. Sci* **11**, 762–771 (2015).
126. Kaur, P., Kalia, S. & Bansal, M. P. Effect of diethyl maleate induced oxidative stress on male reproductive activity in mice: Redox active enzymes and transcription factors expression. *Mol Cell Biochem* **291**, 55–61 (2006).

127. Montecucco, A., Zanetta, F. & Biamonti, G. Molecular mechanisms of etoposide. *EXCLI J* **14**, 95–108 (2015).
128. Hendriks, G. *et al.* The ToxTracker assay: Novel GFP reporter systems that provide mechanistic insight into the genotoxic properties of chemicals. *Toxicological Sciences* **125**, 285–298 (2012).
129. Di, Z. *et al.* Automated Analysis of NF-κB Nuclear Translocation Kinetics in High-Throughput Screening. *PLoS One* **7**, (2012).
130. Du, G. *et al.* Spatial Dynamics of DNA Damage Response Protein Foci along the Ion Trajectory of High-LET Particles. *Radiat Res* **176**, 706–715 (2011).
131. Wickham, H. ggplot2: Elegant Graphics for Data Analysis. *Springer-Verlag, New York* (2009).
132. Dowle, M., Srinivasan, A., Short, T. & Lianogluo, S. Extension of Data.frame. *CRAN R Package* (2016).
133. Kolde, R. Pheatmap: pretty heatmaps. *R package version 61* (2012).
134. Wickham, H. Reshaping Data with the reshape Package. *J Stat Softw* **21**, 1–20 (2007).
135. Wickham, H. The Split-Apply-Combine Strategy for Data Analysis. *J. Stat. Softw* **40**, (2011).
136. Wickham, H. Scale Functions for Visualization. *CRAN R Package.* (2016).
137. Wickham, H. Easily Tidy Data with “spread()” and “gather()” Functions. *CRAN R Package* (2016).
138. Ichimura, Y. *et al.* Phosphorylation of p62 Activates the Keap1-Nrf2 Pathway during Selective Autophagy. *Mol Cell* **51**, 618–631 (2013).
139. Taguchi, K. *et al.* Keap1 degradation by autophagy for the maintenance of redox homeostasis. *PNAS* **109**, 13561–13566 (2012).
140. Corkery, D. *et al.* Regulation of the BRCA1 gene by an SRC3/53BP1 complex. *BMC Biochem* **12**, 50 (2011).
141. Rappold, I., Iwabuchi, K., Date, T. & Chen, J. Tumor Suppressor p53 Binding Protein 1 (53BP1) Is Involved in DNA Damage-signaling Pathways. *J Cell Biol* **153**, 613–620 (2001).
142. Chen, W. *et al.* Direct Interaction between Nrf2 and p21Cip1/WAF1 Upregulates the Nrf2-Mediated Antioxidant Response. *Mol Cell* **34**, 663–673 (2009).
143. Walmsley, R. M. & Billinton, N. How accurate is in vitro prediction of carcinogenicity? *Br J Pharmacol* **162**, 1250–1258 (2011).
144. Singh, N. P., Mccoy, M. T., Tice, R. R. & Schneider, E. L. A Simple Technique for Quantitation of Low Levels of DNA Damage in Individual Cells. *Exp Cell Res* **175**, 184–191 (1988).
145. Smith, C. C., O’Donovan, M. R. & Martin, E. A. hOGG1 recognizes oxidative damage using the comet assay with greater specificity than FPG or ENDOIII. *Mutagenesis* **21**, 185–190 (2006).
146. Duthie, S. J. & McMillan, P. Uracil misincorporation in human DNA detected using single cell gel electrophoresis. *Carcinogenesis* **18**, 1709–1714 (1997).
147. Cordelli, E., Bignami, M. & Pacchierotti, F. Comet assay: a versatile but complex tool in genotoxicity testing. *Toxicol Res (Camb)* **10**, 68–78 (2021).
148. Henderson, L., Wolfreys, A., Fedyk, J., Bourner, C. & Windebank, S. The ability of the Comet assay to discriminate between genotoxins and cytotoxins. *Mutagenesis* **13**, 89–94 (1998).
149. Luzhna, L., Kathiria, P. & Kovalchuk, O. Micronuclei in genotoxicity assessment: From genetics to epigenetics and beyond. *Front Genet* **4**, (2013).
150. Nikolova, T. *et al.* The γH2AX assay for genotoxic and nongenotoxic agents: Comparison of H2AX phosphorylation with cell death response. *Toxicological Sciences* **140**, 103–117 (2014).
151. Westerink, W. M. A., Stevenson, J. C. R., Horbach, G. J. & Schoonen, W. G. E. J. The development of RAD51C, Cystatin A, p53 and Nrf2 luciferase-reporter assays in metabolically competent HepG2 cells for the assessment of mechanism-based genotoxicity and of oxidative stress in the early research phase of drug development. *Mutat Res Genet Toxicol Environ Mutagen* **696**, 21–40 (2010).
152. Simpson, K. *et al.* The BlueScreen-384 assay as an indicator of genotoxic hazard potential in early-stage drug discovery. *J Biomol Screen* **18**, 441–452 (2013).
153. Hendriks, G. *et al.* The Extended ToxTracker Assay Discriminates Between Induction of DNA Damage, Oxidative Stress, and Protein Misfolding. *Toxicological Sciences* **150**, 190–203 (2016).
154. Lauschke, V. M., Shafagh, R. Z., Hendriks, D. F. G. & Ingelman-Sundberg, M. 3D Primary Hepatocyte Culture Systems for Analyses of Liver Diseases, Drug Metabolism, and Toxicity: Emerging Culture Paradigms and Applications. *Biotechnol J* **14**, (2019).
155. McCullough, A. K. & Lloyd, R. S. Mechanisms underlying aflatoxin-associated mutagenesis – Implications in carcinogenesis. *DNA Repair (Amst)* **77**, 76–86 (2019).
156. Sykes, D. B. The emergence of dihydroorotate dehydrogenase (DHODH) as a therapeutic target in acute myeloid leukemia. *Expert Opin Ther Targets* **22**, 893–898 (2018).

157. Dasari, S. & Bernard Tchounwou, P. Cisplatin in cancer therapy: Molecular mechanisms of action. *Eur J Pharmacol* **740**, 364–378 (2014).
158. Deans, A. J. & West, S. C. DNA interstrand crosslink repair and cancer. *Nat Rev Cancer* **11**, 467–480 (2011).
159. Sahasranaman, S., Howard, D. & Roy, S. Clinical pharmacology and pharmacogenetics of thiopurines. *Eur J Clin Pharmacol* **64**, 753–767 (2008).
160. Wang, Y. *et al.* Distinct roles of cytochrome P450 reductase in mitomycin c redox cycling and cytotoxicity. *Mol Cancer Ther* **9**, 1852–1863 (2010).
161. Dougherty, M. T. *et al.* Unifying biological image formats with HDF5. *Commun ACM* **52**, 42–47 (2009).
162. Fox, B. C. *et al.* Validation of reference gene stability for APAP hepatotoxicity studies in different in vitro systems and identification of novel potential toxicity biomarkers. *Toxicology in Vitro* **24**, 1962–1970 (2010).
163. Livak, K. J. & Schmittgen, T. D. Analysis of relative gene expression data using real-time quantitative PCR and the 2-ΔΔCT method. *Methods* **25**, 402–408 (2001).
164. Mav, D. *et al.* A hybrid gene selection approach to create the S1500+ targeted gene sets for use in high-throughput transcriptomics. *PLoS One* **13**, 1–19 (2018).
165. Love, M. I., Huber, W. & Anders, S. Moderated estimation of fold change and dispersion for RNA-seq data with DESeq2. *Genome Biol* **15**, 1–21 (2014).
166. Seo, J.-E. *et al.* Performance of high-throughput CometChip assay using primary human hepatocytes: a comparison of DNA damage responses with in vitro human hepatoma cell lines. *Arch Toxicol* **94**, 2207–2224 (2020).
167. McCarthy, A. R., Hollick, J. J. & Westwood, N. J. The discovery of nongenotoxic activators of p53: Building on a cell-based high-throughput screen. *Semin Cancer Biol* **20**, 40–45 (2010).
168. Ladds, M. J. G. W. *et al.* A DHODH inhibitor increases p53 synthesis and enhances tumor cell killing by p53 degradation blockage. *Nat Commun* **9**, (2018).
169. Kawanishi, M. *et al.* Genotoxicity and reactive oxygen species production induced by magnetite nanoparticles in mammalian cells. *J Toxicol Sci* **38**, 503–511 (2013).
170. McCool, K. W. & Miyamoto, S. DNA damage-dependent NF-κB activation: NEMO turns nuclear signaling inside out. *Immunol Rev* **246**, 311–326 (2012).
171. Kirkland, D. *et al.* Updated recommended lists of genotoxic and non-genotoxic chemicals for assessment of the performance of new or improved genotoxicity tests. *Mutat Res Genet Toxicol Environ Mutagen* **795**, 7–30 (2016).
172. Ren, Z. *et al.* Endoplasmic Reticulum Stress Induction and ERK1/2 Activation Contribute to Nefazodone-Induced Toxicity in Hepatic Cells. *Toxicological Sciences* (2016).
173. Wang, M. & Kaufman, R. J. Protein misfolding in the endoplasmic reticulum as a conduit to human disease. *Nature* **529**, 326–335 (2016).
174. Chevet, E., Hetz, C. & Samali, A. Endoplasmic Reticulum Stress-Activated Cell Reprogramming in Oncogenesis. *Cancer Discov* **5**, (2015).
175. Braakman, I. & Hebert, D. N. Protein Folding in the Endoplasmic Reticulum. (2013).
176. Hetz, C. & Papa, F. R. The Unfolded Protein Response and Cell Fate Control. *Mol Cell* **69**, 169–181 (2018).
177. Carrara, M., Prischi, F., Nowak, P. R., Kopp, M. C. & Ali, M. M. U. Noncanonical binding of BiP ATPase domain to Ire1 and Perk is dissociated by unfolded protein CH1 to initiate ER stress signaling. *Elife* **4**, e03522 (2015).
178. Shen, J., Chen, X., Hendershot, L. & Prywes, R. ER stress regulation of ATF6 localization by dissociation of BiP/GRP78 binding and unmasking of Golgi localization signals. *Dev Cell* **3**, 99–111 (2002).
179. Oikawa, D., Kimata, Y., Kohno, K. & Iwawaki, T. Activation of mammalian IRE1α upon ER stress depends on dissociation of BiP rather than on direct interaction with unfolded proteins. *Exp Cell Res* **315**, 2496–2504 (2009).
180. Sundaram, A., Appathurai, S., Plumb, R. & Mariappan, M. Dynamic changes in complexes of IRE1α, PERK, and ATF6 α during the endoplasmic reticulum stress. *Mol Biol Cell* **29**, 1376–1388 (2018).
181. Calfon, M. *et al.* IRE1 couples endoplasmic reticulum load to secretory capacity by processing the XBP-1 mRNA. *Nature* **415**, 92 (2002).
182. Lee, A.-H., Iwakoshi, N. N. & Glimcher, L. H. XBP-1 regulates a subset of endoplasmic reticulum resident chaperone genes in the unfolded protein response. *Mol Cell Biol* **23**, 7448–7459 (2003).
183. Oda, Y. *et al.* Derlin-2 and Derlin-3 are regulated by the mammalian unfolded protein response and are required for ER-associated degradation. *J Cell Biol* **172**, 383–393 (2006).

184. Yoshida, H. *et al.* A time-dependent phase shift in the mammalian unfolded protein response. *Dev Cell* **4**, 265–271 (2003).
185. Shaffer, A. L. *et al.* XBP1, downstream of Blimp-1, expands the secretory apparatus and other organelles, and increases protein synthesis in plasma cell differentiation. *Immunity* **21**, 81–93 (2004).
186. Harding, H. P., Zhang, Y. & Ron, D. Protein translation and folding are coupled by an endoplasmic-reticulum-resident kinase. *Nature* **397**, 271 (1999).
187. Lu, P. D., Harding, H. P. & Ron, D. Translation reinitiation at alternative open reading frames regulates gene expression in an integrated stress response. *J Cell Biol* **167**, 27–33 (2004).
188. Ameri, K. & Harris, A. L. Activating transcription factor 4. *Int J Biochem Cell Biol* **40**, 14–21 (2008).
189. Han, J. *et al.* ER-stress-induced transcriptional regulation increases protein synthesis leading to cell death. *Nat Cell Biol* **15**, 481–90 (2013).
190. Harding, H. P. *et al.* Regulated translation initiation controls stress-induced gene expression in mammalian cells. *Mol Cell* **6**, 1099–1108 (2000).
191. Urra, H., Dufey, E., Lisbona, F., Rojas-Rivera, D. & Hetz, C. When ER stress reaches a dead end. *Biochim Biophys Acta Mol Cell Res* **1833**, 3507–3517 (2013).
192. Marciniak, S. J. *et al.* CHOP induces death by promoting protein synthesis and oxidation in the stressed endoplasmic reticulum. *Genes Dev* **18**, 3066–3077 (2004).
193. Chen, X., Shen, J. & Prywes, R. The lumenal domain of ATF6 senses ER stress and causes translocation of ATF6 from the ER to the Golgi. *Journal of Biological Chemistry* (2002).
194. Ye, J. *et al.* ER stress induces cleavage of membrane-bound ATF6 by the same proteases that process SREBPs. *Mol Cell* **6**, 1355–1364 (2000).
195. Yoshida, H., Matsui, T., Yamamoto, A., Okada, T. & Mori, K. XBP1 mRNA is induced by ATF6 and spliced by IRE1 in response to ER stress to produce a highly active transcription factor. *Cell* **107**, 881–891 (2001).
196. Yamamoto, K. *et al.* Transcriptional induction of mammalian ER quality control proteins is mediated by single or combined action of ATF6α and XBP1. *Dev Cell* **13**, 365–376 (2007).
197. Yoshida, H. *et al.* ATF6 activated by proteolysis binds in the presence of NF-Y (CBF) directly to the cis-acting element responsible for the mammalian unfolded protein response. *Mol Cell Biol* **20**, 6755–6767 (2000).
198. Hartung, T. *et al.* Systems toxicology: Real world applications and opportunities. *Chem Res Toxicol* **30**, 870–882 (2017).
199. Kuijper, I. A., Yang, H., van de Water, B. & Beltman, J. B. Unraveling cellular pathways contributing to drug-induced liver injury by dynamical modeling. *Expert Opin Drug Metab Toxicol* **13**, 5–17 (2017).
200. Cho, H. *et al.* Signaling dynamics of palmitate-induced ER stress responses mediated by ATF4 in HepG2 cells. *BMC Syst Biol* **7**, 9 (2013).
201. Pincus, D. *et al.* BiP binding to the ER-stress sensor Ire1 tunes the homeostatic behavior of the unfolded protein response. *PLoS Biol* **8**, e1000415 (2010).
202. Erguler, K., Pieri, M. & Deltas, C. A mathematical model of the unfolded protein stress response reveals the decision mechanism for recovery, adaptation and apoptosis. *BMC Syst Biol* **7**, 16 (2013).
203. Trusina, A., Papa, F. R. & Tang, C. Rationalizing translation attenuation in the network architecture of the unfolded protein response. *Proceedings of the National Academy of Sciences* **105**, 20280–20285 (2008).
204. Trusina, A. & Tang, C. The unfolded protein response and translation attenuation: a modelling approach. *Diabetes Obes Metab* **12**, 27–31 (2010).
205. Diedrichs, D. R., Gomez, J. A., Huang, C.-S., Rutkowski, D. T. & Curtu, R. A data-entrained computational model for testing the regulatory logic of the vertebrate unfolded protein response. *Mol Biol Cell* mbc–E17 (2018).
206. Oppelt, A. *et al.* Model-based identification of TNFα-induced IKKβ-mediated and IκBα-mediated regulation of NFκB signal transduction as a tool to quantify the impact of drug-induced liver injury compounds. *NPJ Syst Biol Appl* **4**, 23 (2018).
207. Hiemstra, S. *et al.* Comprehensive landscape of Nrf2 and p53 pathway activation dynamics by oxidative stress and DNA damage. *Chem Res Toxicol* **30**, 923–933 (2016).
208. Niemeijer, M. *et al.* Systems Microscopy Approaches in Unraveling and Predicting Drug-Induced Liver Injury (DILI). in *Drug-Induced Liver Toxicity* 611–625 (Springer, 2018).
209. Garcia-Alonso, L., Ibrahim, M. M., Turei, D. & Saez-Rodriguez, J. Benchmark and integration of resources for the estimation of human transcription factor activities. *Genome Res.* **29**, 1363–1375 (2019).

210. Zhang, Z. Reshaping and aggregating data: an introduction to reshape package. *Ann Transl Med* **4**, (2016).
211. Dowle, M. *et al.* Package 'data. table'. (2018).
212. Erich Neuwirth. RColorBrewer: ColorBrewer Palettes. *CRAN R Package* (2014).
213. McKay, M. D., Beckman, R. J. & Conover, W. J. A comparison of three methods for selecting values of input variables in the analysis of output from a computer code. *Technometrics* **42**, 55–61 (2000).
214. Coleman, T. F. & Li, Y. An interior trust region approach for nonlinear minimization subject to bounds. *SIAM Journal on optimization* **6**, 418–445 (1996).
215. Raue, A. *et al.* Lessons learned from quantitative dynamical modeling in systems biology. *PLoS One* **8**, e74335 (2013).
216. Rosenblatt, M., Timmer, J. & Kaschek, D. Customized steady-state constraints for parameter estimation in non-linear ordinary differential equation models. *Front Cell Dev Biol* **4**, 41 (2016).
217. Raue, A. *et al.* Structural and practical identifiability analysis of partially observed dynamical models by exploiting the profile likelihood. *Bioinformatics* **25**, 1923–1929 (2009).
218. García-Pérez, M. A. & Alcalá-Quintana, R. Converging evidence that common timing processes underlie temporal-order and simultaneity judgments: A model-based analysis. *Atten Percept Psychophys* **77**, 1750–1766 (2015).
219. García-Pérez, M. A. & Alcalá-Quintana, R. Visual and auditory components in the perception of asynchronous audiovisual speech. *Iperception* **6**, 2041669515615735 (2015).
220. Yoo, J. *et al.* GlcNAc-1-P-transferase–tunicamycin complex structure reveals basis for inhibition of N-glycosylation. *Nat Struct Mol Biol* **25**, 217 (2018).
221. Takayanagi, S., Fukuda, R., Takeuchi, Y., Tsukada, S. & Yoshida, K. Gene regulatory network of unfolded protein response genes in endoplasmic reticulum stress. *Cell Stress Chaperones* **18**, 11–23 (2013).
222. Oyadomari, S. & Mori, M. Roles of CHOP/GADD153 in endoplasmic reticulum stress. *Cell Death Differ* **11**, 381–389 (2004).
223. Wu, J. *et al.* ATF6α optimizes long-term endoplasmic reticulum function to protect cells from chronic stress. *Dev Cell* **13**, 351–364 (2007).
224. Ma, Y., Brewer, J. W., Diehl, J. A. & Hendershot, L. M. Two distinct stress signaling pathways converge upon the CHOP promoter during the mammalian unfolded protein response. *J Mol Biol* **318**, 1351–1365 (2002).
225. Scheuner, D. *et al.* Translational control is required for the unfolded protein response and in vivo glucose homeostasis. *Mol Cell* **7**, 1165–1176 (2001).
226. Rutkowski, D. T. *et al.* Adaptation to ER stress is mediated by differential stabilities of pro-survival and pro-apoptotic mRNAs and proteins. *PLoS Biol* **4**, e374 (2006).
227. Ji, C., Mehrian-Shai, R., Chan, C., Hsu, Y.-H. & Kaplowitz, N. Role of CHOP in hepatic apoptosis in the murine model of intragastric ethanol feeding. *Alchol clin exp res* **29**, 1496–1503 (2005).
228. Vitale, M. *et al.* Inadequate BiP availability defines endoplasmic reticulum stress. *Elife* **8**, e41168 (2019).
229. Walter, P. & Ron, D. The unfolded protein response: From stress pathway to homeostatic regulation. *Science (1979)* **334**, 1081–1086 (2011).
230. Kopp, M. C., Larburu, N., Durairaj, V., Adams, C. J. & Ali, M. M. U. UPR proteins IRE1 and PERK switch BiP from chaperone to ER stress sensor. *Nat Struct Mol Biol* **26**, 1053 (2019).
231. Hetz, C., Zhang, K. & Kaufman, R. J. Mechanisms, regulation and functions of the unfolded protein response. *Nature Reviews Molecular Cell Biology 2020 21:8* **21**, 421–438 (2020).
232. Yang, H., Niemeijer, M., van de Water, B. & Beltman, J. B. ATF6 Is a Critical Determinant of CHOP Dynamics during the Unfolded Protein Response. *iScience* **23**, (2020).
233. Malhi, H. & Kaufman, R. J. Endoplasmic Reticulum Stress in Liver Disease. *J Hepatol* **54**, 795–809 (2011).
234. Lebeaupin, C. *et al.* Endoplasmic reticulum stress signalling and the pathogenesis of non-alcoholic fatty liver disease. *J Hepatol* **69**, 927–947 (2018).
235. Urra, H., Dufey, E., Avril, T., Chevet, E. & Hetz, C. Endoplasmic Reticulum Stress and the Hallmarks of Cancer. *Trends Cancer* **2**, 252–262 (2016).
236. Pavlović, N. & Heindryckx, F. Targeting ER stress in the hepatic tumor microenvironment. *FEBS J* (2021) doi:10.1111/FEBS.16145.
237. Al-Rawashdeh, F. Y., Scriven, P., Cameron, I. C., Vergani, P. V. & Wyld, L. Unfolded protein response activation contributes to chemoresistance in hepatocellular carcinoma. *Eur J Gastroenterol Hepatol* **22**, 1099–1105 (2010).

238. Wang, M. & Kaufman, R. J. The impact of the endoplasmic reticulum protein-folding environment on cancer development. *Nature Reviews Cancer 2014 14:9* **14**, 581–597 (2014).
239. Shuda, M. *et al.* Activation of the ATF6, XBP1 and grp78 genes in human hepatocellular carcinoma: A possible involvement of the ER stress pathway in hepatocarcinogenesis. *J Hepatol* **38**, 605–614 (2003).
240. Patel, A. *et al.* The unfolded protein response is associated with cancer proliferation and worse survival in hepatocellular carcinoma. *Cancers (Basel)* **13**, (2021).
241. Wang, X., Terfve, C., Rose, J. C. & Markowetz, F. HTSanalyzeR : an R / Bioconductor package for integrated network analysis of high-throughput screens. **27**, 879–880 (2011).
242. Cuevas, A., Febrero, M. & Fraiman, R. An anova test for functional data. **47**, 111–122 (2004).
243. Peterson, H., Kolberg, L., Kuzmin, I., Arak, T. & Adler, P. g : Profiler : a web server for functional enrichment analysis and conversions of gene lists (2019 update). 1–8 (2019) doi:10.1093/nar/gkz369.
244. Carbon, S. *et al.* The Gene Ontology resource: Enriching a GOld mine. *Nucleic Acids Res* **49**, D325–D334 (2021).
245. Jassal, B. *et al.* The reactome pathway knowledgebase. *Nucleic Acids Res* **48**, D498–D503 (2020).
246. Shannon, P. *et al.* Cytoscape : A Software Environment for Integrated Models of Biomolecular Interaction Networks. *Genome Res* **13**, 2498–2504 (2003).
247. Merico, D., Isserlin, R., Stueker, O., Emili, A. & Bader, G. D. Enrichment Map : A Network-Based Method for Gene-Set Enrichment Visualization and Interpretation. *PLoS One* **5**, (2010).
248. Oesper, L., Merico, D., Isserlin, R. & Bader, G. D. WordCloud : a Cytoscape plugin to create a visual semantic summary of networks. *Source Code Biol Med* **6**, 2–5 (2011).
249. Cerami, E. *et al.* The cBio Cancer Genomics Portal: An open platform for exploring multidimensional cancer genomics data. *Cancer Discov* **2**, 401–404 (2012).
250. Gao, J. *et al.* Integrative analysis of complex cancer genomics and clinical profiles using the cBioPortal. *Sci Signal* **6**, 1–20 (2013).
251. Liu, J. *et al.* An Integrated TCGA Pan-Cancer Clinical Data Resource to Drive High-Quality Survival Outcome Analytics. *Cell* **173**, 400-416.e11 (2018).
252. Wink, S., Hiemstra, S., Herpers, B. & van de Water, B. High-content imaging-based BAC-GFP toxicity pathway reporters to assess chemical adversity liabilities. *Arch Toxicol* **91**, 1367–1383 (2017).
253. Wink, S., Hiemstra, S. W., Huppelschoten, S., Klip, J. E. & van de Water, B. Dynamic imaging of adaptive stress response pathway activation for prediction of drug induced liver injury. *Arch Toxicol* **92**, 1–18 (2018).
254. Yoo, J. *et al.* GlcNAc-1-P-transferase–tunicamycin complex structure reveals basis for inhibition of N-glycosylation. *Nat Struct Mol Biol* **25**, (2018).
255. Wijaya, L. S. *et al.* Integration of temporal single cell cellular stress response activity with logic-ODE modeling reveals activation of ATF4-CHOP axis as a critical predictor of drug-induced liver injury. *Biochem Pharmacol* **190**, (2021).
256. Yeakley, J. M. *et al.* A Trichostatin a expression signature identified by TempO-Seq targeted whole transcriptome profiling. *PLoS One* **12**, (2017).
257. Fan, Z. *et al.* CDK13 cooperates with CDK12 to control global RNA polymerase II processivity. *Sci Adv* **6**, (2020).
258. Hunter, M. *et al.* The P28T mutation in the GALK1 gene accounts for galactokinase deficiency in Roma (Gypsy) patients across Europe. *Pediatr Res* **51**, 602–606 (2002).
259. García, M. *et al.* Phosphofructo-1-kinase deficiency leads to a severe cardiac and hematological disorder in addition to skeletal muscle glycogenosis. *PLoS Genet* **5**, (2009).
260. Bonnard, C. *et al.* A loss-of-function NUAK2 mutation in humans causes anencephaly due to impaired Hippo-YAP signaling. *J Exp Med* **217**, (2020).
261. Cecchi, C. & Boncinelli, E. Emx homeogenes and mouse brain development. *Trends Neurosci* **23**, 347–352 (2000).
262. Kobeissy, F. H. *et al.* Deciphering the Role of Emx1 in Neurogenesis: A Neuroproteomics Approach. *Front Mol Neurosci* **9**, (2016).
263. Lim, J. W. C. *et al.* EMX1 regulates NRP1-mediated wiring of the mouse anterior cingulate cortex. *Development* **142**, 3746–57 (2015).
264. Kisiel, J. B. *et al.* Hepatocellular Carcinoma Detection by Plasma Methylated DNA: Discovery, Phase I Pilot, and Phase II Clinical Validation. *Hepatology* **69**, 1180–1192 (2019).
265. Sun, X. J., Wang, M. C., Zhang, F. H. & Kong, X. An integrated analysis of genome-wide DNA methylation and gene expression data in hepatocellular carcinoma. *FEBS Open Bio* **8**, 1093–1103 (2018).

266. Nanjo, S., Asada, K. & Yamashita, S. Identification of gastric cancer risk markers that are informative in individuals with past H. pylori infection. **15**, 382–388 (2012).
267. Niemeijer, M. *et al.* Transcriptomic mapping of the inter-individual variability of cellular stress response activation in primary human hepatocytes. *bioRxiv* 2021.08.26.457742 (2021) doi:10.1101/2021.08.26.457742.
268. Lucena, M. I. *et al.* Susceptibility to Amoxicillin-Clavulanate-Induced Liver Injury Is Influenced by Multiple HLA Class I and II Alleles. *Gastroenterology* **141**, 338–347 (2011).
269. Kullak-Ublick, G. A. *et al.* Drug-induced liver injury: Recent advances in diagnosis and risk assessment. *Gut* **66**, 1154–1164 (2017).
270. Lu, J. *et al.* Morphological and functional characterization and assessment of iPSC-derived hepatocytes for in vitro toxicity testing. *Toxicological Sciences* **147**, 39–54 (2015).
271. José, M., Lechón, G. & Tolosa, L. Human hepatocytes derived from pluripotent stem cells : a promising cell model for drug hepatotoxicity screening. *Arch Toxicol* **90**, 2049–2061 (2016).
272. Helsen, N. *et al.* Stem cell-derived hepatocytes: A novel model for hepatitis e virus replication. *J Hepatol* **64**, 565–573 (2016).
273. Li, S. *et al.* Valproic acid-induced hepatotoxicity in alpers syndrome is associated with mitochondrial permeability transition pore opening-dependent apoptotic sensitivity in an induced pluripotent stem cell model. *Hepatology* **61**, 1730–1739 (2015).
274. Godoy, P. *et al.* Gene networks and transcription factor motifs defining the differentiation of stem cells into hepatocyte-like cells. *J Hepatol* **63**, 934–942 (2015).
275. Ramaiahgari, S. C. *et al.* The Power of Resolution: Contextualized Understanding of Biological Responses to Liver Injury Chemicals Using High-throughput Transcriptomics and Benchmark Concentration Modeling. *Toxicological sciences* **169**, 553–566 (2019).
276. Tricot, T. I., Helsen, N., F Kaptein, S. J., Neyts, J. & Verfaillie, C. M. Human stem cell-derived hepatocyte-like cells support Zika virus replication and provide a relevant model to assess the efficacy of potential antivirals. *PLoS One* **13**, e0209097 (2018).
277. Czysz, K., Minger, S. & Thomas, N. Dmso efficiently down regulates pluripotency genes in human embryonic stem cells during definitive endoderm derivation and increases the proficiency of hepatic differentiation. *PLoS One* **10**, 1–16 (2015).
278. Liguori, M. J. *et al.* Microarray analysis in human hepatocytes suggests a mechanism for hepatotoxicity induced by trovafloxacin. *Hepatology* **41**, 177–186 (2005).
279. Kadota, K. *et al.* Detection of genes with tissue-specific expression patterns using Akaike's information criterion procedure. *Physiol Genomics* **12**, 251–259 (2003).
280. Pagès, H., Carlson, M., Falcon, S. & Li, N. AnnotationDbi: Annotation Database Interface. *R package version 1.43.1* (2018).
281. Acikgöz, A., Giri, S., Cho, M. G. & Bader, A. Morphological and functional analysis of hepatocyte spheroids generated on poly-HEMA-treated surfaces under the influence of fetal calf serum and nonparenchymal cells. *Biomolecules* **3**, 242–269 (2013).
282. Ghosheh, N. *et al.* Highly Synchronized Expression of Lineage-Specific Genes during *In Vitro* Hepatic Differentiation of Human Pluripotent Stem Cell Lines. *Stem Cells Int* **2016**, 1–22 (2016).
283. Lundquist, P. *et al.* The Impact of Solute Carrier (SLC) Drug Uptake Transporter Loss in Human and Rat Cryopreserved Hepatocytes on Clearance Predictions. *Drug Metab Dispos.* **42**, 469–480 (2014).
284. Wang, H. *et al.* Tunicamycin-induced unfolded protein response in the developing mouse brain. *Toxicol Appl Pharmacol* **283**, 157–167 (2015).
285. Kritsch, D. *et al.* Tribbles 2 mediates cisplatin sensitivity and DNA damage response in epithelial ovarian cancer. *Int J Cancer* **141**, 1600–1614 (2017).
286. Xu, Z. *et al.* Analysis of differentially expressed genes among human hair follicle-derived iPSCs, induced hepatocyte-like cells, and primary hepatocytes. *Stem Cell Res Ther* **9**, (2018).
287. Hurrell, T., Segeritz, C.-P., Vallier, L., Lilley, K. S. & Cromarty, A. D. Proteomic Comparison of Various Hepatic Cell Cultures for Preclinical Safety Pharmacology. *Toxicological Sciences* **164**, (2018).
288. Kang, S. J. *et al.* Chemically induced hepatotoxicity in human stem cell-induced hepatocytes compared with primary hepatocytes and HepG2. *Cell Biol Toxicol* **32**, 403–417 (2016).
289. Brenner, C., Galluzzi, L., Kepp, O. & Kroemer, G. Decoding cell death signals in liver inflammation. *J Hepatol* **59**, 583–594 (2013).
290. Marí, M. *et al.* Redox Control of Liver Function in Health and Disease. *Antioxid Redox Signal* **12**, (2010).
291. Shimada, M., Tsukada, K., Kagawa, N. & Matsumoto, Y. Reprogramming and differentiation-dependent transcriptional alteration of DNA damage response and apoptosis genes in human induced pluripotent stem cells. *J Radiat Res* **60**, 719–728 (2019).

292. Olson, H. *et al.* Concordance of the toxicity of pharmaceuticals in humans and in animals. *Regulatory Toxicology and Pharmacology* **32**, 56–67 (2000).
293. Gupta, R. *et al.* Comparing in vitro human liver models to in vivo human liver using RNA-Seq. *Arch Toxicol* **95**, 573–589 (2021).
294. ter Braak, B. *et al.* Systematic transcriptome-based comparison of cellular adaptive stress response activation networks in hepatic stem cell-derived progeny and primary human hepatocytes. *Toxicology in Vitro* **73**, (2021).
295. Blanchette, A. D., Burnett, S. D., Grimm, F. A., Rusyn, I. & Chiu, W. A. A bayesian method for population-wide cardiotoxicity hazard and risk characterization using an in vitro human model. *Toxicological Sciences* **178**, 391–403 (2020).
296. Alexandre, E. *et al.* Plateable cryopreserved human hepatocytes for the assessment of cytochrome P450 inducibility: Experimental condition-related variables affecting their response to inducers. *Xenobiotica* **42**, 968–979 (2012).
297. Liberzon, A. *et al.* Molecular signatures database (MSigDB) 3.0. *Bioinformatics* **27**, 1739–1740 (2011).
298. Subramanian, A. *et al.* Gene set enrichment analysis: A knowledge-based approach for interpreting genome-wide expression profiles. *Proc Natl Acad Sci U S A* **102**, 15545–15550 (2005).
299. Bell, C. C. *et al.* Comparison of hepatic 2D sandwich cultures and 3D spheroids for long-term toxicity applications: A multicenter study. *Toxicological Sciences* **162**, 655–666 (2018).
300. Shah, I., Antonijevic, T., Chambers, B., Harrill, J. & Thomas, R. Estimating Hepatotoxic Doses Using High-Content Imaging in Primary Hepatocytes. *Toxicological Sciences* **183**, 285–301 (2021).
301. Tabernilla, A. *et al.* In vitro liver toxicity testing of chemicals: A pragmatic approach. *Int J Mol Sci* **22**, (2021).
302. Abdo, N. *et al.* Population-based in vitro hazard and concentration-response assessment of chemicals: The 1000 genomes high-throughput screening study. *Environ Health Perspect* **123**, 458–466 (2015).
303. Lake, A. D. *et al.* The adaptive endoplasmic reticulum stress response to lipotoxicity in progressive human nonalcoholic fatty liver disease. *Toxicological Sciences* **137**, 26–35 (2014).
304. Lee, S., Kim, S., Hwang, S., Cherrington, N. J. & Ryu, D. Y. Dysregulated expression of proteins associated with ER stress, autophagy and apoptosis in tissues from nonalcoholic fatty liver disease. *Oncotarget* **8**, 63370–63381 (2017).
305. Puri, P. *et al.* Activation and Dysregulation of the Unfolded Protein Response in Nonalcoholic Fatty Liver Disease. *Gastroenterology* **134**, 568–576 (2008).
306. Arconzo, M., Piccinin, E. & Moschetta, A. Increased risk of acute liver failure by pain killer drugs in NAFLD: Focus on nuclear receptors and their coactivators. *Digestive and Liver Disease* **53**, 26–34 (2021).
307. Kučera, O. *et al.* Steatotic rat hepatocytes in primary culture are more susceptible to the acute toxic effect of acetaminophen. *Physiol Res* **61**, 93–101 (2012).
308. Ganey, P. E., Luyendyk, J. P., Maddox, J. F. & Roth, R. A. Adverse hepatic drug reactions: Inflammatory episodes as consequence and contributor. *Chem Biol Interact* **150**, 35–51 (2004).
309. Wu, W. *et al.* Inflammatory stress sensitizes the liver to atorvastatin-induced injury in ApoE-/- mice. *PLoS One* **11**, 1–15 (2016).
310. Li, W. *et al.* Crosstalk between ER stress, NLRP3 inflammasome, and inflammation. *Appl Microbiol Biotechnol* **104**, 6129–6140 (2020).
311. Simmons, S. O., Fan, C. Y. & Ramabhadran, R. Cellular Stress Response Pathway System as a Sentinel Ensemble in Toxicological Screening. *Toxicological Sciences* **111**, 202–225 (2009).
312. Snijders, K. E. *et al.* Fluorescent tagging of endogenous Heme oxygenase-1 in human induced pluripotent stem cells for high content imaging of oxidative stress in various differentiated lineages. *Arch Toxicol* **95**, 3285–3302 (2021).
313. Hiemstra, S. *et al.* Dynamic modeling of Nrf2 pathway activation in liver cells after toxicant exposure. *Scientific Reports 2022 12:1* **12**, 1–10 (2022).
314. Srinivas, U. S., Tan, B. W. Q., Vellayappan, B. A. & Jeyasekharan, A. D. ROS and the DNA damage response in cancer. *Redox Biol* **25**, (2019).
315. Heldring, M. M. *et al.* Model-based translation of DNA damage signaling dynamics across cell types. *PLoS Comput Biol* **18**, e1010264 (2022).
316. Chen, Y. *et al.* Engineering Human Stem Cell Lines with Inducible Gene Knockout using CRISPR/Cas9. *Stem Cell* **17**, 233–244 (2015).

317. Takayama, K. *et al.* Efficient generation of functional hepatocytes from human embryonic stem cells and induced pluripotent stem cells by HNF4α transduction. *Molecular Therapy* **20**, 127–137 (2012).
318. Callegaro, G. *et al.* The human hepatocyte TXG-MAPr: gene co-expression network modules to support mechanism-based risk assessment. *Arch Toxicol* **95**, 3745–3775 (2021).
319. Sutherland, J. J. *et al.* Toxicogenomic module associations with pathogenesis: a network-based approach to understanding drug toxicity. *Pharmacogenomics J* **18**, 377–390 (2018).
320. Kumar, M. *et al.* A fully defined matrix to support a pluripotent stem cell derived multi-cell-liver steatohepatitis and fibrosis model. *Biomaterials* **276**, (2021).
321. Takayama, K. *et al.* 3D spheroid culture of hESC/hiPSC-derived hepatocyte-like cells for drug toxicity testing. *Biomaterials* **34**, 1781–1789 (2013).
322. Giobbe, G. G. *et al.* Functional differentiation of human pluripotent stem cells on a chip. *Nat Methods* **12**, 637–640 (2015).
323. Gieseck, R. L. *et al.* Maturation of induced pluripotent stem cell derived hepatocytes by 3D-culture. *PLoS One* **9**, (2014).
324. Takebe, T. *et al.* Massive and Reproducible Production of Liver Buds Entirely from Human Pluripotent Stem Cells. *Cell Rep* **21**, 2661–2670 (2017).
325. Takebe, T. *et al.* Generation of a vascularized and functional human liver from an iPSC-derived organ bud transplant. *Nat Protoc* **9**, 396–409 (2014).
326. Danoy, M. *et al.* Optimized protocol for the hepatic differentiation of induced pluripotent stem cells in a fluidic microenvironment. *Biotechnol Bioeng* **116**, 1762–1776 (2019).
327. Bopp, S. K. *et al.* Regulatory assessment and risk management of chemical mixtures: challenges and ways forward. *Crit Rev Toxicol* **49**, 174–189 (2019).

Abbreviations

2D	two dimensional
3D	three dimensional
AAGLY	amino-acid rich medium supplemented with 2% glycine
AFB	aflatoxin B1
AIC	Akaike information criterion
ANOVA	analysis of variance
AnV	annexin-V
AOP	adverse outcome pathway
ARE	anti-oxidant response element
AARE	amino acid response element
ATP	adenosine triphosphate
ATCC	American Type Culture Collection
AUC	area under the curve
BAC	bacterial artificial chromosome
BCA	bicinchoninic acid
BIC	Bayesian information criterion
BMC	benchmark concentration
BRE	brequinar
BSA	bovine serum albumin
cDNA	complementary DANN
CI	confidence interval
CIS	cisplatin
Cmax	maximum serum drug concentration
CPT	cisplatin
CV	coefficient of variation
DDR	DNA damage response
DEG	differentially expressed genes
DEM	diethyl maleate
DILI	drug-induced liver injury
DMSO	dimethyl sulfoxide
DMEM	dulbecco's modified eagle medium
DSB	double stranded breaks
EC50	half maximal effective concentration
ECL	enhanced chemiluminescent
ER	endoplasmic Reticulum
ESRE	ER stress response element
eGFP	enhanced green fluorescent protein
FACS	Fluorescence-activated Cell Sorting
FBS	fetal bovine serum
FC	fold change
FDR	false discovery rate
G	glycosylated
GEM	gemcitabine
GEO	Gene Expression Omnibus
GFP	green fluorescent protein
GO	gene ontology
GSEA	gene set enrichment analysis
HCC	hepatocellular carcinoma
HCI	high-content imaging
HCS	high-content screening
HDP	human diploid fibroblasts
hiPSC	human induced pluripotent stem cell
HLA	human leukocyte antigen
HLC	hepatocyte-like cell
IC_{50}	half-maximal inhibitory concentration
iDILI	idiosyncratic DILI
IPA	ingenuity pathway analysis
KO	knock-out
LDM	liver differentiation medium
maxFC	maximal fold change
MAQC	microarray quality control
MEF	mouse embryonic fibroblasts
MIE	molecular initiation event
MMC	mitomycin C
MoA	mode-of-action
mRNA	messenger RNA
NAFLD	non-alcoholic fatty liver disease
NAM	new approach method
NES	normalized enrichment score
NGRA	next generation risk assessment
NS	not significant
ODE	ordinary differential equation
OECD	Organisation for Economic Co-operation and Development
OSR / OX	oxidative stress response
p_{adj}	adjusted p-value
PBS	phosphate-buffered saline
PCA	principal component analysis
PCR	polymerase chain reaction
PDI	protein disulfide isomerases
PHH	primary human hepatocyte
PI	propidium iodide
PPIase	prolyl peptidylcis–transisomerases
PoD	point-of-departure

PVDF	polyvinylidene fluoride
RIPA	radioimmunoprecipitation assay
RNAi	RNA interference
ROS	reactive oxygen species
rpm	rounds per minute
RPMI	Roswell Park Memorial Institute
RT	room temperature
RT-qPCR	real time quantitative PCR
SD	standard deviation
SDS-page	sodium dodecyl-sulfate polyacrylamide gel electrophoresis
SE	standard error
siRNA	small interfering RNA
SNP	single nucleotide polymorphisms
TBL	total bilirubin
TBS	tris-buffered saline
TCGA	The Cancer Genome Atlas
TDVF	toxicodynamic variability factor
TF	transcription factor
TUN	tunicamycin
UF	uncertainty factor
UG	unglycosylated
ULN	upper limit of the normal range
UPR	unfolded protein response
WGCNA	weighted gene co-regulation network analysis
WT	wildtype

Nederlandse samenvatting

Het optreden van leverschade door geneesmiddelen is een belangrijke reden voor het uit de handel nemen van geneesmiddelen of het vroegtijdig beëindigen van verdere ontwikkeling van het geneesmiddel tijdens preklinische of klinische studies. Het ontstaan van leverschade kan in het ergste geval resulteren in het nodig hebben van een lever transplantatie door leverfalen of zelfs leiden tot de dood. Daarom is het zeer belangrijk om een accurate voorspelling van leverschade door geneesmiddelen te verkrijgen tijdens een vroeg stadium van de ontwikkeling van geneesmiddelen. Er zijn drie vormen van geneesmiddel-gemedieerde leverschade, namelijk direct, idiosyncratisch en indirect. De directe vorm is voorspelbaar, afhankelijk van de dosering en treedt vaak op kort na blootstelling. Idiosyncratische leverschade is niet doseringsafhankelijk, moeilijk te voorspellen en komt weinig voor (1 op de 100.000 patiënten). De derde vorm van leverschade, indirect, is onlangs toegevoegd als nieuwe categorie waarbij verergering van al bestaande leverziekte een rol speelt. Aangezien het alleen bij een klein aantal patiënten voorkomt en moeilijk te voorspellen is in preklinische en klinische studies, is het van groot belang om in kaart te brengen waarom bepaalde patiënten gevoeliger zijn voor de ontwikkeling van geneesmiddel-gemedieerde leverschade.

De lever bestaat voor een groot deel uit hepatocyten, maar ook stellaatcellen, Kupffer cellen en leversinusoïdale endotheelcellen zijn aanwezig. Hepatocyten zijn verantwoordelijk voor de stofwisseling, aanmaak van gal en het omzetten en onschadelijk maken van giftige stoffen. Echter blootstelling aan deze stoffen, zoals bepaalde geneesmiddelen en hun metabolieten, kunnen een bepaalde mate van stress veroorzaken in hepatocyten. Om dit weg te vangen hebben cellen specifieke adaptatie-mechanismes door middel van de activatie van specifieke stress responsen, zoals de NRF2 gereguleerde oxidatieve stress respons, endoplasmatisch reticulum (ER) stress respons gemedieerd door activatie van drie sensoren (ATF6, PERK en IRE1), p53 gereguleerde DNA schade respons en de immuun respons via NF-κB signaleringscascade. Echter wanneer het stress niveau te hoog is of te lang duurt, zal er een omschakeling plaatsvinden naar het initiëren van celdood. De activering van deze stress responsen tijdens blootstelling aan geneesmiddelen is ook één van de vroege stappen dat kan leiden tot leverschade. Daarom kan het volgen en kwantificeren van de activering van deze responsen tot een betere voorspelling van leverschade leiden.

Voor het kunnen volgen van deze stress responsen tijdens blootstellingen, zijn er eiwitten specifiek voor iedere respons voorzien van een fluorescent eiwit in leverkanker HepG2 cellen. Zodoende kan een stress respons reporter panel worden gecreëerd om activering van toxische responsen te meten. Door te combineren met confocale microscopie, kan het fluorescentie niveau in cellen bepaald worden, hetgeen indicatief is voor stress respons activatie. Ook kan er op transciptoom niveau gekeken worden naar activatie van specifieke biologische processen door middel van TempO-seq analyse, een gerichte RNA-sequencing techniek die high throughput

screening van toxische responsen veroorzaakt door kandidaat geneesmiddelen mogelijk maakt. Wanneer dit wordt gecombineerd met de blokkering van de expressie van bepaalde genen door middel van RNA interferentie, kan er specifiek worden gekeken naar de rol van die individuele genen in stress respons activatie. In dit proefschrift hebben we de regulatie van deze stress responsen bestudeerd gebruikmakend van deze technieken. Ook hebben we in kaart gebracht wat de variabiliteit is in activatie van deze stress responsen binnen de humane populatie. Dit zal bijdragen aan het verkrijgen van meer inzicht en verbeteren van de voorspelling van geneesmiddel-gemedieerde leverschade.

Ten eerste wordt er in **hoofdstuk 2** een overzicht gegeven van het bouwen van de stress respons HepG2 reporter panel en het gebruik daarvan voor het screenen van geneesmiddelen voor een betere voorspelling van de ontwikkeling van leverschade. De verschillende stappen voor het maken en gebruik van deze reporters worden uitgelegd: selecteren van stress respons genen, maken van DNA constructen waarin de sequentie van het fluorescent eiwit is ingebouwd aan het eind of start van het eiwit-coderend gedeelte van het stress respons gen, transfectie van het DNA construct in de HepG2 cellen, selectie, validatie, beschrijving van analyse methodes en gebruiksdoeleinden.

De verschillende stress respons processen kunnen ook mogelijk elkaar beïnvloeden tijdens blootstellingen en daarmee verschil geven in gevoeligheid voor het ontwikkelen van leverschade. Daarom is het van belang om dit beter in kaart te brengen. In **hoofdstuk 3**, bekijken we het samenspel tussen de oxidatieve stress en DNA schade respons gebruikmakend van de HepG2 reporters in combinatie met confocale microscopie. Concentratie afhankelijke activatie dynamiek voor beide stress responsen werd gekarakteriseerd na blootstelling met zowel oxidatieve stress (diethyl maleaat) en DNA schade respons (etoposide) inducerende stoffen. Hierbij gaf blootstelling aan etoposide ook activatie van SRXN1, een target gen van transcriptie factor NRF2 binnen de oxidatieve stress respons, indicatief voor een mogelijke crosstalk tussen de twee responsen. Inderdaad, inhibitie van KEAP1, een sensor en remmer van de oxidatieve stress respons, leidde tot verhoogde activatie van de DNA schade respons al bij lagere concentraties van etoposide. Verdere gen inhibitie studies door middel van RNA interferentie gaf meer inzicht in hoe KEAP1 de DNA schade respons kon beïnvloeden.

Naast de keuze van de te meten eindpunten voor het maken van een accurate voorspelling van leverschade, is de keuze van het test systeem ook van belang. Het kweken van HepG2 cellen in 3D als spheroids in een Matrigel matrix zorgt ervoor dat ze niet meer gaan delen waardoor ze ook geschikt worden voor langere blootstellingen. Ook zien we een verhoogd expressie van hepatocyte markers en zijn ze meer metabool actief waardoor ook metaboliet-specifieke effecten kunnen worden opgepikt ten opzichte van 2D. Verder heeft ook het medium waarin de cellen gekweekt worden invloed op de differentiatie status van de cellen en kan dit een effect hebben op de gevoeligheid voor het oppikken van geneesmiddelen die leverschade veroorzaken.

In **hoofdstuk 4** hebben we daarom de invloed bekeken van de kweekmethode van de HepG2 DNA schade reporters op het identificeren van genotoxische stoffen. Reporter cellen werden gekweekt in 2D of 3D in combinatie met standaard medium of medium waarbij een hoge hoeveelheid aminozuren werden toegevoegd (AAGLY). Dit AAGLY medium zorgt voor verdere differentiatie en expressie van CYP enzymen door middel van het veranderen van het metabolisch profiel en zorgt ook voor een proliferatie stop. De gebruikte kweekmethodes hadden sterke invloed op de gevoeligheid voor het oppikken van deze stoffen, waarbij voor sommige stoffen proliferatie en andere stoffen die afhankelijk zijn van metaboliet formatie voor toxische effecten een betere differentiatie status nodig was.

Activatie van de ER stress respons speelt ook een belangrijke rol in de ontwikkeling van leverschade bij sommige stoffen. In de omschakeling van adaptieve naar celdood signalering tijdens blootstellingen, speelt de transcriptie factor CHOP een grote rol. Daarom is het van belang om meer inzicht te krijgen in de regulatie van CHOP tijdens ER stress. In **hoofdstuk 5** combineren we computationeel modelleren en confocale microscopie van HepG2 ER stress reporters na blootstelling aan tunicamycin, een ER stress-inducerende stof. Na het construeren van een model van de ER stress respons werd duidelijk dat met name ATF6, een transcriptie factor en een sensor van de ER stress respons, invloed had op de initiële activatie dynamiek van CHOP. Dit was verder gevalideerd door middel van inhibitie van gen expressie van ATF6 middels RNA interferentie, wat voornamelijk een sterke verlaging van CHOP gaf in de initiële fase van activatie. Hieruit blijkt de cruciale rol van ATF6 in CHOP regulatie tijdens ER stress.

Om meer inzicht te krijgen in de regulatie van CHOP en ER stress, laten we in **hoofdstuk 6** zien dat we door middel van een grootschalige RNA interferentie screen van 3,457 genen in HepG2 CHOP reporter cellen nieuwe regulators van de ER stress respons kunnen identificeren. Na het inhiberen van de expressie van individuele genen en blootstelling met tunicamycin, kwantificeren we de CHOP expressie met confocale microscopie in HepG2 CHOP reporter cellen. Na een validatie screen, konden we 74 genen identificeren waarvan 18 genen mogelijke negatieve en 56 genen mogelijke positieve regulators waren van CHOP. De invloed van deze 74 genen op andere componenten van de ER stress respons (ATF4, XBP1 en BIP) werd geïdentificeerd en getest met andere ER stress-inducerende stoffen (thapsigargin en omeprazole). Transcriptoom perturbaties na inhibitie van een selectie van 10 genen in HepG2 en primaire humane hepatocyten (PHHs) na blootstelling aan tunicamycin werd bekeken. Hieruit bleek dat de transcriptie factor, EMX1, een sterke invloed had op meerdere ER stress signaleringscascades in zowel HepG2 als PHHs. Het volledig in kaart brengen van de regulatie van ER stress signalering kan bijdragen aan een betere voorspelling van leverschade.

Op het moment zijn PHHs nog steeds de gouden standaard voor het testen van geneesmiddelen voor levertoxiciteit in de preklinische fase van de ontwikkeling. Echter is er een beperkte beschikbaarheid aan PHHs, dedifferentiëren ze snel en moet er rekening worden gehouden met

inter-donor variabiliteit. Een nieuwe bron van hepatocyten zijn humane geïnduceerde pluripotente stamcellen (hiPSCs) gedifferentieerd naar hepatocyte-achtige cellen (HLCs). Echter is er verdere karakterisering nodig voor het gebruik als test systeem voor hepatotoxiciteit screening. In **hoofdstuk 7** vergelijken we het verschil in stress respons activatie van hiPSC-HLCs met andere in vitro lever modellen (PHHs en HepG2) door middel van transcriptoom analyse na blootstelling aan stress respons-inducerende stoffen. HLCs bleken heel gevoelig te zijn voor oxidatieve stress en immuun respons inductie vergeleken met PHHs. De ER stress respons was het sterkst geïnduceerd in PHHs. Voor de DNA schade respons waren zowel HepG2 als hiPSC cellen het meest gevoelig mede door de proliferatie capaciteit van deze cellen.

Voor het verder verbeteren van de voorspelling van leverschade door geneesmiddelen, is het cruciaal om inzicht te hebben in de variabiliteit tussen verschillende patiënten. Hiervoor hebben we in **hoofdstuk 8** gekeken naar de variabiliteit van stress respons activatie in vijftig verschillende PHHs van verschillende patiënten na blootstelling aan specifieke stress-inducerende stoffen in een brede concentratie reeks. Concentratie-respons modellering maakt het mogelijk om benchmark concentraties te bepalen en de gevoeligheid tussen de verschillende PHHs te vergelijken waar tot aan ~850-maal verschil geobserveerd was. Humane populatie modellering onthulde dat het gebruiken van een kleine PHH panel tijdens geneesmiddelen screening sterk de variabiliteit onderschat en de waarschijnlijkheid om de juiste human populatie variabiliteit te schatten klein is. Op dit moment wordt er standaard een veiligheidsfactor van $10^{1/2}$ gebruikt voor het corrigeren voor de variabiliteit van toxicodynamiek binnen de humane populatie. Echter op basis van deze data is deze standaardfactor niet genoeg en in sommige gevallen zelfs twee keer te laag. Daarom is het van groot belang om op data gebaseerde veiligheidsfactoren te gebruiken voor het corrigeren voor variabiliteit tussen patiënten.

In het kort, in dit proefschrift is een verbeterde inzicht in de regulatie van stress respons signaleringscascades verkregen tijdens blootstellingen aan stress-inducerende stoffen. Dit zal bijdragen aan het beter begrijpen en voorspellen van geneesmiddel-gemedieerde leverschade. Door het vergelijken van verschillende lever in vitro modellen in stress respons activatie kan er een betere keuze worden gemaakt in de selectie van geschikte lever in vitro modellen voor een bepaalde vraagstelling. Op basis hiervan kan een integrale aanpak worden opgesteld voor het screenen van geneesmiddelen op potentie van ontwikkeling van leverschade. Door de variabiliteit in kaart te brengen van stress response activatie tussen patiënten kan op een nauwkeurige manier worden gecorrigeerd voor de uiteindelijke risicobeoordeling van geneesmiddelen.

About the author

Marie Cornelia (Marije) Niemeijer was born in Zuidhorn, The Netherlands, on 14th of September 1991. She went to the Stedelijk College Eindhoven for bilingual preparatory scientific education and obtained her VWO diploma with profile Nature and Health and the international baccalaureate certificate English language in 2009. She started her study Bio-pharmaceutical Sciences at Leiden University and retrieved her Bachelor degree in 2012 and Master degree in 2014 cum laude with the specialization Toxicology. During her Master studies, she characterized oxidative stress related genes using a RNA interference approach combined with confocal imaging at the division of Toxicology of Leiden Academic Centre for Drug Research (LACDR) at Leiden University (Leiden, The Netherlands) under supervision of dr. Bram Herpers. She also has developed a RNA interference method in primary human and rat hepatocytes to study mechanisms of drug-induced hepatotoxicity at the department of Drug Metabolism and Pharmacokinetics at Janssen Pharmaceutical Companies (Beerse, Belgium) under supervision of dr. Anita Dankers. Thereafter, she started her PhD with the title 'Unfolding the regulation of stress response pathways upon liver injury' within the IMI MIP-DILI and EU-ToxRisk project at the division of Drug Discovery and Safety, LACDR, Leiden University under supervision of prof. dr. Bob van de Water. Since March 2019, she continued as a researcher on the regulation of stress response activation during long-term chemical and nanoparticle exposures using 3D liver in vitro models within the Horizon2020 PATROLS project and in collaboration with Unilever. In 2021, she studied the regulation of ER stress signaling in liver organoids derived from alpha-1 antitrypsin deficiency patients at the department of Surgery at Erasmus MC (Rotterdam, The Netherlands) under supervision of prof. dr. Luc van der Laan. Since June 2022, she continued as post-doctoral researcher within the RISK-HUNT*3R* project at the division of Drug Discovery and Safety at the LACDR, working on the utility of human induced pluripotent stem cell reporter panel for hepatotoxicity screening purposes. In addition, within the TD-TRAQ project funded by EFSA she will focus on understanding the human inter-individual variability of toxic responses.

A

Contact Information

@: marijedg14@outlook.com

T : +31 (0) 681450728

List of publications

Quantitative high content imaging of cellular adaptive stress response pathways in toxicity for chemical safety assessment.
Wink S, Hiemstra S, Huppelschoten S, Danen E, **Niemeijer M**, Hendriks G, Vrieling H, Herpers B, van de Water B.
Chem Res Toxicol. 2014. doi: 10.1021/tx4004038.

Comprehensive Landscape of Nrf2 and p53 Pathway Activation Dynamics by Oxidative Stress and DNA Damage.
Hiemstra S*, **Niemeijer M***, Koedoot E, Wink S, Klip JE, Vlasveld M, de Zeeuw E, van Os B, White A, van de Water B.
***Both authors contributed equally**
Chem Res Toxicol. 2017. doi: 10.1021/acs.chemrestox.6b00322.

Preclinical imaging methods for assessing the safety and efficacy of regenerative medicine therapies.
Scarfe L, Brillant N, Kumar JD, Ali N, Alrumayh A, Amali M, Barbellion S, Jones V, **Niemeijer M**, Potdevin S, Roussignol G, Vaganov A, Barbaric I, Barrow M, Burton NC, Connell J, Dazzi F, Edsbagge J, French NS, Holder J, Hutchinson C, Jones DR, Kalber T, Lovatt C, Lythgoe MF, Patel S, Patrick PS, Piner J, Reinhardt J, Ricci E, Sidaway J, Stacey GN, Starkey Lewis PJ, Sullivan G, Taylor A, Wilm B, Poptani H, Murray P, Goldring CEP, Park BK.
NPJ Regen Med. 2017. doi: 10.1038/s41536-017-0029-9.

Systems Microscopy Approaches in Unraveling and Predicting Drug-Induced Liver Injury (DILI).
Niemeijer M, Hiemstra S, Wink S, Den Hollander W, Braak B, van de Water B.
Chapter in book: Chen, M., Will, Y. (eds) Drug-Induced Liver Toxicity. Methods in Pharmacology and Toxicology. Humana, New York, NY. 2018. doi: 10.1007/978-1-4939-7677-5_29.

System Microscopy of Stress Response Pathways in Cholestasis Research.
Schimming JP, Ter Braak B, **Niemeijer M**, Wink S, van de Water B.
Chapter in book: Vinken, M. (eds) Experimental Cholestasis Research. Methods in Molecular Biology, vol 1981. Humana, New York, NY. 2019. doi: 10.1007/978-1-4939-9420-5_13

ATF6 Is a Critical Determinant of CHOP Dynamics during the Unfolded Protein Response.
Yang H*, **Niemeijer M***, van de Water B, Beltman JB.
***Both authors contributed equally**
iScience. 2020. doi: 10.1016/j.isci.2020.100860.

Utility of Extrapolating Human S1500+ Genes to the Whole Transcriptome: Tunicamycin Case Study.
Mav D, Phadke DP, Balik-Meisner MR, Merrick BA, Auerbach S, **Niemeijer M**, Huppelschoten S, Baze A, Parmentier C, Richert L, van de Water B, Shah RR, Paules RS.
Bioinform Biol Insights. 2020. doi: 10.1177/1177932220952742.

From fatty hepatocytes to impaired bile flow: Matching model systems for liver biology and disease.
Kunst RF, **Niemeijer M**, van der Laan LJW, Spee B, van de Graaf SFJ.
Biochem Pharmacol. 2020. doi: 10.1016/j.bcp.2020.114173.

In Vitro Three-Dimensional Liver Models for Nanomaterial DNA Damage Assessment.
Llewellyn SV, **Niemeijer M**, Nymark P, Moné MJ, van de Water B, Conway GE, Jenkins GJS, Doak SH.
Small. 2021. doi: 10.1002/smll.202006055.

Systematic transcriptome-based comparison of cellular adaptive stress response activation networks in hepatic stem cell-derived progeny and primary human hepatocytes.
Ter Braak B*, **Niemeijer M***, Boon R, Parmentier C, Baze A, Richert L, Huppelschoten S, Wink S, Verfaillie C, van de Water B.
***Both authors contributed equally.**
Toxicol In Vitro. 2021. doi: 10.1016/j.tiv.2021.105107.

Towards an advanced testing strategy for genotoxicity using image-based 2D and 3D HepG2 DNA damage response fluorescent protein reporters.
Ter Braak B*, **Niemeijer M***, Wolters L, Le Dévédec S, Bouwman P, van de Water B.
***Both authors contributed equally.**
Mutagenesis. 2021 doi: 10.1093/mutage/geab031.

Integration of temporal single cell cellular stress response activity with logic-ODE modeling reveals activation of ATF4-CHOP axis as a critical predictor of drug-induced liver injury.
Wijaya LS, Trairatphisan P, Gabor A, **Niemeijer M**, Keet J, Alcalà Morera A, Snijders KE, Wink S, Yang H, Schildknecht S, Stevens JL, Bouwman P, Kamp H, Hengstler J, Beltman J, Leist M, Le Dévédec S, Saez-Rodriguez J, van de Water B.
Biochem Pharmacol. 2021. doi: 10.1016/j.bcp.2021.114591.

The human hepatocyte TXG-MAPr: gene co-expression network modules to support mechanism-based risk assessment.
Callegaro G, Kunnen S, Trairatphisan P, Grosdidier S, **Niemeijer M,** Den Hollander W, Guney E, Piñero J, Furlong LI, Webster Y, Saez-Rodriguez J, Sutherland J, Mollon J, Stevens J, van de Water B.
Archives of Toxicology. 2021. doi: 10.1007/s00204-021-03141-w.

Fluorescent tagging of endogenous Heme oxygenase-1 in human induced pluripotent stem cells for high content imaging of oxidative stress in various differentiated lineages.
Snijders KE, Fehér A, Táncos Z, Bock I, Téglási A, van den Berk L, **Niemeijer M**, Bouwman P, Le Dévédec SE, Moné MJ, Van Rossom R, Kumar M, Wilmes A, Jennings P, Verfaillie CM, Kobolák J, Ter Braak B, Dinnyés A, van de Water B.
Arch Toxicol. 2021. doi: 10.1007/s00204-021-03127-8.

Recapitulating Cholangiopathy-Associated Necroptotic Cell Death In Vitro Using Human Cholangiocyte Organoids.
Shi S, Verstegen MMA, Roest HP, Ardisasmita AI, Cao W, Roos FJM, de Ruiter PE, **Niemeijer M**, Pan Q, IJzermans JNM, van der Laan LJW.
Cell Mol Gastroenterol Hepatol. 2022. doi: 10.1016/j.jcmgh.2021.10.009.

Model-based translation of DNA damage signaling dynamics across cell types.
Heldring MM, Wijaya LS, **Niemeijer M**, Yang H, Lakhal T, Le Dévédec SE, van de Water B and Beltman JB.
PLoS Computational Biology. 2022. doi: 10.1371/journal.pcbi.1010264.

Assessing the transferability and reproducibility of 3D in vitro liver models from primary human multi-cellular microtissues to cell-line based HepG2 spheroids.
Llewellyn SV, Kermanizadeh A, Ude V, Jacobsen NR, Conway GE, Shah UK, **Niemeijer M**, Moné MJ, van de Water B, Roy S, Moritz W, Stone V, Jenkins GJS, Doak SH.
Toxicol In Vitro. 2022. doi: 10.1016/j.tiv.2022.105473.

Mapping inter-individual variability of toxicodynamics using high throughput transcriptomics and primary human hepatocytes from 50 donors..
Niemeijer M, Wiecek W, Huppelschoten S, Bouwman P, Baze A, Parmentier C, Richert L, Paules R, Bois F, van de Water B.
BioRxiv. 2021. doi: 10.1101/2021.08.26.457742.
Environmental Health Perspectives. 2022. Under review.

Discovery of EMX1 as master regulator of the unfolded protein response and drug sensitivity of liver cells.

Niemeijer M, Tahir N, Kartal P, Vlasveld M, Callegaro G, Bouwman P and van de Water B. Ready for submission. 2022.